INL/EXT-15-36541

Light Water Reactor Sustainability Program

Industry Application
Emergency Core Cooling System
Cladding Acceptance Criteria
Early Demonstration

Ronaldo H Szilard, Cesare Frepoli, Joseph P Yurko, Robert Youngblood, Andrea Alfonsi, Angelo Zoino, Cristian Rabiti, Hongbin Zhang, Paul D Bayless, Haihua Zhao, Gregg Swindlehurst, Curtis L Smith

September 2015

DOE Office of Nuclear Energy

INL/EXT-15-36541

Light Water Reactor Sustainability Program

Industry Application
Emergency Core Cooling System
Cladding Acceptance Criteria
Early Demonstration

Principal Investigator:
Ronaldo H Szilard, INL

Integrated Evaluation Model Framework:
Cesare Frepoli, FPoliSolutions
Joseph P Yurko, FPoliSolutions
Robert Youngblood, INL

Core Design Analysis:
Andrea Alfonsi, INL
Angelo Zoino, University of Rome
Cristian Rabiti, INL

Thermal-Hydraulics Analysis:
Hongbin Zhang, INL
Paul D Bayless, INL
Haihua Zhao, INL

Industry Application Implementation:
Gregg Swindlehurst, GS Nuclear Consulting

RISMC Pathway Lead:
Curtis L Smith, INL

September 2015

Idaho National Laboratory
Idaho Falls, Idaho 83415

http://www.inl.gov/lwrs

Prepared for the
U.S. Department of Energy
Office of Nuclear Energy
Under DOE Idaho Operations Office
Contract DE-AC07-05ID14517

EXECUTIVE SUMMARY

The U. S. NRC is currently proposing rulemaking designated as "10 CFR 50.46c" to revise the loss-of-coolant-accident (LOCA)/emergency core cooling system (ECCS) acceptance criteria to include the effects of higher burnup on cladding performance as well as to address other technical issues. This report presents a first step towards developing a tool for managing safety margin under the proposed rule. The development is one of several "industry applications" being addressed within the Risk-Informed Safety Margin Characterization (RISMC) Pathway, as part of the DOE Light Water Reactor Sustainability (LWRS) research and development Program.

The impact of the final 50.46c rule on the industry may involve updating of fuel vendor LOCA evaluation models; NRC review and approval; and licensee submittal of new LOCA evaluations or re-analyses and associated technical specification revisions for NRC review and approval. The proposed rule implementation process, including both industry and NRC activities, is expected to take four-to-six years following the rule effective date. The proposed rule may motivate the need to use advanced cladding designs. A loss of operational margin may result due to the more restrictive cladding embrittlement criteria. Initial and future compliance with the proposed rule may significantly increase vendor workload and licensee cost as a spectrum of fuel rod initial burnup states may need to be analyzed to demonstrate compliance. Consequently, there will be an increased focus on licensee decision making related to LOCA analysis to minimize cost and impact, and to manage margin.

The proposed rule would apply to a light water reactor and to all cladding types. The key points of the proposed rule are as follows:

- Cladding performance cannot be evaluated in isolation. Both cladding and ECCS performance need to be considered in a coupled manner.
- Models for cladding performance even within the design basis will need to be updated for regulatory purposes.
- Effort needs to be expended in searching regulatory issue space for the limiting case(s).

The RISMC Toolkit is sufficiently mature to offer a potential solution to this LOCA/ECCS analysis. The use of the Toolkit will provide to the plant owner/operator a vehicle to inform decisions to manage margins related to compliance with the proposed 10 CFR 50.46c rule. Note that the margins being analyzed in this application include aspects of safety, operations, and economics. This margin characterization is the driver behind the RISMC Industry Application #1 (IA1) and provides justification of this project demonstration. The industry will need to comply with the proposed rule within the following four-to-six years (the timeline for implementation is still being discussed among the industry stakeholders and will depend on factors such as methodology changes, amount of work to be submitted for regulatory approval, and regulatory reviews).

The risk-informed margins management approach for IA1 will provide a means of quantifying the impact on the key LOCA analysis figures-of-merit: peak cladding temperature (PCT), equivalent cladding reacted (ECR), and core-wide oxidation (CWO) of a change in LOCA analysis inputs. The information that the risk analysis and associated tools provide can then be used for decision making and margin management.

As described in this report, the IA1 "Early Demonstration" analysis uses a representative 4 loop Westinghouse pressurized water reactor (PWR) system in order to apply a framework to characterize the behavior of complex LOCA phenomena in a realistic way. By integrating the probabilistic element in RISMC with deterministic methods for LOCA analysis, we provide a novel approach to solving these types of multi-physics problems. Specific to IA1, the steps we demonstrated for the Early Demonstration are:

- First, we construct a reduced order model (ROM) which allows us to characterize inputs and outputs to be optimized.

- Second, we construct a reactor system representing a typical 4-Loop Westinghouse PWR, and search for a core design and loading pattern that can operate such a system for 18 months of full power operation. This core design consists of energy characteristics typically desired from current large PWRs in the U.S.
- Third, we simulate a postulated large-break loss-of-coolant accident with a reactor systems code coupled to our demonstration core design. Using this coupled system, we analyze the behavior of LOCA transients over three fuel cycles.
- Fourth, using sampling, we apply the RISMC methodology to the above coupled system models to analyze a couple thousand scenario simulations to characterize, with high confidence, the representative plant and core response to such postulated scenarios. This risk-informed analysis allows us to determine the margin characteristics of important safety and economic metrics for the plant.

Ultimately for IA1, we want to construct an Integrated Evaluation Model (IEM) that addresses an integrated approach to core design, transient analysis, thermal-hydraulics, and risk management. Via the RISMC methodology, the primary characteristic of this integrated multi-physics toolkit is that (in contrast with current approaches) every physics model is resolved using coupling which addresses the complexities of the analysis issues.

As an example of an industry use, we envision an owner/operator using the IEM tool to "characterize" the core designed for operation. The figure below illustrates this process, where the IEM maps an envelope of maximum ECR as a function of cycle exposure (the red "surface"). This allows the operator to have a realistic assessment of a planned core operation. This design characterization process is intended to streamline the existing core reload analysis process. Using the RISMC Toolkit, the goal is that the owner/operator could re-analyze their design in a more efficient way than using traditional reload design analysis processes.

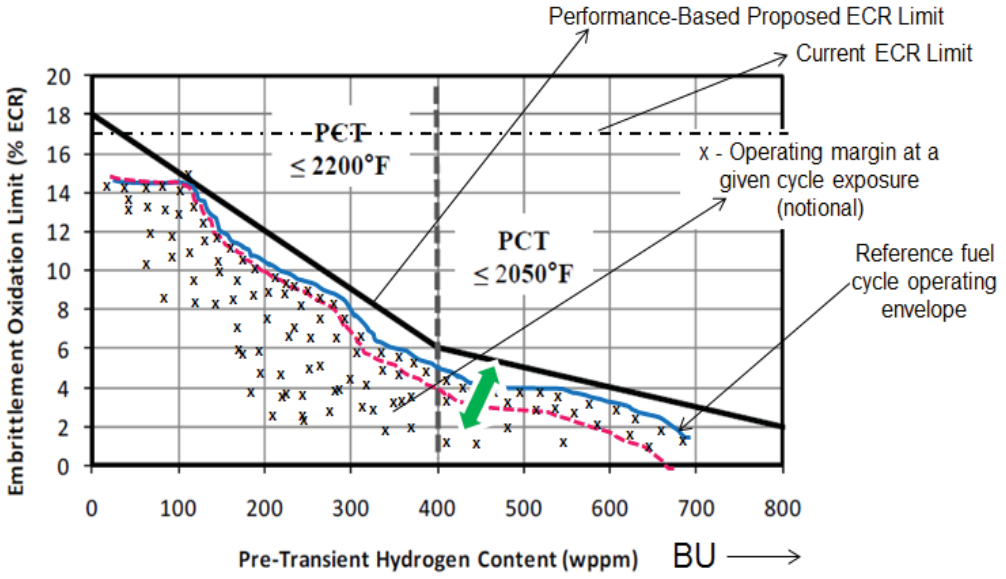

Eventually, we will be able to incorporate optimization schemes in the IEM that can reshape a desired parameter envelope (in this case ECR) as an optimization feature of a planned core operation. For example, we will have the ability to move a characterized surface (red line) to a new desired state (blue line) and, as result, improve desired metrics (as illustrated by the green arrow above) such as fuel utilization/economics. The end outcome allows the plant owner/operator to incorporate probabilistic LOCA analysis as an integrated element of the reload analysis process, including the ability to satisfy regulatory changes while improving operations through enhanced margin management.

CONTENTS

FIGURES

TABLES

ACRONYMS

ACC	Accumulator
AEC	Atomic Energy Commission
ANOVA	Analysis of Variance
AOR	Analysis of Record
BEAVRS	Benchmark for Evaluation and Validation of Reactor Simulations
BELOCA	Best Estimate Loss-of-Coolant Accident Analysis
BEPU	Best-Estimate Plus Uncertainty
BOC	Beginning of Cycle
BU	Burn-Up
CD	Core Design
CDF	Core Damage Frequency
CDF	Cumulative Density Function
CFR	Code of Federal Regulations
CI	Confidence Interval
CP	Cathcart-Pawel Correlation
CPU	Central Processing Unit
CSAU	Code Scaling, Applicability, and Uncertainty
CWO	Core-Wide Oxidation
DET	Dynamic Event Tree
DG	Draft Regulatory Guide
DOE	Department of Energy
ECC	Emergency Core Cooling
ECCS	Emergency Core Cooling System
ECR	Equivalent Cladding Reacted
EPRI	Electric Power Research Institute
EOC	End of Cycle
FA	Flow Area
FAST	Fourier Amplitude Sensitivity Test
FLEX	Diverse and Flexible Coping Strategies
FOM	Figure of Merit
FRC	Fractional Rate Change
FRD	Fuel Rod Design

FSA	Fractional Scaling Analysis
GDC	General Design Criteria
GE	General Electric
GI	Generic Issue
GP	Gaussian Process
GWD/MTU	Gigawatt-Days per Metric Ton of Uranium
HA	Hot Assembly
H-DET	Hybrid Dynamic Event Tree
HR	Hot Rod
HPC	High Performance Computing
HPI	High Pressure Injection
HTC	Heat Transfer Coefficient
IA	Industry Application
IA1	Industry Application #1
ID	Inside Diameter
IEM	Integrated Evaluation Model
INL	Idaho National Laboratory
KS	Kolmogorov-Smirnov
LAR	License Amendment Request
LB-LOCA	Large Break Loss-of-Coolant Accident
LERF	Large Early Release Frequency
LF-MCMC	Likelihood-Free Markov Chain Monte Carlo
LHR	Linear Heat Rate
JCO	Justification of Continued Operation
JPO	Justification for Past Operation
LOCA	Loss-of-Coolant Accident
LPI	Low Pressure Injection
LWRS	Light Water Reactor Sustainability
MC	Monte Carlo
MCF	Monte Carlo Filtering
MCMC	Markov Chain Monte Carlo
MLO	Maximum Local Oxidation
MOC	Middle of Cycle
MOOSE	Multiphysics Object Oriented Simulation Environment
MSIV	Main Steam Line Isolation Valve

NFI	Nuclear Fuels Industries
NPP	Nuclear Power Plant
NRC	Nuclear Regulatory Commission
NTTF	Near-Term Task Force
NUREG	Nuclear Regulatory Report
OD	Outside Diameter
ODE	Ordinary Differential Equation
PCT	Pea Cladding Temperature
PHISICS	Parallel and Highly Innovative Simulation for the INL Code System
PIRT	Phenomena Identification and Ranking Table
PORV	Power Operated Relief Valves
PRA	Probabilistic Risk Assessment
PWR	Pressurized Water Reactor
PWROG	PWR Owners Group
RAVEN	Risk Analysis in a Virtual Control Environment
R&D	Research and Development
RBHT	Rod Bundle Heat Transfer
RCP	Reactor Coolant Pump
RCS	Reactor Coolant System
RELAP5-3D	Reactor Excursion and Leak Analysis Program Version 5-3D
RELAP7	Reactor Excursion and Leak Analysis Program Version 7
RG	Regulatory Guide
RHS	Right Hand Side
RIMM	Risk-Informed Margin Management
RISMC	Risk-Informed Safety Margin Characterization
ROM	Reduced Order Model
ROP	Reactor Oversight Program
RPV	Reactor Pressure Vessel
RSA	Regionalized Sensitivity Analysis
SA	Sensitivity Analysis
SBO	Station Blackout
SDP	Significant Determination Process
SECY	NRC Action Memorandum
SI	Safety Injection
SSCs	Structures, Systems, and Components

TCD	Thermal Conductivity Degradation
TH	Thermal Hydraulic
TPG	Technical Program Group
UQ	Uncertainty Quantification
V&V	Verification and Validation
WEC	Westinghouse Electric Company
WPPM	Weight Parts per Million

Industry Application Emergency Core Cooling System Cladding Acceptance Criteria Early Demonstration

1. INTRODUCTION

1.1 Problem Definition

The U. S. NRC is currently proposing rulemaking designated as "10 CFR 50.46c" to revise the loss-of-coolant-accident (LOCA)/emergency core cooling system (ECCS) acceptance criteria to include the effects of higher burnup on cladding performance as well as to address other technical issues. This report presents a first step towards developing a tool for managing safety margin under the proposed rule. The development is one of several "industry applications" being addressed within the Risk-Informed Safety Margin Characterization (RISMC) Pathway, as part of the DOE Light Water Reactor Sustainability (LWRS) research and development Program.

The RISMC toolkit is now sufficiently matured to offer a potential solution to the LOCA problem and provide to the plant owner/operator a vehicle to manage margins and inform decisions if compliance with the revised 10 CFR 50.46 is challenged by changes in the operational envelope.

This is the driver behind the RISMC Industry Application 1 (IA1), and motivates this project, "Risk Informed Margin Management (RIMM)." In this project, margin is measured relative to the 10 CFR 50.46c proposed rule which is expected to be amended in 2016. The industry will need to comply with the proposed rule within four to six years of the change (the timeline for implementation is still being discussed among the NRC, fuel vendors, and licensees, and will depend on many factors, such as methodology changes, amount of work to be submitted for regulatory approval, and regulatory reviews).

Following work done in INL-EXT-15-35073, where the LOCA/ECCS problem was initially described, our purpose is to show the viability of RISMC methods and tools and their value to the industry stakeholder by demonstrating this application on a realistic PWR problem, solving a large break LOCA postulated event using a set of methods and tools that will lead to informed operating decisions aimed at characterizing safety margins realistically, and optimizing such margins on a safe, reliable operating environment considering the economics of the fuel cycle.

A LOCA safety analysis involves several disciplines which are computationally loosely (externally) coupled to facilitate the process and maintenance of legacy codes and methods. A review of a few examples of analyses performed by vendors such as AREVA and Westinghouse Electric Company (WEC) is instructive to define the state-of-the-art in the industry.

The key disciplines involved in a LOCA analysis are:

- Core physics;
- Fuel rod thermomechanics;
- Clad corrosion;
- LOCA thermal-hydraulics;
- Containment behavior.

The figures of merit (FOMs) are the relevant search parameters tied to the acceptance criteria of the rule. The proposed rule would replace the prescriptive analytical requirements of the previous rule [peak clad temperature (PCT)<2200°F, MLO<17%, etc.], with performance-based requirements.

The Draft Regulatory Guide DG-1263 defines an acceptable analytical limit on peak cladding temperature and integral time at temperature for the zirconium-alloy cladding materials tested in the U.S. Nuclear Regulatory Commission's (NRC's) loss-of-coolant accident (LOCA) research program. This analytical limit is based on the data obtained in the NRC's LOCA research program.

Referring to DG-1263, for example, the analytical limit presented in Figure 1-1 will be substituted for the existing 17% limit. The hydrogen content (weight-ppm) depends on the burnup value and material characteristic of the cladding, i.e. performance to embrittlement under irradiation for a specific cladding alloy. The ductile-to-brittle threshold, defined in Figure 1-2, is an acceptable analytical limit on integral time at temperature (as calculated in local oxidation calculations using the Cathcart-Pawel (CP) correlation.

The other Draft Regulatory Guides, DG-1261 and DG-1262 describe experimental techniques that are acceptable to the U.S. Nuclear Regulatory Commission (NRC) for determining these limits in general.

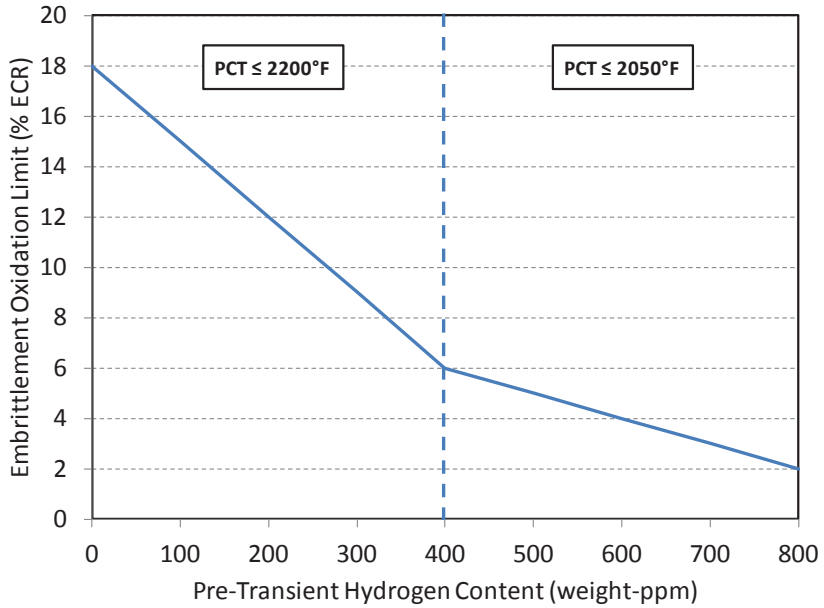

Figure 1-1. 10CFR 50.46c Proposed Limits. An acceptable Analytical Limit on Peak Cladding Temperature and Integral Time at Temperature (as Calculated in Local Oxidation Calculations).

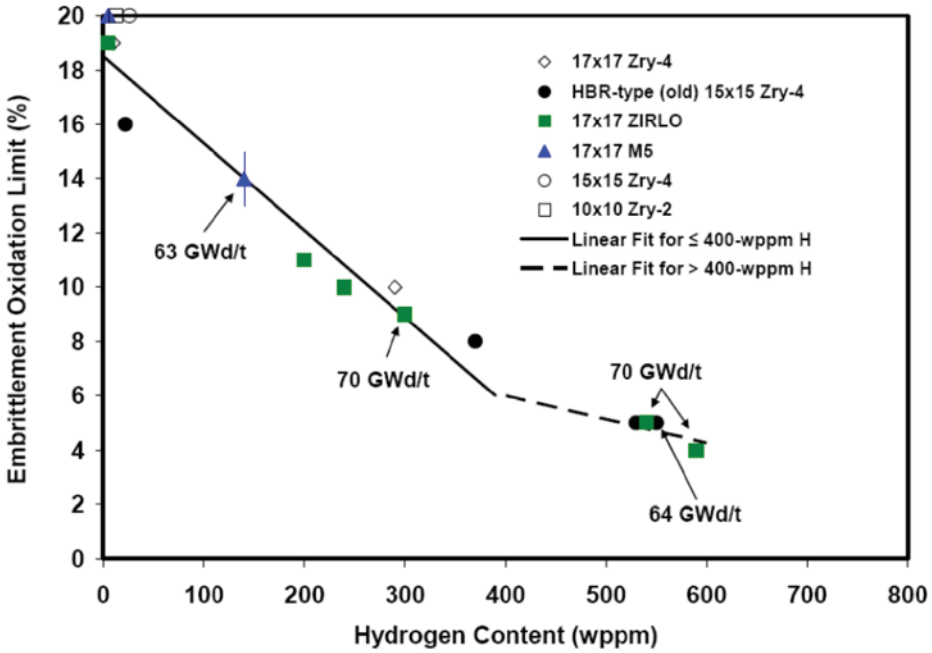

Figure 1-2. Ductile-to-Brittle Transition Oxidation Level as a Function of Pretest Hydrogen Content in Cladding Metal for As-Fabricated, Pre-Hydrided, and High-Burnup Cladding Materials. [DG-1263]

Note that the temperature limit (at least when the pre-transient hydrogen content is less than 400 wppm) is still the same, i.e. 2200°F. However, the margin to embrittlement significantly decreases as the fuel is irradiated in the core and the cladding hydrogen concentration increases.

As a result of local oxidation, a measure of time-at-temperature is anticipated to be the controlling FOM under the proposed rule. In general term the two criteria equivalent cladding reacted (ECR) and PCT should be treated jointly.

1.2 Problem Scope

Given the acceptance criteria levied by the proposed rule, a question is raised: How can we best configure the core and operate the plant while still satisfying the regulatory acceptance criteria? Figure 1-3 shows a high-level concept of one way to address the needs created by the proposed rule. Establishing compliance with the new acceptance criteria will require quantification of more complicated FOMs, which in turn calls for application of more detailed models and more complicated analyses of those models. Moreover, the issue of how best to optimize core configuration in light of the new criteria is still a topic of research. Correspondingly, the early phases of Figure 1-3 include consideration of both safety and performance, and anticipate a need to consider many variations on core configuration and initial conditions in order to formulate the appropriate strategy.

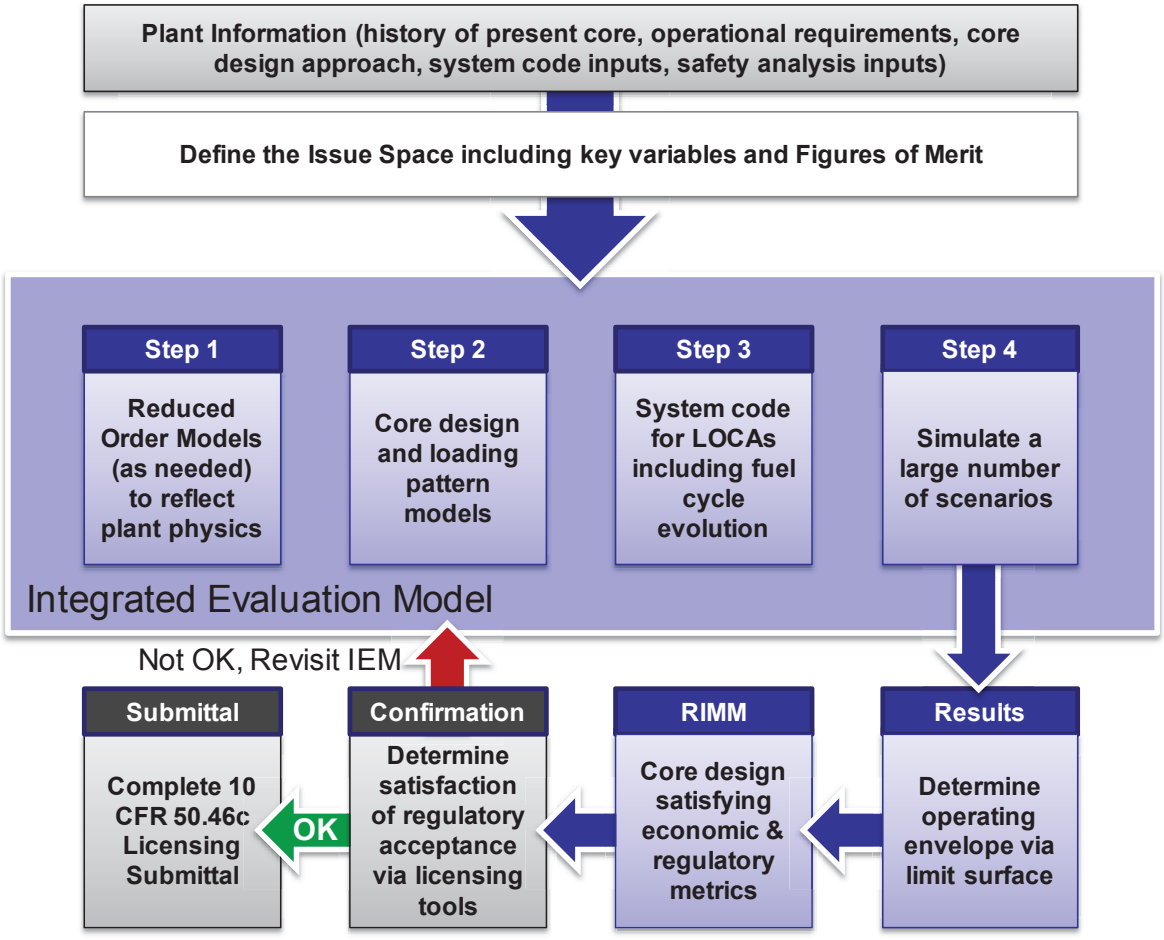

Figure 1-3. Overview of a Notional Process for Optimizing Core Configuration and Demonstrating Acceptable Safety Performance.

Figure 1-3 starts at the top, where current plant information is gathered along with operational issues to be addressed in the analysis. This information is then fed into "Issue Space" formulation, where relevant control variables and key uncertainties are identified. These two groups of information both feed into the Integrated Evaluation Model (IEM) which embodies the complete integrated analysis model including the specification of the components and systems comprised in the plant that need to be modeled; the applicable physics and chemistry of their interaction; and plant safety models and data. Currently, for reasons discussed in the main body of the report, it appears that more detailed plant models will be required under the proposed rule. The IEM will be used to search the Issue Space for a core configurations (and operating plans) that (a) has adequate margin to the acceptance criteria and (b) provides enhanced economics.

The scope of IA1, and this report, is also shown in Figure 1-3. The process *up to* the last two steps (Confirmation and Submittal, shaded in grey) are included in the research and development within RISMC. This process will be used to identify a candidate core configuration(s) / operation plan(s) that meets the RIMM requirements. Within the process envisioned here, IA1 will not develop the licensing tool; instead it will develop the IEM, a margin management tool whose safety claims need to be validated by the licensing tool for licensing purposes. In the event that the results of the confirmatory analysis are unsatisfactory, the analysis is designed to loop back, as shown by the arrow leading out of "Confirmation."

1.3 Problem Proposition

The RIMM IA1 methodology and tool will provide a means of quantifying the impact on the key LOCA analysis figures of merit PCT, ECR, and core-wide oxidation (CWO) of a change in LOCA analysis inputs. This information would be obtained without the resource requirement, cost, and schedule, of an actual LOCA reanalysis using a LOCA evaluation model. The information that the tool provides can then be used for decision making and margin management.

1.3.1 Value Proposition for the Industry

Nuclear installation designers, vendors and licensees (plant owner/operators) operate in a regulated environment. Traditionally, the economics of the industry prevent large deviations from well established procedures within the licensing basis of the evaluation models which are already in place. For example, the complex multi-physics LOCA problem is solved via operator splitting where various engineering disciplines are interfaced with well-set rules which have been developed over the years consistently with specific acceptance criteria and regulatory requirements. Further, the propagation of uncertainties across the various functional groups is addressed by defining bounding assumptions at the interfaces which limit the possibility that the impact of an issue in a specific discipline (error discovered, design change or other) to cross-over to other physics in an efficient fashion.

Such traditional processes and interfaces do not easily adapt to new integrated methods and cannot fully leverage the progress that has been made in computation and numerical algorithms. Also there is a difficulty in absorbing new knowledge in the processes which is now recognized by regulators and the industry as a whole. In other words the methods are limited in their responsiveness.

Even state-of-the-art best-estimate plus uncertainty methods provide little information on the actual margin available in the plants. Most margin resides in engineering judgment and conservative assumptions which were built to deal with the imperfect knowledge.

Moving forward, the industry is expected to develop better standardized databases and improved interfaces across the various engineering disciplines as more automation is implemented in the processes. This will enable consideration of new paradigms to manage the uncertainties across the various disciplines with a truly multi-physics approach to the LOCA problem.

The RIMM IA1 project is expected to create value by anticipating these trends and focusing on developing a methodology that effectively addresses the limitations presented above. The primary goal is to explore an *integrated* approach for knowledge and uncertainty management, as illustrated in Figure 1-4.

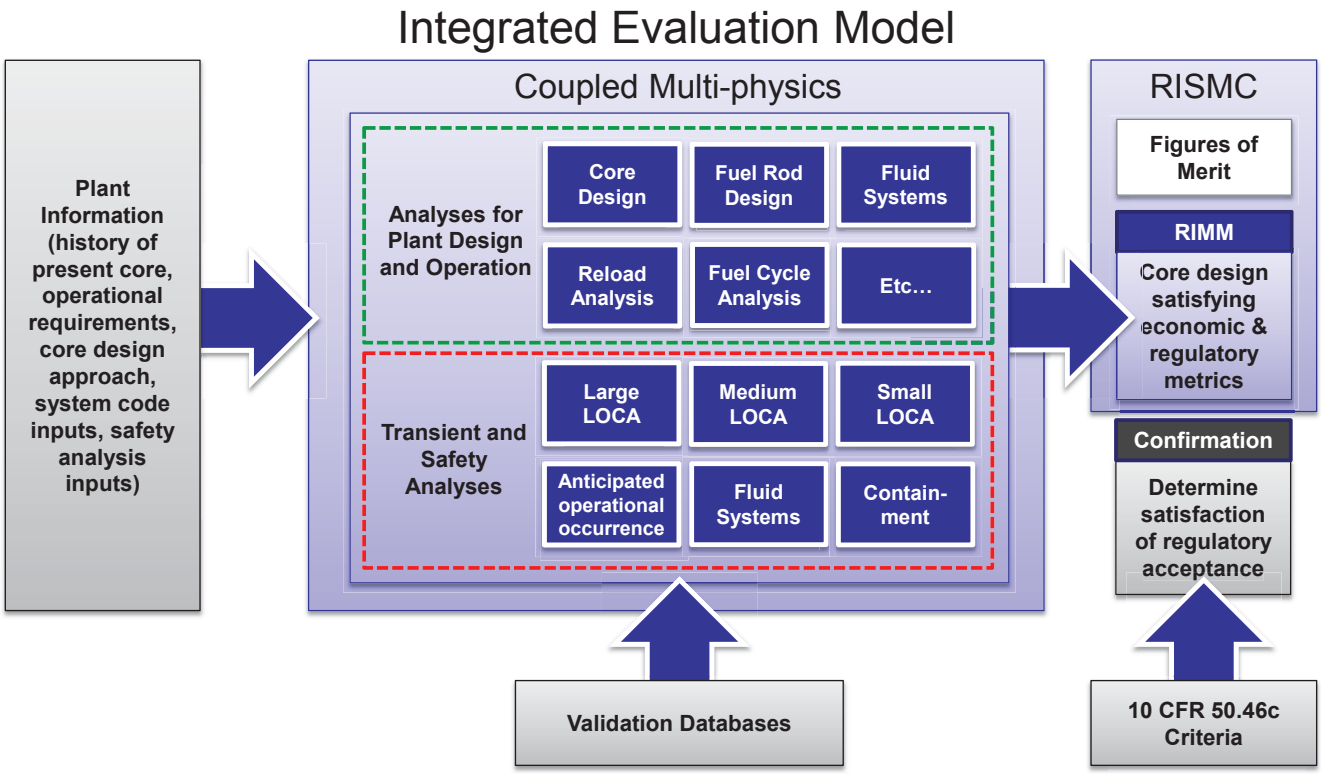

Figure 1-4. Flow Chart of the RIMM Integrated Evaluation Model. [derived from INL-EXT-15-35073]

The vision for the RIMM IEM is summarized in the following propositions:

- Provide a responsive toolkit for the plant operator which enables rapid decisions on considered changes within the LOCA issue space (as regulated under the new 10 CFR 50.46c). The goal is to greatly reduce the response cycle.
- Enable current knowledge to be factored into the process to enhance safety and operation optimization.
- Quantify currently-unquantified uncertainties (to the extent practical) and trends to a realistic representation of the LOCA which provides insights on the design.
- Foster an approach that can lead to new knowledge and understanding of the LOCA scenarios which could be "locked" in the engineering assumption of licensing calculations. Enable a more effective "exploration" of the issue space in order to improve core design.
- Eliminate issues associated with the Wilks' approach (including variability in the estimator, risk of under-prediction of or over-prediction of FOM, lack of knowledge in what is limiting in the design, incapacity to perform sensitivity studies, etc.)
- A "plug-and-play" design of the multiphysics tool which enables plant owner/operators and vendors to consider and further develop the RIMM Framework for use with their established codes and methods.

Note that the RIMM IEM is not intended to replace licensing Analyses of Record (AORs) but rather to replace or aid the engineering judgment applied in managing those AORs. In other words, the RIMM IEM is a margin management tool. This objective is achieved by representing the plant realistically, but in a way that makes it feasible to explore the issue space thoroughly, with all the uncertainties included and by considering and managing the entire body of knowledge.

For practical purposes, the value proposition problem can be broken up in two parts: characterization and optimization, as described below.

1.3.2 Characterization Problem

As an analysis result, the owner/operator will use the RIMM IEM tool to "characterize" the core designed for operation. Figure 1-5 illustrates this process, where the IEM maps an envelope of maximum ECR as a function of cycle exposure. This allows the operator to have a realistic assessment of an operating core, and conceivably be more prepared for a quick response re-analysis in case a problem might occur.

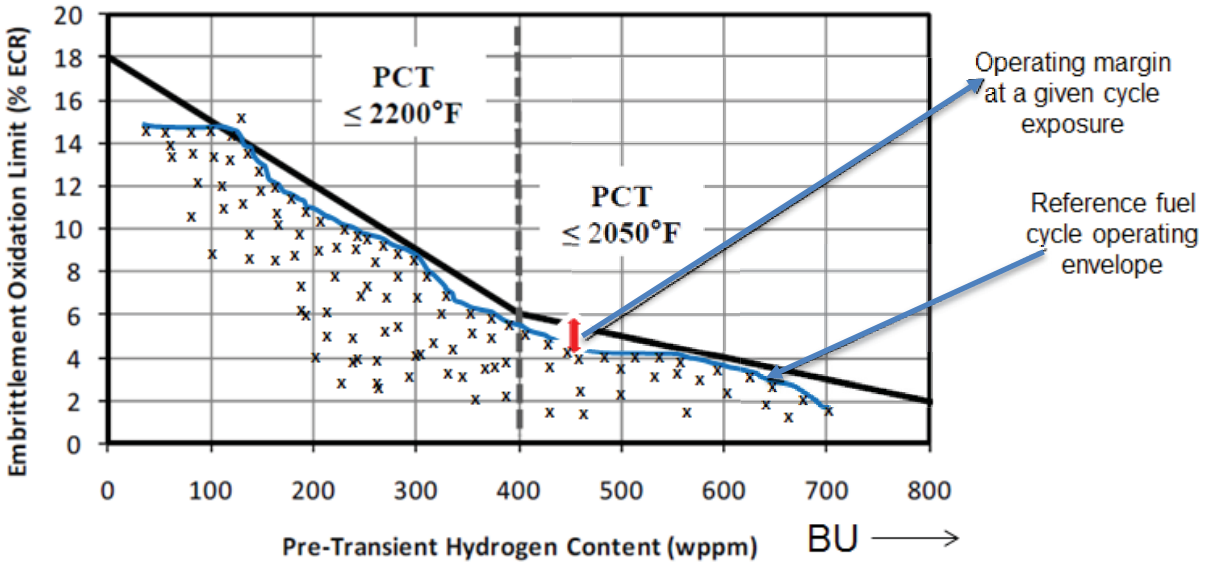

Figure 1-5. Characterization of a Hypothetical Core (the points and curves displayed are notional values, i.e., they are not actual calculations, they are representations of a certain outcome for illustration purposes).

1.3.3 Optimization Problem

The characterization of a reference core with the IEM tool is intended to simplify the existing reload analysis process, although not intended to replace the existing licensing process. In principle, a reload engineer that has trained the IEM tools to analyze a given core design can re-analyze such reference design in much faster time than using a traditional reload design analysis process.

Eventually, we will be able to incorporate optimization schemes in the IEM toolset that can quickly reshape a desired parameter envelope (in this case ECR) as an optimization feature of a core design process, as illustrated in Figure 1-6. In practice, such a step will require additional changes of today's design process, in order to incorporate LOCA analysis as an integrated element of the reload analysis process.

Note that the concept described above is simplified, and it serves the purpose of only illustrating the approach proposed. In practice, the IEM will need to evaluate a multi-dimensional problem not easily visualized as points on a burnup-oxidation plot.

Computational constraints to analyzing highly complex systems with many variables to be considered have kept us in the past from executing these types of schemes. Today, with the development of the RISMC Toolkit built in a state-of-the-art computational environment, we are able to implement complex multi-physics approaches solving fully-coupled systems problems in near-real time.

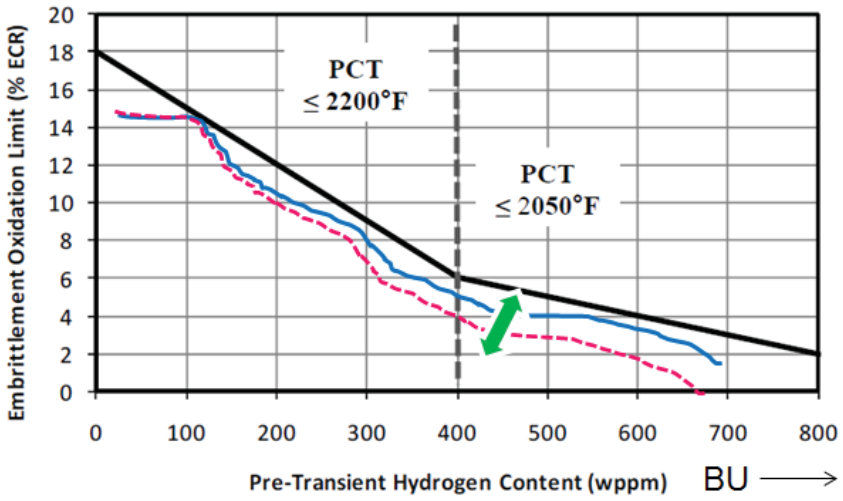

Figure 1-6. Optimization of a characterized core (the curves displayed do not represent actual calculations; they represent a desired pattern for demonstration purposes only).

1.3.4 Fuel Vendor Proposition

For a fuel vendor, the RIMM IA1 methodology and tool is envisioned as a LOCA analysis scoping tool with the following potential uses:

- Provide quantitative estimates of design or operational margin loss or gain associated with various combinations of changes in LOCA analysis inputs
- Provide quantitative estimates of impact on the LOCA analysis figures-of-merit due to limitations in LOCA analysis inputs
- Develop marketing strategies related to LOCA analysis
- Provide LOCA inputs related studies in response to customer inquiries and requests
- Respond to LOCA-related regulatory inquiries and requests for additional information

It is also possible that the RIMM IA1 technology could be advanced in the future to a level of fidelity and maturity that it could be used for some licensing or regulatory situations. An example would be the reporting of LOCA analysis ΔPCT and ΔECR due to LOCA analysis input errors that are required by 10 CFR 50.46.

1.3.5 Owner-Operator Proposition

For an owner-operator, the RIMM IA1 methodology and tool has two distinct types of potential applications. The more likely type of potential applications is for LOCA analysis-related work contracted to the fuel vendor, which could include the following potential uses:

- Obtain quantitative estimates of design or operational margin loss or gain associated with various combinations of changes in LOCA analysis inputs
- Obtain quantitative estimates of impact on the LOCA analysis figures-of-merit due to limitations in LOCA analysis inputs (including reporting of LOCA analysis ΔPCT and ΔECR due to LOCA analysis input errors that are required by 10 CFR 50.46)

A less likely but possible type of potential application is to use the RIMM IA1 methodology and tool as an independent owner/operator LOCA analysis capability. This capability could be used to perform vendor-independent LOCA scoping or audit calculations that would facilitate decision making related to the impact of plant and fuel design changes, as well as provide an enhanced vendor oversight capability. An owner/operator could develop this capability with in-house staff or by outsourcing.

2. FRAMEWORK DESCRIPTION AND REDUCED ORDER MODELS

2.1 Overview of Reduced Order Models (ROMs)

The purpose of this work was to develop a first proof of concept of the RIMM IEM. To achieve fast prototyping, most of the physical disciplines associated with a realistic Large Break LOCA (LB-LOCA) analysis are approximated by Reduced Order Models (ROMs). In this context, the term Reduced Order Model (ROM) denotes simplified physical models (sometimes referred to as "glass box" models). In the full implementation of the RIMM IEM, the ROMs will be replaced by the corresponding simulators (RELAP, PHISICS, Fuel Performance code, etc.).

The key disciplines involved in a LOCA analysis are:

- Core physics;
- Fuel rod thermomechanics;
- Clad corrosion;
- LOCA thermal-hydraulics;
- Containment behavior.

Before describing the setup of the framework, the LOCA scenario and physical phenomena involved are described in the following section.

2.1.1 Physics

2.1.1.1 Description of Large Break LOCA Scenario

The Large Break LOCA scenario considered in this analysis is initiated by a large break of one of the cold legs (Figure 2-1). The cold leg is typically considered as the most limiting location as it limits the ECCS injection in the cold leg, it promotes flow stagnation in the core, and it cause ECCS injection bypass. The transient is characterized by three distinct periods: blowdown, refill, and reflood. The scenario is described for a PWRs equipped with U-tube steam generators. The analysis was originally presented in the "LOCA Compendium" (NUREG-1230).

The blowdown period extends from the initiation of the break until the primary side depressurizes sufficiently that emergency core cooling (ECC) water can start to penetrate the downcomer (20-30 seconds into the transient). The flow out of the break is large, but limited by critical flow phenomena.

No control rod insertion is credited in the event. The boiling and flashing which occurs in the core as result of the rapid depressurization is sufficient to shut down the fission process.

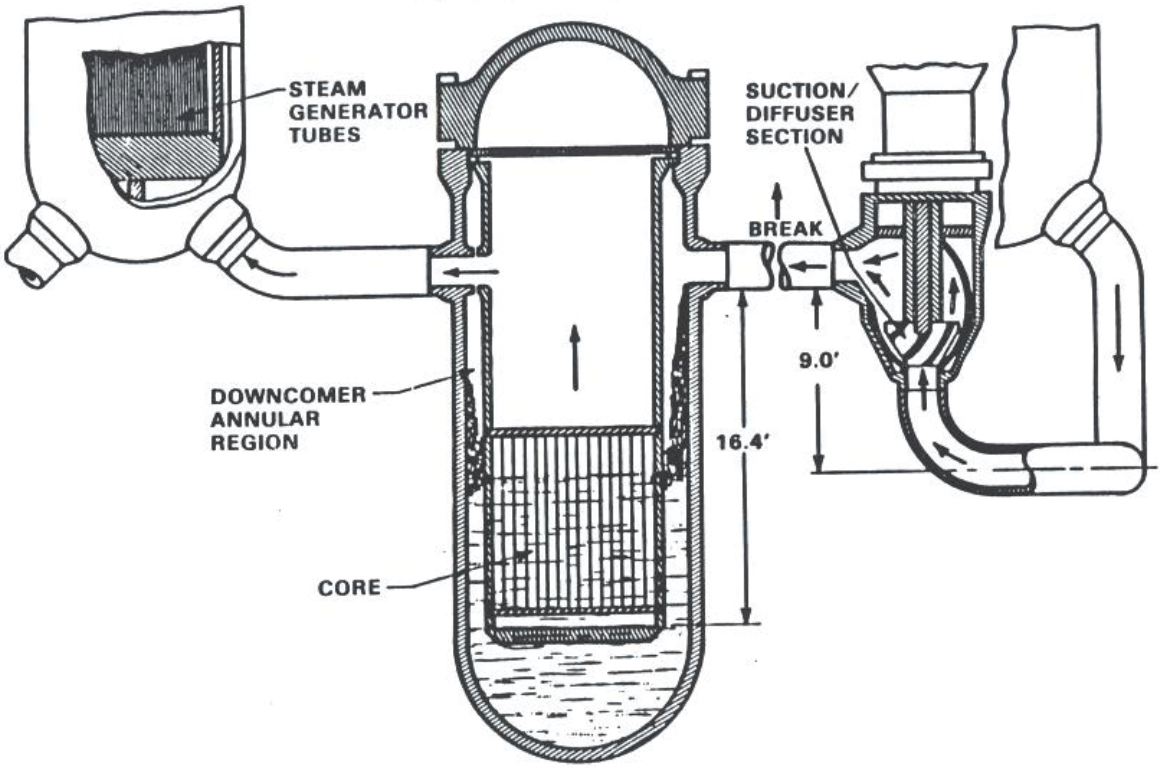

Figure 2-1. Schematic of Double Ended Guillotine Break.

The reactor coolant pumps (RCPs) are assumed to be either functioning or coasting down depending on the off-site power availability assumption. Even if the RCPs are running, the performance will be degraded by the voids. The break flow will eventually reverse the flow in the core and a stagnation situation can be reached in the core (Figure 2-2). The hot fuel rods quickly exceed the critical heat flux, as the core flow reverses, resulting in a sharp reduction in heat transfer to the coolant. As the pressure decreases, the reversed flow induced by the break diminishes and positive core flow can be reestablished.

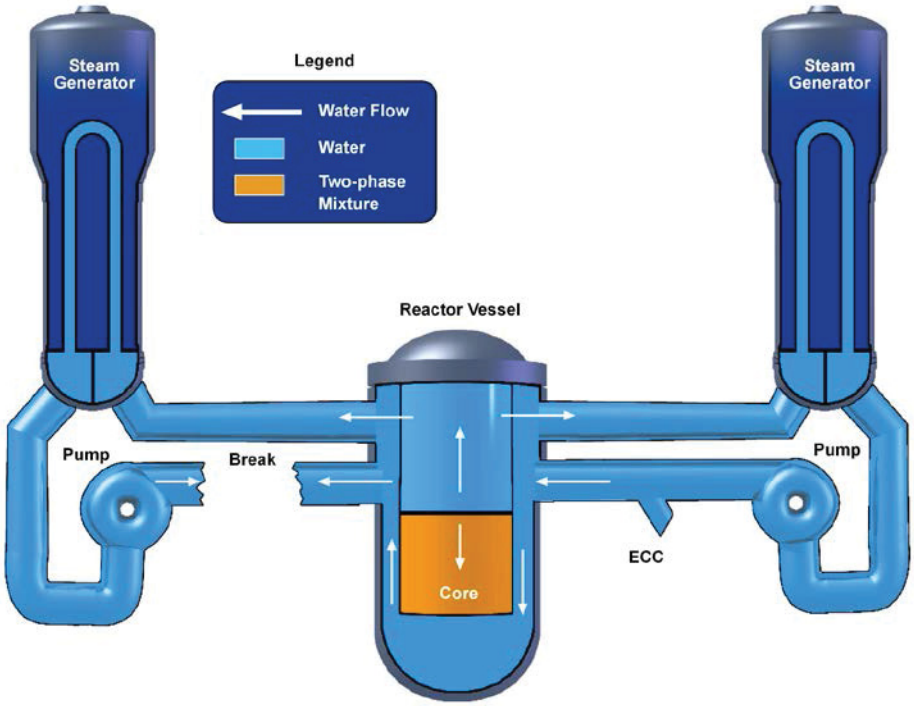

Figure 2-2. Start of the LB-LOCA.

During the blowdown phase, the cladding temperature first rises rapidly as the initial stored energy in the fuel pellets is transferred to the cladding. After the initial heatup, the cladding temperature will decrease due to the down flow of high velocity steam through the core. The lower power regions in the core may even quench during this blowdown cooling phase.

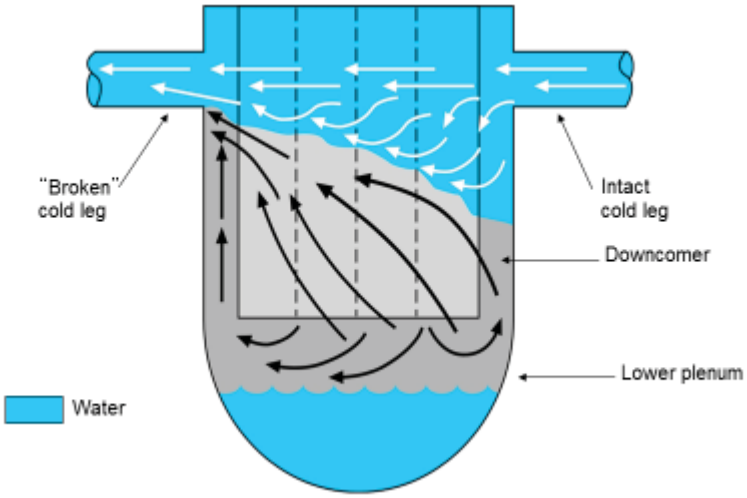

Figure 2-3. Sketch of ECCS Bypass.

Between 10 to 20 seconds after the break, the RCS pressure decreases below the accumulator pressure. The accumulators begin injecting cold water into the cold legs, but the initial injection is swept out of the vessel and into the broken cold leg by the continuing high flow of steam from the core (Figure 2-3). This is due the counter current flow limitation condition in the downcomer.

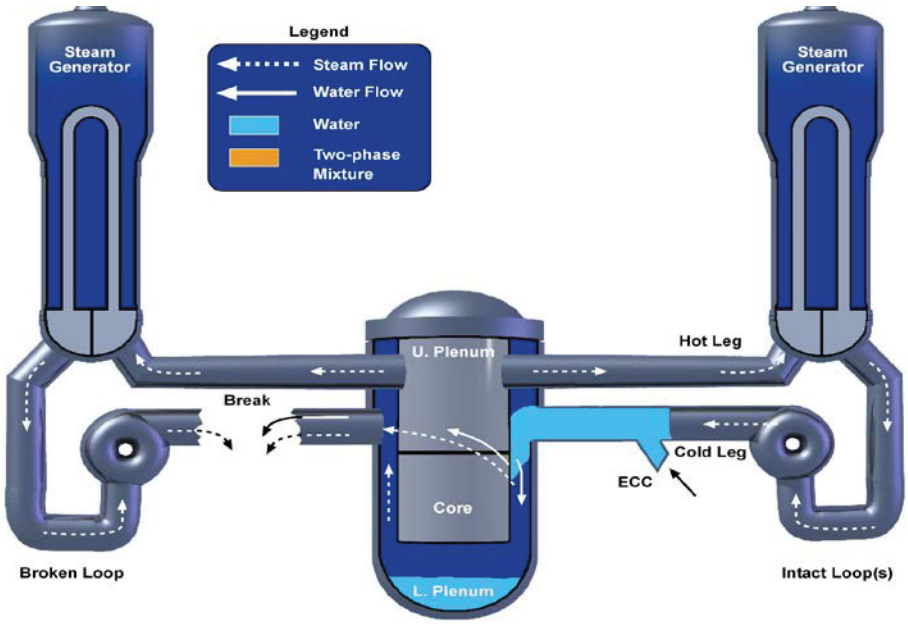

Figure 2-4. Refill Phase.

Approximately 20 to 30 seconds after the break, the RCS pressure approaches the containment pressure and break flow becomes un-choked. This initiates the refill phase. The ECCS water from the accumulators and the pumped safety injection refill the lower plenum and establishes a level in the downcomer (Figure 2-4). As the coolant enters the core, the reflooding process begins.

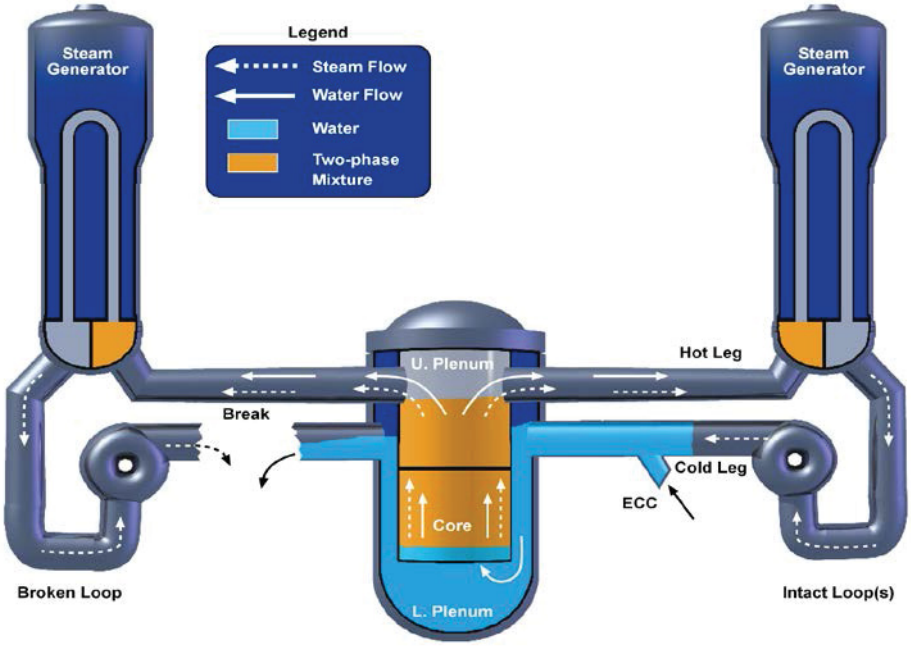

Figure 2-5. Beginning of Reflood.

The reflood of the core is gravity driven. The water head in the downcomer and the backpressure in the upper plenum determines the core flooding rate. The flow into the core is initially oscillatory, as cold water rewets the hot fuel rods, generating steam which in turns create a local pressurization in the core creating a feedback mechanism and a manometric effect between the level in the downcomer and the level in the core.

As the core gradually quenches, steam is generated as the fuel rod dump their stored energy in the liquid and droplets entrained in the steam. This steam, and the water it entrains flows through the vessel upper plenum, the broken loop hot leg, the steam generator, and the pump before it can be vented out the break (Figure 2-5).

As the accumulators empty nitrogen gas is discharged in the system (Figure 2-6). As nitrogen enters the loop and the downcomer steam condensation is suppressed which creates a temporary pressurization in the downcomer and core liquid insurge during reflood.

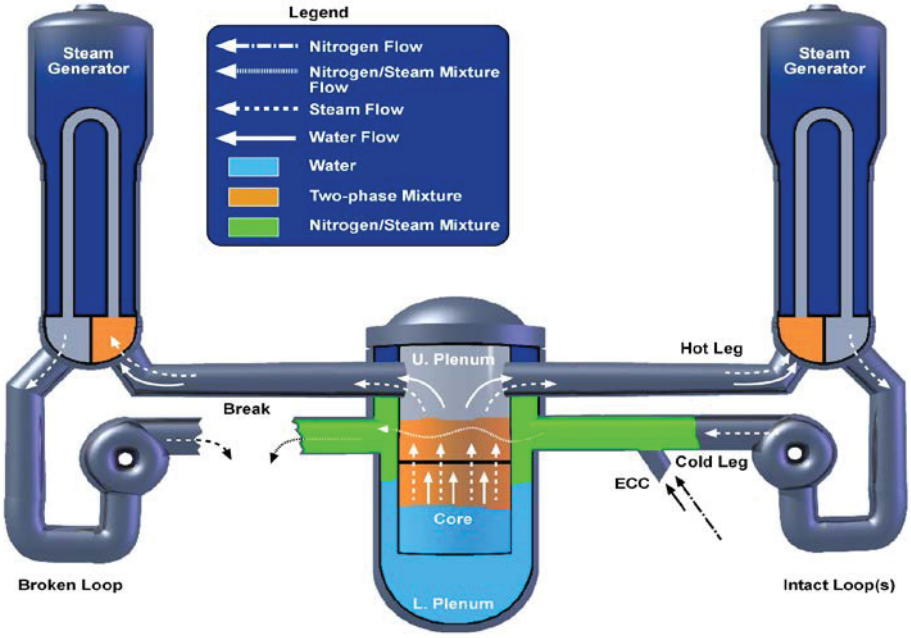

Figure 2-6. Nitrogen Injection at the End of Accumulator Discharge.

The droplets that enter the steam generators vaporize, increasing the flow path resistance. This is known as the ‘steam binding effect Figure 2-7). Core reflood is a relatively slow process. As the bottom elevations are quenched, the top elevations continue to gradually heat up and eventually turnaround once the cooling rate exceeds the decay heat rate. The cooling mechanism is controlled by dispersed flow film boiling where droplets act as the ultimate heat sink to de-superheat steam at higher elevation (Figure 2-8). The reflood transient may last for several minutes.

Figure 2-9 and Figure 2-10 show the typical transient for the primary pressure and peak clad temperature (PCT) transient.

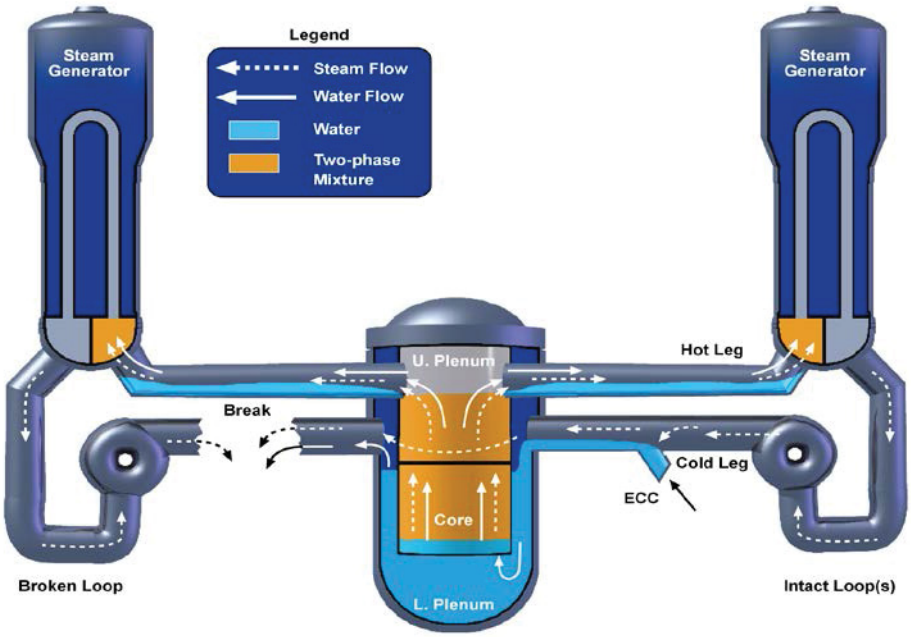

Figure 2-7. Steam Binding Effect.

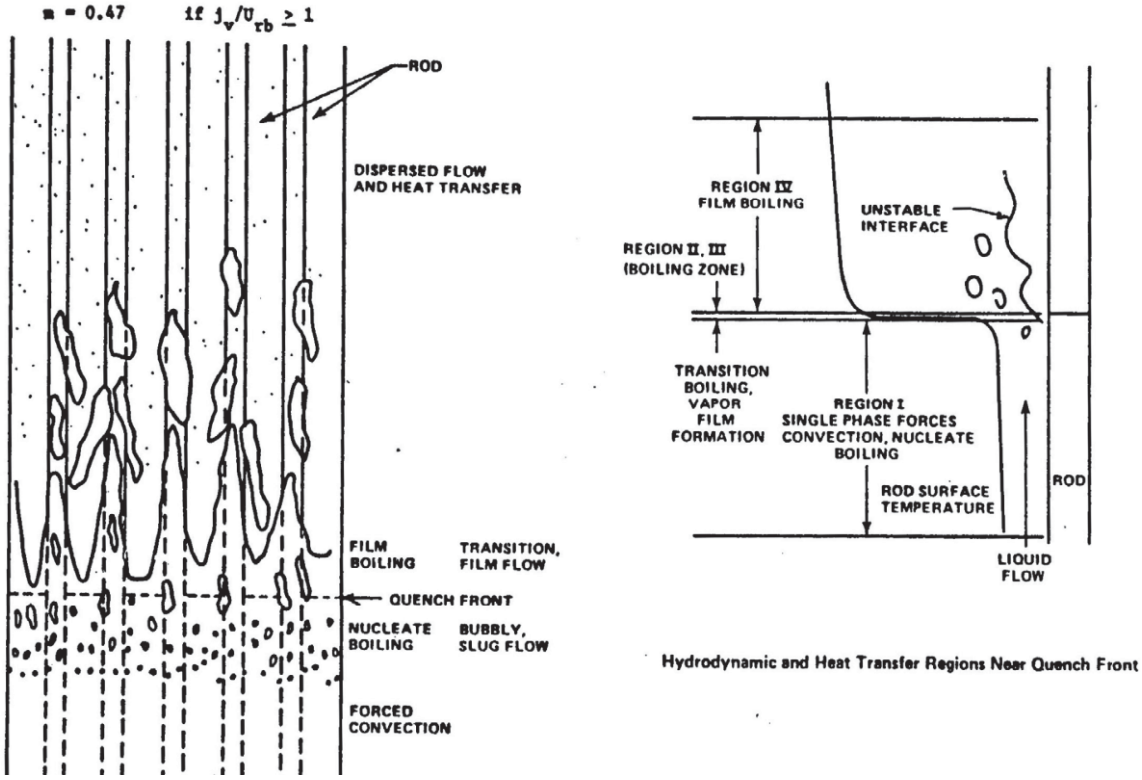

Figure 2-8. Reflood Phenomena.

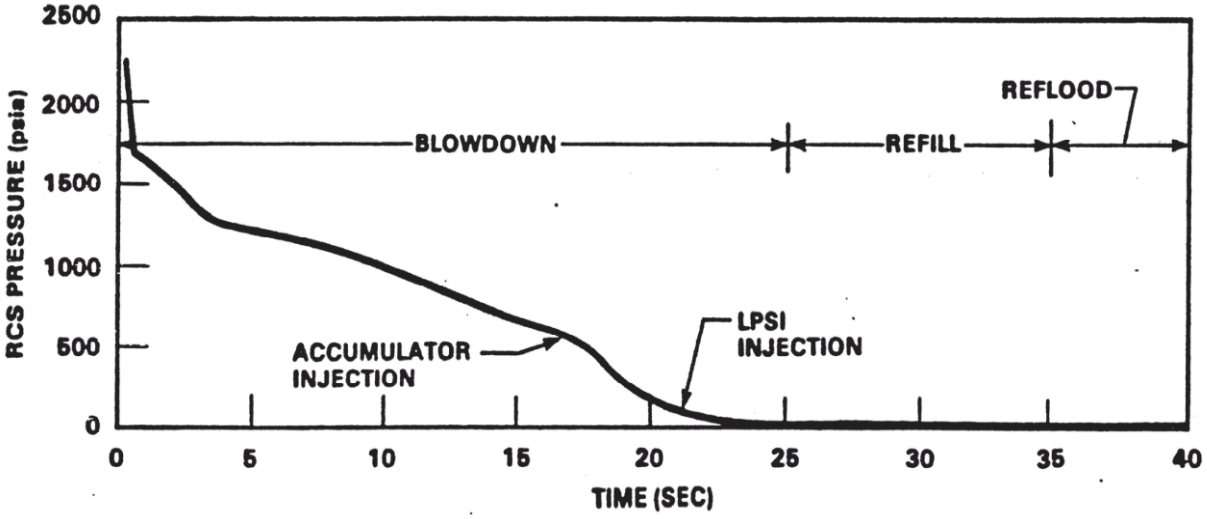

Figure 2-9. Depressurization during a LB-LOCA.

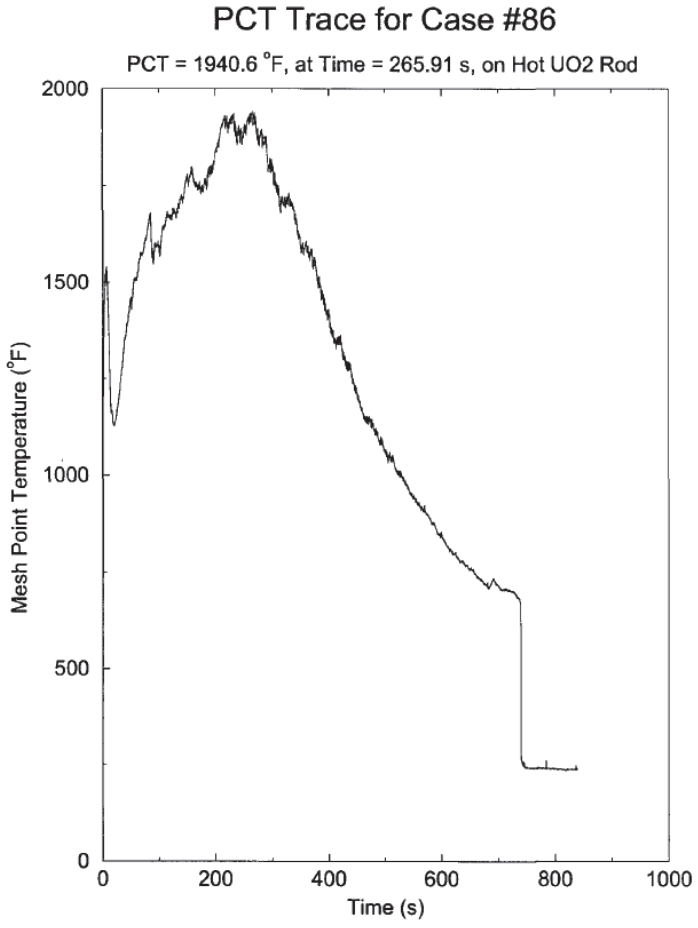

Figure 2-10. PCT Trace during a LB-LOCA.

2.1.2 Figures of Merit (FOMs)

The PCT and ECR values are the figures of merit in a LOCA safety analysis. Under the proposed rule the limits to the 10 CFR 50.46c are presented is Draft Guide 1263 (see also Fig. 1-1).

The analytical limit can be expressed as follows:

$$ECR_{5046} = \begin{cases} 18 - \dfrac{12}{400} H2 & \text{if H2<400 wppm} \\ 6 - \dfrac{4}{400}\left(H2 - 400\right) & \text{if H2>400 wppm} \end{cases} \quad (1)$$

Note that the 50.46c proposed rule also reduced the PCT limit when hydrogen content is greater than 400 wppm.

The reacted clad thickness expression is given in Appendix A-1 and must be converted to % ECR. ECR is defined as the total thickness of cladding that would be converted to stoichiometric ZrO2 from all the oxygen contained in the fuel cladding as ZrO2 and oxygen in solid solution in the remaining metal phase.

2.1.3 Integrated Evaluation Model (IEM) data stream for LOCA

In the late 1980's the Technical Program Group (TPG) developed the Code Scaling, Applicability, and Uncertainty (CSAU) methodology for the United States Nuclear Regulatory Commission. Today, most of the Best-Estimate Plus Uncertainty (BEPU) methodologies approved for license-grade application conform to the CSAU practices.

During the development of the CSAU, in an effort to quantify the uncertainty in estimating the response to a postulated Large Break LOCA (LB-LOCA) event in a PWR, the TPG provided a simplified method to predict the peak clad temperature (PCT) response to the event in their 1990 paper on Nuclear Engineering and Design.

The technique developed by Catton, despite being very simplistic, provides insights on the main drivers to a LB-LOCA transient response. Catton's simplified model is used as the basis for the LB-LOCA ROM developed for the RIMM eDemo.

The objective of the project was first to expand on the method proposed by Catton (1990) by also examining recent information published by the same authors in 2009 in their presentation of the Fractional Scaling Analysis (FSA). The details of the development of the ROM is segregated to Appendix A-1. Here note that the various disciplines within the RIMM IEM have been simplified in the ROMs.

Several inputs have been considered to feed the calculation stream of the IEM Framework Demo. The following table describes those inputs in principle but omit the details on how the inputs are exactly derived or defined within the ROMs. Those details are provided in Appendix A-1. Note that some inputs apply to more than one discipline.

There are controlled inputs and uncertain inputs for each engineering discipline. Again, the choice of the specific value used in this Framework Demo has to be taken in context. The ROMs are set up to illustrate the procedure with somewhat realistic values but they are not intended to provide the capability of an evaluation model.

The control inputs for the core design are specified in Table 2-1. The core design (CD) uncertain inputs are specified in Table 2-2. Table 2-3 shows inputs that are shared by core design and fuel rod design. Table 2-4 collects the key geometric and system operating condition inputs to set up the LOCA ROM. Table 2-5 summarizes list of uncertain inputs considered in the LOCA ROM, the exact details on each of the uncertain inputs are given in Appendix A-1. Although not a true one-to-one comparison, the LOCA ROM uncertain inputs are analogous to various uncertain inputs considered in real LOCA analyses. There are a total of 27 unique uncertain inputs in the three ROMs.

Table 2-1. Core Design Control Input Parameters.

Parameter	Units	Value
Number of feed assemblies $N_{A,0}$	-	65
Number of once-irradiated assemblies $N_{A,1}$	-	80
Number of twice-irradiated assemblies $N_{A,2}$	-	48
Total number of assemblies $N_{A,tot}$	-	193
Low power region radial power ratio	-	0.4
Cycle length	Months	18
First Cycle AVG Assembly BU	GWd/MTU	20
Second Cycle AVG Assembly BU	GWd/MTU	40
Maximum Discharge BU	GWd/MTU	62.0

Table 2-2. Core Design Specific Input Uncertainties.

Parameter	Units	Min Value	Max Value
Hot assembly within the fresh fuel region F DELTA H $F_{\Delta H}^{0,H}$	-	1.65	1.70
Hot assembly within the once-irradiated region F DELTA H $F_{\Delta H}^{1,H}$	-	1.65	1.70
Time in cycle	Months	0	18

Table 2-3. Core Design and Fuel Rod Specific Input Uncertainties.

Parameter	Units	Nominal Value	Uncertainty - Standard Deviation (%)
Clad thermal conductivity	W/m-K	13.85	25
Coolant H.T.C	W/m^2-K	34000	15
Gap conductance	W/m^2-K	5700	50
F_q	-	2.25	15
Peak power axial location $x = \frac{z}{H}$	-	0.5	25
Core total power	MWt	3411	1
Core total mass flowrate	kg/s	17400	1
Core coolant inlet temperature	C	286	1
Burnup	GWD/MTU	25	15
$F_{\Delta H}$	-	1. 675	2.5

For the LB-LOCA analysis a generic four loop PWR was considered. Geometric and key plant data were taken from various sources and the associated inputs are listed in the following Table 2-4.

Table 2-4. Geometric, Fuel and ECCS Generic Data for a 4-Loop PWR.

Parameter	Units	Value
RCS volume	m^3	3060
Break area	m^2	0.451
Lower plenum volume	m^3	20
Core flow area	m^2	5.5
Fuel rod diameter	mm	9.5
Clad thickness	mm	0.57
Core height	m	3.66
Number of fuel rods	-	50952
ACC mass flow rate (assumed constant)	kg/s	3 x 798
SI mass flow rate	kg/s	2 x 145

Table 2-5. LB-LOCA Input Uncertainties.

Parameter	Units	Nominal Value	Uncertainty (Relative Stdev) (%)
Catton coefficient *a* for blowdown heat-up	-	60	15
Initial RCS pressure	MPa	15.5	0.5
Final RCS press	MPa (psia)	0.276 (40)	1
Blowdown time parameter	-	3.5	1
Break discharge coefficient	-	1.0	15
Blowdown cooling H.T.C. multiplier	-	0.05	15
Blowdown cooling Catton coefficient 1	-	1.09	10
Blowdown cooling Catton coefficient 2	-	0.9	10
Refill heatup rate	K/s	5.2	10
Refill bypass ratio	-	0.4	15
Reflood Catton coefficient	-	339	15
Reflood Catton exponent	-	1.14	15
Quench front rate multiplier	-	0.25	25
Quench front temperature	C	450	10

2.1.3.1 Core Physics

The ROM for the core physics is a simplified representation of the core for the purpose of obtaining a representative value for the assembly power and burnup distribution within the core.

The core is divided into three regions:

- The fresh fuel region (Region 0)
- The once-burnt region (Region 1)
- The twice-burnt region (Region 2)

A Hot Assembly (HA) is defined in each region being the assembly with the highest axially integrated power within each region. Every HA contains a Hot Rod (HR) which is assumed to have a 6% augmented power relative to the average rod power within that HA. The core power distribution is simply characterized by the following ratios:

$F_{\Delta H} =$ Ratio of the integral of linear power along the hot rod (rod with the highest power) to the average rod power in the core

$F_Q =$ Ratio of the maximum local rod linear power density to average fuel rod linear power density

$\bar{P} = \frac{F_{\Delta H}}{\gamma} =$ Ratio of the hot assembly power to the core average assembly power in the core.

The factor γ is the ratio between the power of the hot rod in an assembly and the average rod power within that assembly. F_Q is used to define the axial power shape. A triangular shape was assumed to enable a simple scheme to range F_Q, $F_{\Delta H}$ and the location of the peak linear heat rate as expected in a traditional best-estimate LOCA analysis. As an example, the triangular power shape used in the Rod Bundle Heat Transfer (RBHT) test facility (NUREG/CR-6975) is shown in Figure 2-11 (The details of the various expressions are provided in Appendix A-1).

Assembly power is assumed constant through the cycle of operation. Each rod is assumed to "burn" at a rate proportional to its respective power and therefore at a constant rate through time. This is a gross approximation because in reality the linear heat rate in a specific assembly will vary during the cycle as result of breeding and depletion.

Considering that the core is divided in three regions with one HA per region and one HR within each HA, the burnup distribution as a function of the time in cycle is computed with simple relationships (as detailed in Appendix A-1) which are presented in Figure 2-12. Figure 2-12 summarizes the results of 10,000 random samples from the core physics ROM.

The discharge burnup in Region 2 (the twice-burnt region) was set to ensure the maximum discharge burnup is below the current regulatory limit (62 GWD/MTU).

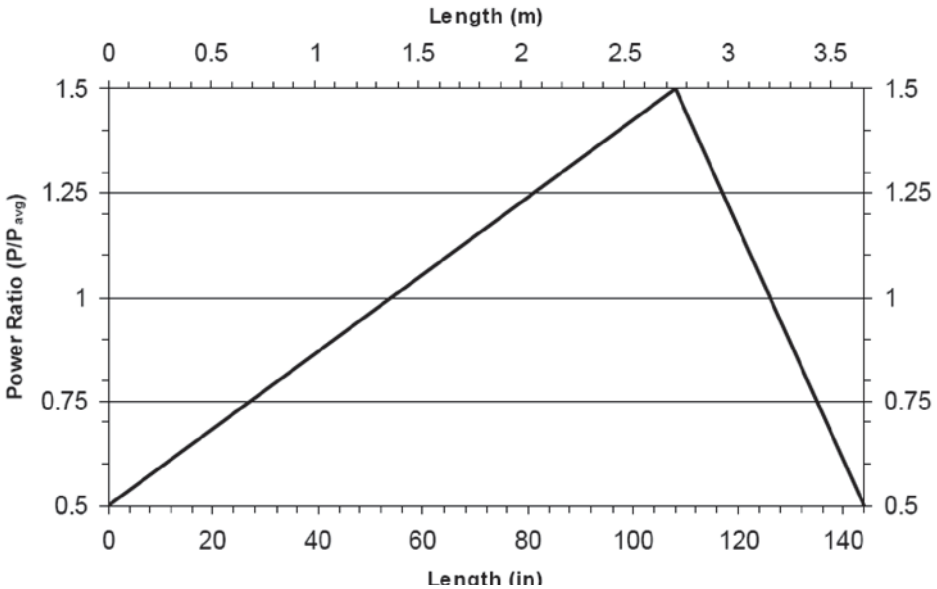

Figure 2-11. Triangular Axial Power Shape.

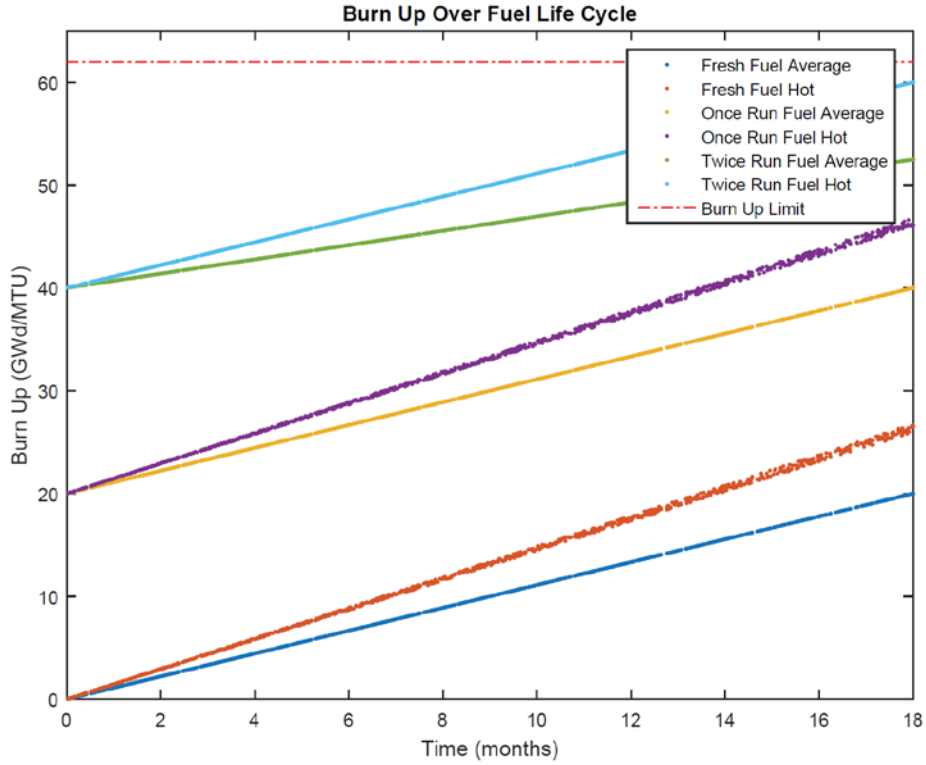

Figure 2-12. Burnup for Each of the Three Regions and Corresponding Hot Assemblies.

2.1.3.2 Fuel Rod Design

The only process considered to describe the fuel rod is the thermal resistance network from the pellet centerline to the clad surface. A thermal resistance network expression is first used to relate the fuel thermal conductivity integral at the fuel centerline temperature to that at the fuel pellet surface temperature. The derivation of the equations is presented in Appendix A-1.

The thermal conductivity correlation used in this ROM was taken from FRAPCON-3.4 (NUREG/CR-7022) which adopted the expression developed by the Nuclear Fuels Industries (NFI) model.

2.1.3.3 Steady-State Pre-LOCA Event

For a given core power distribution and core coolant flow, the axial bulk coolant temperature profile is calculated. Then the steady-state clad surface temperature distribution for a given fuel pin is computed from the coolant temperature axial distribution using a simple resistance network calculation.

The steady-state pin weighted average temperature is very important because it is related to the stored energy within the pin at the start of the LOCA. The pin weighted average temperature is computed relative to the clad surface temperature. The resistance between the two temperatures is expressed as an "effective thermal conductivity" following Catton et al.'s (2009) FSA work as discussed in Appendix A-1.

2.1.3.4 LOCA Event

The clad surface temperature transient calculation is divided into the traditional LB-LOCA phases:

- Blowdown heatup
- Blowdown cooling
- Refill heatup
- Reflood

Each phase uses different assumptions and approximations in order to estimate the clad surface temperature through time. The blowdown heatup phase was broken into two sub-phases, an initial rapid temperature rise followed by a much more gradual increase in the temperature. This approach was chosen to reflect that very early on in the transient (less than ~5 seconds), the temperature rise is dominated by the stored-energy release and the subsequent temperature redistribution within the fuel pin. After this, the clad surface temperature evolves in a more complex fashion because of the interaction of the stored-energy release, decay heat generation, and complex flow field dynamics which impact the convective cooling on the surface of the fuel pin. Approximating this behavior was beyond the scope of this ROM. Therefore, the gradual heatup is an attempt to represent a time averaged temperature increase over this portion of the transient.

Within the blowdown heatup and blowdown cooling sub-phases, the maximum clad surface temperature rise and decrease are estimated as well as the points in time these temperatures occur at. Between these points in time, the clad surface temperature is approximated via simple linear trends. The refill sub-phase clad surface temperature response through time is approximated with a simple adiabatic heatup relationship, following the Catton CSAU and FSA work. During reflood, a parabolic trend through time was used to better capture the peak and turn around before a particular axial elevation quenches.

The complete details on the assumptions and derivations of the equations utilized to compute the clad temperature response during LOCA is presented in Appendix A-1.

Figure 2-13 shows as example a reference case solution obtained with the ROM. More results will be provided later in Section 2.2.

The similarity between Figure 2-13 and Figure 2-10 demonstrate that the ROM satisfies its intent.

2.1.3.5 Computation of PCT and ECR

The correlation recommended for the estimation of the local cladding oxidation rate, expressed in ECR (%), is based on the Cathcart and Pawel (1977) model (see NUREG-17). See Appendix A-1 for details. The ECR is computed by integrating the clad temperature response through time. The additional heat source associated with the exothermic reaction is neglected for the purpose of the ROM.

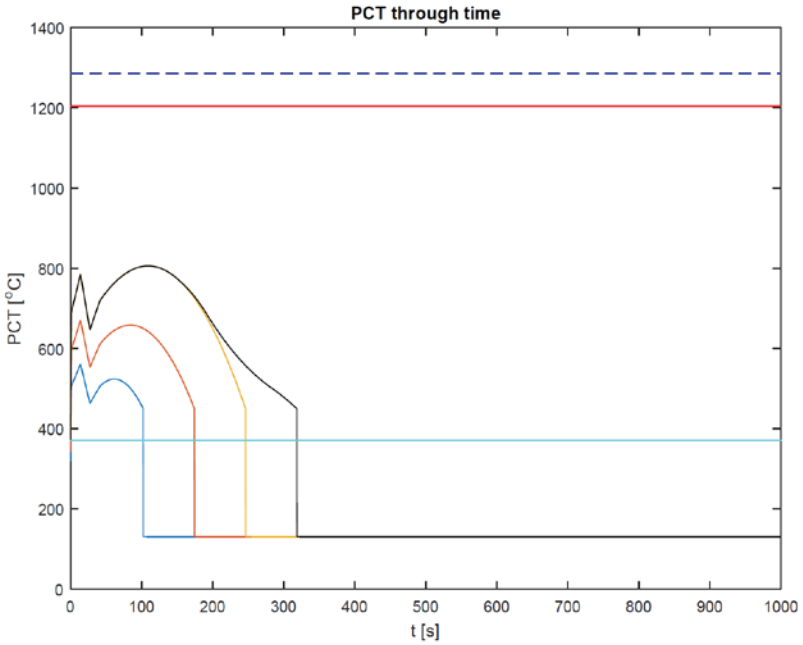

Figure 2-13. Reference Case for LOCA ROM: Clad Temperatures at Three Axial Locations in the Hot Rod (Blue: Quarter Core Height, Orange: Midcore Height, Yellow: Three Quarter Core Height) and PCT Transient (in Black), Additional Lines Are, Red: NRC Limit of 2200 ^{O}F, Cyan: Max Steady-State Clad Temperature, Dashed Blue: Max Steady-State Pin Weighted Average Temperature.

2.1.4 Uncertainty Quantification (UQ) Summary Statistics

The uncertainty in the uncertain input parameters are propagated onto the various Figures of Merit (FOMs) via Monte Carlo Sampling. The resulting uncertainties in each FOM (the PCT and ECR) are summarized by histograms as well as estimators on several summary statistics: the mean, median, standard deviation, 5th and 95th quantiles. The mean and median estimators provide statistics on central tendency, while the standard deviation and quantiles provide statistics on dispersion. The standard error for each estimator is also provided. The following sub-sections detail the calculation for each estimator and its corresponding standard error.

Specifically for nuclear safety analysis, the 95th quantile is the statistic that is compared to the Regulatory limit. Therefore the estimated 95th quantile and its associated standard error is compared to Wilks-based estimators, which are the prevalent estimator of choice currently.

Each of the estimators and their corresponding standard errors are given by Harding et al. (2014). The mathematical expressions for the summary statistics and their definitions are discussed in detail in Appendix A-2.

2.1.5 Sensitivity Analysis (SA)

To quote Saltelli: "The objective of sensitivity analysis (SA) of model output can be defined (loosely) as 'to ascertain how a given model (numerical or otherwise) depends on its input [parameters]'. There are two primary ways of structuring SA, local and global. Local SA various one parameter at a time while keeping all of the other parameters fixed at their nominal values. The input is varied by a small perturbation to estimate partial derivatives for the output response with respect to each input parameter. This information can be used to perform Uncertainty Quantification (UQ) through Taylor series expansions. Thermal hydraulic system codes do not use this approach for UQ because of the large variations in some of the uncertain input parameters.

Global SA is somewhat harder to define, but it has two key attributes: first that the whole range of values of the input parameters are considered, and second that all inputs are varied at the same time. The fact that the "whole range" of the inputs are considered represents that Global SA is linked to UQ. The input parameter ranges that are being considered are based on their (assumed) uncertainty distributions. The input parameters influence the output through both their (local) sensitivity as well as their uncertainty. A particular input that is "very" uncertain, might control the resulting uncertainty in the output than other input parameters even if the output is not particularly "sensitive" to that input over a local space.

The following subsections provide several different types of SA procedures that allow answering the following objectives:

- Identify and prioritize the most influential input parameters
- Identify the input parameters that are mostly responsible for producing realizations of the output in a given region

The above bullet points are not the only objectives SA can help answer, but those are the two this work specifically focused on. See the books by Saltelli ("Sensitivity Analysis in Practice" and "Global Sensitivity Analysis: The Primer") for a complete list of all SA objectives. The first objective is achieved with variance-based SA algorithms, specifically the method of Sobol' and the Fourier Amplitude Sensitivity Test (FAST). The second objective is achieved through Monte Carlo Filtering (also known as Regionalized Sensitivity Analysis) and Limit Surfaces (implemented with likelihood-free Markov Chain Monte Carlo). The assumptions, mathematical relationships, and implementation details for each of these methods are described in detail in Appendix A-2.

One final type of SA is included in this work. This SA type is intended for analyzing the impact of an assumption on a particular input parameter. This type will be referred to as "Distributional SA". Distributional SA does not fit into any of the previously described categories. It is global in that all of the uncertain input parameters are still varied simultaneously over their entire ranges of possible values. It is essentially a sensitivity to various assumptions. Those assumptions can be the specified (assumed) sampling distribution on any one of

the uncertain input parameters, or even values of inputs that were considered to be constant. Unlike the other SA methods used in this work, Distributional SA does not have a large number of references in the open literature. Because of this, its steps are summarized as follows. The original assumptions will be referred to as the base case, while the modified assumptions will be referred to as the modified case. The steps involved are rather straightforward:

- Perform UQ via Monte Carlo sampling on the base case
- Modify the specific assumption, re-perform UQ via Monte Carlo sampling
- Compare the resulting distributions and summary statistics on the outputs of interest

If the resulting output distributions are different between the base case and the modified case, then that assumption change was indeed an important change. The other SA types should therefore be re-performed to see if the input sensitivities also changed with the modified case. Additional details on Distributional SA are also given Appendix A-2.

2.2 Framework Demonstration with Reduced Order Models Results

The Framework Demo UQ results are provided for the "full" or complete IEM consisting of the Core Design (CD), Fuel Rod Design (FRD) and Large-Break LOCA (LB-LOCA) ROMs. The following sections summarize the IEM results on PCT and ECR for a reference case, UQ via Monte Carlo sampling, and the effect of sample size on the Monte Carlo standard error estimates.

2.2.1 Reference Case Results

The reference case consists of running the IEM with all of the inputs at their nominal values. Although figures are generated for each of the three regions in the core (the fresh fuel, once-burnt, and twice-burnt) only the fresh fuel region is shown below. The reference case results highlight the various time phases within the LB-LOCA transient.

Figure 2-14 is the PCT through time for the average and hot assemblies within the fresh fuel region (region 0) and once-irradiated region (region 1). The PCT behaves as expected, with a very rapid initial heatup during blowdown. After reaching its maximum during that time phase, the PCT drops due to blowdown cooling, before reaching its minimum at the end of the depressurization phase. The PCT increases rapidly during the refill phase, before entering the reflood phase. Before roughly 200 seconds, the PCT appears to follow a quadratic trend through time. Afterwards, the PCT has a complex dynamic due to the quench front traveling upwards along the fuel rod. Once the elevation corresponding to the PCT location quenches, the axial location directly above that location is the new PCT. This occurs until the rod completely quenches.

Figure 2-15 shows the ECR versus axial elevation for the average and hot assemblies within region 0. The nominal value for the location of the peak linear heat rate is the core mid-plane. This is why the max ECR occurs half way up the core height. Both the reference PCT and ECR results illustrate that the nominal response is clearly well below the Regulatory limits.

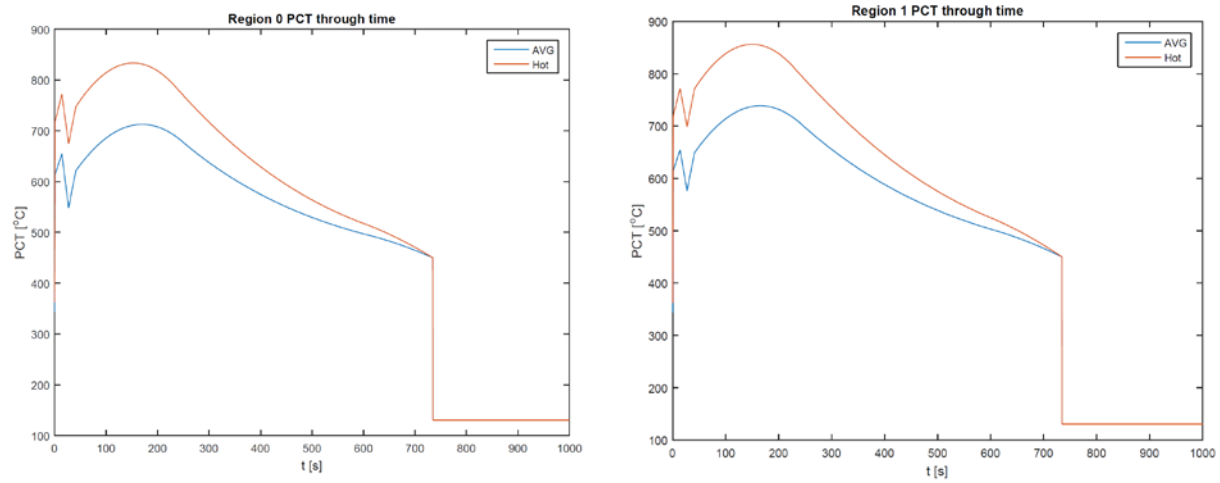

Figure 2-14. Reference Case Results for the PCT vs Time within the Fresh Fuel and Once Irradiated Region.

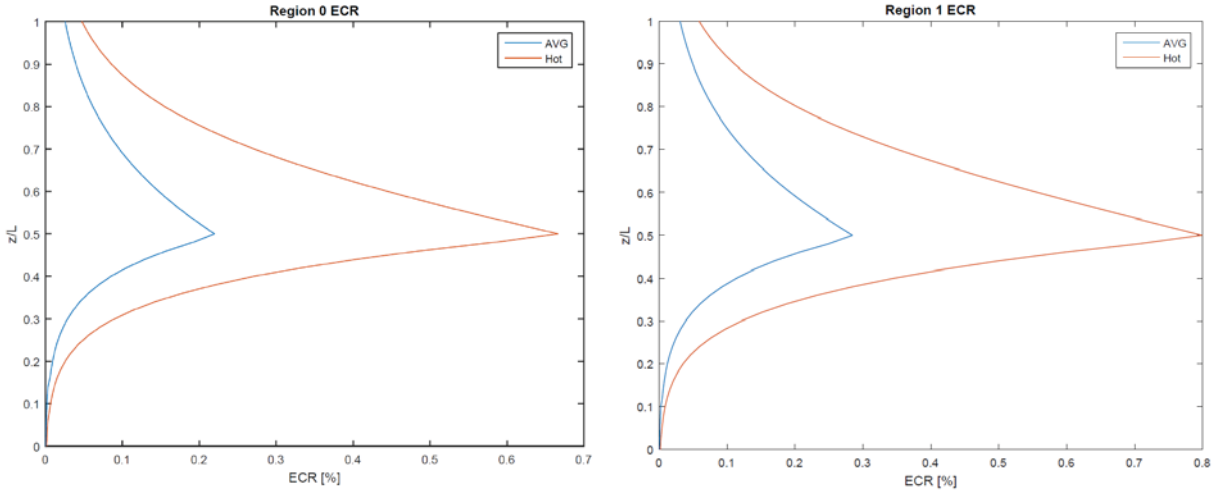

Figure 2-15. Reference Case Results for the ECR vs Axial Elevation within the Fresh Fuel and Once Irradiated Regions.

2.2.2 Uncertainty Quantification Results

2.2.2.1 Predictions through Time

The input parameter uncertainties are propagated via Monte Carlo sampling. The results in this section use 10,000 Monte Carlo samples. The quantiles on the PCT through time are shown in Figure 2-16 below. The left plot are the quantiles on both the hot and average assemblies within region 0, while the right plot are the quantiles on the hot and average assemblies within region 1 (the once-burnt region). The specific quantiles shown are the 2.75th, 5th, 25th, 50th, 75th, 95th, and 97.5th quantiles. The red shaded region corresponds to the probability mass for the hot assembly, while the blue shaded region is the probability mass for the average assembly within each region. Figure 2-16 shows that in both regions, the 95th quantile on the average assembly PCT is roughly equal to the 75th quantile on the hot assembly PCT.

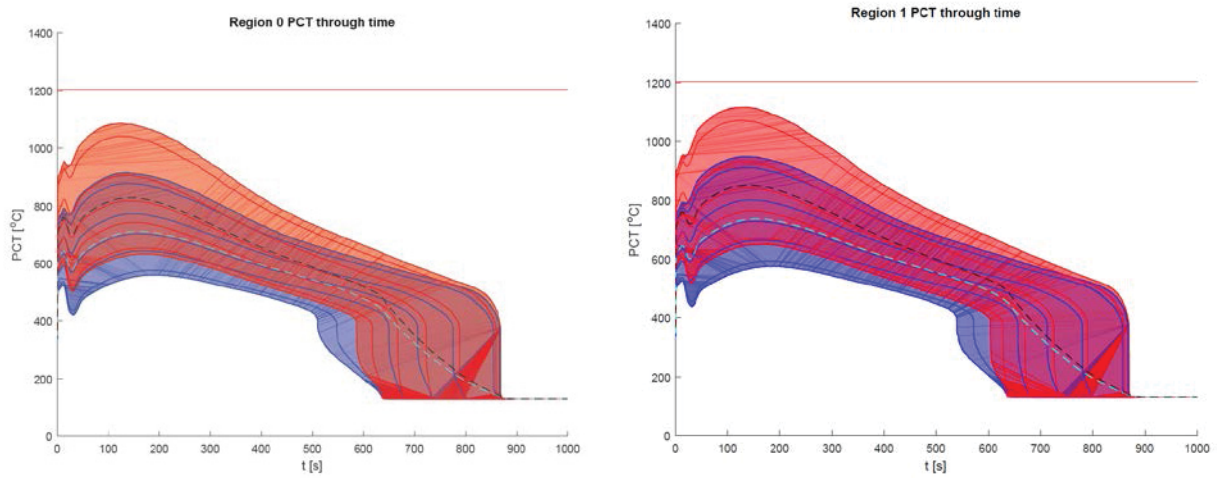

Figure 2-16. Quantiles on the PCT vs Time within both the Fresh Fuel and Once-Burned Regions.

Analogous plots on the ECR in regions 0 and 1 are shown in Figure 2-17. It is interesting to note that there is a significant increase in the ECR value between the 75th and 95th quantiles. This suggests that the ECR distribution has a very long tail (which will be confirmed in the next section).

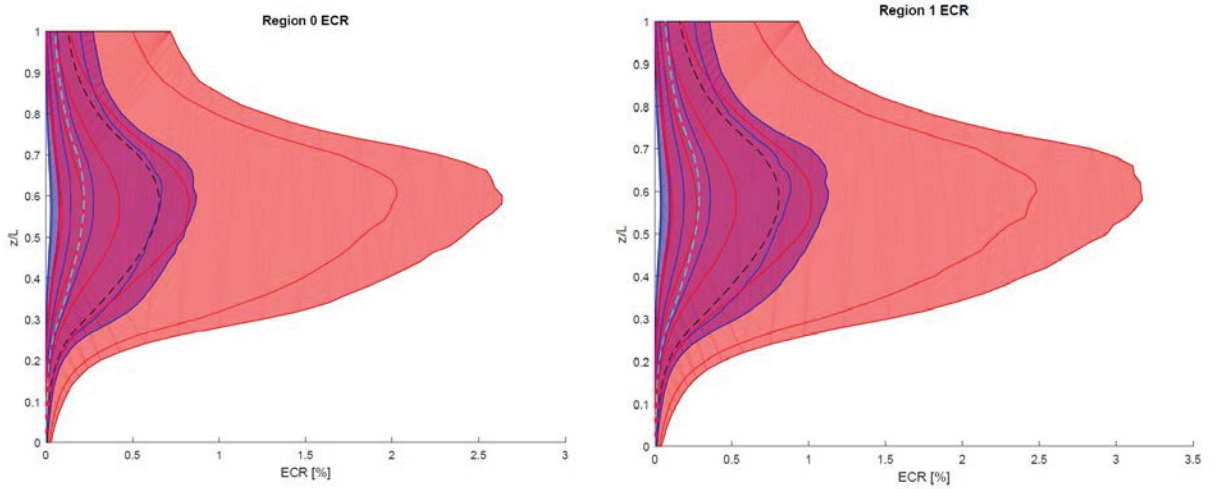

Figure 2-17. Quantiles on the ECR vs Axial Elevation within both the Fresh Fuel and Once-Burned Regions.

2.2.2.2 UQ Summary Figures

Within the context of the current NRC rule, the safety metrics of interest are the time and location independent PCT and ECR. These two outputs of interest are summarized in histograms in Figure 2-18 and Figure 2-19 below. The PCT distribution appears to be roughly Gaussian, with a mode shifted slightly left of the center. The ECR distribution however is clearly very non-Gaussian with, as expected from the previously shown results, a very long tail. The PCT histogram alone demonstrates there is a finite probability that the PCT exceeds the NRC limit (~1204 ^{O}C ≈ 2200 ^{O}F), though the probability is quite small. From the ECR histogram, it is clear though that there is a finite probability of the Framework demo ECR reaching relatively high percentage values (greater than 6%). In addition, Figure 2-20 gives the scatter plot between the time and location independent PCT and ECR. The results are consistent with the quadratic relationship between the PCT and ECR. It is important to note that a scatter plot does not provide the probability of a combination occurring. It provides the useful trend that the highest ECR values only occur with the highest PCT values. The extreme cases shown in the upper right portion of Figure 2-20 are however very unlikely.

However, with the proposed rule change the PCT and ECR histograms given in Figure 2-18 and Figure 2-19 **cannot** be used to demonstrate compliance. With the proposed rule change, the Regulatory limit on ECR

depends on the region of the core due to the hydrogen content's dependence on burnup. Figure 2-19 alone cannot be used to estimate the probability of the ECR exceeding the Regulatory limit. Demonstrating compliance under the proposed rule is therefore not as straightforward as it was previously under the current rule. "Global proxies" such as the core wide maximum PCT and ECR no longer define the safety state of the plant. A rod's pre-transient hydrogen content defines the Regulatory limit for that particular rod, thus each rod effectively has its own PCT and ECR limit values.

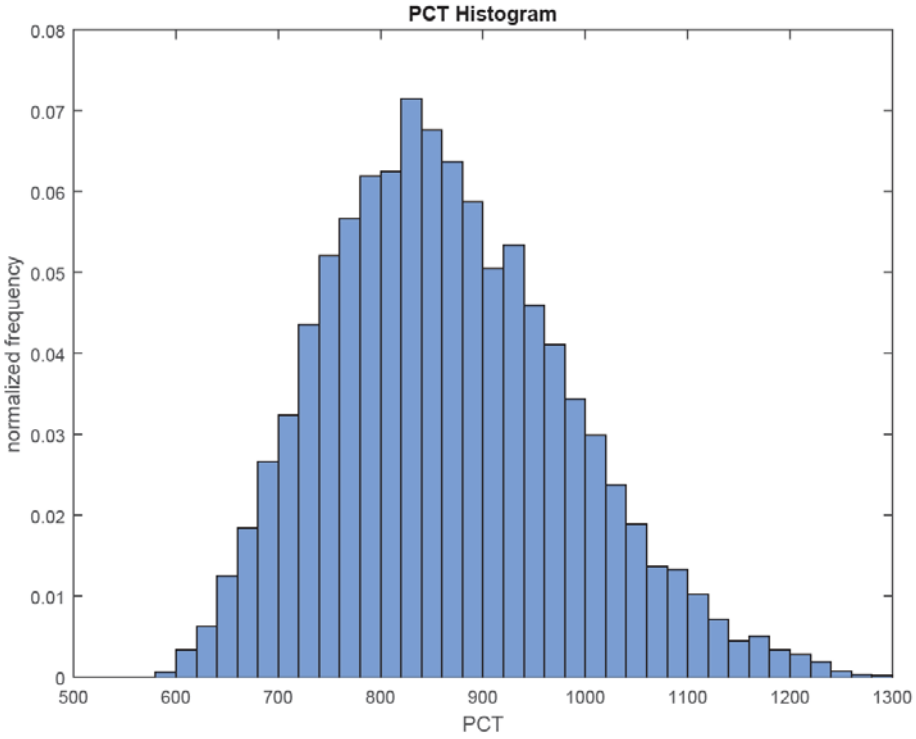

Figure 2-18. Histogram on the Location and Time Independent PCT Value.

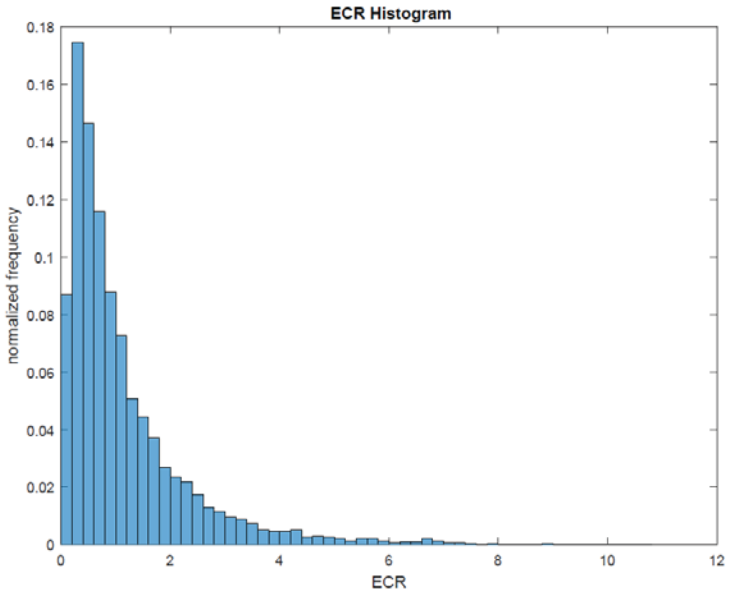

Figure 2-19. Histogram on the Location and Time Independent ECR Value.

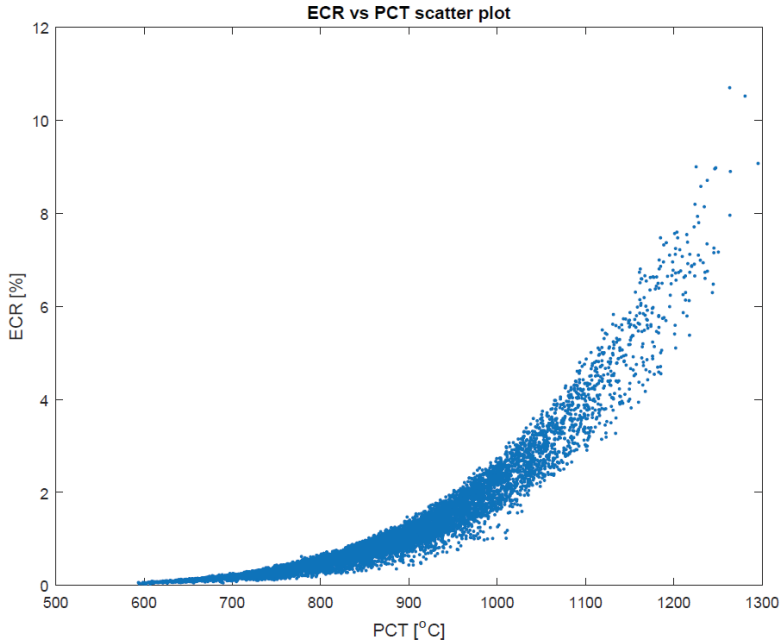

Figure 2-20. Correlation plot between the ECR and PCT.

With the proposed rule change, the Regulatory limits on PCT and ECR depend on the pre-transient hydrogen content. At a pre-transient hydrogen content of 400 [wppm] the Regulatory limit on the PCT decreases and the ECR limit changes slope. The PCT and ECR samples within each region of the core are plotted versus the region pre-transient hydrogen content in the left hand side plots of Figure 2-21 and Figure 2-22, respectively. In the figures the legends 0, 1, 2 correspond to the average power rod in the three regions and 0H, 1H and 2H are the corresponding hot rods within the same regions.

The pre-transient hydrogen content is computed from the burnup within each region, and effectively provides a scatter plot between the PCT and ECR with time in cycle within each region. It is difficult to infer any statistical trend between PCT exceeding the Regulatory limit and the pre-transient hydrogen content (time in cycle) from Figure 2-21. Sensitivity Analysis (SA) algorithms could be used to identify such trends or patterns from the results. Since the Regulatory limit on ECR does depend on the time in cycle, the margin in ECR decreases with time in cycle. As shown in Figure 2-22, there are random ECR results that even exceed the Regulatory limit line starting at roughly three quarters of the way into the cycle length. Just as with Figure 2-20, however, it must be noted that scatter plots do not provide the probability of an event occurring. The fact that there are samples above the PCT and ECR limits therefore does not mean the Framework demo results are out of Regulatory compliance. Summary statistics must be computed from these samples at different pre-transient hydrogen contents. These summary statistics can therefore be compared to the Regulatory limit values at a specific pre-transient hydrogen content to assess if the plant is compliant with the proposed rule or not.

The right hand side plots in Figure 2-21 and Figure 2-22 summarize the 10,000 Monte Carlos samples in each region of the core by their 5^{th}, 50^{th} (median), and 95^{th} quantile Monte Carlo estimators at ten different pre-transient hydrogen content values. The shaded zones in the right hand side plots depict the interval between the 5^{th} and 95^{th} quantile estimators for each region of the core. Each quantile estimator includes an error bar which estimates its $95^{\%}$ confidence interval. The ten different pre-transient hydrogen content values were chosen using 10 evenly spaced quantiles of the hydrogen content samples associated with each region of the core. The ten specific values are therefore 10 “bins” of nearly equal number of samples. The quantiles are estimated from the samples within each “bin”. A single hydrogen content (H2) “bin” has roughly 1000 samples, and so the quantile standard errors are based on 1000 samples rather than 10,000 samples. The shaded zones and median estimators illustrate how the PCT and ECR distributions within each core region change as corrosion accrues during the cycle.

Compliance for the hypothetical plant analyzed by the IA1 demo is demonstrated by comparing the PCT and ECR 95th quantile estimators and their associated upper 95% confidence interval bounds to the Regulatory limits as a function of pre-transient hydrogen content. Thus, if the 95th quantile estimates are acceptable summary statistics to demonstrate compliance, the fictional plant being analyzed is in compliance with the proposed rule throughout the entire cycle. It is important to note that the ROMs used throughout this Framework demo should not be looked on a quantitative basis relative to a real plant. The purpose of the ROM is to illustrate how to process and interpret the results.

Since the 95th quantile estimators are significantly below the Regulatory limit lines, the cases above the Regulatory limit lines in Figure 2-21 and Figure 2-22 are therefore exceedingly rare. Such rare events are possible in Monte Carlo sampling, and it should be stressed that compared to the conventional Wilks-based approach, a single case is not chosen to represent the safety state of the plant. The safety metric distributions are analyzed in detail and prescribed quantile values are compared to the Regulatory limits. As shown in Figure 2-21 and Figure 2-22, core wide proxies are no longer sufficient to demonstrate compliance because the ECR limit is a very strong function of the pre-transient hydrogen content.

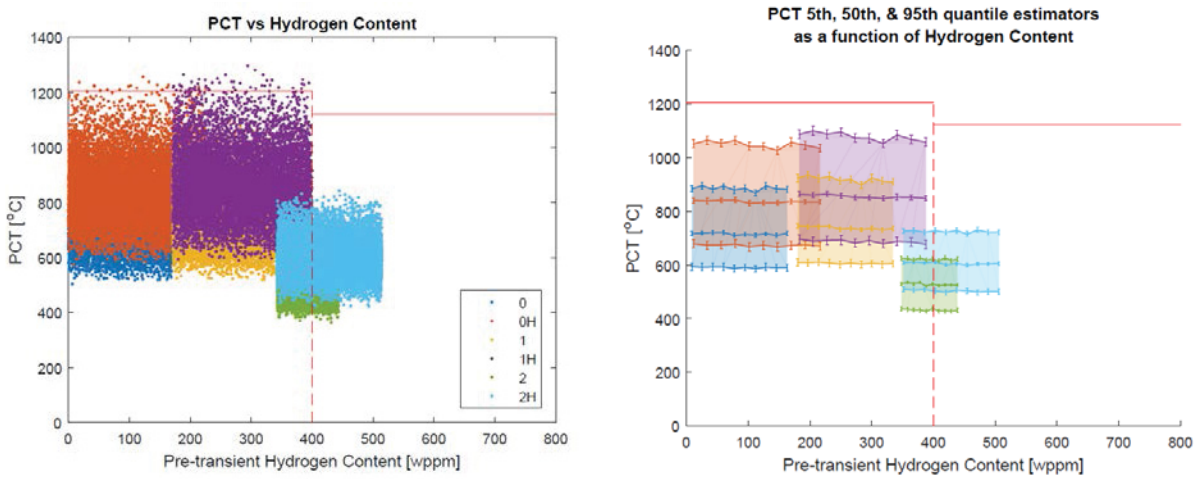

Figure 2-21. PCT vs Hydrogen Content within Each Region of the Core (Left: All Monte Carlo Samples, Right: Summary Statistics Used to Demonstrate Compliance with the Proposed Rule).

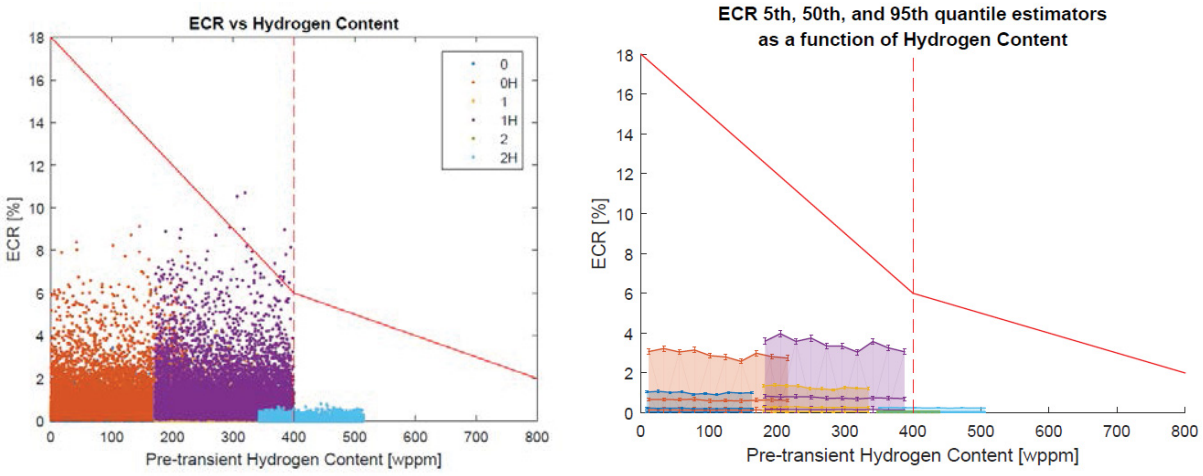

Figure 2-22. ECR vs Hydrogen Content within Each Region of the Core (Left: All Monte Carlo Samples, Right: Summary Statistics Used to Demonstrate Compliance with the Proposed Rule).

2.2.3 Effect of Monte Carlo Sample Size

The UQ results shown in the previous section demonstrate the uncertainty in the predictions throughout the disciplines within the IEM. However, as described in Appendix A-2, all Monte Carlo estimators are subject to imprecision due to the finite sample size. This section goes into detail on the influence of the sample size on the accuracy and precision of the Monte Carlo estimators on the key outputs of interest, the PCT and ECR.

The input parameter uncertainty was propagated via Monte Carlo sampling numerous times at different sample sizes. The standard error was computed for each of the estimators outlined in Appendix A-2, but only the mean and 95th quantile estimators and their corresponding standard errors are presented here.

2.2.3.1 Sample Size Impact on PCT

Figure 2-23 below provides two plots, the upper plot shows the estimator on the mean PCT value with 95% confidence interval approximated as $\text{mean}(PCT) \pm 2 \cdot SE_M$, while the bottom plot shows SE_M as a function of the sample size. Figure 2-24 provides similar plots but on the estimator for the 95th quantile and its corresponding standard error. Comparing the bottom plots between Figure 2-23 and Figure 2-24 shows that the standard error on the 95th quantile is roughly twice that of the standard error on the mean, as described in Appendix A-2.

Both figures show two similar and important trends. First, that the estimator has considerable variability with less than 1000 samples. And second, the standard error is large until it "stabilizes" at 1000 samples. The first five sample sizes correspond to 59, 100, 124, 256, and 260 samples. As shown in Figure 2-24, the 95th quantile estimator varies over a roughly 50 ^{O}C interval between 1050 ^{OC} and 1100 ^{O}C. This variability is "allowable" given the large standard error on the 95th quantile estimator as illustrated by the very large 95% confidence intervals. For 100 samples, the 95% confidence interval is roughly 100 ^{O}C. The true unknown 95th quantile is somewhere within this interval with 95% confidence. Reducing this uncertainty associated with the finite sample size requires running more samples.

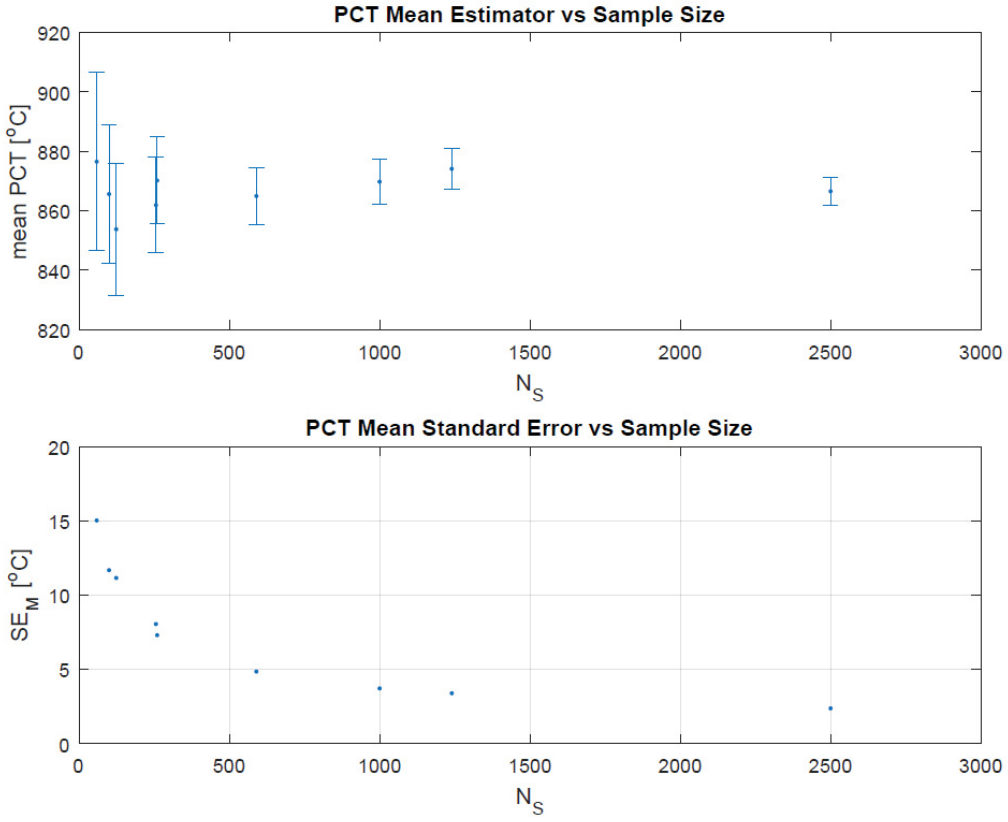

Figure 2-23. PCT Mean Estimator 95% Confidence Interval and Standard Error vs Sample Size.

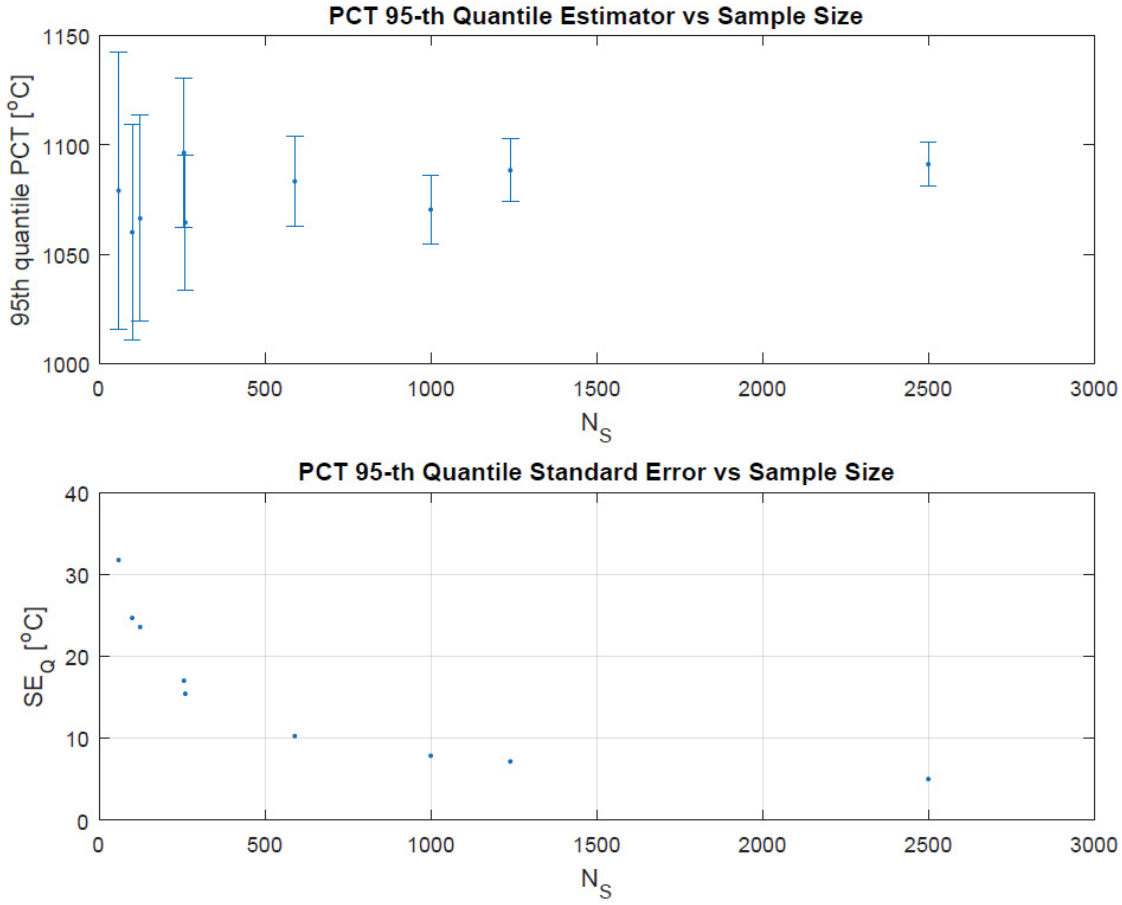

Figure 2-24. PCT 95th Quantile Estimator 95% Confidence Interval and Standard Error vs Sample Size.

The impact of even larger sample sizes on the PCT 95th quantile estimator is shown in Figure 2-25. The number of samples are shown on a log scale in both plots in Figure 2-25. There still exists considerable variability in the estimator even with sample sizes greater than 1000 samples. The standard error on the 95th quantile decreases below 5 ^{O}C after 2500 samples.

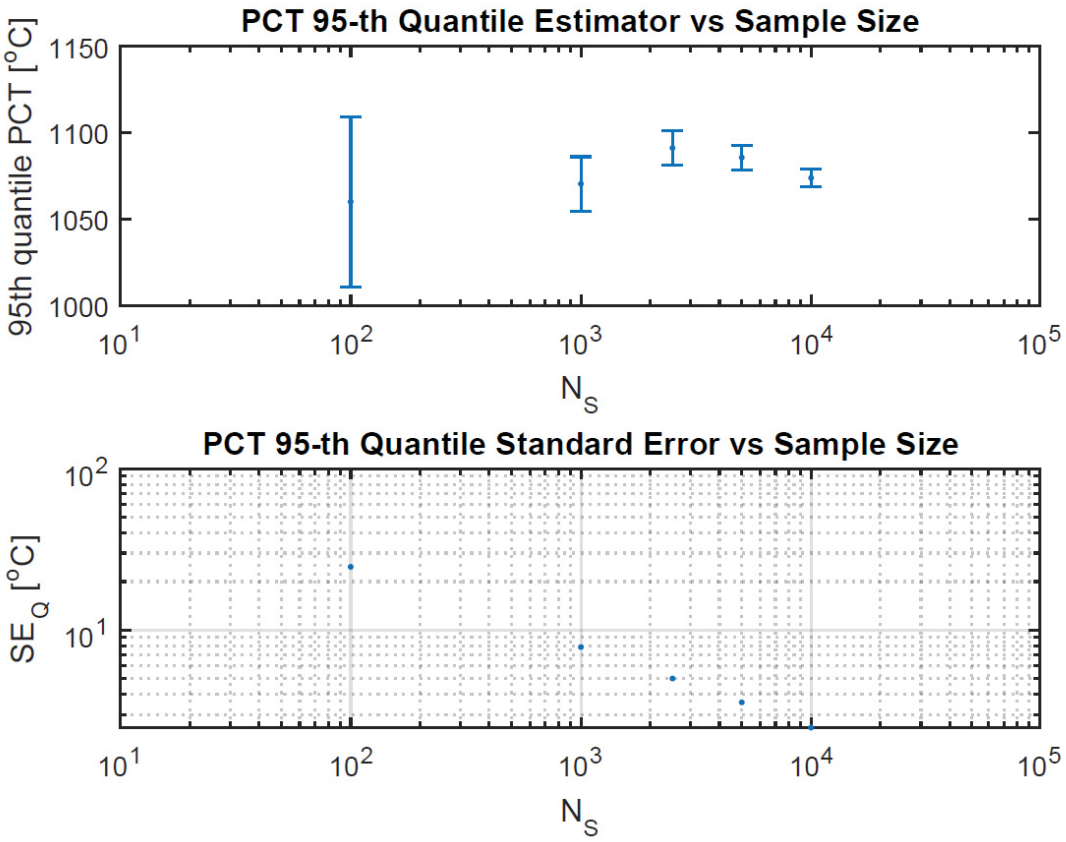

Figure 2-25. PCT 95th Quantile Estimator 95% Confidence Interval and Standard Error vs Larger Sample Sizes.

2.2.3.2 Sample Size Impact on ECR

As shown in Section 2.2.2.2, the ECR distribution is very non-Gaussian. The impact of the sample size on the ECR mean and 95th quantile estimators is however very similar to the trends on the PCT estimators. This is shown by Figure 2-26 and Figure 2-27 below.

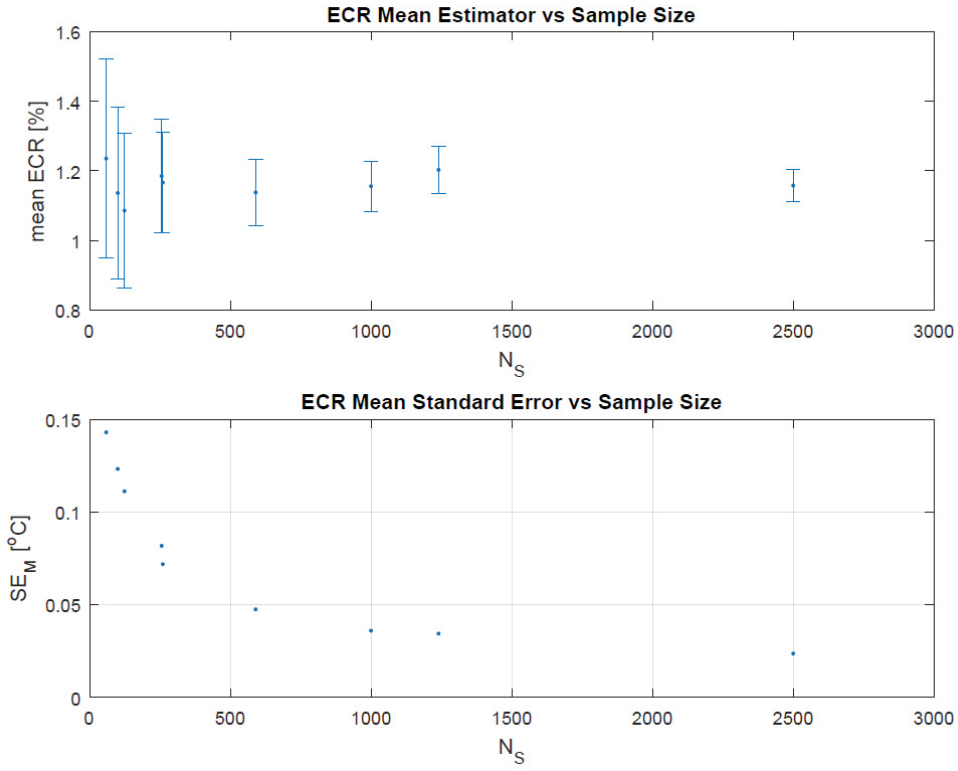

Figure 2-26. ECR Mean Estimator 95% Confidence Interval and Standard Error vs Sample Size.

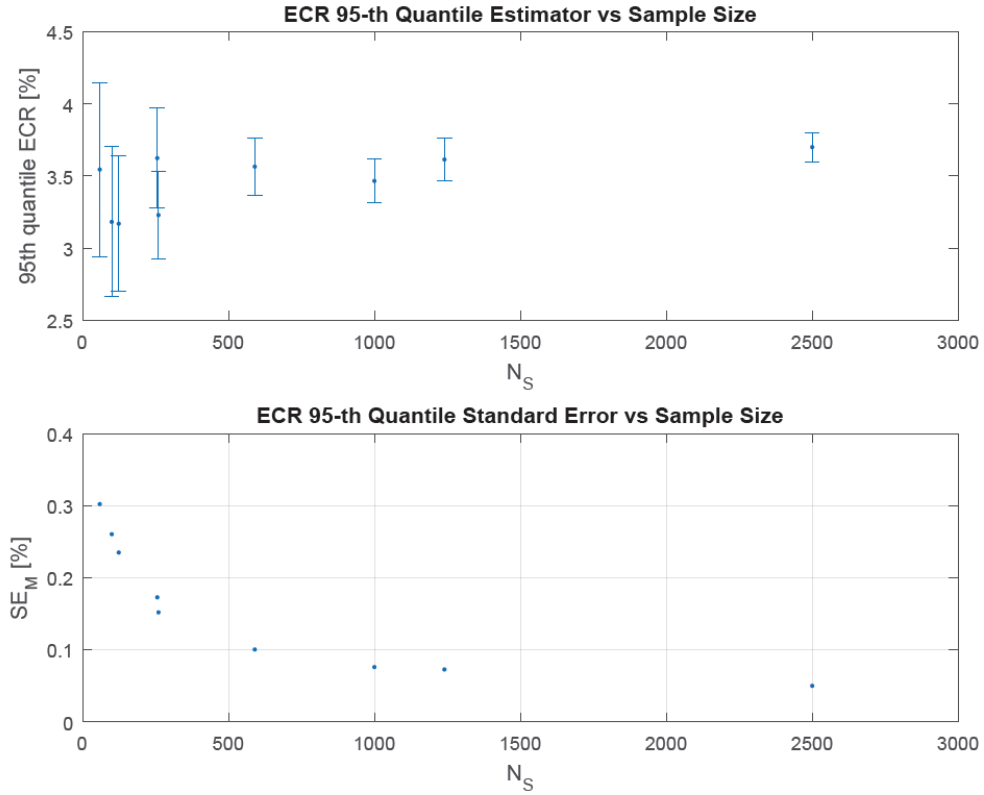

Figure 2-27. ECR 95th Quantile Estimator 95% Confidence Interval and Standard Error vs Sample Size.

2.2.4 Comparison with Wilks-Based Estimators

The Monte Carlo sampling estimator to the 95th quantile is compared to various Wilks-based estimators. A single Monte Carlo sampling sequence is divided up into N_{WG} "Wilks groups" depending on the required sample size for a particular Wilks-based estimator. The classic 95/95 estimate with 59 samples would have $N_{WG} = 10$ if $N_S = 590$ Monte Carlo samples. The Wilks based estimator is itself a random quantity. There are therefore 10 consecutive samples of the random 95/95 59 sample Wilks-based estimator "within" 590 Monte Carlo samples. These samples can be summarized with estimators on the mean and standard deviation. As the Monte Carlo sample size increases, the number of Wilks groups also increases which allows estimating the mean and standard deviation on a Wilks-based estimator with higher precision. The Wilks-based estimator distribution is then compared to the Monte Carlo sampling estimator on the 95th quantile.

2.2.4.1 PCT Comparison

Figure 2-28 shows the 95th quantile estimator on PCT for five different Monte Carlo sampling sequences each run with 1000 samples. Using five separate Monte Carlo sampling sequences provides an estimate to the variability on the Monte Carlo estimator itself, in addition to the estimated standard error within a particular sequence. The Monte Carlo estimator (and its associated approximate 95% confidence interval) is shown in black. The Wilks based estimators are also summarized with error bars, however the error bars represent the asymptotic Gaussian distribution on each estimator. The central point is the mean estimate on the Wilks-based estimator with the error bar extremes capturing $\pm$ two standard deviations around this mean. Thus, there is 95% probability that the "true" Wilks-based estimator is within the interval illustrated by the error bar. The 95/95 59 sample Wilks estimator is in red, with its mean estimate marked by a red "X". The 95/95 124 sample Wilks estimator is in blue, with its mean estimate marked by a blue "O". The green error bar is the max value from 124 samples, with its mean marked by a green "+". With 1000 Monte Carlo samples, the 59 sample Wilks estimator distribution is estimated with 16 samples, while the 124 sample Wilks estimator distributions are estimated with 8 samples. There is also the additional uncertainty on the mean and standard deviation of the Wilks based estimators due to the finite sample size, but that additional uncertainty is not illustrated in Figure 2-28.

Figure 2-28 reveals several important trends. First and foremost, the Monte Carlo estimator is less than the Wilks based estimators. Second, besides being less than the 95/95 59 sample Wilks based estimator, the higher-order 95/95 124 sample Wilks based estimator has a decreased standard deviation. The higher-order Wilks based estimator therefore has less variability than the lower-order estimator, as expected. Even though the Monte Carlo estimator's confidence interval is fairly large (approximately 30 ^{O}C), it is quite clear that the Monte Carlo estimators are well below the Regulatory limit of ~1204 ^{O}C. In contrast, if a single Wilks-based analysis was performed there is a chance that the 95/95 59 sample Wilks-based estimator would conclude that the PCT exceeds the Regulatory limit. Even though the mean value for the 95/95 59 sample Wilks-based estimator is always less than 1200 ^{O}C, the red error bar extends well beyond the Regulatory limit.

Another very important concept revealed by Figure 2-28, is that there is a finite chance that the Wilks-based estimator is less than the Monte Carlo estimator. The 95/95 Wilks-based estimators inherently allow 5% probability that they are less than the true unknown 95th quantile. Comparing the variability in the Wilks-based estimators to the Monte Carlo estimator can approximate this condition. However, the uncertainty on the Monte Carlo estimator due to the finite sample size must also be considered. The difference between the lower red error bar and the black dot provides an analogy for the probability that the 95/95 59 sample Wilks-based estimator is less than the true 95th quantile. This interval is not a small fraction of the total interval spanned by the red error bar. When the difference between the lower red error bar and the upper black error bar is considered, the interval increases. Thus, when the uncertainty on the Monte Carlo estimator on the 95th quantile is considered, the probability that the Wilks-based estimator is less than the true unknown 95th quantile appears larger than 5%. These qualitative results are consistent with Hessling and Hedberg (2015), but more work is required to quantify these intuitions.

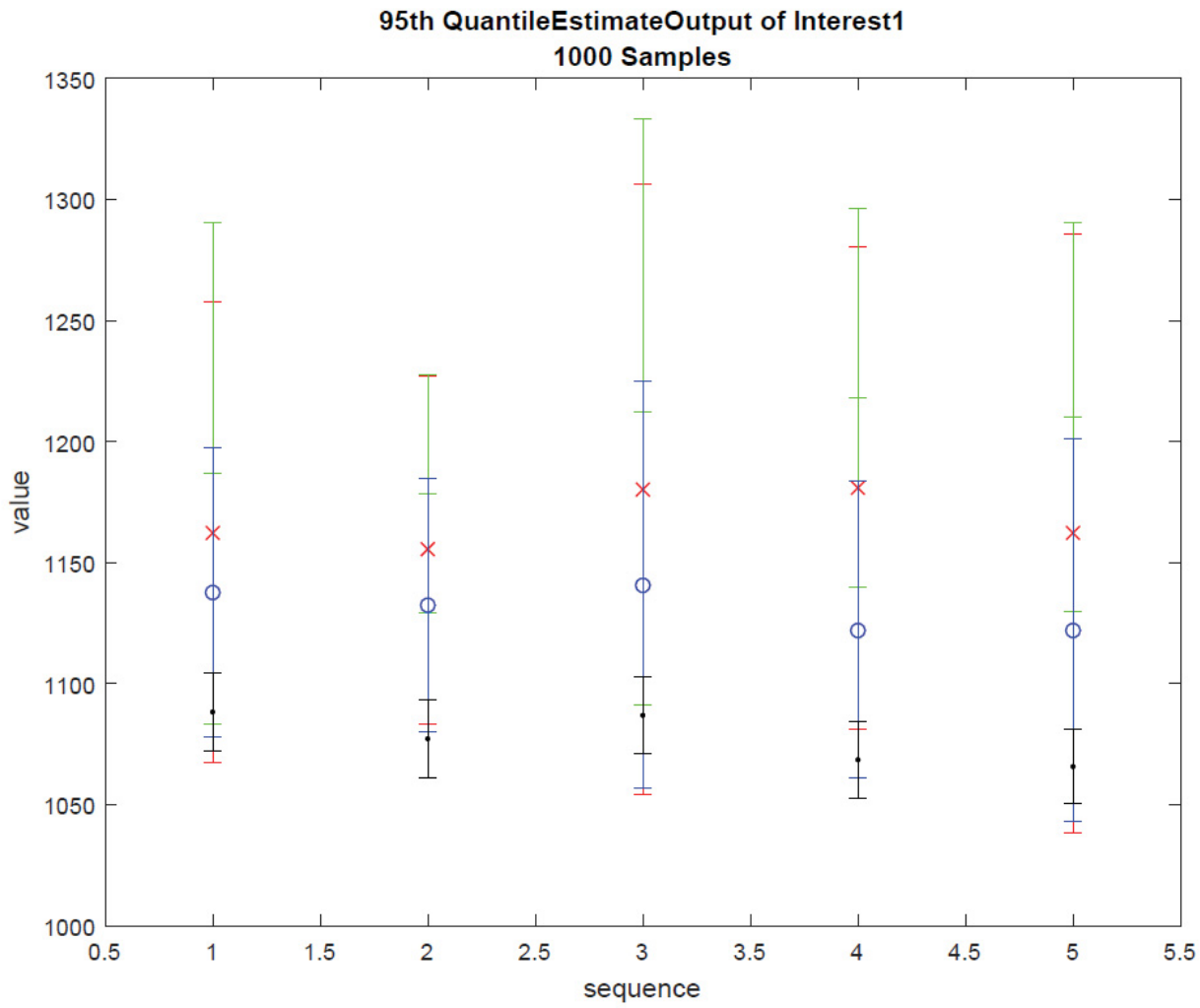

Figure 2-28. PCT 95th Quantile Monte Carlo Estimators vs Wilks-Based Estimators for 5 Different Monte Carlo Sequences Each with 1000 Samples (Black: Monte Carlo Estimator, Red: Wilks Max of 59 Samples 95/95 Estimator, Green: Wilks Max of 124 Samples 95/~98 Estimator, Blue: Wilks 3rd Highest of 124 Samples 95/95 Estimator).

Figure 2-29 below shows the same results as Figure 2-28, except now with 5000 Monte Carlo samples. The trends described previously with fewer samples are consistent with those shown in Figure 2-29. The primary difference is that the Monte Carlo estimators have a reduced uncertainty, since more samples are used. There are now also 84 groups of 59 samples. Thus, the mean and standard deviation on the 95/95 59 sample Wilks-bases estimators are more precise than the error bars shown in Figure 2-28. Even with more samples, the issue of the Wilks-based estimator under predicting the true unknown 95th quantile are therefore still present.

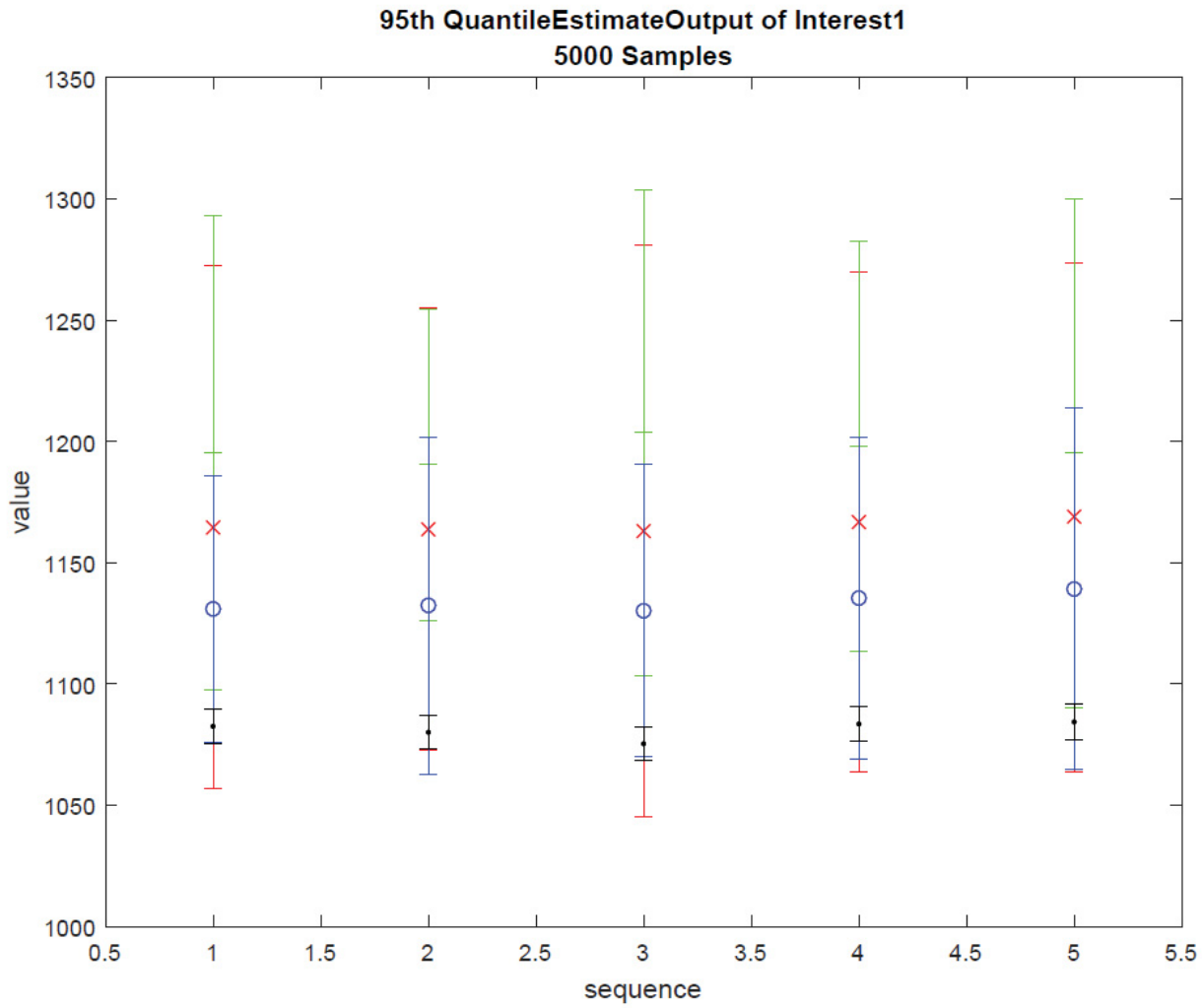

Figure 2-29. PCT 95th Quantile Monte Carlo Estimators vs Wilks-Based Estimators for 5 Different Monte Carlo Sequences Each with 5000 Samples (Black: Monte Carlo Estimator, Red: Wilks Max of 59 Samples 95/95 Estimator, Green: Wilks Max of 124 Samples 95/~98 Estimator, Blue: Wilks 3rd Highest of 124 Samples 95/95 Estimator).

2.2.4.2 ECR Comparison

Figure 2-30 and Figure 2-31 provide the Monte Carlo and Wilks-based estimators to the ECR. These figures have the same colors and trends as those described for the PCT results. The primary difference is that the Wilks-based estimators are much more uncertain relative to the Monte Carlo estimators.

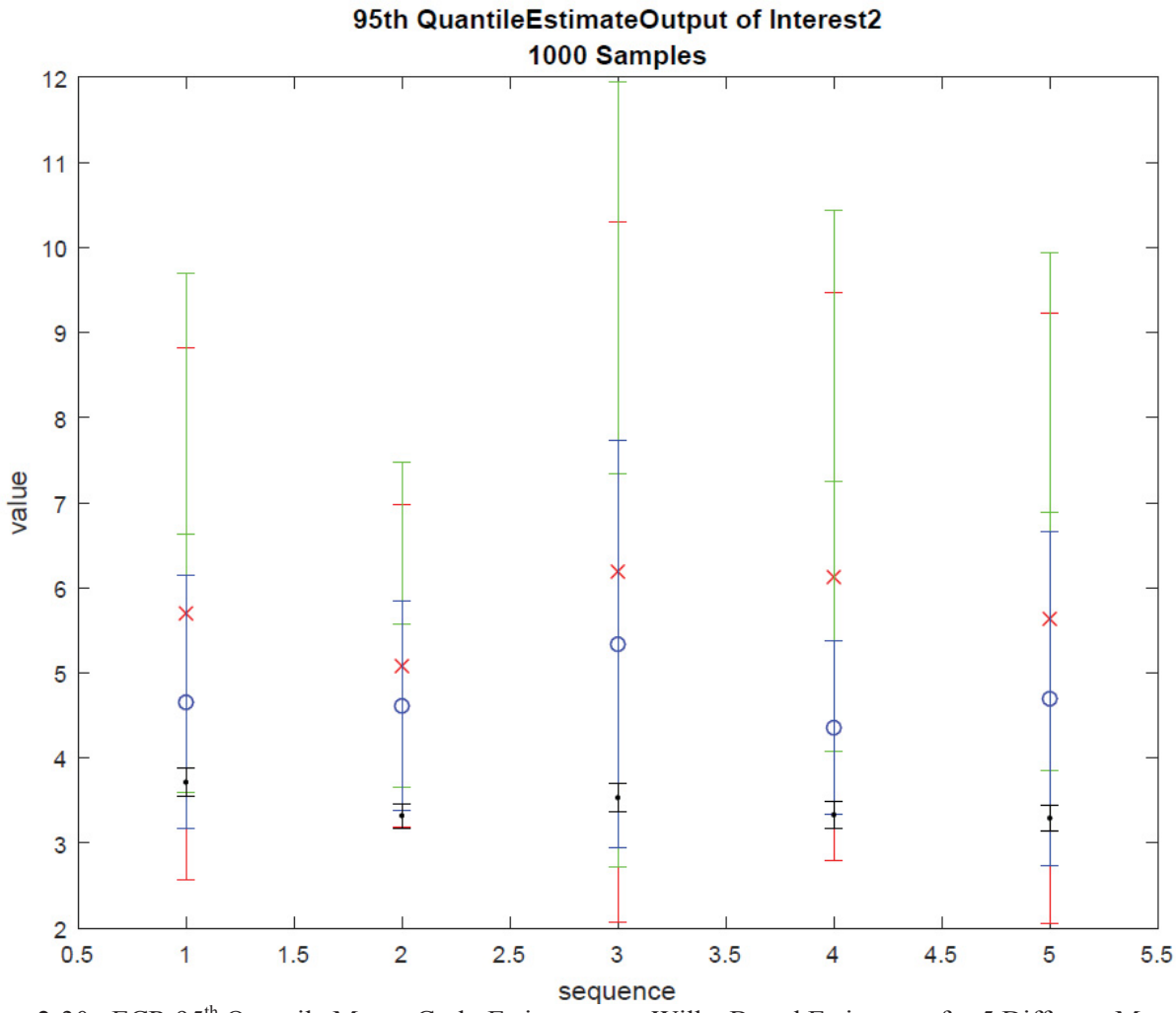

Figure 2-30. ECR 95th Quantile Monte Carlo Estimators vs Wilks-Based Estimators for 5 Different Monte Carlo Sequences Each with 1000 Samples (Black: Monte Carlo Estimator, Red: Wilks Max of 59 Samples 95/95 Estimator, Green: Wilks Max of 124 Samples 95/~98 Estimator, Blue: Wilks 3rd Highest of 124 Samples 95/95 Estimator).

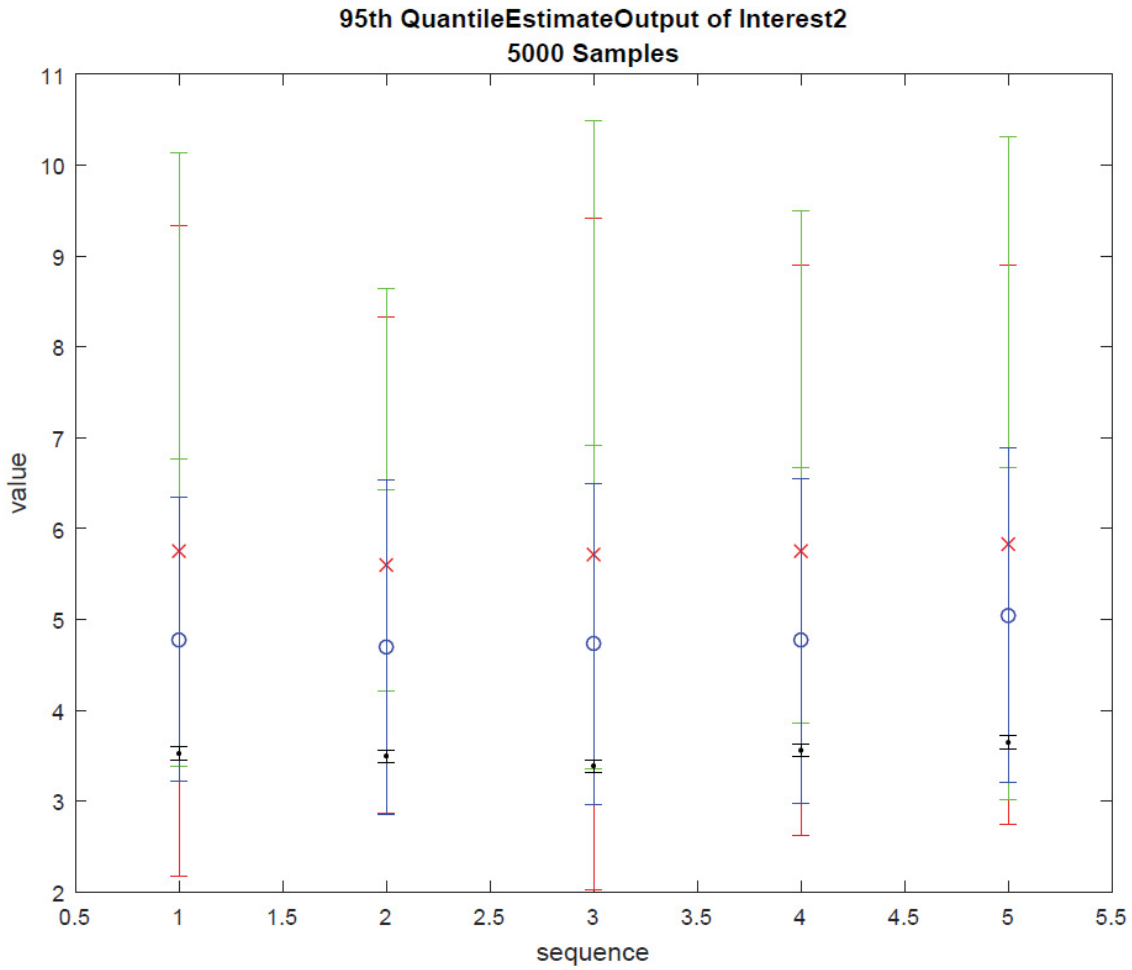

Figure 2-31. ECR 95th Quantile Monte Carlo Estimators vs Wilks-Based Estimators for 3rd Highest of 124 Samples 95/95 Estimator).

2.2.4.3 Wilks Comparison Summary

The **important issues observed** from the Framework Demo Monte Carlo UQ comparison to Wilks based estimators are:

- The Wilks-based estimators have substantial variability
- The Wilks-based estimators can have considerable conservative bias relative to the true unknown 95th quantile. This bias could be detrimental for a Utility/Licensee.
- Switching to Monte Carlo quantile estimators with large sample sizes remedies both situations. Large sample sizes have small variability on the Monte Carlo quantile estimator. Large sample sizes provide more accurate estimates to the true quantile, which therefore can remove the over-prediction bias with Wilks based estimators; this would recover margin for the Utilities/Licensees.
- The primary drawback of moving to large sample size Monte Carlo sampling is the computational expense and associated manpower required to document such analyses.

2.2.5 Sensitivity Analysis (SA) Results

The following subsections provide the Framework Demo results for the different SA algorithms described in Appendix A-2. The results are typically presented by showing some sensitivity measure for each of the inputs to

the Framework Demo IEM. The various figures below list the input parameters as numbers, rather than with names or symbols. Table 2-6 below lists the IEM uncertain input numbers with the name for each parameter. Input parameters 12 and 13 are dummy inputs, by definition there is no trend or correlation between the outputs and these two inputs. If any of the SA types reveal that inputs 12 and 13 are important then there was a bug in the implementation or more samples will be needed. Therefore, including the dummy inputs can help provide a diagnostic for quality assurance purposes.

It is of course important to note that the quantitative results reported in this section apply only to the Framework demo. Certain trends will be consistent with realistic LB-LOCA analyses (as intended by the construction of the LB-LOCA ROM), but the presented results are specific to this work. The primary purpose of this section is to go through how the output of the various SA types can be used to improve the understanding of the IEM. This section also highlights important diagnostics and implementation issues to consider when implementing these types of SA algorithms.

Table 2-6. Uncertain Input Parameter Numbers and Names.

Uncertain Input Number	Uncertain Input Name	Notes
1	Time in cycle	
2	Region 0 hot assembly $F_{\Delta H}$	
3	Region 1 hot assembly $F_{\Delta H}$	
4	Clad thermal conductivity	
5	Coolant heat transfer coefficient (steady-state)	
6	Gap conductance	
7	F_Q	
8	Peak linear heat rate axial elevation location	
9	Core total power (steady-state)	
10	Core total mass flow rate (steady-state)	
11	Core inlet temperature (steady-state)	
12	Dummy	
13	Dummy	
14	Heat-up Catton parameter (CSAU)	Analogous to heat transfer coefficient during blowdown heatup
15	Initial system pressure	
16	Final system pressure	
17	Blowdown time tuning parameter	
18	Break discharge coefficient	
19	Blowdown cooling heat transfer coefficient multiplier relative to blowdown heatup	Analogous to heat transfer coefficient during blowdown cooling
20	Blowdown cooling Catton parameter 1 (CSAU)	Analogous to heat transfer coefficient during blowdown cooling
21	Blowdown cooling Catton parameter 2 (CSAU)	Analogous to heat transfer coefficient during blowdown cooling
22	Refill heatup rate parameter	
23	Refill bypass ratio	
24	Reflood Catton coefficient (CSAU)	Analogous to heat transfer coefficient during reflood heatup
25	Reflood Catton exponent (CSAU)	Analogous to heat transfer coefficient during reflood heatup
26	Quench front rate multiplier relative to cold reflood rate	
27	Quench temperature	

2.2.5.1 Variance-Based SA

2.2.5.1.1 Sobol Indices

Main Effect Indices

The main effect (first order) Sobol indices for each input parameter to the PCT and ECR are shown in Figure 2-32 and Figure 2-33, respectively. The obvious take away from both figures is that the PCT and ECR variance is dominated by three uncertain input parameters:

- Input 7 – F_Q
- Input 14 – Heat-up Catton parameter (CSAU)
- Input 20 - Blowdown cooling Catton parameter 1 (CSAU)

Inputs 14 and 20 are both analogous to the heat transfer coefficient within their respective time domain. The fact that these two input parameters significantly impact both the PCT and ECR variance represents that the uncertainty in the heat transfer mechanisms during the blowdown portion of the transient significantly impacts the variance of the outputs of interest.

Input 7, F_Q, is an operational input whose uncertain range is specified to allow operation up to the Tech Spec limit. The fact that an operational input's variance significantly impacts the variance of the outputs of interest, suggests that the validity of the assumptions present within the creation of the operational input sampling distribution must be scrutinized. For example, if the upper bound on F_Q is not realistic but imposed by Regulatory requirements, margin could be recovered if it can be justified to use more operationally realistic ranges for the input.

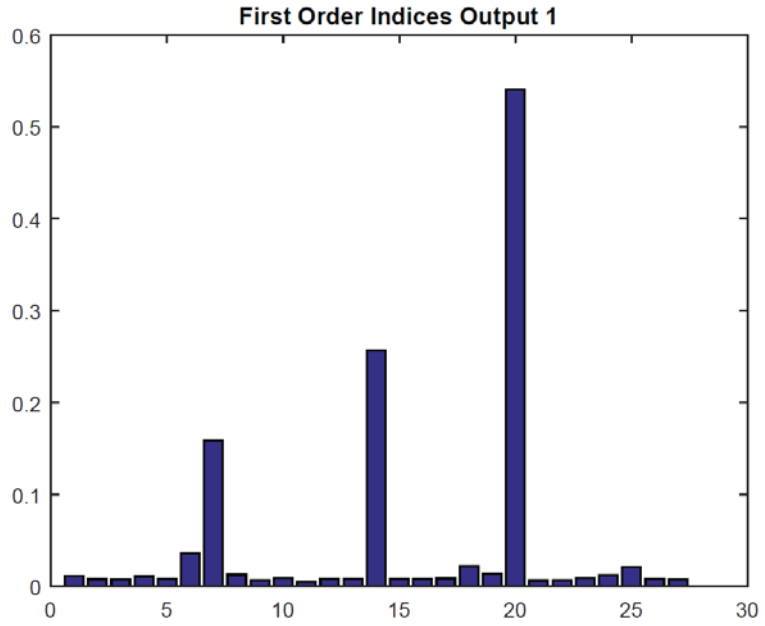

Figure 2-32. First Order (Main Effect) Sobol Indices on the PCT.

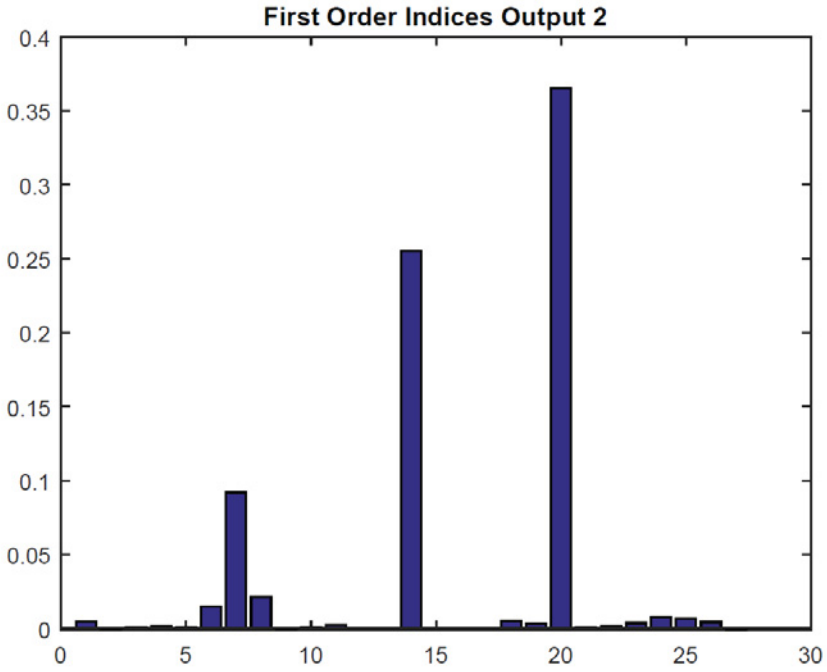

Figure 2-33. First Order (Main Effect) Sobol Indices on the ECR.

Total Effect Indices

The total effect Sobol indices for each input parameter on the PCT and ECR are shown in Figure 2-34 and Figure 2-35, respectively. The total effect indices make it seem that all inputs are of equal importance to the PCT variance. However, it is important to remember exactly what the total effect indices represent. The total effect index captures the main effect and all interactions a particular input parameter is involved with. Therefore, even if a particular input has nearly zero main effect contribution to the output variance, that input parameter can interact with the other input parameters (as long as the model in not-additive). The results in Figure 2-34 therefore suggest that there is definitely a significant amount of interaction between the different input parameters that contribute to the variance in the PCT. The exact partitioning of the total sensitivity indices into various higher-order interactions (two-way, three-way, etc…) is however not part of the total effect index calculation.

Figure 2-34. Total Effect Sobol Indices on the PCT.

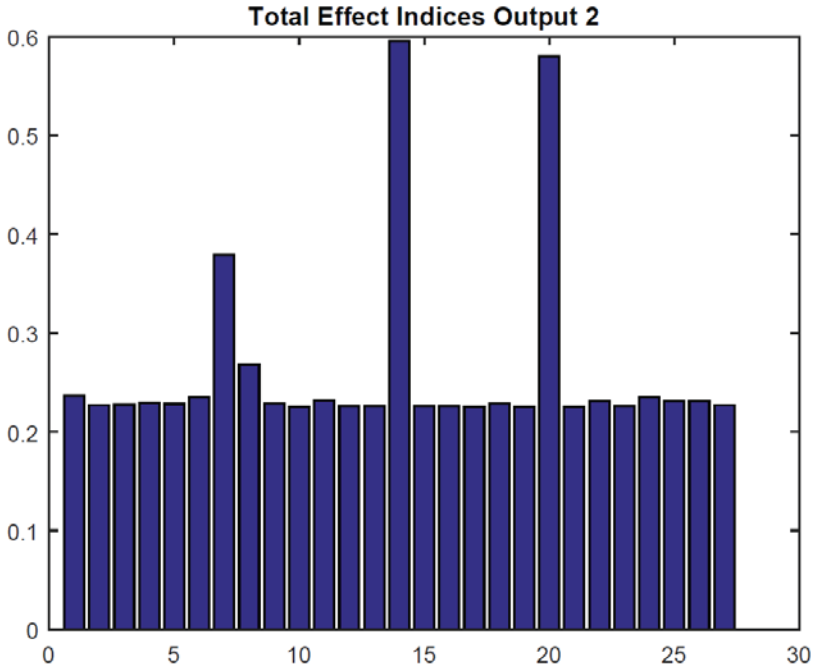

Figure 2-35. Total Effect Sobol Indices on the ECR.

Effect of Sample Size

The previous results used 5000 Monte Carlo samples per sequence. Therefore there were a total of $5000 \cdot (27 + 2) = 145000$ simulations run. Obviously this is a significant computational expense, which only

increases if more Monte Carlo samples were used per sequence. It should be noted though that each of the $D + 2$ Monte Carlo sequences can be run in parallel. Because the Sobol indices are estimated with Monte Carlo estimators to the variance, the Sobol indices can be significantly impacted by small sample sizes. Essentially, if the standard error is large, the standard error can induce odd or even unphysical results.

A simple diagnostic to help ensure that enough samples have been run is to check the sum of the main effect Sobol indices. The main effect indices should never exceed 1. If the computational model is perfectly additive, they should sum to exactly 1. The main effect indices can however sum to a value greater than 1 when the standard error on the variance estimator is large. Figure 2-36 shows the main effect Sobol indices estimated with only 500 Monte Carlo samples per sequence. Their sum is clearly greater than 1. Although Figure 2-36 correctly identifies the same three dominate inputs (inputs 7, 14, and 20), the fact that the main effect Sobol indices all sum greater than 1 means the results are not trustworthy and more samples are required.

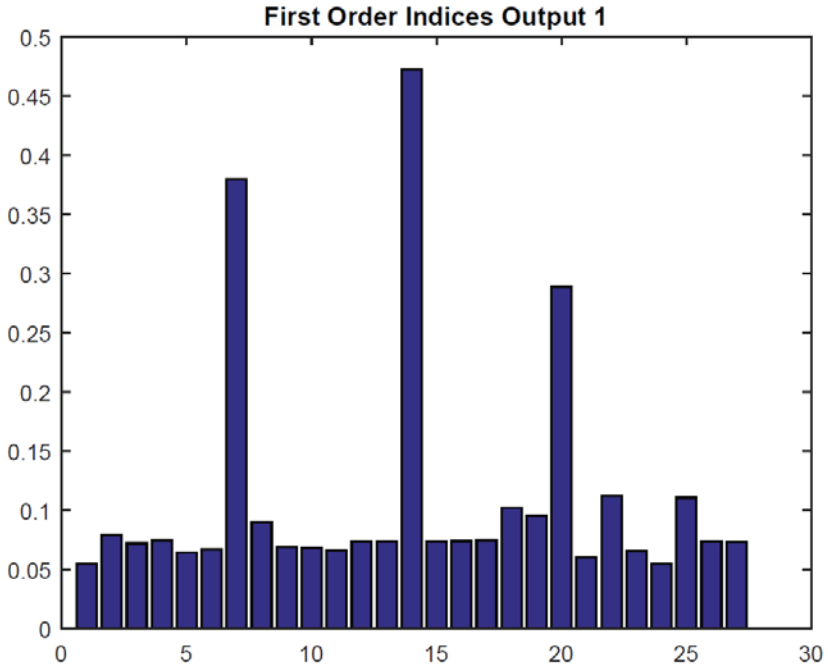

Figure 2-36. First Order (Main Effect) Sobol Indices on the PCT Computed with Only 500 Samples per Sequence.

2.2.5.1.2 FAST

The main effect sensitivity indices as estimated by FAST are shown in Figure 2-37 and Figure 2-38, for the PCT and ECR, respectively. Although the sensitivity indices are different quantitatively compared to the main effect Sobol indices estimated via Monte Carlo sampling, the qualitative results are the same. The same three input parameters dominate the variance of PCT and ECR, inputs 7, 14, and 20. The fact that two separate variance-based SA algorithms rank the inputs consistently helps provide confirmation that these are in fact the three dominant inputs.

As with the main effect Sobol indices, the FAST results show that the dummy inputs (12 and 13) are considered to be unimportant to the variance of either the PCT or the ECR.

The FAST algorithm is much more efficient than estimating the Sobol indices via Monte Carlo sampling. As mentioned previously, the Sobol indices required 145,000 IEM simulations. The FAST sensitivity indices, however, were estimated with roughly 8,000 IEM simulations. Although this makes it seem that FAST is clearly superior to using Monte Carlo sampling, the literature makes it seem that FAST becomes less reliable with larger number of inputs. The algorithm used in this work to determine the frequency set can only provide

frequencies up to 50 input parameters. If there are more than 50 inputs, a different algorithm would have to be found or even developed.

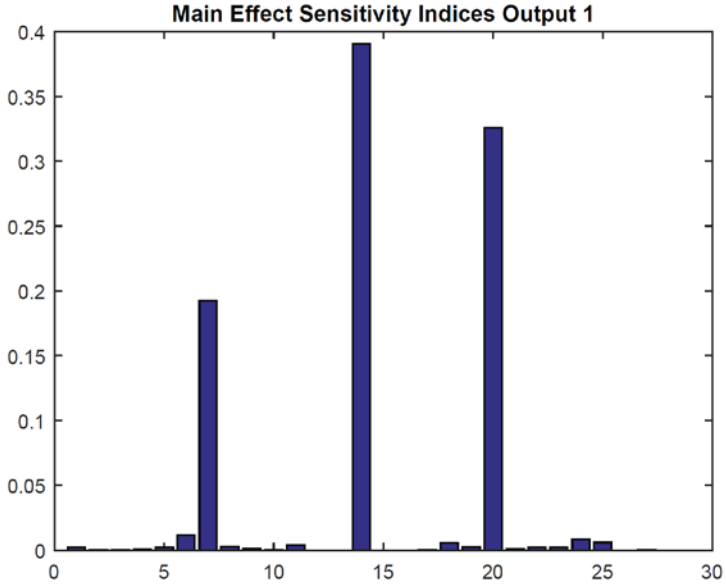

Figure 2-37. Main Effect Sensitivity Indices on the PCT Estimated by FAST.

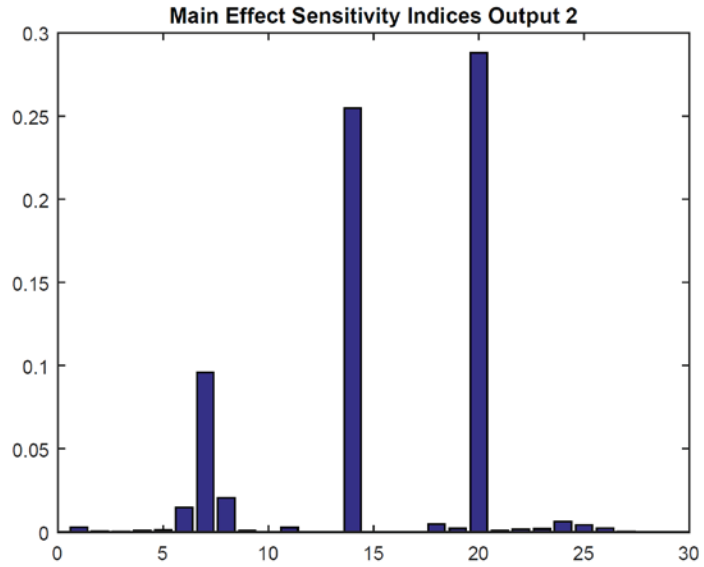

Figure 2-38. Main Effect Sensitivity Indices on the ECR Estimated by FAST.

2.2.5.1.3 Variance-Bases SA Summary

Variance-based SA ranks input parameters in terms of which inputs contribute the most to the output's variance. The Framework demo offered several useful insights which should be considered when implementing such analyses in real problems:

- When using Monte Carlo sampling to estimate the Sobol indices, the sum on the main effect indices provides a simple diagnostic on the sample size. If the sum is greater than 1 then more samples will be needed.
- Dummy inputs can be used to help provide an additional diagnostic. If the SA results suggest the dummy input is important the algorithm has not been implementing correctly (there is a bug in the code), or more

samples are needed. Once the algorithm has been verified as working as it is intended, more samples should remedy the situation.

- Multiple types of SA algorithms should be used to help provide confirmation that the results are correct.
- FAST is very efficient compared to Monte Carlo sampling and appears to be an elegant approach to variance-based SA as long as there are less than 50 inputs.

2.2.5.2 Monte Carlo Filtering (MCF)

The Monte Carlo Filtering (MCF) results are presented as bar graphs showing the Kolmogorov–Smirnov (KS) test statistic for each uncertain input parameter. The critical values for the 1% and 10% significance levels are shown as red and black horizontal lines, respectively. Any input parameter with a bar plot above the red line is therefore of critical importance to the output exceeding the desired threshold value. If a bar plot is between the black and red lines, the corresponding input parameter is important, and if the bar plot is beneath the black line that input parameter is insignificant.

The MCF results are presented just for the PCT, but similar results can be shown for the ECR. The specific threshold values were selected as the 5th, 50th (median), and 95th quantiles of the PCT.

2.2.5.2.1 MCF Applied to Quantiles of the PCT

The MCF results are shown in Figure 2-39, Figure 2-40, and Figure 2-41 for the 5th, 50th, and 95th quantiles, respectively. As with the variance based results, inputs 7, 14, and 20 are of critical importance and appear to be the most input parameters that dictate if the PCT exceeds the three selected quantile values. MCF reveals that these three inputs are very important over the entire range of the PCT values, spanning the 5th through 95th quantiles.

Other input parameters change their importance depending on the threshold value of interest. For example, input 11 (the core inlet temperature) is critically important to the PCT exceeding its 5th and 50th quantiles. However, MCF via the KS test considers input 11 to be insignificant to the PCT exceeding its 95th quantile. This reveals that the input parameters influence the output (the PCT in this demonstration) differently over the range of the output. This aspect is not presented in variance-based SA, and can therefore provide useful supplemental information to the information gained from Sobol indices and FAST.

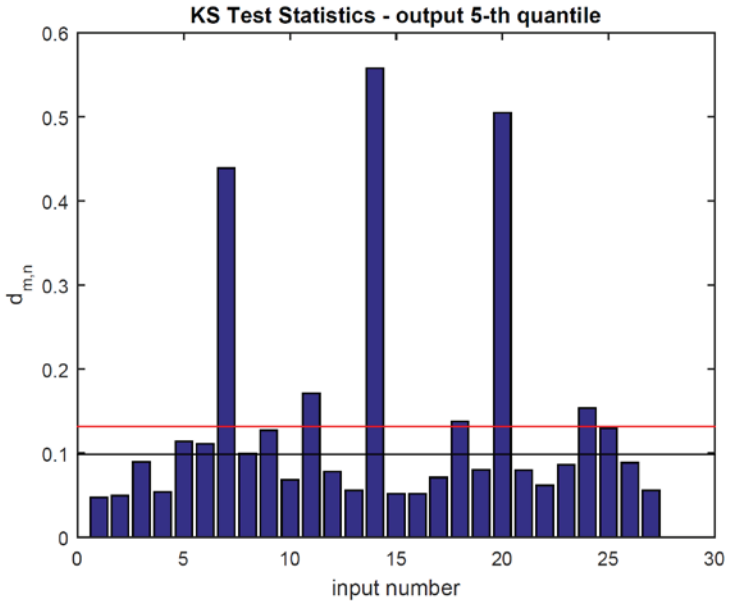

Figure 2-39. KS Test Statistics for Each Uncertain Input Parameter on the PCT Exceeding its 5th Quantile.

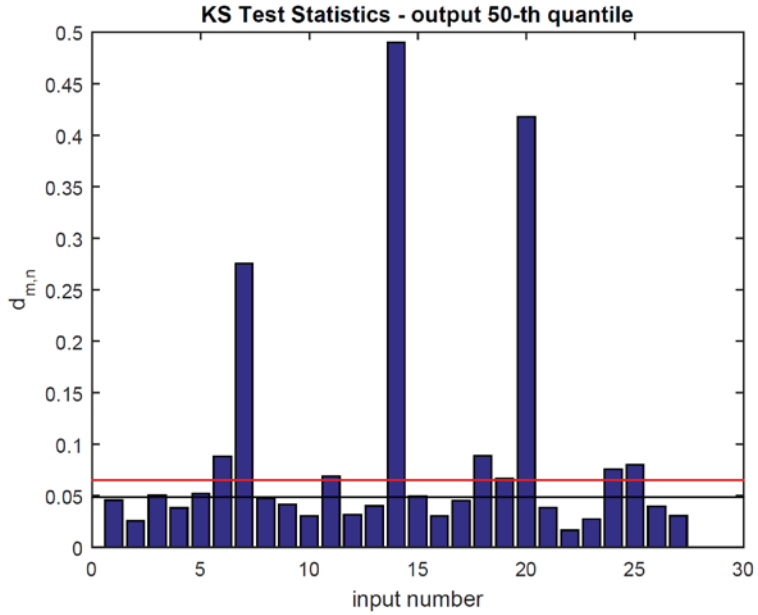

Figure 2-40. KS Test Statistics for Each Uncertain Input Parameter on the PCT Exceeding its 50th Quantile (Median).

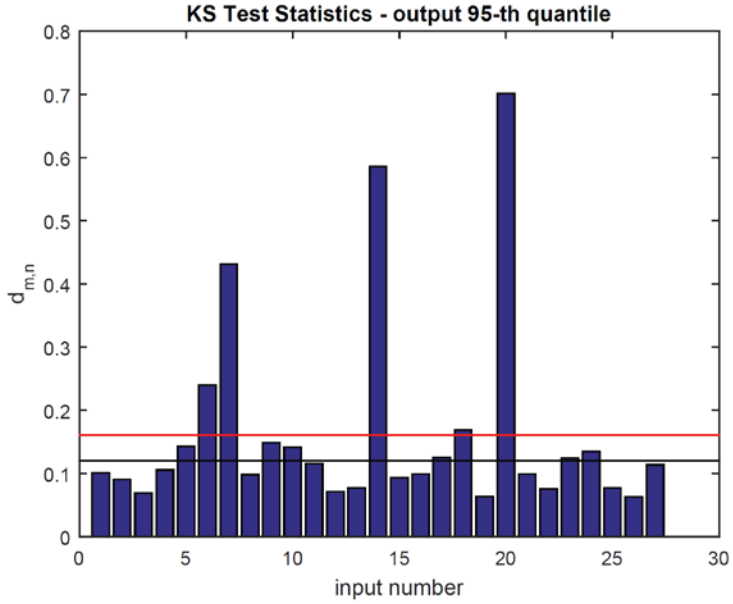

Figure 2-41. KS Test Statistics for Each Uncertain Input Parameter on the PCT Exceeding its 95th Quantile.

2.2.5.2.2 Impact of Sample Size

As with any method revolving around Monte Carlo sampling, the MCF results will be impacted by the finite sample size. Too few samples could skew the results and lead to ranking the important inputs incorrectly. The MCF results shown previously used 2500 Monte Carlo samples. With only 250 samples however, the KS test statistics on the 95th quantile of the PCT produce vastly different importance rankings, as shown in Figure 2-42 below. Input 13 is one of the two dummy inputs, but the MCF rankings shown in Figure 2-42 suggest that input 13 is critically important to the PCT exceeding its 95th quantile. This incorrect conclusion is remedied by using more samples.

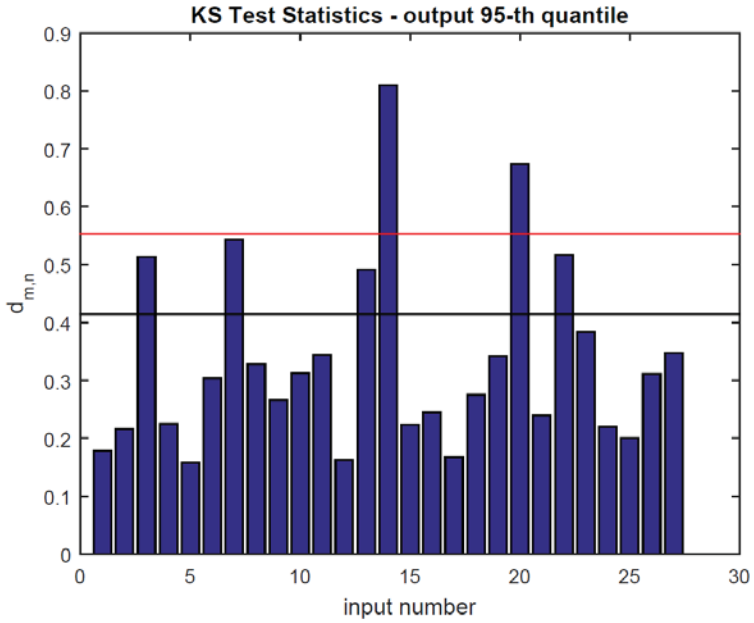

Figure 2-42. KS Test Statistics for Each Uncertain Input Parameter on the PCT Exceeding its 95th Quantile When Only 250 Samples Were Used.

2.2.5.3 Limit Surface

The limit surface was setup to find all combinations of the uncertain input parameters that produced PCT results that exceeded the NRC limit of 2200 ^{O}F. The likelihood-free Markov Chain Monte Carlo (LF-MCMC) described in the Appendix A-2 sub-section on limit surfaces was used to find these input parameter combinations. A total of 10^5 samples were used, with the first 10^4 discarded as burn-in, yielding 9×10^4 samples drawn from the limit surface. Because of the very high dimensional space (27 inputs), it is difficult to visualize this surface in a simple manner. The surface is summarized by the "posterior" histograms of the Markov chain samples in Figure 2-43 below. Each subplot provides a histogram of the "prior" which is just the assumed sampling distribution for each input in red and the "posterior" samples drawn from the limit surface in a dark green. For the framework demo, all of the uncertain inputs were assumed to be uniform. The histograms are shown for scaled inputs where 0 corresponds to the lower bound and 1 is the upper bound on each uniform distribution. If a particular input's posterior histogram is nearly uniform such as input 12 (one of the dummy inputs) there is no preferential set of values for that input that leads to the PCT exceeding the NRC limit. On the other hand, if an input's posterior histogram is very different from the prior uniform such as input 7 (F_Q) then there are particular values of that input that lead to the PCT exceeding the NRC limit.

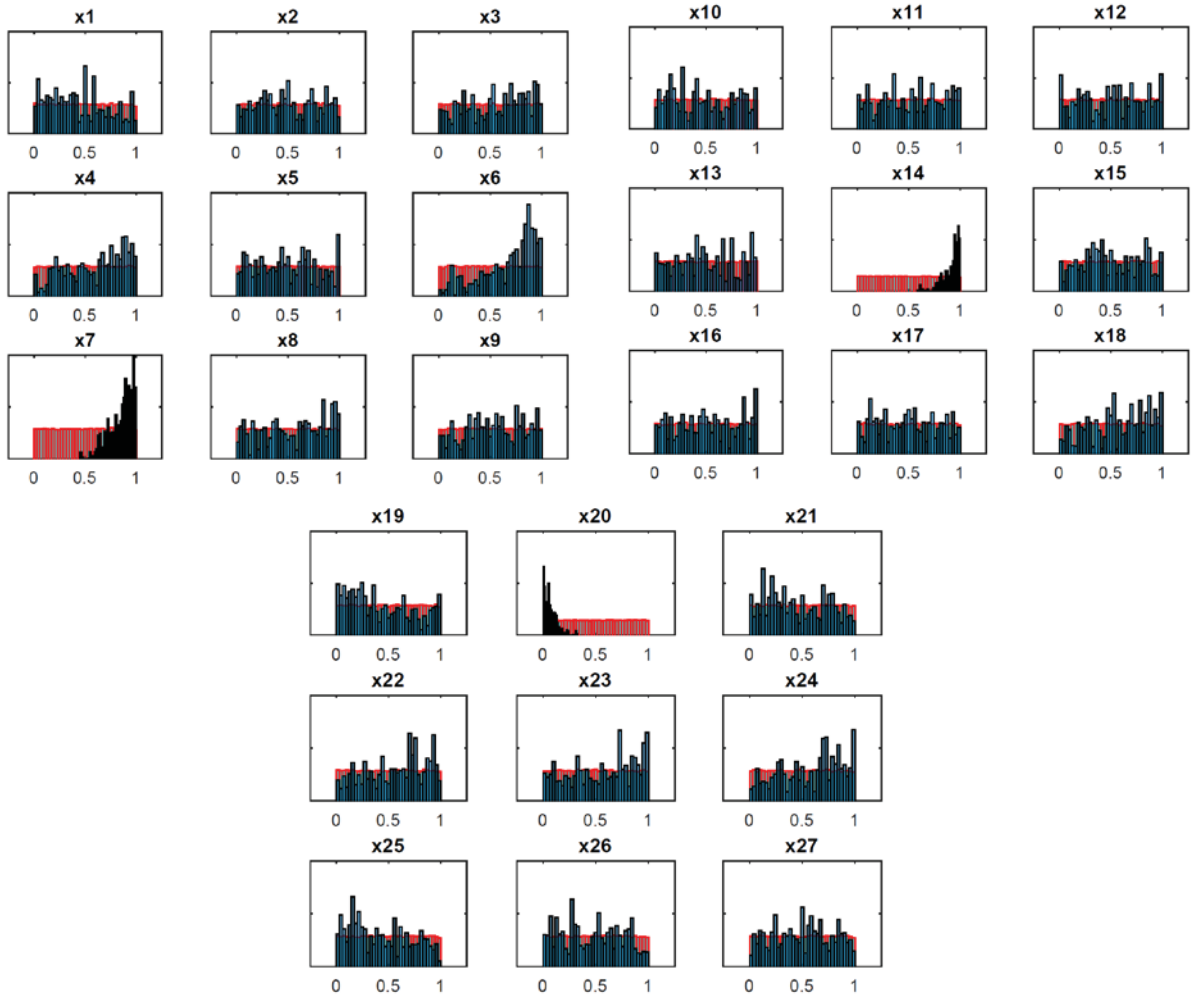

Figure 2-43. "Posterior" vs "Prior" Histograms which Summarize Draws from the Limit Surface for Each of the 27 Uncertain Input Parameters.

2.2.5.4 Distributional SA

Distributional SA here defines assessments of the effect on the output caused by change to distributions or assumptions of the inputs. To demonstrate Distributional SA, the maximum value of input 7 (F_Q) was increased from 2.83 to 2.9. Note that this is one of the three important inputs determined by the global SA discussed before.

To quantify the impact, the full MC needs to be repeated. The significance of the effect is judged by comparing the resulting output distributions via a Kolmogorov–Smirnov (KS) test, as well as by comparing the 95th quantile estimates.

Figure 2-44 shows that the Kolmogorov–Smirnov (KS) null hypothesis test was not rejected, making the effect not significant for PCT. Same apply to the ECR (Figure 2-45).

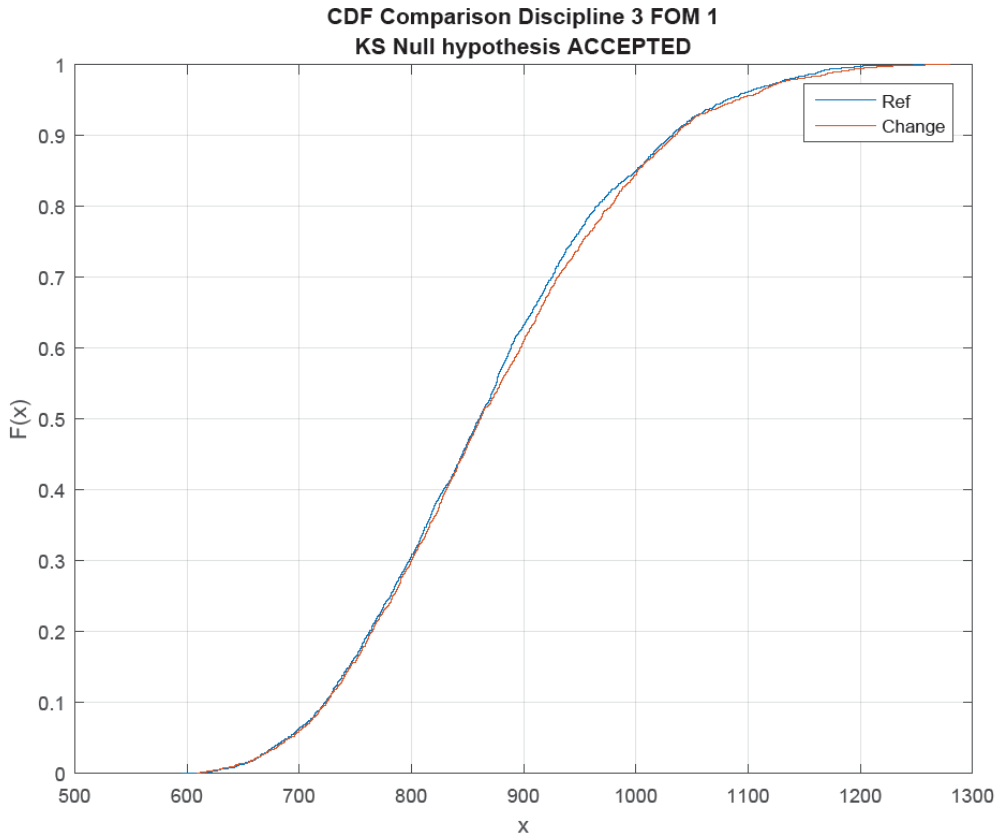

Figure 2-44. CDF Comparison on LB-LOCA Response (PCT).

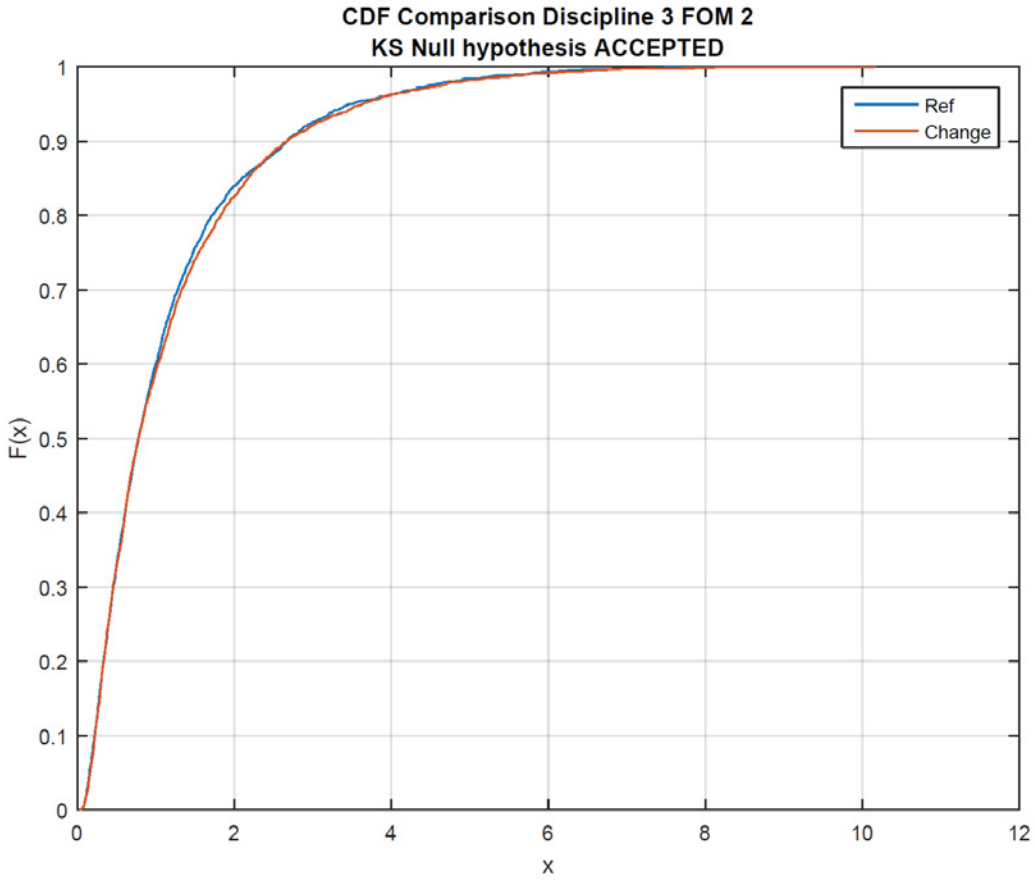

Figure 2-45. CDF Comparison on LB-LOCA Response (ECR).

One issue with the KS hypothesis test is that it checks the impact on the distribution as a whole. However the interest is on an extreme quantile (say the 95th quantile). A more direct check is to compare the 95th quantile estimates with the corresponding confidence interval. A significant effect would yield the two confidence intervals to not overlap. The 95th quantile estimators on the PCT and ECR for the original and modified cases are shown in Figure 2-46 and Figure 2-47, respectively. It is clear to see that although the 95th quantile estimator on PCT and ECR both increase with the increase on F_Q's upper bound. However, because the 95th quantile estimators' confidence intervals overlap for both PCT and ECR, it is difficult to discern if the increase is completely due to this change, or just a product of the finite sample size. It is interesting to note that the overlap of the ECR confidence intervals is less than that for the PCT confidence intervals.

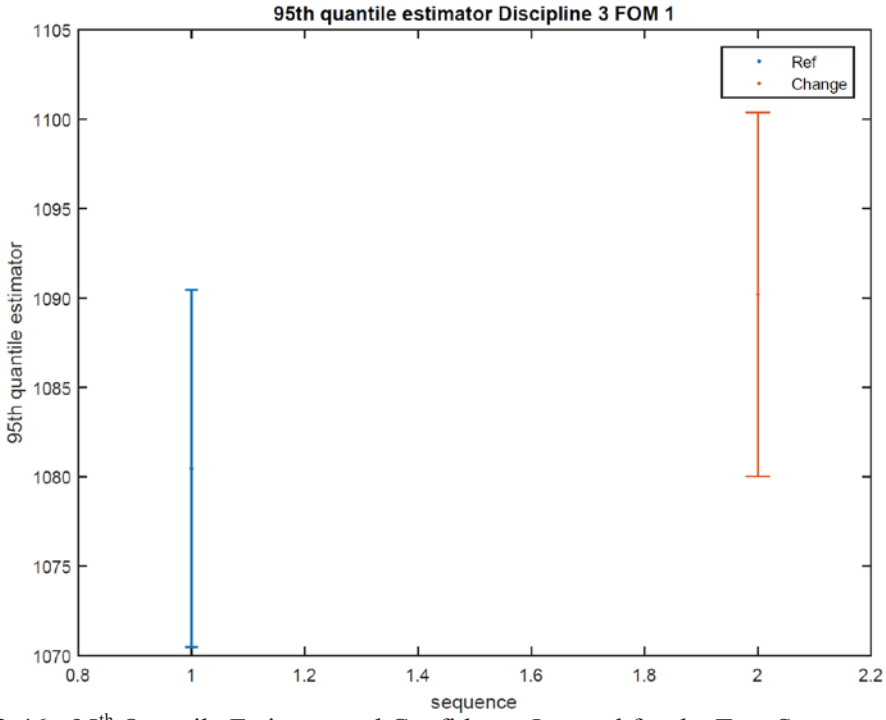

Figure 2-46. 95th Quantile Estimate and Confidence Interval for the Two Sequences (PCT).

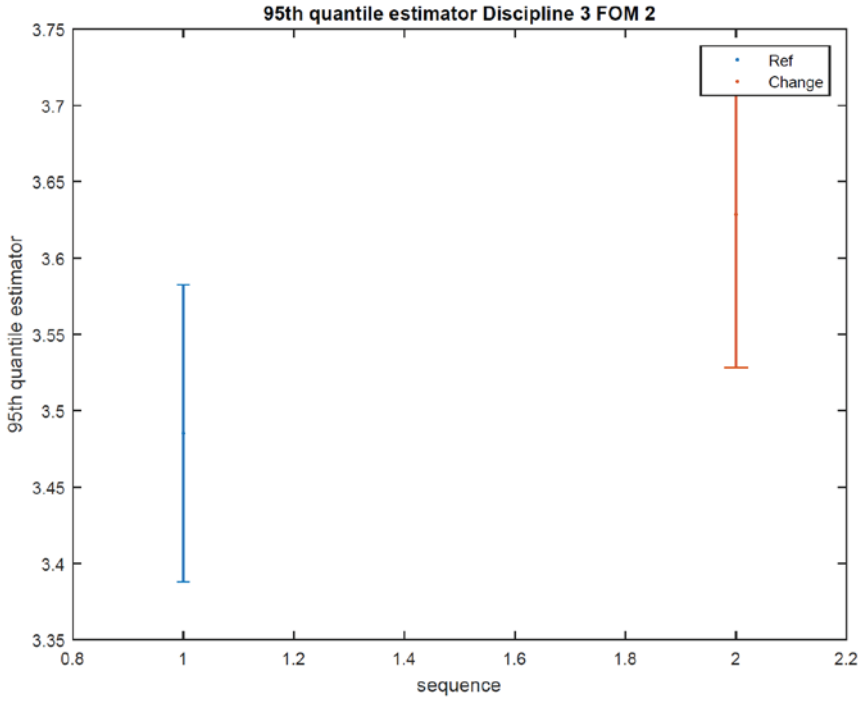

Figure 2-47. 95th Quantile Estimate and Confidence Interval for the Two Sequences (ECR).

The decision of whether an assumption change impacts the 95th quantile estimator must be made in the context of this desired precision level. Therefore, the desired precision level on the 95th quantile needs to be established before the analysis is carried out. The desired precision level is of course set by the number of Monte Carlo samples used to perform UQ.

2.3 Computational Requirement and Implementation Strategy for the LOCA Analysis

The most important conclusion from Section 2.2 is the need to use better estimators than Wilks-based estimators. The sample size has to increase by one or two orders of magnitude to provide reliable answers to the problems of interest in the RIMM IEM context. The main advantage of using Monte Carlo estimators compared to Wilks-based estimators is that an estimate is given with a confidence level. A Wilks-based estimator already has the confidence "embedded" in the estimate itself, which therefore removes that information from the analyst's control.

Another benefit of "full" Monte Carlo sampling is that Monte Carlo is independent on the number of inputs **and** outputs being considered. With the proposed rule change, the number of outputs that must be tracked must increase since the ECR limit (and to a lesser extent the PCT limit) depends on a fuel rod's burnup and time in the core. A Wilks-based estimator that ensures all of the rods analyzed in a LOCA analysis are within compliance would have to deal a potentially large number of possible outcomes. The minimum sample size would increase substantially as well as driving up the level of conservatism for the Wilks-based estimator.

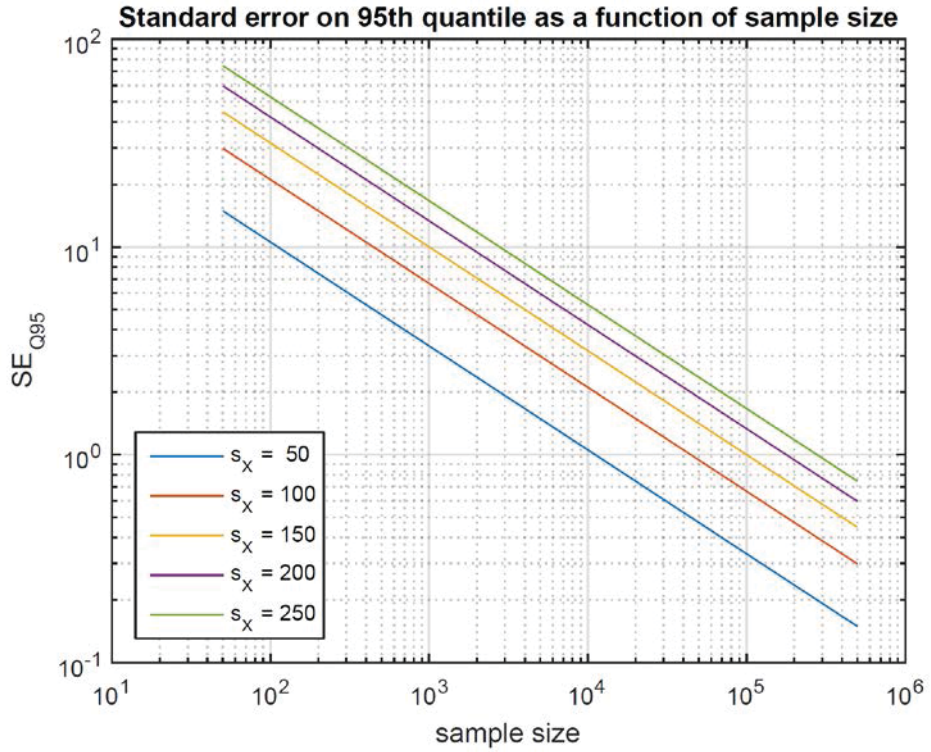

Figure 2-48. Standard Error (In Degrees C) on 95th Quantile as a Function of Sample Size.

The use of full MC simulation addresses those issues since the number of samples is dependent upon the desired level of precision of the estimators of interest. The drawback is the need to generate very large samples of the quantities of interest, most likely one or two orders of magnitude larger than current industry practice. The standard error on the 95th quantile estimator depends on the sample standard deviation as explained in Appendix A-2. Figure 2-48 shows the standard error on the 95th quantile estimator for various sample standard deviations as a function of Monte Carlo sample size. Figure 2-48 can be used to provide an estimate for the required number of samples to achieve a particular level of precision if the sample standard deviation of a quantity of is roughly known. For example, if we are interested in estimating the 95th quantile of PCT from a sample of Large Break LOCA simulations of a typical PWR and we would like to achieve a 95% confidence interval spanning 10

^{O}C which corresponds to a standard error of 2.5 ^{O}C, the anticipated standard deviation of the PCT population is of the order of 100 ^{O}C. The sample size required to achieve that precision is of the order of 8,000. However, if the sample standard deviation is closer to 150 ^{O}C over 10,000 samples would be needed to achieve the same level of precision.

As far as the global SA, the example presented in Section 2.2 suggested the need of hundreds of thousands of simulations must be run to obtain the Sobol indices. The Sobol indices are estimated with Monte Carlo estimators to the variance, therefore the Sobol indices can be significantly impacted by small sample sizes. Essentially, if the standard error is large, the standard error can induce odd or even unphysical results. FAST is more efficient compared to Monte Carlo sampling and appears to be an elegant approach to variance-based SA as long as there are less than 50 inputs. For this specific demonstration, roughly 8000 simulations were required to implement FAST. If the simulation code has more than 27 inputs, more simulations would be needed.

As with any method revolving around Monte Carlo sampling, the MCF results are impacted by the finite sample size. Too few samples could skew the results and lead to ranking the important inputs incorrectly. The MCF results shown previously used 2500 Monte Carlo samples. Distributional SA also requires a similar number of simulations. The limit surface search presented requires similar numbers of simulations as the Sobol indices. Because of the high dimensional space considered, it is expected that any limit surface search algorithm would require a massive sample size as well.

Implementing these types of SA algorithms therefore raises several questions:

1. Can we generate these large samples (~100,000) in practice?
2. If not, what are the alternatives?

First, let us assume that we can in fact generate hundreds of thousands of samples. There are two issues:

a. Computational requirements
b. Robustness and reliability of the computer codes used to perform the simulations

The typical run time for a single LOCA simulation on today's computers is of the order of 6 hrs. All the simulations can be run in parallel (with the exception of MCMC simulations). To achieve a turnaround of 24 hrs a massive cluster of 25,000 CPUs would be needed. This class of computer is available at many US National Laboratories.

The other issue (b) is possibly the most serious issue. This has to do with the code robustness and reliability. Failure rates (run stopping before completion) of 10% are typical. Therefore the analyst would need to deal with 10,000 failed runs. Manual intervention to 'fix' the runs is out of question. The remedy to this issue is to improve code numerics and/or develop automation to handle these failures without human intervention.

These capabilities would require significant investment of resources in terms of both capital and personnel to achieve. Therefore, alternatives that reduce the computational burden are highly advantageous.

The computational gap can be covered with the adoption of fast running surrogate models or emulators. This capability is intended for the next stage of the RIMM project which plans to use emulators to approximate the IEM input/output relationship. After an initial set of computer code evaluations are performed to build or train the surrogate, the surrogate model is used in place of the computer code in the Monte Carlo sampling scheme. The surrogate model based approach to UQ was proposed as part of the original CSAU method for propagating uncertainties. It was dropped in favor of the Wilks-based approach due to computational limitations of the time and issues dealing with the additional uncertainty of the surrogate. Modern computer hardware and open source machine learning algorithms allow over coming these original short comings to the surrogate model based UQ method. When using a surrogate model based approach, it is very important to include an estimate of the surrogate's own predictive uncertainty. Gaussian Process (GP) emulators are a common type of surrogate that provides an estimate to its own predictive uncertainty. Having access to such information allows the analyst to know when additional "full" computer simulations are needed to improve the emulator's predictive quality.

There are other types of surrogate models that provide similar estimates to their predictive uncertainty. Determining the "best" or more appropriate emulator to use for an IEM would be the subject of future work.

Note that emulators need to be trained by simulations so the "full" IEM must still be run. It is expected that these initial "training runs" will dominate the computational burden as long as building the emulator and making subsequent predictions with the emulator are relatively computationally cheap. A general rule of thumb is that 10 training simulations are needed per input parameter, but the exact number can vary as high as 50 training runs. With 100 input parameters, the number of training runs would be on the order of 1000 to 5000. The goal is that these 1000 to 5000 runs would provide similar predictive quality via the emulator as running the "full" IEM simulation 100,000 times or more.

It is important to note that once an emulator has been built from a set of training runs, the "full" IEM simulations do not need to be rerun. Thus, an analysis could be repeated numerous times very cheaply thanks to the emulators. In contrast, if the "full" IEM simulations are always used, the IEM simulations must always be rerun whenever an analysis is repeated. The emulators also offer the ability to respond quickly to certain types of questions. For example, given the high cost of a typical LOCA safety analysis, current practice is to consider expanded ranges of the inputs which not only cover the current state (or range) of the plant but project state of the plant into the future to ensure the analysis holds over the course of several fuel cycles. For example the axial power shape envelop is sometimes constructed a priory based on current and future fuel cycles to prevent the need for re-analysis at each reload.

Fast running emulators could be trained over the expanded range even though UQ is conducted over a more restricted range which better represents the actual state of the plant. If some condition should occur that requires the analysis repeated outside the initial restricted UQ range, but is within the expanded range which trained the emulator, the emulator could repeat the UQ without having to rerun the "full" IEM. It is even conceivable to develop this technology further to enable an on-line LOCA margin monitoring system. This would be a system that estimates the PCT or ECR on a continuous base to determine the instantaneous margin to the limit. There could be opportunity for operational flexibility if margin is monitored continuously rather than at predefined unknown conditions, often bounded.

3. FUEL CYCLE ANALYSIS AND CORE DESIGN

In order to obtain detailed burn-up information, a core design simulation strategy needed to be employed. In Figure 3-1 the calculation flow for an exhaustive neutronic reactor design strategy is schematically reported. As it can be inferred, the core design is composed of several consequential steps, employed through as many different calculation methodologies (simulation codes). The first phase is related to the generation of the homogenized neutron cross-sections, which are going to be used in the successive reactor calculation. The computation of these parameters is commonly performed through lattice codes. Simplistically, their principal goal is related to the computation of a detailed neutron flux in the core (2-Dimensional approximation). The calculation can be performed either considering individually all the unique assemblies constituting the reactor core (taking in account all the different compositions, geometry discontinuities, neighbor assemblies, etc.) or modeling the whole reactor core (exploiting eventual symmetries, in order to reduce it at least to ¼ core). The flux solution is then used to perform an energy-space collapsing to compute the homogenized neutron cross sections that will be used in the sub-sequential reactor calculation. Each lattice calculation is performed considering all the different combination of the state variables that characterize the reactor (burn-up, moderator temperature, boron concentration, etc.). The final homogenized cross section will be therefore available in tables tabulated versus the above-mentioned variables. The second phase is related to the reactor calculation that, as already mentioned, approximates the reactor as constituted by homogenized regions (the reactor is seen as Cartesian or hexagonal regions where the physical property of the medium are considered homogenous). This phase is performed using nodal reactor physics packages, coupled with Thermal Hydraulic codes.

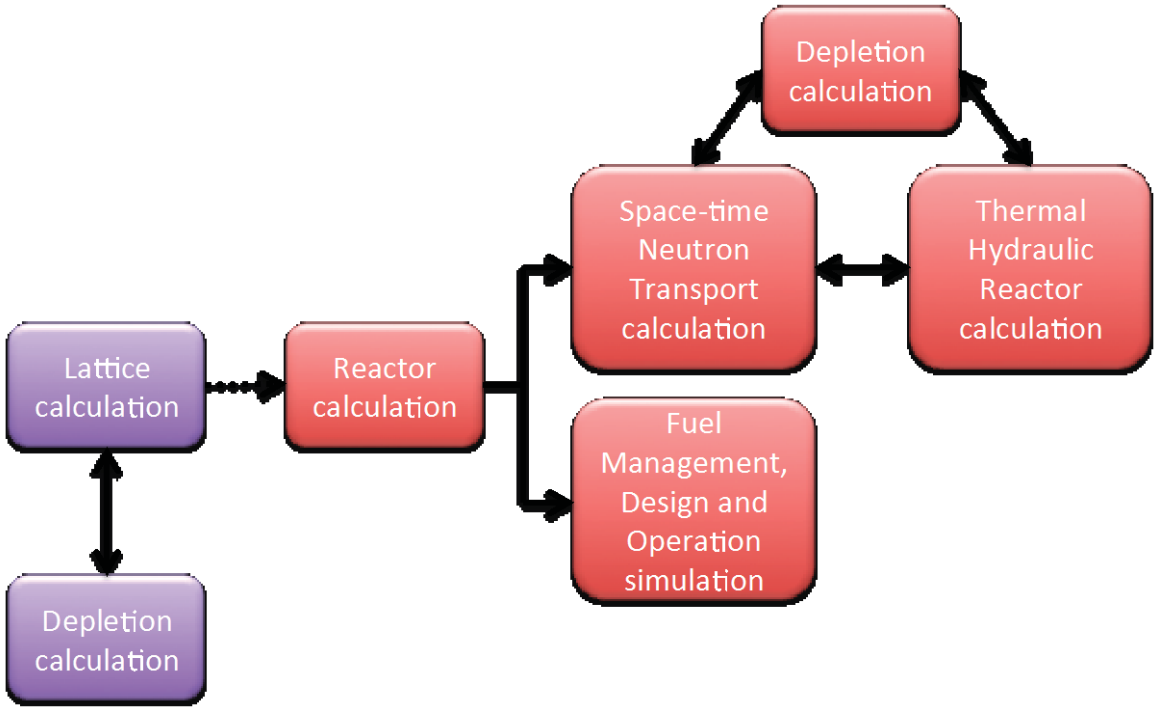

Figure 3-1. Core Design Strategy Scheme.

3.1 Lattice Physics and Cross Section Generation

In the nuclear field, the software HELIOS-2 (Studsvik ScandPower) is a known to be one of the most popular lattice codes. HELIOS-2 currently employs two different methodologies for the solution of the transport equation, the method of the characteristics and the collision probability solver. Resonance self-shielding is calculated via the subgroup method, with a transport-based Dancoff calculation. The predictor-corrector method is used for depletion, and the depletion path allows arbitrary state changes, generalized decay capabilities, and

branch-off calculations at any point in the solution path (in order to compute the flux solution for different combination of state variables).

HELIOS-2 has been extensively validated against measured critical experiments, continuous-energy Monte Carlo calculations, and international isotopic benchmarks - delivering exceptional accuracy for traditional, non-traditional, and experimental fuel designs.

3.2 Reactor Physics Core Design

PHISICS (Parallel and Highly Innovative Simulation for the INL Code System) code toolkit is being developed at the Idaho National Laboratory. This package is intended to provide a modern analysis tool for reactor physics investigation. It is designed to maximize accuracy for a given availability of computational resources and to give state-of-the-art tools to the nuclear engineer. This is obtained by implementing several different algorithms and meshing approaches among which the user will be able to choose, in order to optimize his computational resources and accuracy needs. The software is completely modular in order to simplify the independent development of modules by different teams and future maintenance. The different modules currently available in the PHISICS package are a nodal and semi-structured transport core solver (INSTANT), a depletion module (MRTAU), a time-dependent solver (TimeIntegrator), a cross section interpolation and manipulation framework (MIXER), a criticality search module (CRITICALITY) and a fuel management and shuffling component (SHUFFLE). PHISICS can be run in parallel to take advantage of multiple computer cores (10 to 100 cores). In addition, the package is coupled to the system safety analysis code RELAP5-3D.

3.3 Reference Core Design

The reference plant, which has been chosen for the purpose of this project, is a typical Pressurized Water Reactor. The modeling of this reactor is based on the "Benchmark for Evaluation and Validation of Reactor Simulations (BEAVRS)." BEAVRS is a detailed PWR benchmark containing real plant data for assessing the accuracy of reactor physics simulation tools for the first 2 operational cycles.

Figure 3-2 shows the radial layout of the reactor, including the reflector and the pressure vessel and the key plant parameters, respectively.

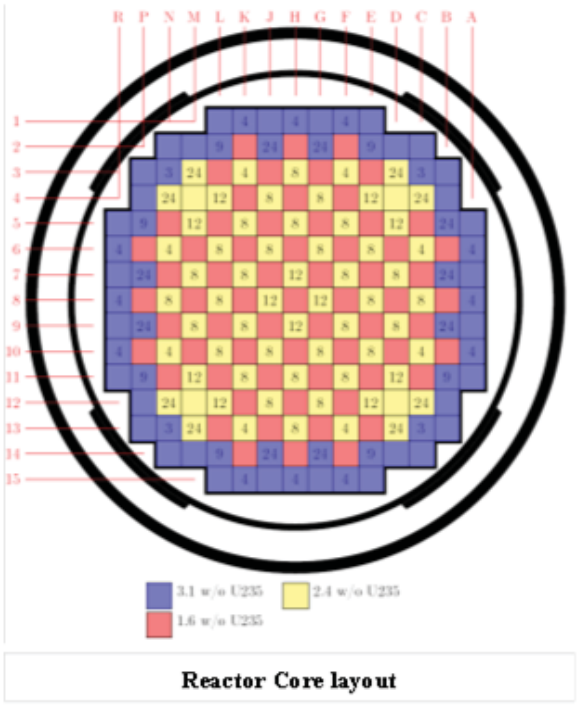

Reactor Core layout

Key plant parameters

Core Lattice	
No. Fuel Assemblies	193
Loading Pattern	w/o U-235
Region 1	1.61 %
Region 2	2.40 %
Region 3	3.10 %
Control	
Control Rod Material	Ag-80%, In-15%, Cd-15%
No. Control Rod Banks	57
No. Burnable Absorber Rods in Core	946
Burnable Absorber Material	Borosilicate Glass, 12.5 w/o B_2O_3
Performance	
Power	3411 MWth
Operating Pressure	15.51 MPa
Isothermal Coolant Temperature	564.82 K

Figure 3-2. BEAVRS Benchmark.

For the calculation of the homogenized cross sections, the lattice code HELIOS-2 (Studsvik ScandPower) has been used. In order to identify the number of cross sections sets needed to employ in this calculation, the "proximity" approach has been employed: even if the number of compositions are limited, an assembly is considered different with respect to another, in case the neighbor ones are different (e.g. different composition, structural material, instrumentation tube locations, etc.). This approach led to the identification of 29 different cross sections sets for the fuel region and one for the radial reflector, composed by the baffle, water between the baffle and the barrel, the barrel and the thermal shield. In Figure 3-3, cross sections libraries geometrical allocation is reported. The lattice calculations are generally employed in starting from pre-collapsed multi-group neutron energy structures. For the computation of the different cross sections sets, lattice calculations have been performed starting from a 44-energy group structure, then collapsed into an 8 group structure in the homogenization procedure. In Table 3-1 the collapsed energy structure is reported.

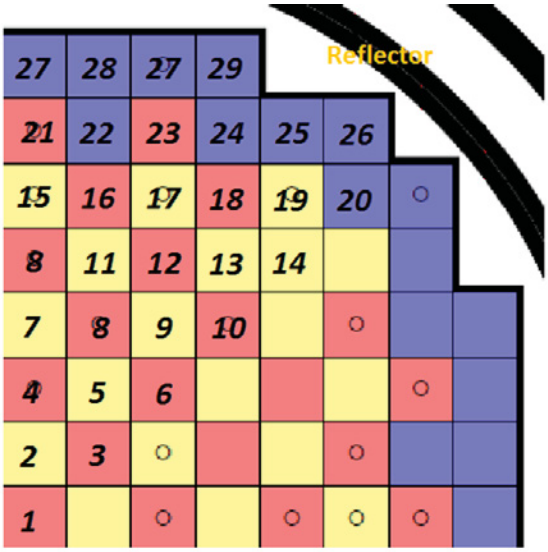

Figure 3-3. Geometric Location of Cross Sections Sets.

Table 3-1. Collapsed Energy Structure.

Group	Upper energy bound (eV)
1	2.00E+07
2	2.23E+06
3	8.21E+05
4	9.12E+03
5	1.30E+02
6	3.93E+00
7	6.25E-01
8	1.46E-01

The reactor calculation involves the simulation of the reactor during several operational cycles and during transient/maneuver events. In order to exchange feedback between the core design tools (PHISICS) and the Thermal-hydraulic code (RELAP5-3D), the ***Microscopic*** cross sections sets are tabulated with respect to several field parameters. Table 3-2 shows a simplified tabulation of points selected for this demonstration.

Table 3-2. Cross-Sections Tabulations.

Boron concentration (ppm)	1.0e-06	1.0e+03	1.9e+03
Moderator density (kg/m^3)	640.8	833.0	945.2	1000.0
Fuel temperature (K)	573.5	1073.5	1573.5
Burn-up (GWd/tHM)	0.00	0.15	50.00

The tabulation dimensions bring to the construction of a complete N-Dimensional (4-Dimensional in this case) grid that is characterized by 108 tabulation points (in total).

3.4 Multi-Cycle and Xenon Transient Strategy

In order to assess the compliance of the existing power plants to the proposed rule, the LOCA accident scenario needs to be initiated from equilibrium cycle conditions. Hence, the reactor evolution needs to be followed for several operational cycles, until reaching the reference equilibrium cycle. Simplistically, from a loading point of view, the equilibrium cycle can be considered as the cycle from which the fuel-reloading pattern is almost constant (i.e. same composition and spatial loading of the fuel batches). The equilibrium cycle might be "reached" after several reloads (~20-30). In this study, we assume that the equilibrium cycle is reached after the 10th reload (the 11th cycle is considered to be equivalent to the equilibrium cycle).

The PHISICS code is currently coupled with the Thermal Hydraulic (TH) code RELAP5-3D. For the first 10 cycles of the operation, the TH model of the reactor has been performed considering the reactor core only (without a primary or a secondary system). This choice has been taken since the first 10 cycles are used to compute the exposure history of the assemblies but are not active part of the LOCA simulation. For this reason, the primary system is modeled only considering the upper and lower plenum of the core. In order to be as accurate as possible for the determination of the initial conditions in the 11th cycle, the first ten cycles are modeled using one core channel per fuel assembly (193 in total). The radial reflector is modeled as a bypass channel (6% of the mass flow). Figure 3-4 shows the RELAP5-3D nodalization for the first 10 cycles.

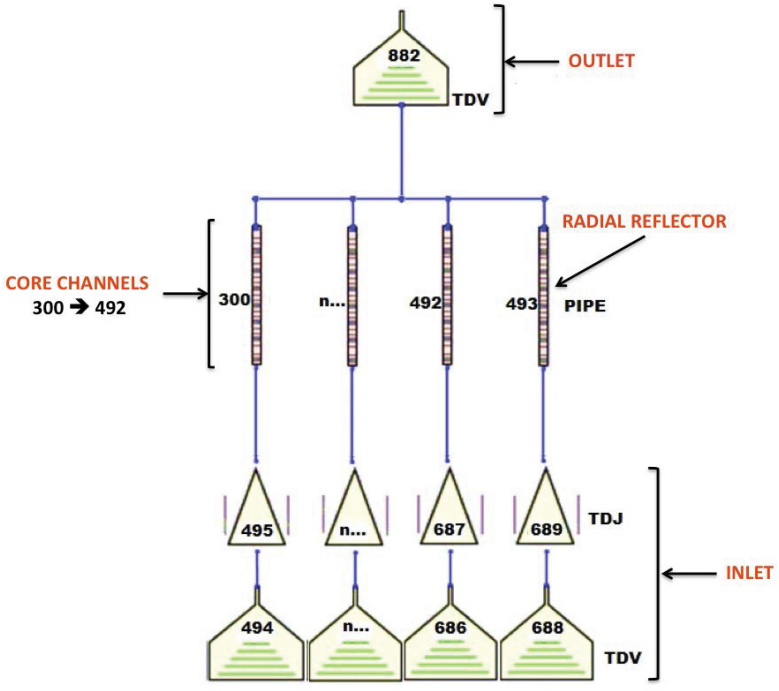

Figure 3-4. RELAP5-3D Nodalization.

The BEAVRS benchmark provides data for the first 2 cycles only (1 reloading pattern); for the sub-sequential 3rd through 11th cycles, new reloading patterns have been constructed. The BEAVRS reloading pattern is a "high-leakage/low-energy" one. For this work, our goal was to perform analysis on a modern reloading pattern; the first developed 5 cycles' patterns represent a gradual migration from the BEAVRS "high-leakage/low-energy" to a desired "low-leakage/high/energy" reloading pattern; with the sub-sequential pattern representing the reference final "low-leakage/high/energy" pattern. The reloading patterns are shown in Figure 3-6, Figure 3-7 and Figure 3-8.

The neutron cross-sections set have been computed considering the reactor layout and configuration reported in the BEAVRS benchmark. For the reference equilibrium core design the same set of cross-sections have been used, even if, a rigorous approach would have led to the re-computation of the cross-section sets for each reload pattern shown in Figures 3-6 through 3-8, being those substantially different with respect to the reference cycle. For the purpose of this early demonstration, the cross-sections have not been re-computed for every cycle as it would have occurred in a more rigorous commercial core design setting, hence accepting a certain level of approximation in the obtained results. For example, this approximation can be noticed in the fresh fuel enrichment for the equilibrium cycle (Figure 3-8), which is ~5.4%, quite higher than what expected for an operational 18-months PWR (~4.8%). For the purposes of an initial early demonstration, this discrepancy can be accepted; however, when performing a commercial-type core reload analysis, these cross-sections must be computed rigorously.

All the batch enrichments have been computed in order to reach, at the equilibrium, a cycle length of 18 months. In addition, in order to maintain the reactor "critical" (keff = 1.0), the boron concentration is automatically adjusted by the PHISICS code; when its value falls below 5 ppm, a new cycle is automatically initiated (automatic multi-cycle capability). Figure 3-5 shows the boron evolution for all the ten cycles. It can be noticed that the end of cycle for all the simulated cycles is ~ 18 months ± 10 days and the peak boron concentration is below 2000 ppm, critical value at which the void reactivity coefficients can become positive. [Bilic, 1998]

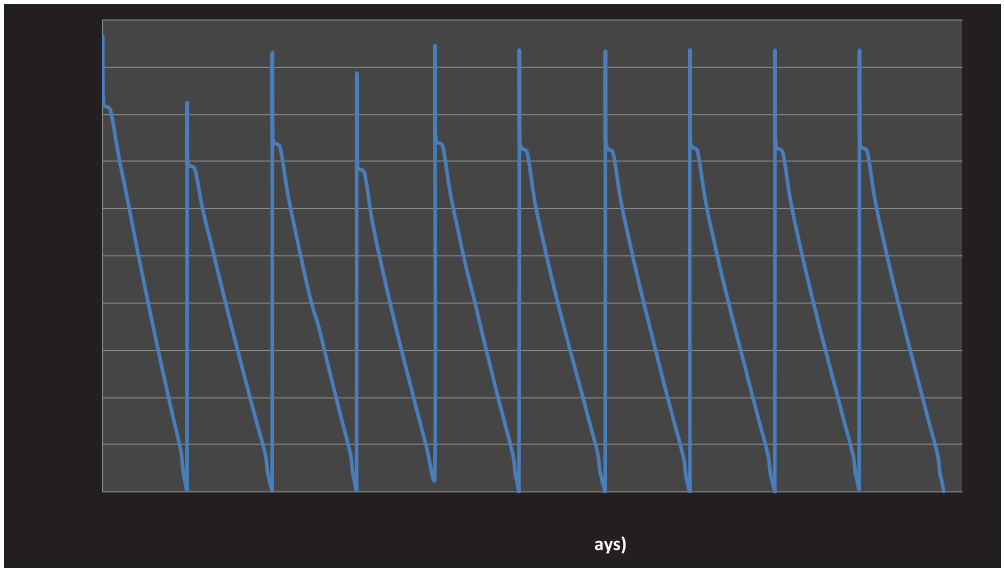

Figure 3-5. Boron Concentration Evolution for 10 Cycles.

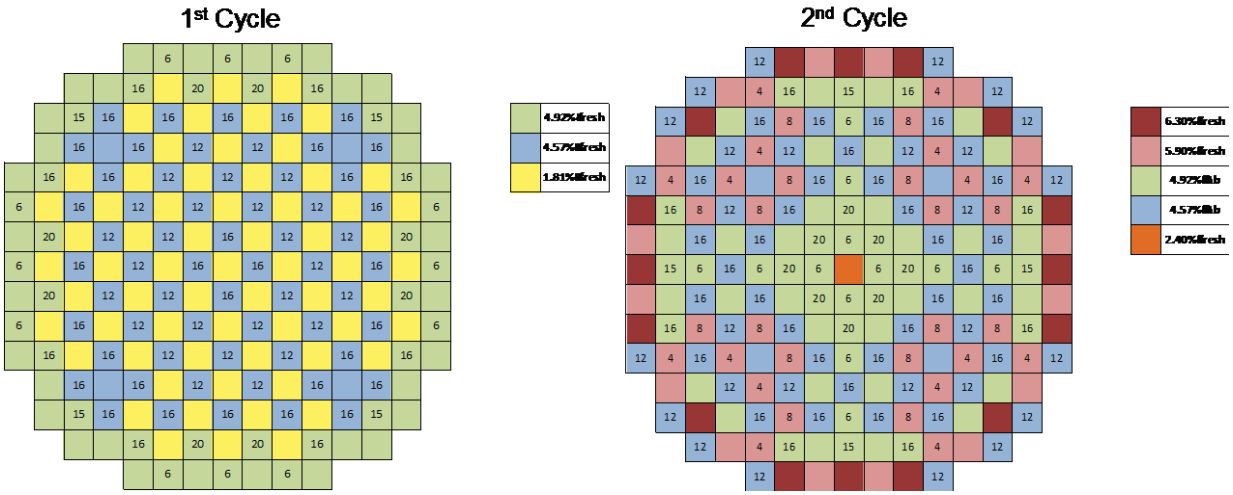

Figure 3-6. 1st Cycle and 2nd Cycle Reloading Patterns.

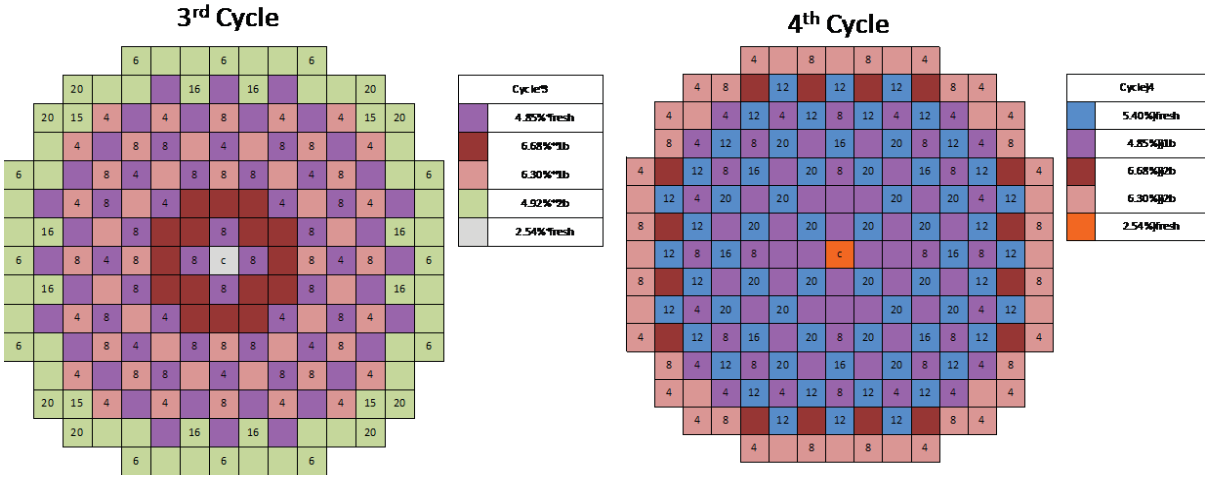

Figure 3-7. 3rd Cycle and 4th Cycle Reloading Patterns.

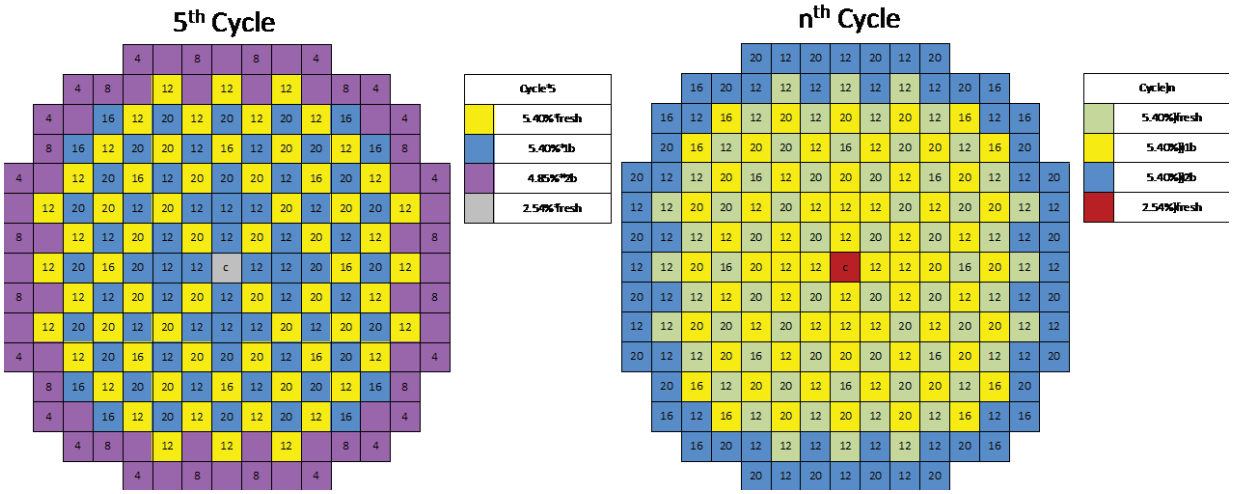

Figure 3-8. 5th Cycle and Equilibrium Cycle Reloading Patterns.

The approach for the analysis of LOCA scenarios determines the need to consider a detailed burn-up calculation, which strongly impacts the cladding oxidation phenomena. As an example, in Figure 3-9, the assembly-wide (radial) integrated power and peaking factors are reported for the Beginning, Middle and End of cycle (10th). In addition, Figure 3-10 shows the detailed fuel exposure (burn-up) for the same points in time. It is worth to mention that, even if the axial peaking factors are not reported here, the total peaking factors (axial times radial) are similar to what is expected from an operational PWR (see Table 3-4).

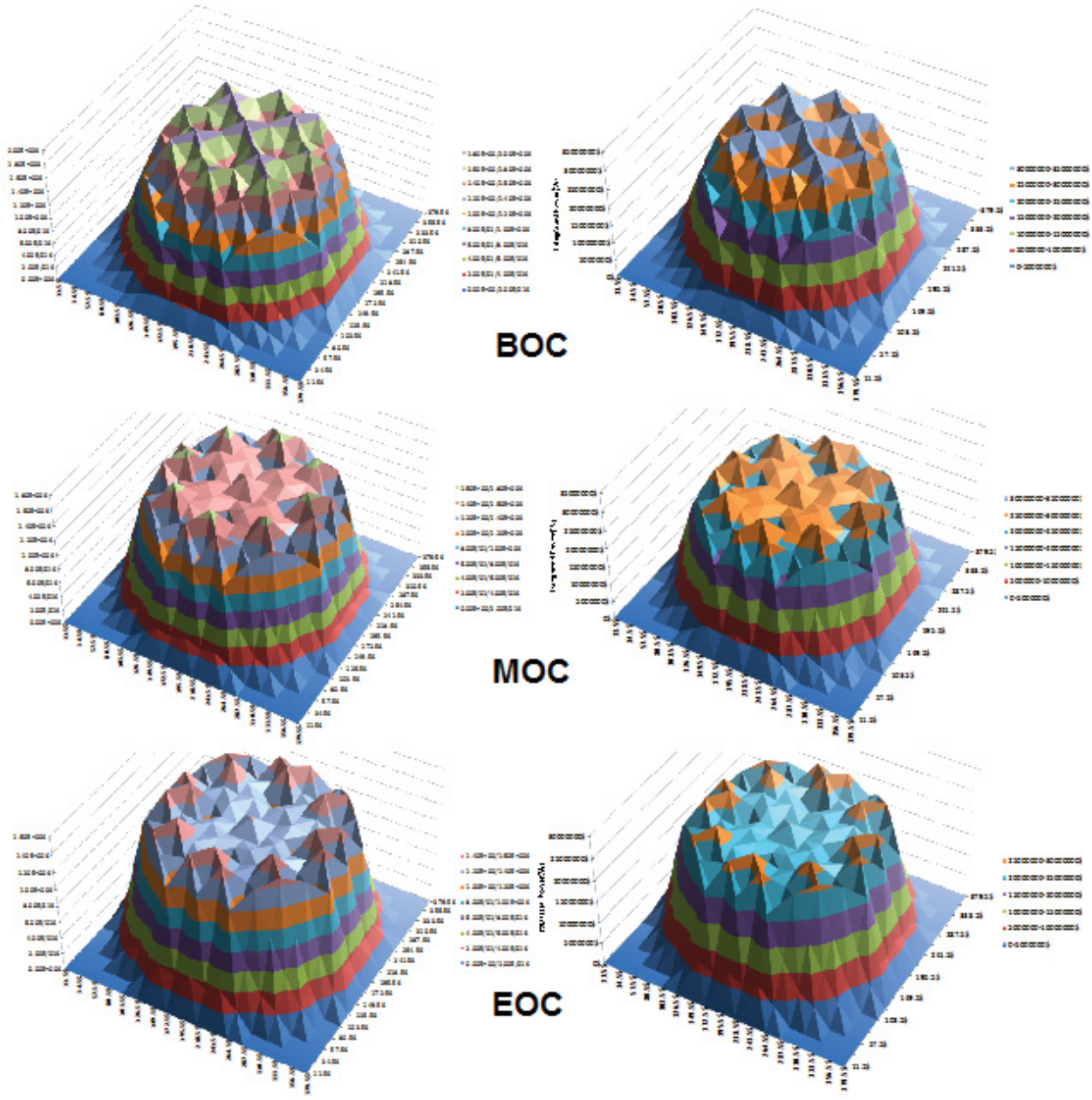

Figure 3-9. Radial Power Peaking Factors and Integrated Power for BOC, MOC and EOC (10th Cycle).

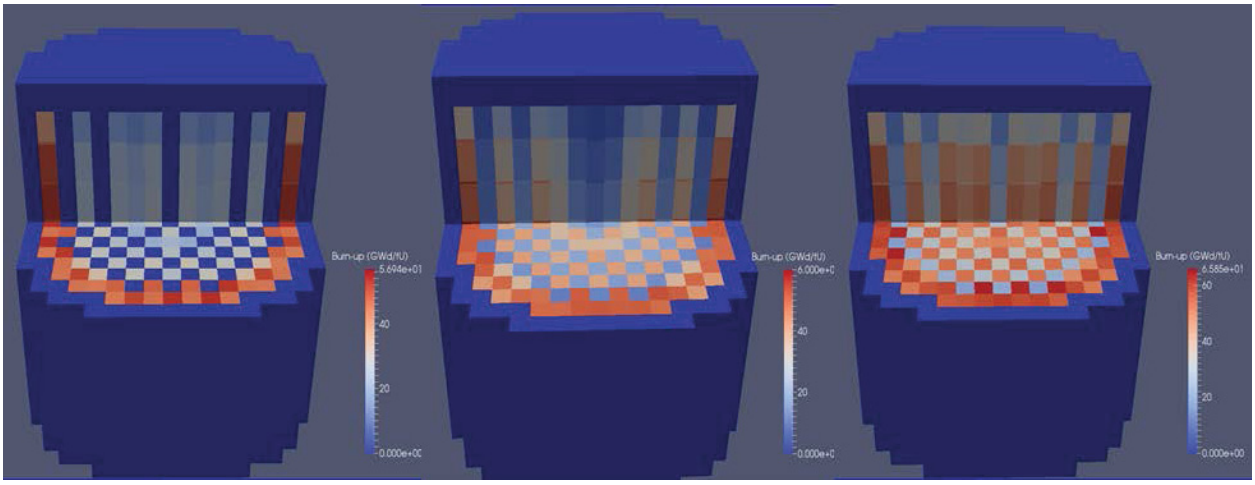

Figure 3-10. BOC, MOC, EOC Burn-Up by Node.

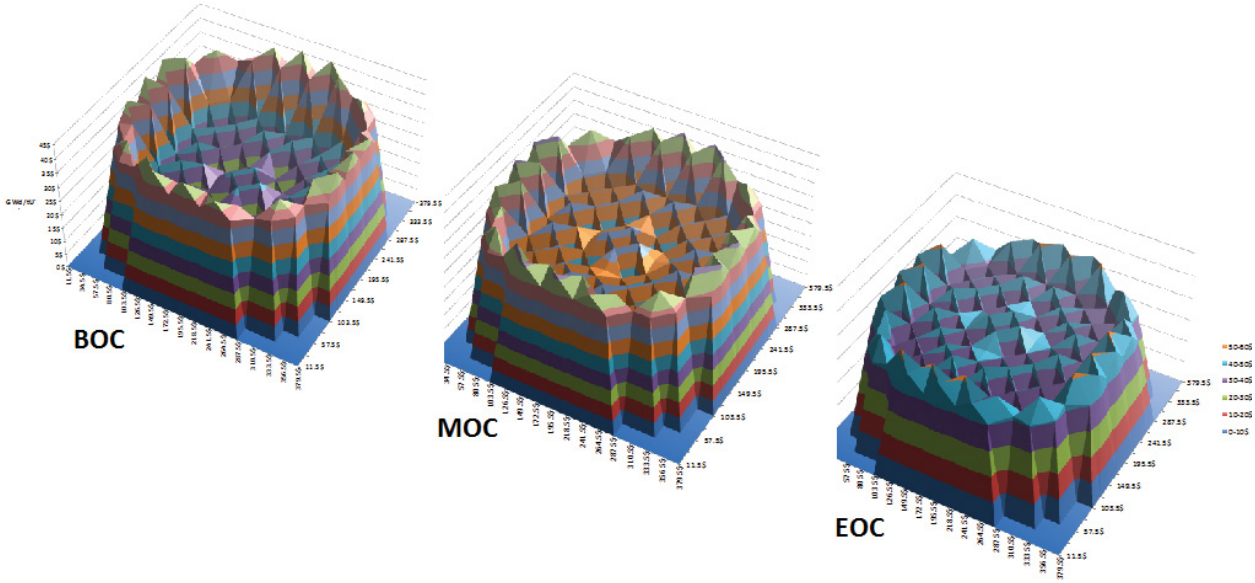

Figure 3-11. Axially Averaged Assembly Burn-Up for BOC, MOC, and EOC.

Exposure (GWd/tU)

Begin of Cycle

44.48$	38.19$	42.32$	37.64$				
0.00$	39.41$	0.00$	39.14$	37.06$	38.09$		
20.50$	0.00$	22.78$	0.00$	25.78$	42.12$	38.02$	
0.00$	23.35$	0.00$	22.00$	0.00$	25.86$	38.33$	
20.53$	0.00$	19.82$	0.00$	22.03$	0.00$	43.80$	37.85$
17.50$	16.01$	0.00$	19.54$	0.00$	23.22$	0.00$	44.43$
21.46$	0.00$	15.71$	0.00$	23.30$	0.00$	38.93$	38.31$
0.00$	21.46$	17.50$	20.53$	0.00$	20.50$	0.00$	44.48$

Middle of Cycle

47.55$	40.83$	45.05$	39.21$				
11.97$	47.13$	10.68$	44.52$	39.75$	39.45$		
33.16$	16.35$	33.74$	13.48$	33.78$	45.81$	39.36$	
18.44$	38.30$	16.18$	34.23$	14.71$	33.77$	40.89$	
34.38$	17.51$	35.95$	18.39$	34.22$	13.29$	48.76$	39.32$
33.38$	32.75$	18.42$	35.73$	16.15$	34.02$	10.47$	47.02$
37.74$	18.25$	32.52$	17.53$	38.25$	16.32$	46.65$	40.92$
18.98$	37.74$	33.38$	34.38$	18.44$	33.16$	11.97$	47.55$

End of Cycle

49.60$	42.60$	47.00$	40.40$				
18.50$	51.60$	16.80$	47.90$	41.60$	40.50$		
39.40$	24.20$	39.40$	20.60$	38.50$	48.40$	40.40$	
26.80$	45.20$	23.50$	40.20$	22.20$	38.50$	42.70$	
40.60$	25.10$	43.20$	26.70$	40.20$	20.30$	51.90$	40.40
40.50$	40.20$	26.30$	43.00$	23.50$	39.60$	16.50$	48.80
44.90$	26.10$	39.90$	25.10$	45.20$	24.20$	51.10$	42.70
27.10$	44.90$	40.50$	40.60$	26.80$	39.40$	18.50$	49.60

Figure 3-12. BOC, MOC and EOC Axially Averaged Assembly Burn-Up Summary ¼-Core Maps.

Figure 3-11 shows the plots of the assembly-average burn-up for the same points in time, which are summarized in Figure 3-12. As it can be seen, the maximum average burn-up is below the general accepted limit of 65 GWd/tU.

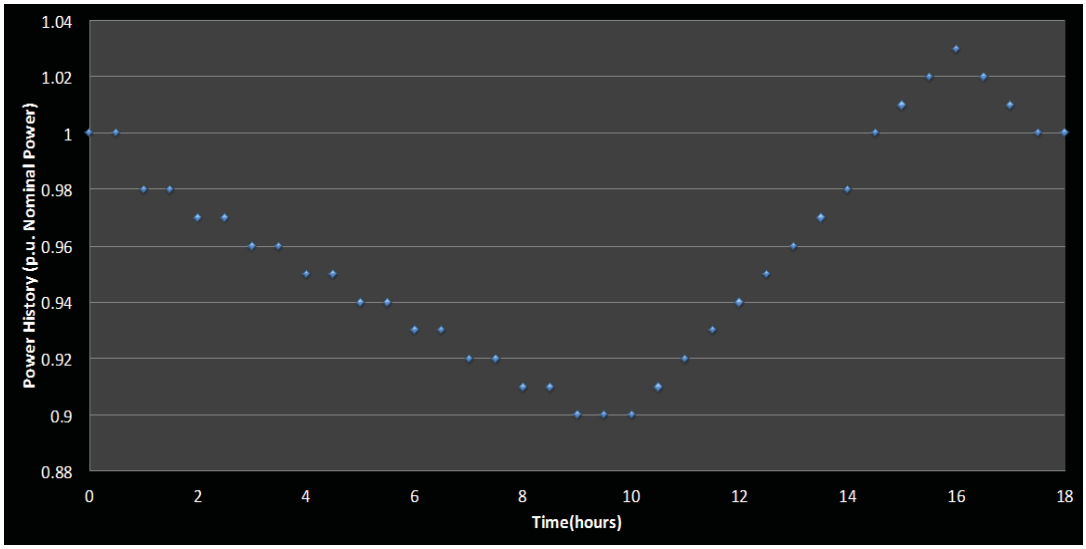

Figure 3-13. Load Following Maneuvers Power Evolution.

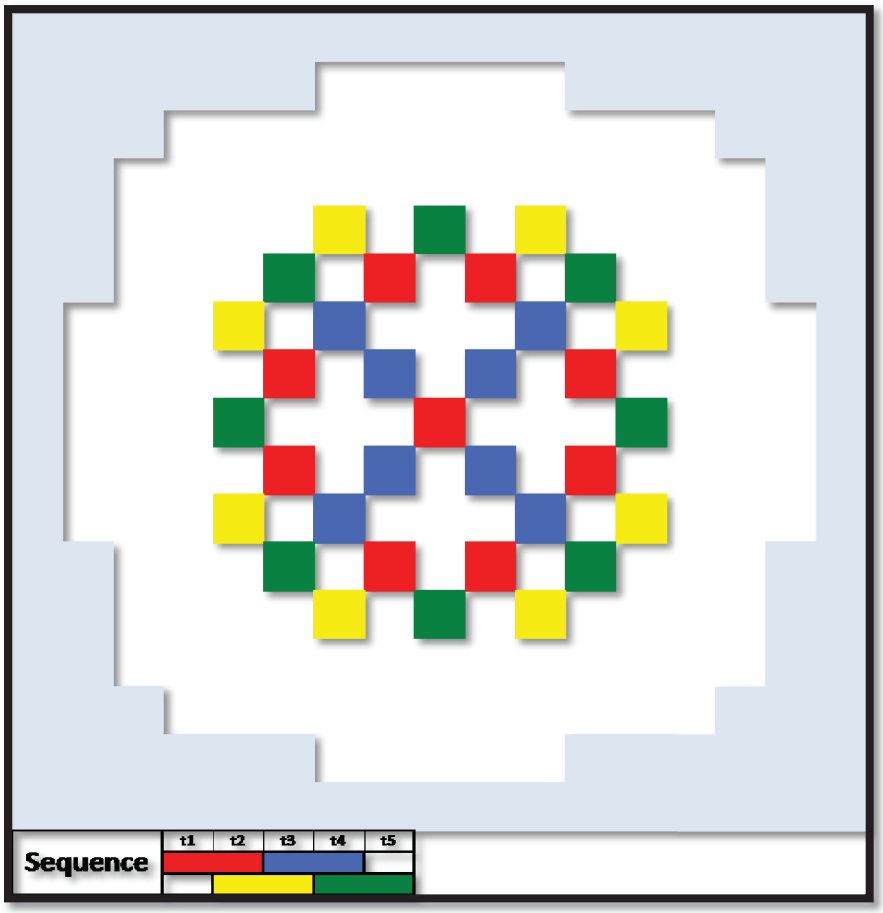

Figure 3-14. Control Rod Positions and Insertion Sequence.

As it is well known, the core status at BOC, MOC and EOC does not determine challenging conditions for the LOCA analysis. This is due to the fact that the LOCA scenarios for the assessment of the safety margins are generally performed considering the reactor right after a maneuver that can initiate, for example, a Xenon transient. For the scope of this work, a load-following maneuver has been considered, as shown in Figure 3-13.

For this type of maneuver the power history is an input of the simulation, hence the reactivity insertion due to the cooling down of the reactor (less power, same mass flow rate, Doppler effect), is automatically compensated by the PHISICS code, determining, through its Criticality Search module, the critical insertion of the Control Rods. In Figure 3-14, the Control Rod Banks are shown, with five banks being considered. The different banks get inserted in the sequence shown in Figure 3-14. For example, the first bank is inserted until half of its length and, when half of it is already inserted, bank two starts getting inserted contemporaneously.

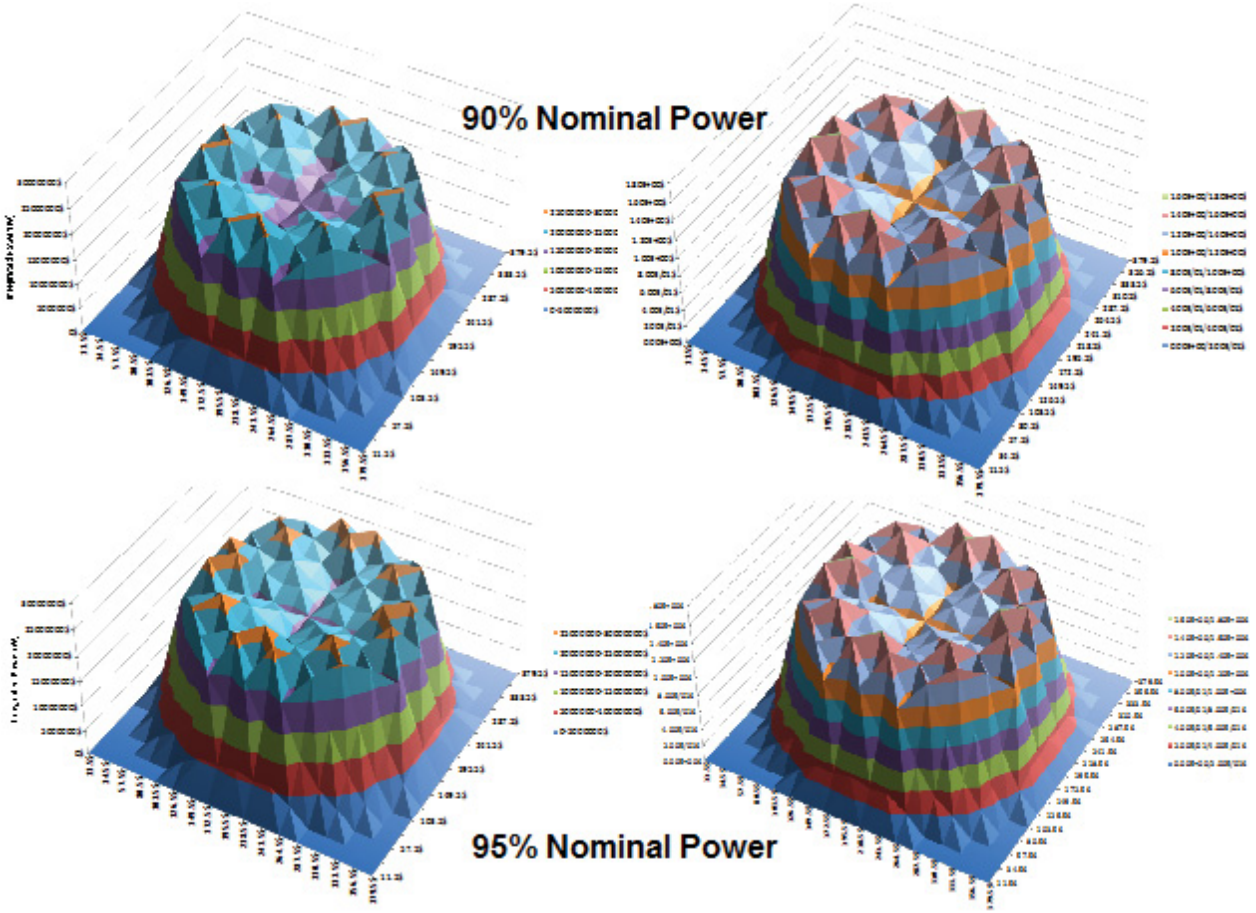

Figure 3-15. Axially Integrated Assembly Power (Left) and Radial Peaking Factors (right) at MOC.

At the end of the maneuver, the LOCA analysis is initiated, having as boundary conditions the current status of the plant (burn-up, power shape, etc.).

As reported in section 4, 8 points in time have been chosen to perform the LOCA analysis (BOC, 50 days, 100 days, 200 days, 300 days, 400 days, 500 days and EOC). The maneuver shown in Figure 3-13 has been performed for all these 8 cycle exposure points chosen for the initiation of the LOCA analysis, each point in time with a maximum skewed power shape. As an example, Figure 3-15 shows the 2D integrated power and relative radial peaking factors for MOC at 90% and 95% of rated power. In addition, Figures 3-16, 3-17 and 3-18 show the radial and axial packing factors at the end of the maneuvers for BOC, MOC (300days) and EOC. As it can be inferred, the power shape changes consistently with the presence of the discontinuities represented by the control rods.

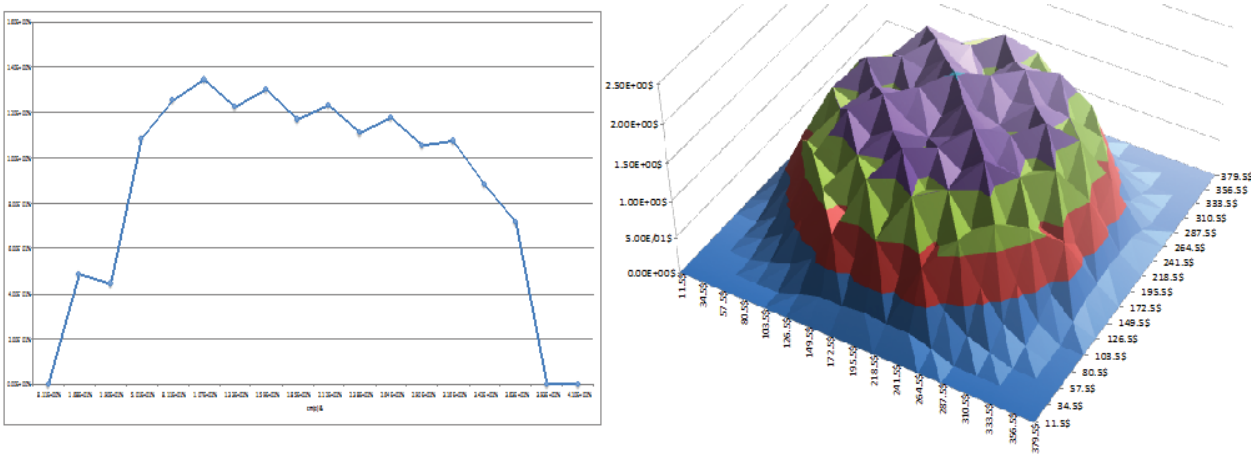

Figure 3-16. Axial (Left) and Radial (Right) Assembly Peaking Factors at the End of the Load-Following Maneuver, Initiated at the Beginning of Cycle.

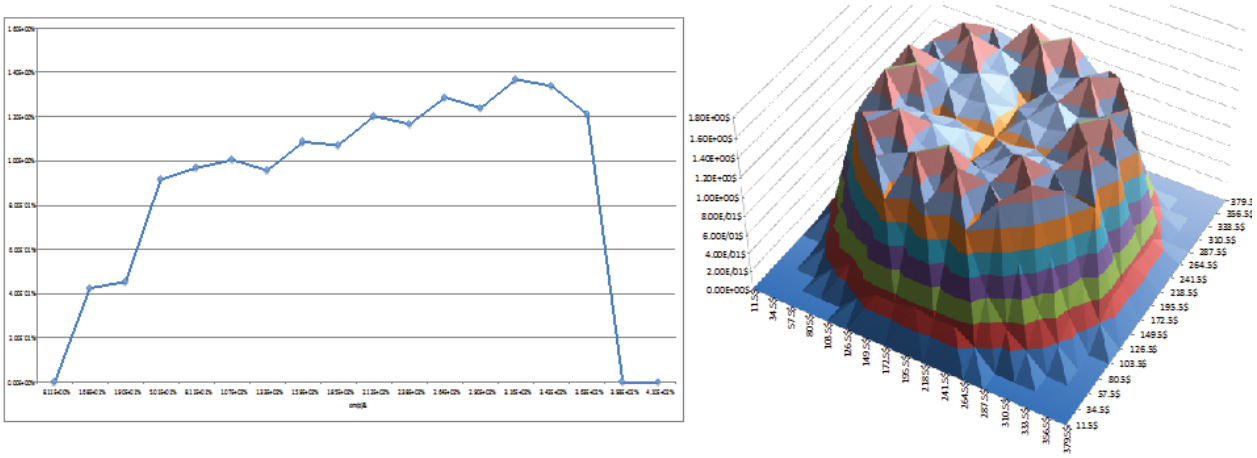

Figure 3-17. Axial (Left) and Radial (Right) Assembly Peaking Factors at the End of the Load-Following Maneuver, Initiated at the Middle of Cycle.

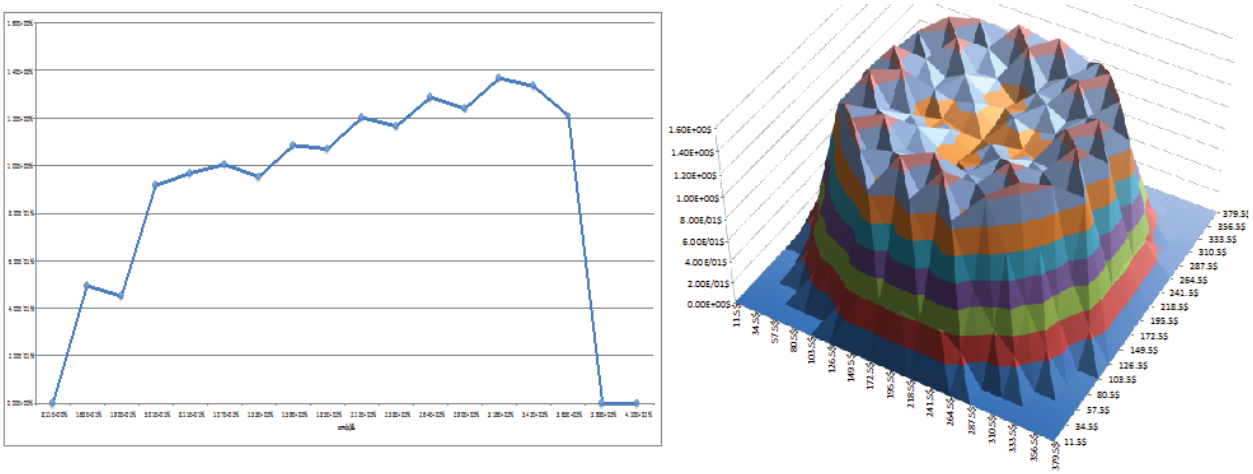

Figure 3-18. Axial (Left) and Radial (Right) Assembly Peaking Factors at the End of the Load-Following Maneuver, Initiated at the End of Cycle.

3.5 Fuel Rod Design and Fuel Performance Model

Fuel rod design data are necessary inputs for core design, system analysis, and fuel performance analysis. Detailed thermo-mechanical fuel rod response models (fuel performance models) are one of key models for any integral LOCA analysis. Fuel performance models are available from dedicated fuel performance codes, such as US NRC steady state fuel performance code FRAPCON [PNNL-19418], US NRC transient fuel performance code FRAPTRAN [NUREG/CR-7023], and advanced fuel performance code BISON [J. D. Hales, 2015] currently being developed at INL. The steady state fuel performance models calculate the temperature, pressure, cladding oxide layer thickness, cladding hydrogen content, and deformation of a fuel rod as functions of time-dependent fuel rod power, initial enrichment and coolant boundary conditions. The cladding hydrogen content for a fuel rod will be used to determine the horizontal location of the ECR results in the new embrittlement oxidation limit diagram. The transient fuel performance models calculate the transient performance of fuel rods including heat conduction, heat transfer from cladding to coolant, elastic-plastic fuel and cladding deformation, cladding oxidation, fission gas release, and fuel rod gas pressure during reactor transients and hypothetical accidents such as loss-of-coolant accidents, anticipated transients without scram, and reactivity-initiated accidents.

As discussed in the problem definition report [INL-EXT-15-35073], we envision four stages of coupling methods between system code and fuel performance code. The first stage for the early demonstration run will use RELAP5-3D's internal fuel performance models for transient simulation with decoupled inputs from separate runs of FRAPCON-3 for steady state input. At this stage, the most important issue is that the stored energy in the fuel pin for the RELAP5 steady state result is equal to the stored energy calculated by the fuel performance code. The stored energy in the fuel rod is calculated by summing the energy of each pellet ring calculated at the ring temperature. The expression for stored energy (J/kg) is

$$E_s = \frac{\sum_{i=1}^{I} m_i \int_{298K}^{T_i} c_p(T)dT}{m}$$

where mi is the mass of ring segment i (kg), Ti is the temperature of ring segment i (K), cp is the specific heat of fuel, m is the total mass of the axial node, and I is the total number of annual rings.

Due to the delay of procuring the FRAPCON-3 software, we are not able to perform the FRAPCON simulations for the early demonstration runs presented in this report. Please see section 5.2 for the discussion on the interface information flow among steady state fuel performance code, system code, and core design package, and best practices on coupling methods to improve the accuracy of the coupled analyses.

3.6 Interface Procedure for LOCA

To manage the data transfer across the various disciplines industry established clear and traceable interface procedure. A memorandum formalizes the basis for the selected core and fuel rod design data that is used to perform a LOCA safety analysis. This procedure is customized to specific processes within the organization which are often proprietary.

The purpose of this Section is to approximate a similar process for the RIMM IEM tool. Such procedure is described in the following Section.

3.6.1 Interface Document Template

Interfaces memos are written to be applicable to all plants that are covered by the methodology. The database tends to be specific to the particular plant application but the basis and rationale behind the generation of such data is applicable to a class of plants, PWR in this case.

A LOCA safety analysis requires the following information which is typically generated within the core engineering disciplines:

1. Fuel assembly type, geometry and hydraulic characteristics
2. Distribution of decay heat and stored energy

3. Rod internal pressure in the hot pin (from fuel rod design)
4. Uncertainty on (1), (2) and (3) and how those are applied

The details of (1) are vendor specifics and detailed not discussed here. The decay heat distribution depends on the power history that precedes the LOCA event for each assembly in the core. LOCA is postulated to occur any time during the cycle. A deterministic (bounding) approach would need to assume the worst time in the cycle. In a best-estimate plus uncertainty analyses the time in cycle is a random variable considered in the uncertainty analysis.

Sections 3.2 and 3.3 of RG 1.157 (Sources of Heat during a Loss-of-Coolant Accident) provide the level of details in characterizing the core that would be needed to perform a Best-Estimate LOCA analysis.

The distribution of decay heat and the distribution of the stored energy in the core is not necessarily the same. The reason is that limiting power distributions cannot persist for a long time period for the decay heat to reach equilibrium. It is often acceptable to neglect this difference and assume decay axial profile and stored energy axial profile be the same.

The fuel rod characteristics are typically provided by the fuel performance code of choice. The modeling of these characteristics is less sophisticated in the LOCA T/H code than in the fuel performance code. Therefore a calibration process between the rod model used in the LOCA simulator and the fuel rod model of the fuel performance code is often necessary to ensure that key parameters such as stored energy and rod internal process match within a prescribed tolerance.

All the key parameters are provided with its uncertainty. These uncertainties are typically proprietary since they are associated with the fuel manufacturing process.

The basis for selecting the various parameters is provided in the next subsections.

3.6.1.1 Loading Pattern

A LOCA analysis requires tracking the performance of the Hot Assembly (HA)1 in the core. Per RG 1.157, the HA needs to be explicitly modeled. The analyst should choose the HA to be bounding. This determination is complex under the proposed rule (10 CFR 50.46c) (more on this in Section 3.4.1.4). The reasons are the tradeoffs between current power and the rod power history (rod burnup). The power history determines the clad hydrogen content and properties of the fuel which vary as the fuel is irradiated.

There are different levels at which the core can be described in a LOCA model. Two options are available to map the core design data to the LOCA model:

- Option 1: Simulate explicitly every assembly in the core (193 channels for a 4-loop PWR)
- Option 2: Divide the core in three regions: a) fresh fuel assemblies; b) second-cycle assemblies and c) their cycle assemblies

It is noted that some assemblies may be discharged at the end of the second cycle rather than 3rd depending on the core management strategy. These are assemblies which would exceed the maximum discharge burnup if kept in the core. However, in general, an assembly will be subject to three cycles of irradiation (18-months cycle).

Option 2 was selected for the RIMM IEM. Figure 3-19 shows the mapping between the core loading patterns to the 6 channels modeled in RELAP. Note that one hot assembly is modeled explicitly in each region.

A hot rod is explicitly modeled with each hot assembly.

[1] "Hot" assembly is here defined as the "Limiting" Assembly under the new rule. In other words the HA is not necessarily the assembly with the maximum power or higher temperature during LOCA but rather the assembly with minimum margin with respect to either PCT or ECR limits. The word "Hot" is retained for consistency with regulatory material.

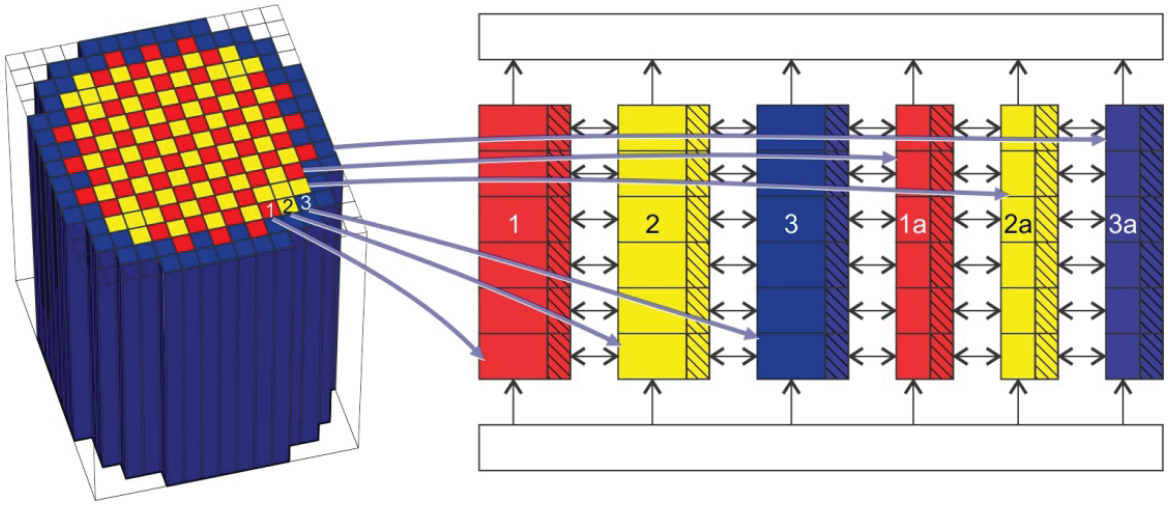

Figure 3-19. Illustration of Assembly Grouping and Homogenization in RELAP-3D Calculations. In this Case We Have Core Regions Mapping to 3 Regions with 3 Hot Assemblies. The Horizontal Arrows Indicate Cross Flow Among All Channels.

3.6.1.2 Radial and Axial Peaking Factors

The radial power distribution is tracked by the "enthalpy rise" peaking factor $F_{\Delta H}$ defined as the ratio of the integral of linear power along the hot rod (rod with the highest power) to the average rod power in the core.

The next power factor is the following (called PBAR): $\overline{P} = \frac{F_{\Delta H}}{\gamma}$, where the factor γ is the ratio between the power of the hot rod in an assembly and the average rod power within that assembly. A value of $\gamma = 1.03$ is assumed here.

The local peaking factor F_Q is defined as the ratio of the maximum local rod linear power density to the average fuel rod linear power density.

The values of $F_{\Delta H}$ and F_Q are monitored by the plant operator during the cycle. The value are tabulated as function of the local burnup when burndown effects are credited. Nominal with and without uncertainties values are presented. For example, Table 3-3 can be found in the LAR material for Turkey Point Units 3 and 4.

Table 3-3. Summary of Peaking Factor Margin and Burndown for Turkey Point Units 3 and 4 for BELOCA Updated Licensing Analyses.

Turkey Point Units 3 and 4
Docket Nos. 50-250 and 50-251

L-2011-561
Attachment 1
Page 35 of 58

Table 5-5
Summary of Peaking Factor Margin and Burndown Supported by PTN BELOCA Updated Analysis

Hot Rod Burnup (GWD/MTU)	FdH (with uncertainties)	FQ Transient (with uncertainties)	FQ Steady-state (without uncertainties)
0	1.6	2.3	1.9
20	1.6	2.3	1.9
30	1.6	2.3	1.9
49	1.33	1.84	1.52
60	1.33	1.84	1.52
65	1.33	1.84	1.52

* The standard BELOCA assumption of [ ]^{a,c}

Or Table 3-4, found in licensing documents for Kewaunee. Figure 3-20 shows the plots with the limit lined together with core design data.

Table 3-4. Peaking Factor Burndown Limits in the Evaluation of TCD, for Kewaunee.

Rod Burnup (MWD/ MTU)	FQ Steady-State	FQ Transient(1)	FΔH (1)(2)
0	2.100	2.500	1.700
30,000	2.000	2.500	1.700
50,000	1.625	2.125	1.406
62,000	1.400	2.125	1.300

(1) Includes uncertainties
(2) Hot assembly average power follows the same burndown, since it is a function of FΔH.

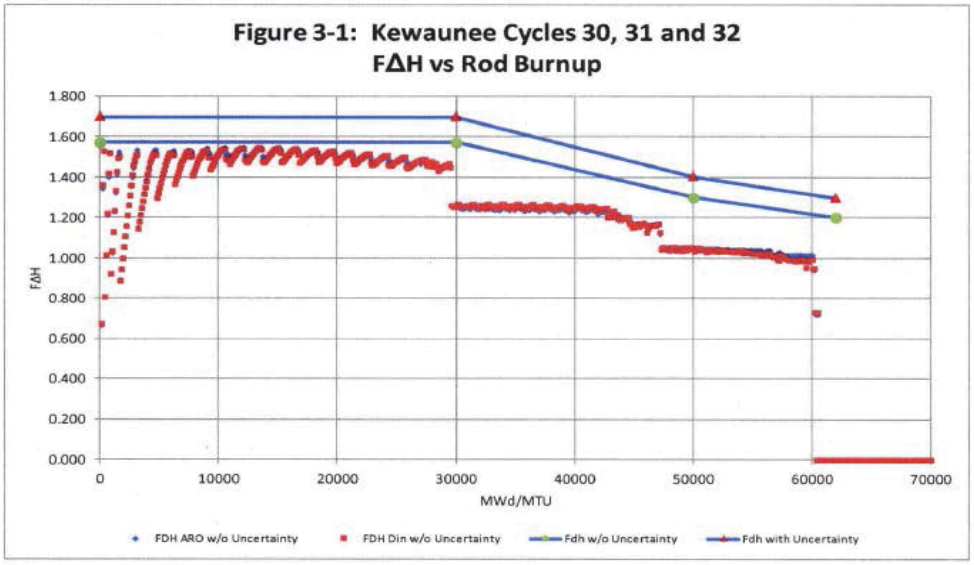

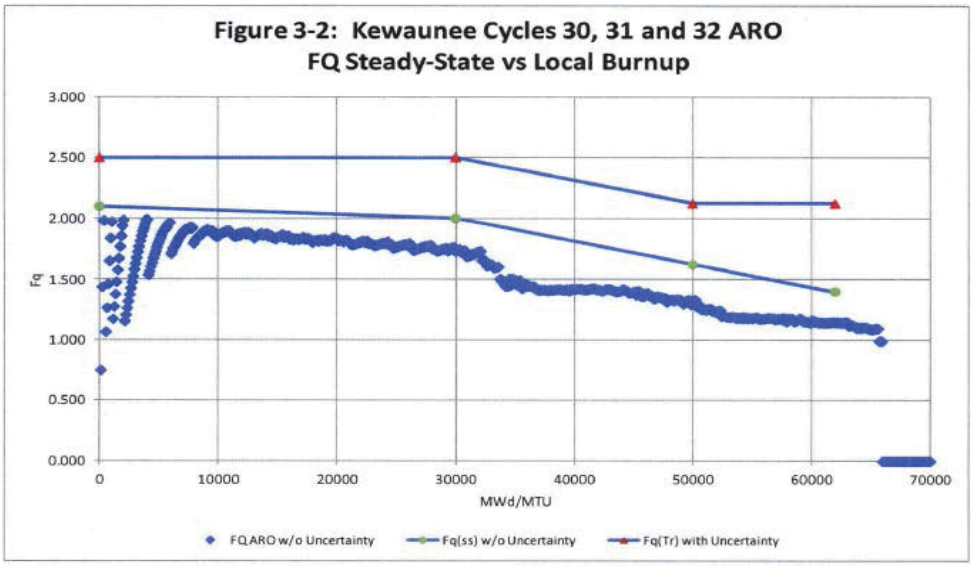

Figure 3-20. Kewaunee Cycles 30, 31 and 32 Burnup Plots.

3.6.1.3 Axial Power Shapes

A power shape methodology is developed to capture all possible axial power shapes that may occurs during power maneuvers (e.g. load follow). The space of possible axial power shapes is generated by the core physics tool by simulating such transients initiated at a given time in the cycle.

A LOCA analysis is performed at it nominal power with its uncertainty (of the order of 2%). Limiting power shape occurs more likely at reduced core power. A realistic analysis would need to consider the relationship between core power and axial power shape space. However for practical reason the following bounding approach is typically adopted:

1. Compute all possible power shapes that may occur when the core power is in the 80-100% range
2. Assume that all powers shape from (1) apply to 100% power level

For the RIMM project the approach is simplified. Only a top skewed power shape is considered and applied with core nominal power.

3.6.1.4 Burnup Methodology

The question to address is "at a given time-in-cycle, what rod produces the highest PCT and what rod produces the minimum ECR margin?" The objective is to find the limiting PCT and ECR among all rods in the core.

The answer to the above question requires the definition of a burnup methodology. The problem is complex under the proposed rule because power of the assembly is not the only limiting factor. The PCT and ECR margin are impacted by power history as well. Moreover phenomena such as rod burst and fuel relocation are strongly affected by the rod internal pressure, which in turn is impacted by the current power and the power history preceding the LOCA event.

The ideal solution to the problem would require modeling all assemblies in the core for any given time in the cycle (Option 1 in Section 3.4.1.1). Instead in the current approximated model only three limiting assemblies are considered, one for each region of the core as discussed in Section 3.4.1.2.

The burnup for the hot assembly in the region is currently selected as the burnup predicted by the core depletion step analysis up that time in cycle. This may yield to non-bounding result because trade-offs between power and power history on PCT and ECR are not fully considered.

Given these limitations the following approach is considered adequate for the eDemo:

1. Select the time in cycle
2. Identify the HA as the assembly with the largest power in the region

The analysis can then be conducted in two modes, depending on the regulatory question to address:

1. Treat time in cycle as a random variable in the uncertainty analysis
2. Bound the time in cycle

Note that, using mode (1), the 95th-quantile with 95% confidence of PCT and ECR is computed to comply with the 10 CFR 50.46c proposed rule.

Mode (2) can be used to identify the limiting time in the cycle. This is beyond simply satisfying the 50.46 rule but useful in design optimization studies.

3.6.1.5 Fuel Rod Characterization

The following two key parameters are computed for each rod modeled in the core:

1. Axial distribution of the pellet average temperature
2. Rod internal pressure or gas moles

Note that (1) depends on the local linear heat rate and burnup while (2) depends on the average rod power and average rod burnup.

3.6.1.6 Summary Table

Table 3-5 summarizes the most important core design parameters used in a LOCA analysis. The list of parameters and their uncertainty is here simplified because a detail description would require knowledge of other design and manufacturing tolerances which are only available to the fuel vendor.

Table 3-5. Core Design Parameters for LOCA Analysis.

Parameter	Range	Distribution
Time in cycle t_{cycle}	0 – 18 months	Uniform
Maximum discharge burnup (GWD/MTU)	62	NA
Nominal Total Peaking Factor $F_Q(t_{cycle})$	Baseload value - Tech Spec Limit	Uniform
Nominal Enthalpy Rise Peaking Factor $F_{\Delta H}(t_{cycle})$	Point Value Tech Spec Limit	Constant
Hot pin to Assembly average LHR (γ)	1.03	Constant
Axial Power Shape	Top Skewed	Bounded
Core Power	98% - 102%	Uniform (Calorimetric Uncertainty)
Decay Heat	Treated with a multiplier to the code predicted nominal decay heat Range: 0.94 – 1.06	Uniform

4. LARGE BREAK LOCA EARLY COMPUTATIONAL RESULTS

4.1 Description of RELAP5-3D Model

For the initial demonstration, a RELAP5-3D plant model is built for a four loop pressurized water reactor designed by Westinghouse. The RELAP5-3D model is a detailed representation of a typical four loop PWR power plant, describing all the major flow paths for both primary and secondary systems, including the main steam and feed systems. Also modeled are primary and secondary power-operated relief valves (PORVs) and safety valves. The emergency core cooling system (ECCS) was included in the modeling of the primary side, and the auxiliary feedwater system was included in the secondary side modeling. A description of the primary and the secondary systems is presented in the following sections.

4.1.1 Reactor Vessel

The reactor vessel model, as shown in Figure 4-1, includes the downcomer, downcomer bypass, lower plenum, core, upper plenum, and upper head. The following leakage paths are represented in the vessel model: downcomer to upper plenum, cold leg inlet annulus to upper plenum, and upper plenum to the upper head by way of the guide tubes. Heat structures represent both external and internal metal mass of the vessel as well as the core rods. Decay heat was assumed to be at the ANS-5.1 standard rate.

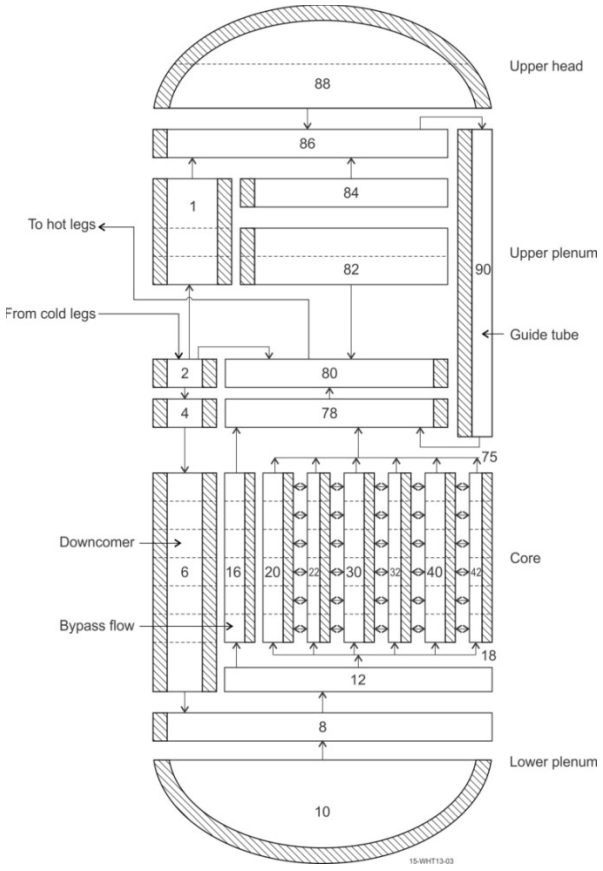

Figure 4-1. RELAP5-3D Nodalization Diagram for the Reactor Vessel.

The reactor core modeling in RELAP5-3D used different homogenization approaches for thermal fluid dynamics calculations from the heat conduction calculations in the fuel rods. For the thermal fluid calculations, a multiple channel approach was used, as illustrated in Figure 3-19 (in Section 3.6). Specifically, the assemblies in the core were grouped together into various regions based on their burnup history. In this work, the assemblies with fresh fuel, once burnt fuel and twice burnt fuel were respectively grouped together. Two flow

channels – one average channel and one hot channel – were built to represent each group of assemblies. Hence there are a total of six flow channels through the fuel assemblies in this study. The channels are connected in the lateral direction to allow cross flows. For the heat conduction calculations in the fuel rods, one heat structure for each fuel assembly was built and connected to the average flow channel such that the clad and fuel temperature for each fuel assembly can be calculated. The highest power assembly in each burnup region was connected to that region's hot channel. Separate heat structures for the hot fuel rod in each of the three highest power assemblies in the three assembly groups were also built and connected to the hot channels. Therefore, there are a total of 196 heat structures in this study (193 assemblies plus 3 hot rods). The combination of multiple flow channels approach with more detailed representation of heat conduction in the fuel rods allows the RELAP5-3D cases to have a reasonable running time to facilitate the large number of runs required by the RISMC methodology, while maintaining appropriate fidelity of the heat conduction calculations needed to support the modeling of each assembly (and hot rods) in the core imposed by the proposed rulemaking.

4.1.2 Reactor Coolant System

Figure 4-2 shows the nodalization diagram of the RELAP5 model of the primary system of the typical four loop PWR. Each of the four primary coolant loops is represented in the RELAP5-3D model. The loops are designated as loop A (upper left), loop B (lower right), loop C (upper right), and loop D (lower left). Each modeled loop contained a hot leg, U-tube steam generator, pump suction leg, pump and cold leg. The pressurizer was attached to the C loop and the pressurizer spray lines were attached to the B and C loop cold leg. Heat structures were added to each volume in the primary loops to represent the metal mass of the piping and steam generator tubes.

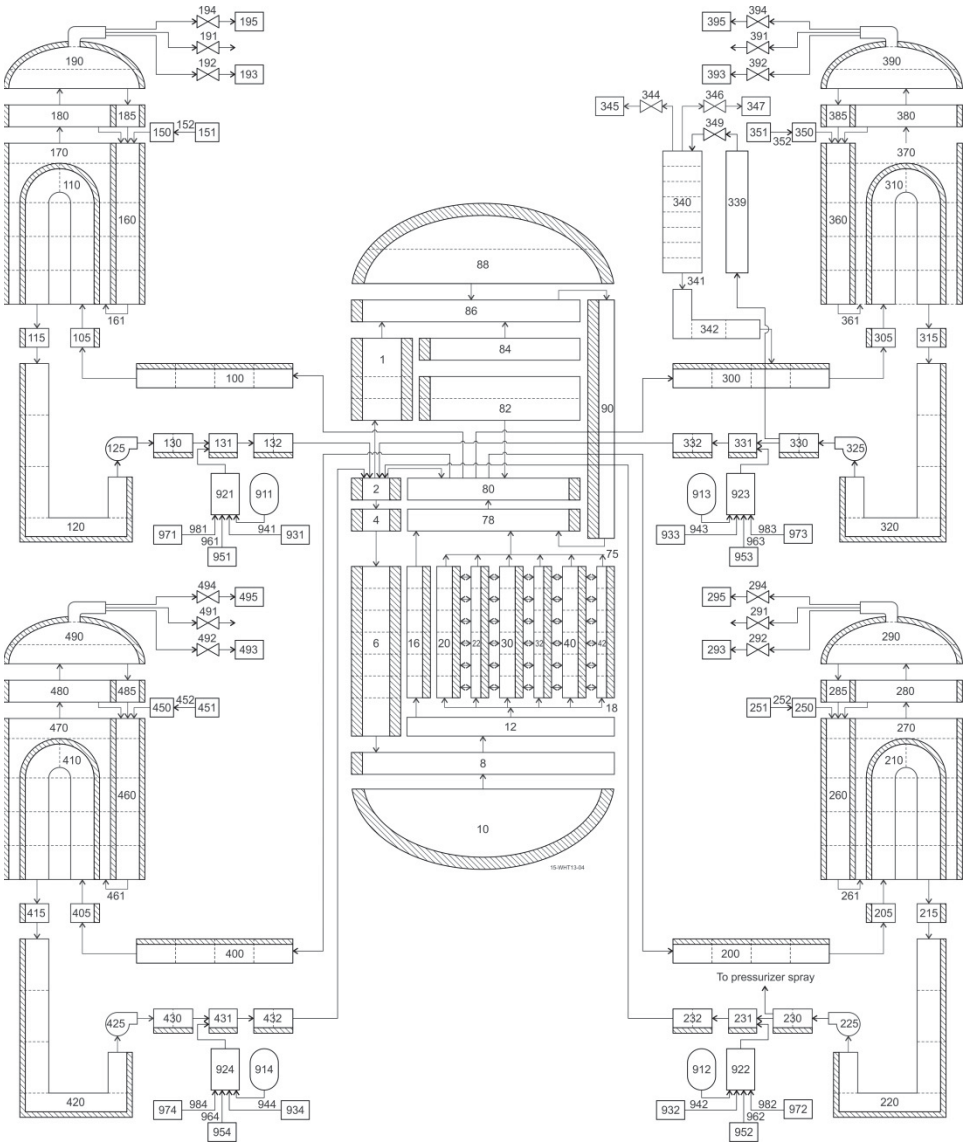

Figure 4-2. RELAP5-3D Model of the Primary System of a Typical Four Loop PWR.

The secondary system of the plant is also modeled. The steam generator secondary side model represents the major flow paths in the secondary and includes the downcomer, boiler region, separator and dryer region, and the steam dome. The major flow paths of the steam line out to the turbine governor valves are modeled. Each line from the steam generator secondary out to the common steam header is modeled individually, and included a main steam line isolation valve (MSIV), a check valve, safety relief valves, and PORVs.

The major flow paths of the feedwater system are modeled. The feedwater system consisted of the main feedwater system and the auxiliary feedwater system. The control system models include a steam dump control system, steam generator level control, pressurizer pressure control system, and pressurizer level control systems, etc.

Heat structures for the secondary system included the internal and external metal mass for each of the steam generators.

4.1.3 ECCS

Attached to each cold leg is a low pressure injection (LPI) connection port and an accumulator with its associated piping. A high pressure injection (HPI) connection is also attached to each cold leg. The LPI and HPI

models were set up to inject one-fourth of the total HPI and LPI flow into each loop. The RELAP5-3D model developed here can be used to perform simulations of various accident scenarios including large break loss-of-coolant accident (LB-LOCA) which is the primary interest of this work. For the LB-LOCA scenario, the break is located at cold leg A of the PWR, as shown in Figure 4-3.

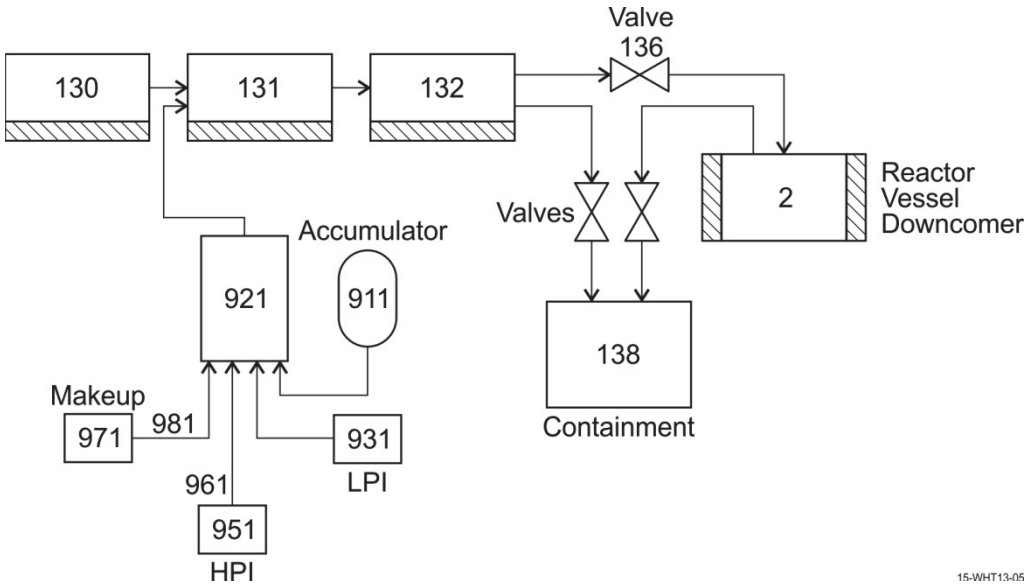

Figure 4-3. Illustration of Simulations of ECCS for LB-LOCA Transients.

4.1.4 Initial and Boundary Conditions, and Steady-State Results

The steady-state initialization calculations were performed first. The initial and boundary conditions and steady-state results for the cycle at 300 days with the nominal input parameters are shown in Tables 4-1 through 4-4.

Table 4-1. Plant Initial and Boundary Conditions.

Plant Initial Operating Conditions	**Unit**	**Calculated or Input Value in RELAP5-3D**
Core Power	MWt	3411
Power Production in Fuel Pellet	%	97.4
Number of Assemblies	[-]	193
Number of rods/assembly	[-]	264
Core Active Length	m	3.65
Average LHR	kW/m	16.99
Maximum LHR	kW/m	36.18
Peaking Factor F_Q	[-]	2.08
Hot Assembly Enthalpy Rise (PBAR)	[-]	1.59
Hot Rod Enthalpy Rise (FdH)	[-]	1.63
Axial power shape	[-]	Top Peaked
Hot Assembly (HA) burnup	GWd/t	13.08
HA type	[-]	Fresh
RCS Fluid conditions		
Total RCS flow (all loops)	kg/s	18935
Total Bypass Ratio	%	4.70
Active Core Flow Rate	kg/s	18046

Bypass Flowrates (details)		
Upper Head Bypass (0.5%)	kg/s	271
Hot leg bypass (1.0%)	kg/s	174
Reflector Bypass (1.5%)	kg/s	444
Control Rods (guide tubes) Bypass (3.0%)	kg/s	Not modeled
Coolant Temperature		
RPV Exit Temperature	°C	325
RPV Inlet Temperature	°C	294
Average Temperature	°C	310
Upper head temperature	°C	292
Pressure and Pressure Drops		
Operating Pressure	MPa	15.51
Core ΔP	MPa	0.20
RPV ΔP	MPa	0.30
Steam Generator ΔP	MPa	0.26
Piping ΔP	MPa	0.12
Total ΔP (Pump Head)	MPa	0.68
Steam Operating Pressure	MPa	6.85
Pressurizer Level	m	9.276
Steam Generator Liquid Mass	kg	196857

Table 4-2. ECCS Parameters.

Accumulator Temperature	°C	37.78
Accumulator Pressure	MPa	4.14
Accumulator + Line Water Volume	m^3	24.81
Accumulator Gas Volume	m^3	14.16
Accumulator Boron Concentration	[-]	0.002
Accumulator Discharge Line Length	m	19.09
Accumulator Discharge Line FA	m^2	0.039
Safety injection temperature	°C	32.2
HPI delay time	sec	50
LPI delay time	sec	50

Table 4-3. Accident Boundary Conditions.

Single failure assumptions	[-]	yes
Offisite power (on or off)	[-]	off
Containment pressure	MPa	0.1
Break type	[-]	Cold leg
Break size	[-]	200%

Table 4-4. Fuel Rod Parameters.

Cladding OD	mm	10.11
Cladding ID	mm	8.3
Pellet outside diameter	mm	8.19
Active fuel length	m	3.6576
Rod Internal Pressure (HR)	MPa	6.9
Rod Internal Pressure (HA)	MPa	6.9
Hot Rod Max Fuel Centerline Temperature	°C	1869

4.1.5 Reference Transient

Following the initiation of a LB-LOCA, a fast depressurization of the primary system ensues. The consequent low pressure would activate the scram signal to shut down the reactor. The water injection from the HPI system, accumulators and later from LPI system are activated to mitigate the core uncovering. The entire process lasts about 10 minutes. To be conservative, in our RELAP5-3D plant model simulation, the shutdown of the reactor following the initiation of LB-LOCA is achieved through the negative reactivity feedback, rather than through the scram of the reactor. Figure 4-4 shows the PCT evolution during one of the LB-LOCA transient cases for the 300 days cycle exposure point. Figure 4-5 shows the ECR evolution during one of the LB-LOCA transient cases for the 300 days cycle exposure point.

It is noted that in our RELAP5-3D models, the cladding deformation model is turned on to account for the double-sided oxidation effect should the cladding rupture. For example, for this particular case, all the fresh fuel rods, the hot rod in the once-burnt fuel region and one assembly in the once-burnt region experienced cladding failure during the LB-LOCA transient.

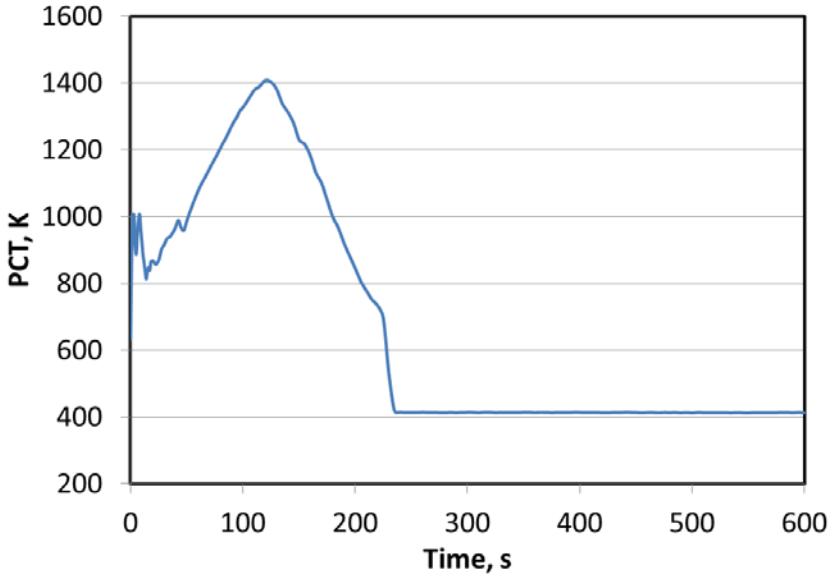

Figure 4-4. Maximum PCT during LB-LOCA Transients for 300 Days Cycle Exposure Point.

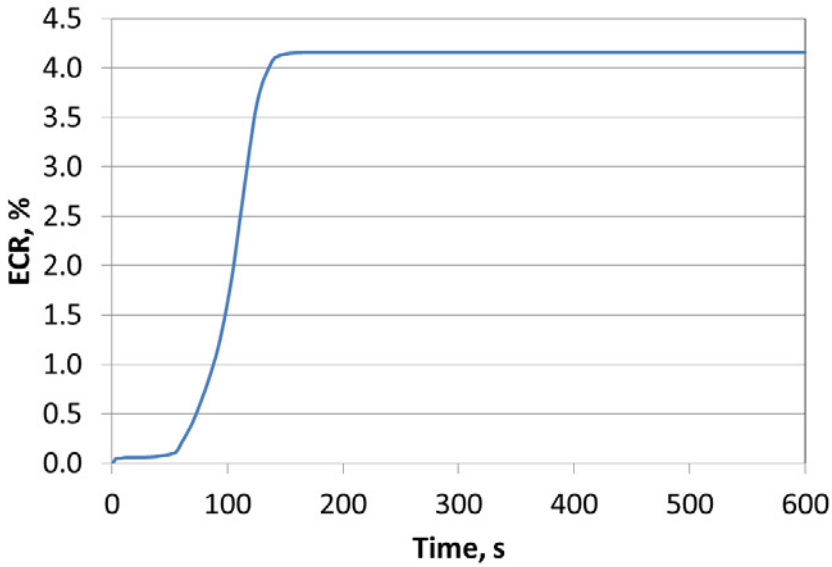

Figure 4-5. Maximum ECR during LB-LOCA Transients for 300 Days Cycle Exposure Point.

4.2 LB-LOCA Runs

In the typical LB-LOCA analysis conducted today (WEC and AREVA) the time in cycle is an additional random variable whose uncertainty is propagated through the analysis. The reason is that a LOCA event is equal-probable in time. The 95/95 probabilistic statement is for the fuel cycle and not for a specific time during the cycle.

This approach is not suitable to core design optimization because it is difficult to determine the worst time during the cycle.

As result for the RIMM the following procedure is considered:

1. Select specific exposure points;
2. For each exposure point propagate all the uncertainties.

4.2.1 Selection of Exposure Points

The exposure points selected for the LB-LOCA calculations would cover the entire range of the cycle length. The selected exposure points are at the beginning of cycle (BOC), 50 days, 100 days, 200 days, 300 days, 400 days, 500 days and end of cycle (EOC). This way, the dynamic response of the plant with regards to LB-LOCA transients would be fully characterized at different core conditions during the entire cycle.

4.2.2 Sampling Strategy

As discussed in Section 2, current practice in the industry is to demonstrate compliance to the rule using Wilks-based estimators and relatively small random sample size of simulations of the event.

The non-parametric statistical sampling technique, originally proposed by Wilks and the Monte Carlo sampling technique are used to determine the upper tolerance limits from unknown distributions by randomly sampling the uncertain input parameters that are important to LB-LOCA transients. Assuming only one outcome (say PCT), using the Wilks formula, the sample size can be determined for a desired population proportion at a given tolerance interval by:

$$\beta = 1 - \gamma^N \tag{1}$$

where β is the confidence level, γ is percentile and N is the number runs required. For instance, if we are interested in determining a 95/95 bounding value of PCT (γ=0.95) with 95% confidence level (β=0.95), N is found to be 59 from Wilks's formula.

The 95/95 bounding value of PCT can be interpreted as providing a coverage of the 95% of the population of calculated PCT values with 95% confidence. In this technique, all the uncertainty parameters are sampled simultaneously in each RELAP5-3D run. The PCT results are then ranked from highest to lowest, with the highest value provides a bounding estimate of the 95/95 PCT.

In additional to PCT, the ECCS/LOCA rule requires a joint-probability statement with other criteria. At a minimum both PCT and ECR limits are considered in the analysis. In the current rule, the PCT has to be less than 2200°F and ECR less than 17%.

Therefore, the outcomes of PCT and ECR all need to be considered to meet the acceptance criteria. According to Frepoli, the sample size needs to be extended beyond the 59 runs which are only sufficient if only one outcome is measured from the sample. If more than one outcome is measured from the sample, the number of runs can be found by solving the following equation for N:

$$\beta = \sum_{j=0}^{N-p} \frac{N!}{(N-j)!j!} \gamma^j (1-\gamma)^{N-j} \tag{2}$$

where p is the number of outcome considered. For our analysis, the figure of merits (FOMs) are the maximum PCT and ECR. According to [Frepoli and Iyengar], by substituting γ=0.95, β=0.95 and p=2 into the above equation, N is found equal to 93.

The issue associated with the variability of the Wilks estimators is extensively discussed in Section 2.2.4.

The proposed 10 CFR 50.46c ruling adds another layer of complication since PCT and ECR are function of the cladding hydrogen pickup ratio before the accident which in turn depends of the local burnup and cladding material (see Section 2). This makes the use of small samples with Wilks impractical even if the analyst is only interested in demonstrating compliance with the rule.

Moreover one of the objectives of the RIMM Industry Applications is to provide tools that can also support design decision (Margin Management). There is not sufficient information in traditional small samples (of the order of 100) size to support such decisions.

The RIMM analytical framework is moving toward the direction of performing full Monte Carlo simulations with simulation sample sizes of the order of ~1000s.

The final objective is an integrated analysis which is based on more than 1000 simulations per exposure point. For the purpose of the eDemo only 3 exposure points considered a large sample. More specifically 1240 RELAP5-3D cases were completed for respectively BOC, 300 days and 500 days exposure point. For all other exposure points the simulation was limited to 124 cases for a total of (3x1240+5x124 = 4340 cases). The choice of 1240 cases in the selected exposure points will become clear later.

Therefore a total of 3720 RELAP5-3D cases have been run at these three exposure points.

4.2.3 RELAP5-3D Model Pedigree and List of Uncertainties

The important phenomena affecting the progression of the LB-LOCA accident are normally determined by the phenomena identification and ranking table (PIRT) process. A large number of studies have been done previously that identified the important phenomena.

The current RELAP5-3D model is representative of a typical 4-loop PWR. For demonstration purposes, with input from FPoliSolutions LLC, a reduced set of parameters with high importance to LB-LOCA has been selected and shown in Table 4-5. The probability distribution functions (PDFs) and their associated minimum and maximum values of some parameters (e.g., fuel-clad gap width, fuel thermal conductivity, clad to coolant heat transfer, critical flow coefficient multiplier at break discharge, and pump degradation) listed in Table 4-5 are determined according to [Wilson and Davis].

Table 4-5. List of Uncertain Parameters.

Parameter	PDF type	Min	Max	Comments
Reactor thermal power	Normal	0.98	1.02	Multiplier
Reactor decay heat power multiplier	Normal	0.94	1.06	Multiplier
Accumulator pressure	Normal	-0.9	1.1	Multiplier
Accumulator liquid volume (ft^3)	Uniform	-8.0	8.0	Additive
Accumulator temperature (^oF)	Uniform	-20	30	Additive
Subcooled multiplier for critical flow	Uniform	0.8	1.2	Multiplier
Two-phase multiplier for critical flow	Uniform	0.8	1.2	Multiplier
Superheated vapor multiplier for critical flow	Uniform	0.8	1.2	Multiplier
Fuel thermal conductivity	Normal	0.90	1.10	Multiplier
T_{avg} (^oF)	Normal	-6	6	Additive
Clad to coolant heat transfer (including film boiling heat transfer coefficient)	Uniform	0.7	1.3	Multiplier
Fuel-clad gap width	Uniform	0.2	1.80	Multiplier
Pump degradation	Uniform	0.5	1.5	Multiplier

4.2.4 Integrated Evaluation Model (IEM) Data Stream

Ultimately the RIMM IEM will include all the physical disciplines involved in a LOCA analysis as illustrated in Figure 1-4 in Section 1.3. Each of the physics domains in the IEM is traditionally analyzed separately in each functional group of the organization involved in the analysis. Data is passed from one functional group to another via formalized interface procedures. The RIMM IEM methodology attempts to remove those interfaces, allowing the information to pass seamlessly between the various disciplines. This allows a more rigorous management of the uncertainties but will require the development of the automation toolkit that enables the data stream required. RAVEN is the chosen tool in this project to perform such automation.

For the purpose of the eDemo the multi-physics aspect was greatly simplified. The core design element is discussed in Sections 3.2 and 3.3 and the fuel performance input was captured in Section 3.5.

4.3 Analysis of Results

The highlights from the analysis of the results are provided in this Section. For more details and insights the reader should refer to Appendix A-3.

First, it has to be recognized that the RIMM IEM was designed to generate large samples of simulations which is a necessary step to achieve the goal of margin characterization.

For the eDemo a large sample was generated at three specific time in cycle: at BOC, at 300 days and 500 days. However to illustrate the process, smaller samples were also drawn at other exposure points for a total of eight exposure points. Results are shown first in Section 4.3.1 using the small sample size and then for the large sample size at the chosen exposure points in Section 4.3.2. The benefit of using MC estimates with large sample are briefly illustrated and more justification can be found in Appendix A-3. Finally Section 4.3.3 discuss the issue of compliance with the proposed rule and how it is characterized in the RIMM IEM methodology.

4.3.1 Non-parametric Statistical Analysis Results (Small Sample Size Results)

A sample of 124 RELAP5-3D cases have been run at each of the eight selected cycle exposure points for LB-LOCA analysis, which resulted a total of 992 RELAP5-3D cases. At each selected cycle exposure point, Wilks estimate of the PCT and ECR are found among the 124 RELAP5-3D runs as the 95/95 upper tolerance limits. Therefore a total of 3 PCT values and 3 ECR values are obtained for each selected cycle exposure point. The location of the limiting assembly in each group of assemblies and its associated burnup are also found.

To demonstrate compliance with the proposed rulemaking for ECCS/LOCA, PCT and ECR are plotted as a function of the pre-transient hydrogen content. Since the detailed fuel performance calculations have not been done yet in this work, the pre-transient hydrogen content is not readily available. Instead, [OG-11-143 PWROG 50.46(b)] was used to correlate the hydrogen content with the fuel rod average burnup for Zircaloy-4 cladding as discussed in Appendix A-3.

For the selected eight exposure points in the cycle, a total of 24 PCT values and 24 ECR values and their corresponding assembly burnup are obtained. Figure 4-6 shows the Wilks 124-sample based 95/95 (rank k=3) PCT and ECR estimators. As discussed in Appendix A-3, the use of rank k=3 of 124 run-set samples mitigate some of the issues associated with the crude estimate that can be obtained from the extreme case of a 59 cases sample.

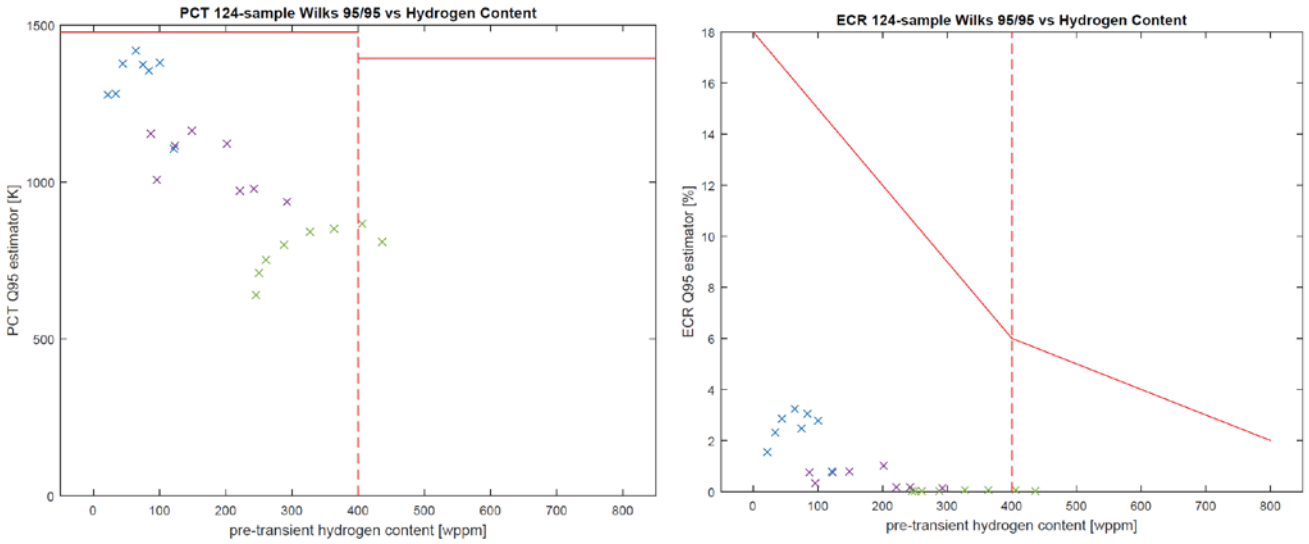

Figure 4-6. Wilks 124-Sample Based 95/95 PCT and ECR Estimators during LB-LOCA Transients (Blue=Fresh fuel, Purple=Once-Burnt, Green=Twice-Burnt).

The entire dataset (all samples within each region of the core) is shown in the left plot in Figure 4-7. The right hand side plot in Figure 4-7 shows the Monte Carlo 95th quantile estimator with corresponding 95th confidence interval represented by the error bar at each exposure point. The approximate 95% confidence interval for the 95th quantile estimator is defined in Appendix A-2. With such a small sample size (124 random samples) the 95th quantile estimators are rather uncertain. The 95% confidence interval around each estimator in the fresh fuel region of the core spans roughly 100 degrees Kelvin. The reason why the other two regions are estimated with more precision is easy to see by inspecting the left hand side plot in Figure 4-7. The once-burnt and twice-burnt regions PCT samples span smaller ranges compared to the fresh-fuel PCT samples, and thus the once and twice burnt region PCTs have smaller sample standard deviation. As described in Appendix A-2, a small sample standard deviation leads to a smaller standard error on the Monte Carlo estimators. The analogous figures for all ECR samples and the Monte Carlo 95th quantile estimators within each region at all of the exposure points are shown in Figure 4-8.

As a reminder, when examining Figure 4-6 through Figure 4-8, the core is characterized by a triplet of PCT and ECR values at any given time in cycle (exposure point). The "triplet state" corresponds to the PCT and ECR values for the hot rods in each of the regions: fresh-fuel (1st cycle), once-burnt (2nd cycle), and twice-burnt (3rd cycle). The triplet is highlighted by the 'ellipse' in Figure 4-7. As time in cycle increases, the "triplet state" moves to the right. For the specific core design considered in this study, the 95th quantile PCT estimator closest to the limit occurs for the hot rod during its first cycle of irradiation. The most limiting ECR condition is a little more difficult to define because the NRC limit decreases with time in cycle, but the highest 95th quantile ECR estimator also occurs in the first cycle of irradiation. Since the first cycle predictions have higher uncertainty throughout the cycle length than the other two regions of the core, it seems that for specific core design considered in this study, the limiting conditions on both PCT and ECR occur in the fresh-fuel region of the core.

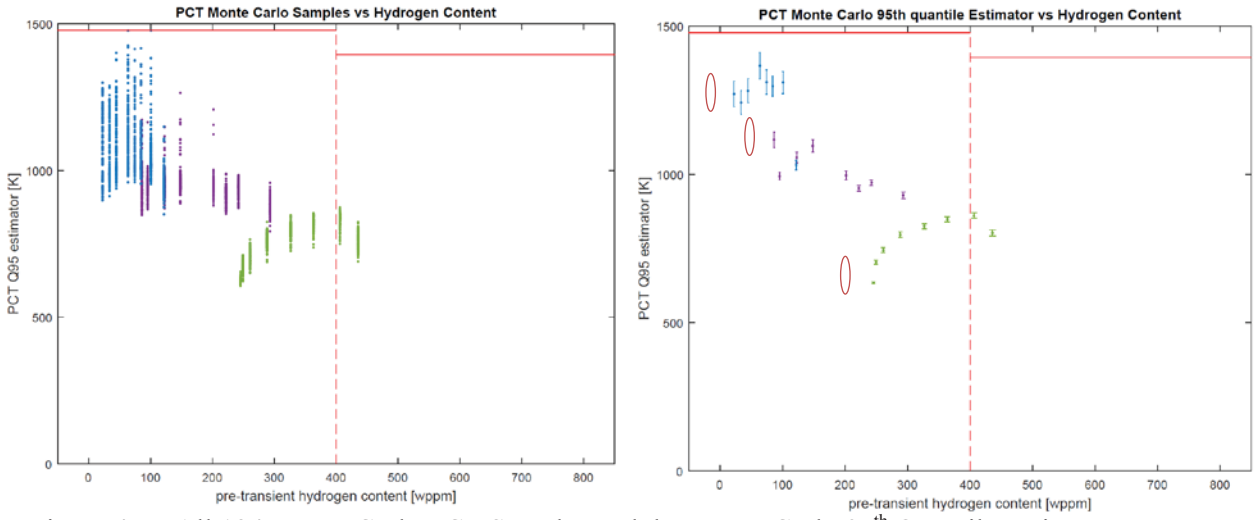

Figure 4-7. All 124 Monte Carlo PCT Samples and the Monte Carlo 95th Quantile Estimators per Exposure Point (Blue=Fresh Fuel, Purple=Once-Burnt, Green=Twice-Burnt), the "Triplet State" at the BOC is Marked by Ellipses.

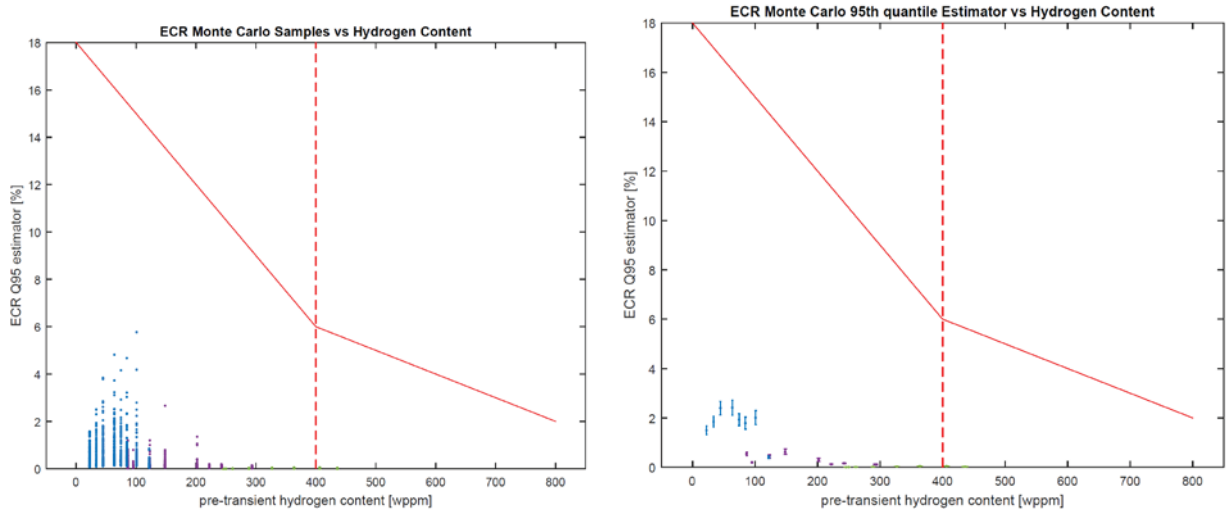

Figure 4-8. All 124 Monte Carlo ECR Samples and the Monte Carlo 95th Quantile Estimators per Exposure Point (Blue=Fresh Fuel, Purple=Once-Burnt, Green=Twice-Burnt).

4.3.2 Monte Carlo Analysis Results (Large Sample Size Results)

With more samples, the benefit of "full" MC analysis over Wilks becomes more apparent. This section used 1240 random samples at three times in cycle, namely the BOC, 300 days and 500 days. Typically, the exact number of Monte Carlo samples is chosen to achieve a desired standard error value. However in this work, 1240 samples were chosen because that gives 10 consecutive sequences of 124 random samples. Ten consecutive 124-sample Wilks based estimators can therefore be evaluated. These 10 samples will be used to represent the possible variability in the 124-sample Wilks based estimator.

Figure 4-9 shows the PCT and ECR results for the three 1240 run-sets performed at BOC, 300 and 500 days, as a function of the pre-transient hydrogen content. Figure 4-7 showed all of the 124 random samples at each of the 8 exposure points considered in the small sample analysis. That figure did not show any samples considerably above the NRC limit. However, with ten times the number of samples several random cases do in fact exceed the Regulatory limit on PCT. This does not mean the design is out of compliance since those cases are associated to a very low probability. Remember that the 50.46 rule simply states "[…] *uncertainty must be*

accounted for, so that, when the calculated ECCS cooling performance is compared to the criteria […], there is a high level of probability that the criteria would not be exceeded". General practice is to estimate the 95th quantile of the possible outcome and ensure that value is below the regulatory limit. More on the interpretation of the rule is given in Section 4.3.3.

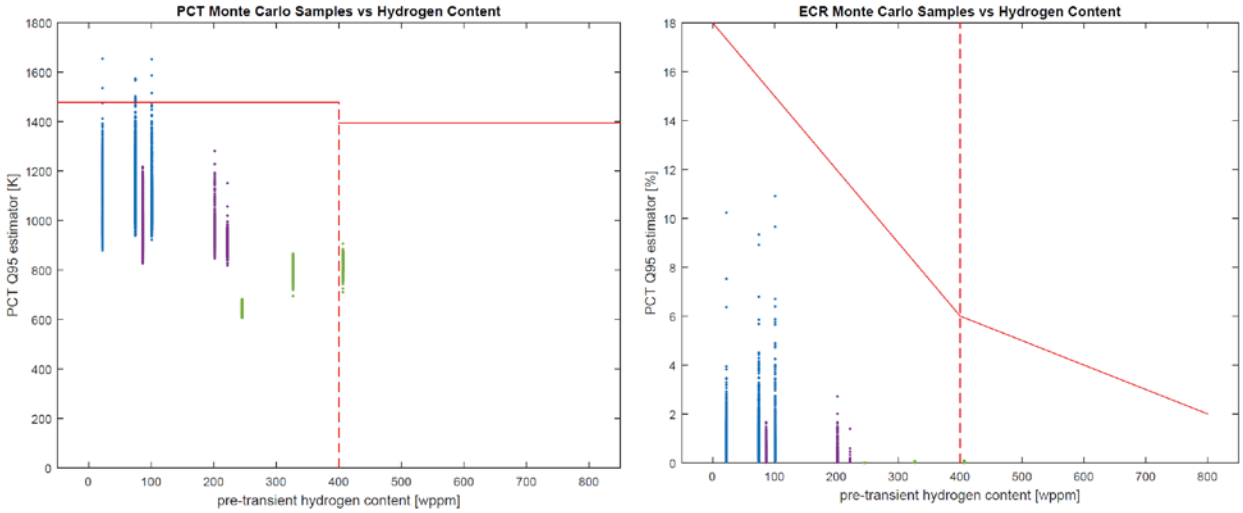

Figure 4-9. All 124 Monte Carlo PCT (Left) and ECR (Right) Samples at the BOC, 300 Days and 500 Days (Blue=Fresh Fuel, Purple=Once-Burnt, Green=Twice-Burnt).

Just as in the previous section, various 95th quantile estimators will be compared to the NRC limits on both PCT and ECR. However with 1240 samples compared to 124 samples, the "full" Monte Carlo estimator will be evaluated with higher precision. As already mentioned there are 10 consecutive samples of the 124-sample Wilks estimator, as well as 21 consecutive samples of the 59-sample Wilks estimators. These samples are used to estimate the mean Wilks based estimator, along with its associated standard error. To illustrate the variability on the Wilks based estimators, a vertical line is included between the minimum and maximum Wilks based estimator sample values. A particular random realization of the Wilks based estimator can occur anywhere along that vertical line, though the most likely value is near the mean Wilks based estimator value.

Figure 4-10 and Figure 4-11 provide the Wilks based estimators on the PCT and ECR, respectively. In each figure, the left hand side plot shows the 59-sample Wilks based estimator and the right hand side plot shows the 124-sample Wilks based estimator. The mean Wilks based estimators are shown as error bars with their colors indicating the core region, just as in the previous figures. The vertical lines which span the range of the Wilks based estimator samples are shown behind their corresponding mean Wilks based estimator. The most important observation to take away from Figure 19 and Figure 20 is that the 124-sample Wilks based estimator clearly has less variability than the 59-sample Wilks based estimator. For example, at the BOC the 59-sample Wilks based estimator in cycle 1 spans a range of nearly 400 K. The upper portion of that range is clearly out of compliance. The 124-sample Wilks based estimator, however, spans a range of only roughly 100 K. This concept is even more pronounced on the ECR, since as shown in Figure 4-9 the cycle 1 ECR samples have very long tails.

With Monte Carlo estimators, the number of outputs that must be tracked does not impact the required number of samples. The PCT and ECR "full" Monte Carlo 95th quantile estimators with their associated confidence intervals as the three exposure points considered in the 1240 sample size data set are shown in Figure 4-12.

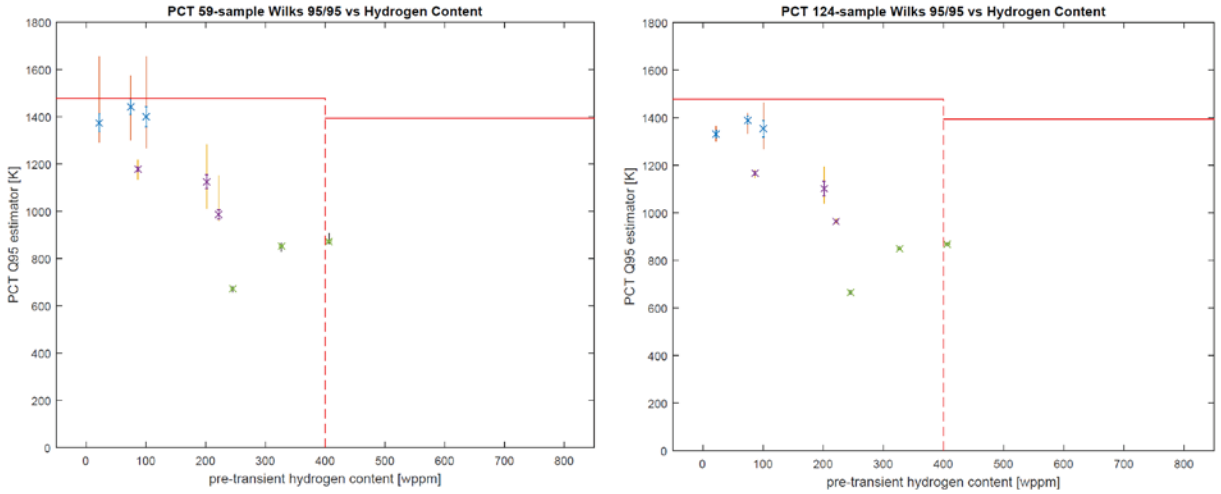

Figure 4-10. Wilks 59-Sample Based 95/95 PCT Estimators During LB-LOCA Transients (Blue=Fresh Fuel, Purple=Once-Burnt, Green=Twice-Burnt).

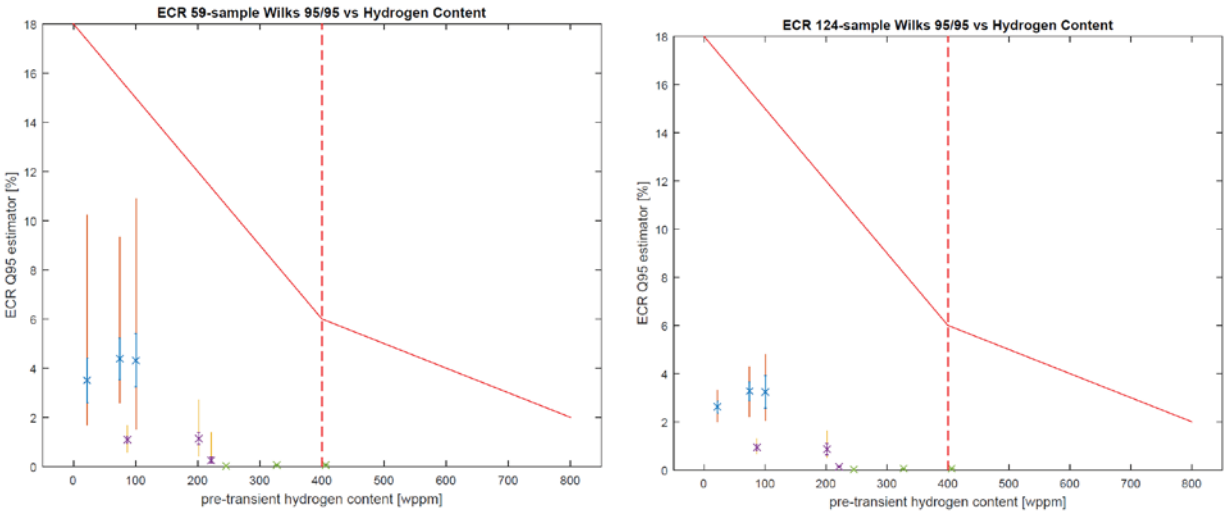

Figure 4-11. Wilks 124-Sample Based 95/95 ECR Estimators During LB-LOCA Transients (Blue=Fresh Fuel, Purple=Once-Burnt, Green=Twice-Burnt).

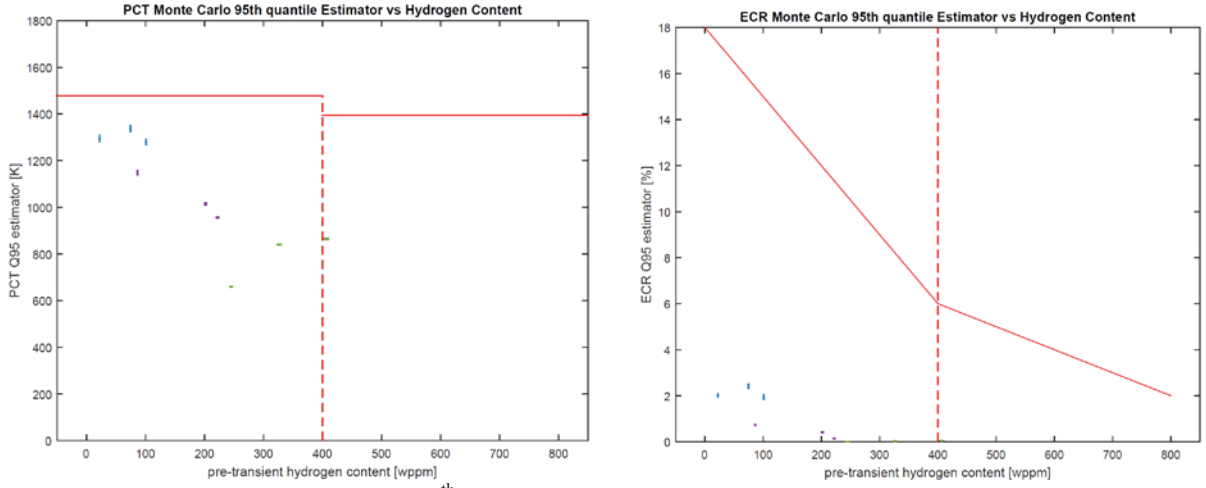

Figure 4-12. Monte Carlo 95th Quantile PCT and ECR Estimators During LB-LOCA Transients (Blue=Fresh Fuel, Purple=Once-Burnt, Green=Twice-Burnt).

Figure 4-13 provides the scatter plot between the cycle 1 PCT and ECR at the BOC, which exhibits the expected trend of a quadratic relationship between oxidation and PCT. In addition to the samples, Figure 4-13 also provides the 95th quantile estimators and associated confidence intervals based on the marginal PCT and ECR distributions. Looking at the ECR at a particular PCT value provides the conditional distribution of ECR. As shown in Figure 4-13, at the "slice" along the PCT 95th quantile estimator there is a finite chance that the ECR exceeds its 95th quantile estimator, as well as a finite chance that the ECR is below its 95th quantile estimator. This study focused on comparing the marginal PCT and marginal ECR 95th quantile estimators to the NRC limits. The marginal distribution on PCT integrates out the effect of ECR, and vice versa.

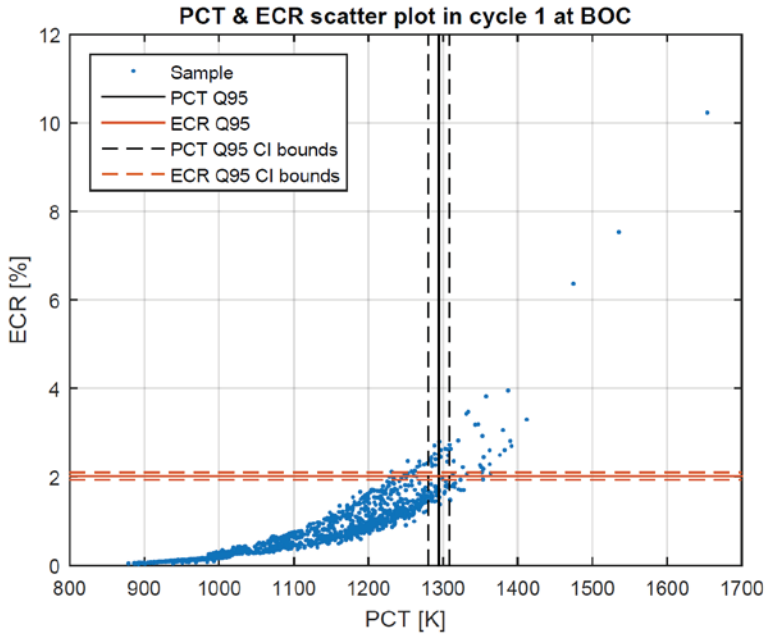

Figure 4-13. Scatter Plot between PCT and ECR for Cycle 1 at BOC (Large Sample N=1240).

4.3.3 Method to Demonstrate Compliance under the Proposed Rule

Firstly, it is important to stress that the RIMM IEM tool is intended to go beyond simply addressing the issue of compliance with the ECCS rule. The RIMM IEM value is in its capabilities of characterizing and managing margin in the plant under the paradigm of the proposed rule. Nevertheless the issue of compliance is of particular relevance in the frame of the 10 CFR 50.46c proposed rule. For Best-Estimate safety analysis the NRC regulatory guidance asks for "a statement of uncertainty". Compliance can only be demonstrated by ensuring to the regulator that for a specific application, there is a very low probability that the limits (now a surface) can be exceeded. The definition of the preferred procedure to show compliance is up to the applicant (licensee). The NRC will judge the adequacy of the statement in the context of the approval of an "Evaluation Model". Often the procedure considered is in fact linked to details of the specific methodology.

This section suggests a possible method by which compliance can be demonstrated with the RIMM IEM methodology.

Under the proposed ECCS LOCA rule, it is expected that ECR criterion will be more limiting because the NRC ECR limit continuously decreases with increasing hydrogen content. the margin to the limit is primarily determined by the margin to the ECR limit whereas the limit the PCT limit is essentially unchanged with the exception of heavily irradiated fuel (>400 wppm pre-transient hydrogen content). For a given cladding material, the hydrogen content (wppm) is a function of the burnup. For the same cladding material such high hydrogen content may not be attainable within the current allowed burnup limit of 62 GWD/MTU. In that case, the

proposed PCT is essentially the same as the current PCT rule. However this conclusion is far from being general.

There is also uncertainty in the mapping between burnup and hydrogen content in a given rod. This is new discipline in itself and not considered yet at this stage of the program. The relationship was simply approximated by Eq. (1) in Appendix A-3.

Under the proposed rule it is difficult a-priori to establish the condition of the hot assembly at a given time in cycle because of the many trade-offs between the linear heat rate, the effect of thermal conductivity degradation, rod internal pressure and margin to ECR limit at the burnup and associated hydrogen content.

As result, there is no longer a single proxy like a core-wide PCT or maximum ECR value that can be compared to the limits (aka 2200 F and 17%). Moreover Wilks approach heavily relies on a safety metric based on few outputs (1 to 3). The applicant is asked to obtain a 95/95 join-probability statement among those outputs. Using Wilks, rank 1 of a sample of 124 is needed for a 95/95 joint-probability on 3 outcome. As the number of outcomes increases further as demanded by the proposed rule, the minimum sample size will escalate significantly. Note that the variability on the extreme case of a sample also increases as the sample size increases. The Wilks approach become soon impractical.

These are among the reasons why RIMM IEM is moving toward MC estimators with large sample sizes.

Under the RIMM IEM methodology, the proposed method to demonstrate compliance with the proposed rule can be stated as follow*: For every represented hot rod in the core estimate the 95th quantile maximum ECR and PCT. Specifically use a MC estimate of the 95th quantile with its 95% confidence interval for each hot rod in the core. The design is acceptable if for each hot rod the upper bound of the confidence interval of PCT and ECR is below the limit curve at the local hot rod conditions.*

There are additional benefits associated with MC approach. As we stated before, MC estimates come with a confidence interval (level of precision). A plant with intrinsically significant margin to the limit may perform a less costly analysis than a plant with less margin because a lower level of precision in the estimate is needed to show compliance. These trade-offs are not possible under the Wilks paradigm. This is again in line with the objective of developing a margin management tool.

5. NEXT STEPS

The best estimate plus uncertainty analysis (BEPU) methodology has been demonstrated in Section 4 using the RELAP5-3D code for a postulated large break LOCA transient for a typical four loop PWR.

The ordered non-parametric statistical approach and the Monte Carlo statistical approach are used to determine the statistical upper tolerance limits for PCT and ECR. The results indicate that safety margins can be gained by switching from the de-facto industry standard of the Wilks non-parametric statistical approach to the Monte Carlo statistical approach by utilizing the modern computing facilities such as INL's high performance computers (HPC).

One important missing piece from this work is the fuel performance calculations, which are required to provide more accurate steady-state initializations of the fuel rod conditions. Therefore one important piece of the future work includes incorporating fuel performance calculations into the RELAP5-3D model. Other future work includes combining the probabilistic risk analysis (PRA) and BEPU analysis to perform LB-LOCA analysis for the NRC's proposed rulemaking on the ECCS/LOCA performance acceptance.

For Fiscal Year 2016 we will consider all the above aspects into a full demonstration of the RIMM Integrated Evaluation Model with potential industry stakeholders. A full demonstration of this Industry Application will include the use of existing tools as well as advanced tools as they become available to the RISMC framework.

5.1 Steps to Integrate LOCA into Reactor Core Design

This section covers the future plan and steps in order to integrate the Core Design (see Section 3) into the LOCA analysis.

In the next fiscal year, the neutronic/thermal-hydraulic suite that is going to be used is still uncertain and will depend on future considerations based on industry stakeholder participation and INL core design group feedbacks. In our view, there are several possible options are available, and we list a few of these options below:

1) PHISICS/RELAP5-3D, used for all the analysis presented in this report;
2) MAMMOTH/RELAP-7;
3) CASL VERA-CS core simulator with an eventual coupling to BISON and RELAP5-3D;
4) CASMO/SIMULATE, as it is extensively used for current industry applications, coupled to TRACE;
5) TRACE/FRAPCON, as it is currently used by the NRC to investigate LOCA and post-LOCA phenomena;
6) NESTLE-UTK/ORIGEN, coupled to COBRA-TF.

In the following, we are going to use the expression "Reactor Physics/TH suite" to refer to one of the options listed above.

For the Early Demonstration analysis presented in the previous sections, a 4-step approach has been employed (see Figure 5-1):

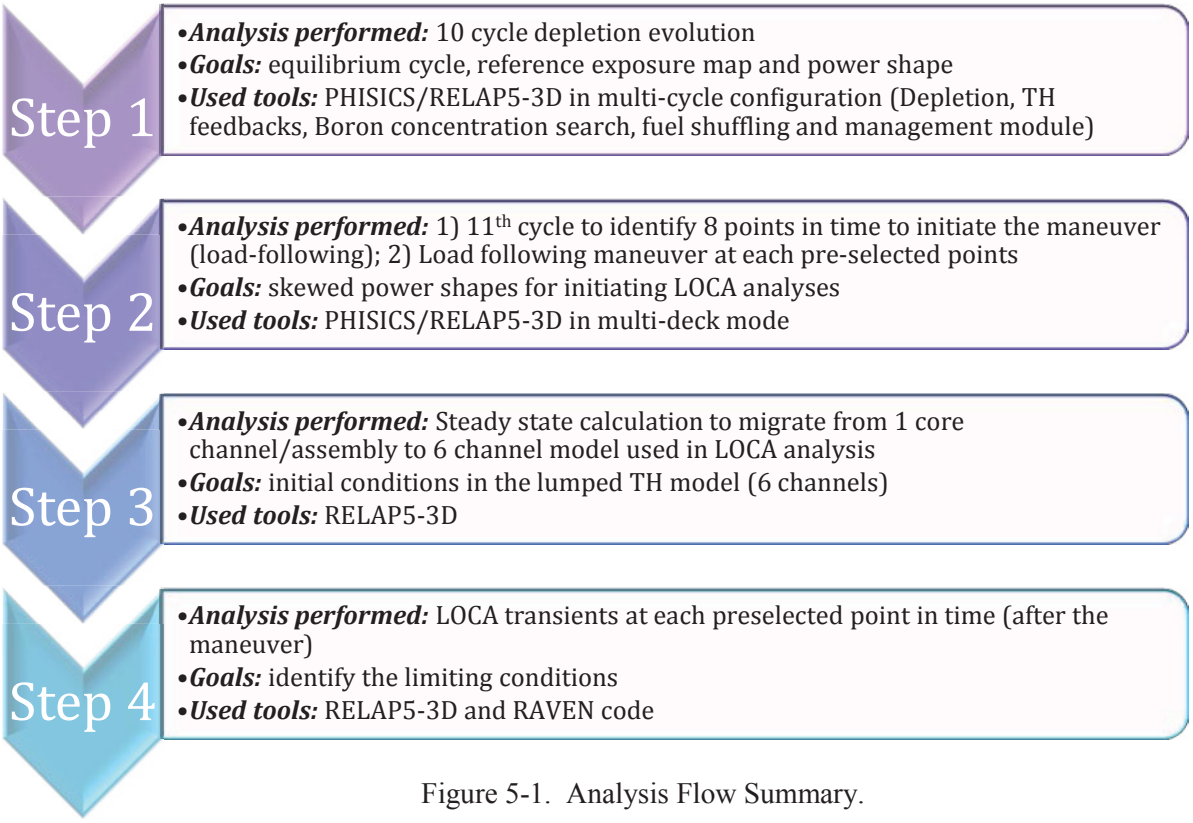

Figure 5-1. Analysis Flow Summary.

1. Core Design for reaching the equilibrium cycle: multi-cycle depletion evolution with TH feedbacks, boron concentration search (criticality) and fuel shuffling, using the coupled suite PHISICS/RELAP5-3D. This preliminary step has been needed to identify the reference condition (fuel composition and power shape) for the equilibrium cycle (10th), that has been considered as the reference cycle during which the LOCA scenario is initiated;
2. Based on the 10th cycle conditions (EOC), another analysis has been initiated to simulate the 11th cycle. During the 11th cycle, multiple points (in time) have been selected to initiate a Load-following transient (that brought to a Xenon transient). The NPP conditions at the selected 8 points in time (BOC, 50, 100, 200, 300, 400, 500, EOC) have been used as initial conditions for the Load-following analysis (see section 3.5). As already pointed out, the transition between the depletion evolution (cycle 11) and the load-following has been performed automatically using the "multi-deck" capability of the couple suite PHISICS/RELAP5-3D;
3. At the end of the load-following, for each of the 8 points, the reactor conditions (burn-up, power shape, etc.) have been used to initiate a new steady state TH analysis (no neutronics), to perform the transition from the 1-core channel/assembly model (RELAP5-3D), used in step 1 and 2, to the 6 core channel model used for the LOCA analysis (see section 4 for details on the LOCA model);
4. The LOCA analyses have been performed (sampling the uncertain parameters through the RAVEN code).

Even if this approach has been effective enough for the purpose of this deliverable, the 2nd through 4th steps will be collapsed. Independently on the Reactor Physics/TH toolkit, the LOCA model needs to be modified. Based on the current workflow, in the 3rd step, some "by hand" work needs to be performed in order to migrate the TH nodalization from a one-core channel/assembly to a six-core channel model:

1. The 3 core channels that represent the hot pins in each fuel region (fresh, once-burned and twice-burned fuel regions) need to be mapped, by hand, to the corresponding heat structure in the kinetic model. This needs to be done for each point in time, at which the LOCA scenario is initiated;

2. As mentioned in Step 3, an additional steady state calculation needs to be performed in order to stabilize the 6-core channel model with the power distribution taken from the one-core channel/assembly model.

This approach is only feasible if few points in time (during the cycle) are considered in the LOCA analysis. Obviously, for a complete and integrated PRA analysis, the full space (in time) needs to be considered, since the LOCA accident can happen in every moment during the cycle; this would bring to an unpractical number of "by hand" modifications (core channel mapping with heat structure) of the input for the steady state calculations in step 3, since the "hot pins" location change during the cycle.

In order to overcome these limitations and automatize the process three possible approaches can be followed:

a. The LOCA model needs to be modified in order to embed the 1-core channel/assembly TH nodalization used in steps 1-2 without the need to perform any intermediate step of steady state and "by hand" mapping;

b. Several thermal regions could be defined for each depletion zone in the LOCA model. This approach could result in a compromise between the strategy a) and c), in case approach a will result being too computational expensive.

c. The 6-core channel model can be kept, but an intermediate script (e.g. in Python) needs to be written in order to wrap the steps 2 through 4, automatically modifying the separated decks (bullet 1) in the above list.

The current idea is to pursue option "a", or "b" if "a" is not affordable, since it is going to facilitate the future plan described in Appendix A-4 (e.g. direct mapping between exposure nodalization and core channels for limiting condition identification, etc.).

With the proper modifications mentioned above, the RAVEN code is going to be able to drive the Reactor Physics/TH analysis in a "once-through" approach, from the simulation of the 11th cycle with load-following to the LOCA analysis itself, sampling all the uncertain parameters, including the timing, during the cycle, from the start of the LOCA scenario.

5.2 Fuels Performance Integration into Safety Analysis

5.2.1 Systems Code, Core Design, and Fuels Performance Interface

All codes for reactor core design, fuel performance, and reactor system analysis need fuel rod design information as input parameters. To guarantee data consistency, a common set of fuel design input data should be shared among all the codes. Table 5-1 shows common fuel rod design input data for different codes. Note that not all the fuel rod design data in a group are required for a specific code. However, as long as some data from one group are required for a code, the group is selected.

Table 5-1. Common Data from Fuel Rod Design for Different Physics in LOCA Analysis.

Fuel Rod Data	Fuel Performance	Core Design	System Code
Rod geometry information such as cladding outer diameter, cladding thickness, fabricated gap, active fuel length, and plenum length	☑	☑	☑
Spring dimensions such as outer diameter of plenum spring, diameter of the plenum spring wire, and number of turns in the plenum spring	☑	☑	☐
Pellet shape such as height (length) of each pellet, height (depth) of pellet dish, pellet end-dish shoulder width, Chamfer height and width	☑	☐	☐
Pellet isotopics such as fuel pellet U-235 enrichment, oxygen-to-metal atomic ratio, weight fraction of gadolinia in urania-gadolinia fuel pellets, Boron-10 enrichment in ZrB2, parts per million by weight of moisture in the as-fabricated pellets, and parts per million by weight of nitrogen in the as-fabricated pellets	☑	☑	☐
Pellet fabrication such as as-fabricated apparent fuel density, open porosity fraction for pellets, the fuel pellet surface arithmetic mean roughness, etc.	☑	☑	☑
Cladding fabrication such as cladding type, the cladding surface arithmetic mean roughness, as-fabricated hydrogen in cladding, etc.	☑	☑	☑
Rod fill conditions such as initial fill gas pressure, Initial fill gas type and their mole fractions	☑	☑	☑
Fuel assembly geometry such as pitch	☑	☑	☑

5.2.1.1 Information Flow from Core Design to FRAPCON

Power history and axial power profile averaged for each assembly from the output of core design codes are required for FRAPCON simulation. The linear heat generation rate (kW/m) at each time step of the FRAPCON simulation should be provided. Either axial averaged value or peak value can be used. FRAPCON-3 has a maximal number of time steps at 1000. A time step between 1 day and 50 days is recommended. The axial power profile plus the average or peak linear heat generation rate can specify the power for each FRAPCON node.

Figure 5-2 shows the average linear heat generation rates for the hot channels in the fresh fuel group and the twice burned fuel group. The burnup values represent the discharge burnup for the corresponding assemblies. Hot channels for different exposure groups (fresh, once-burn, and twice-burn) are selected according to maximal total assembly power within the exposure group. Note that the maximal burnup value 51.9 GWd/MTU is still quite lower than the current allowable maximal burnup value 62 GWd/MTU [INL/EXT-15-35073]. In order to challenge the high burnup fuels, the current core design should be further improved to reach the limit burnup.

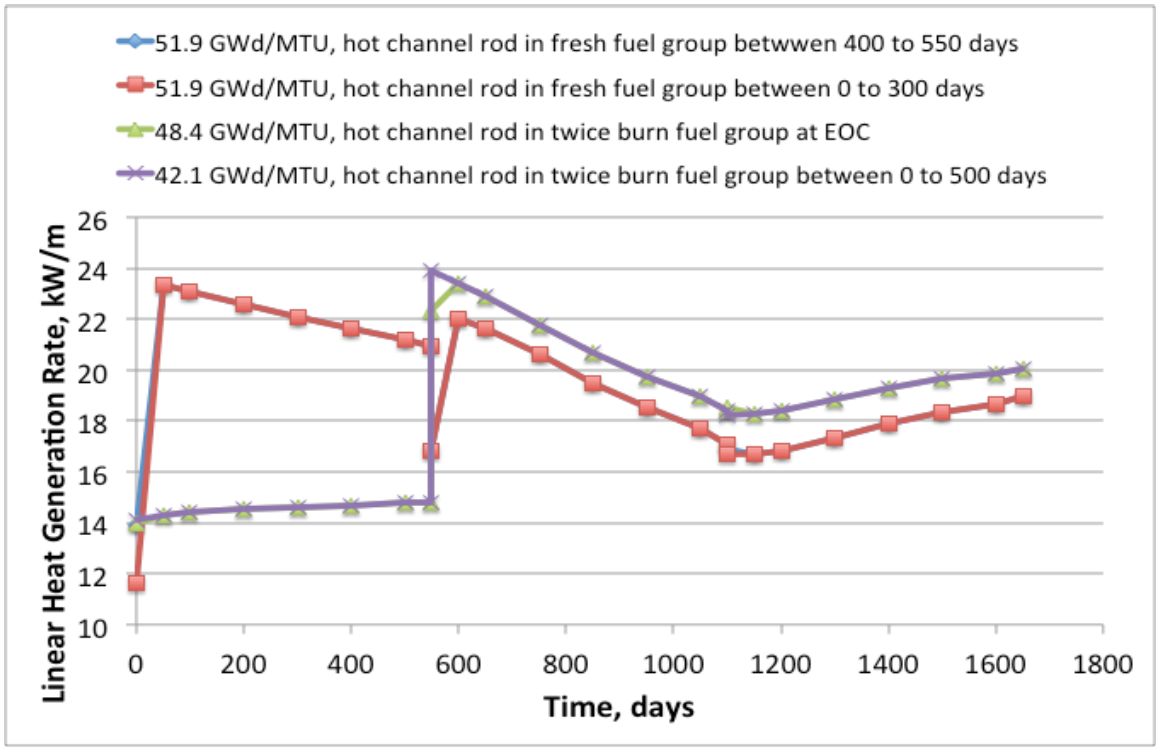

Figure 5-2. Average Linear Heat Generation Rates for Some Hot Channels.

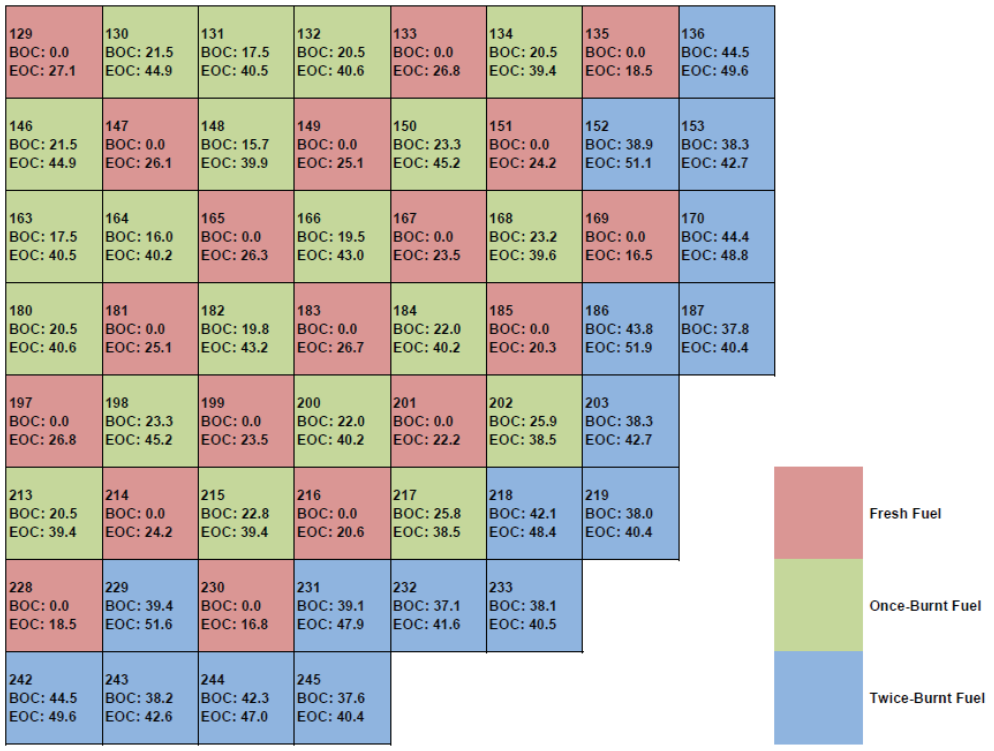

Figure 5-3. Equilibrium Cycle Load Pattern and Assembly Average Burnup at the Beginning of the Cycle and at the End of Cycle; in Each Assembly the First Line Shows the Assembly Number, the Second Line Shows the Burn-Up at BOC, and the third line Shows the Burnup at EOC.

Figure 5-3 shows the equilibrium cycle load pattern and assembly average burnup at the beginning of the cycle and at the end of cycle. The first row and first column are located at the symmetric line. The assembly 201 is one of the two hot assemblies in the fresh fuel group (blue line in Figure 5-2). The assembly 218 is one of the two hot assemblies in the twice burn fuel group (green line in Figure 5-2). For this given core design, the twice burned fuel average discharge exposure is 45.19 GWd/MTU. The typical discharge exposure for a high energy large PWR core (4-loop) is more close to the limit of 62 GWd/MT than what it was achieved in this demonstration design [Porter, 2015].

5.2.1.2 Information Flow from a Systems Code to FRAPCON

TH data from the output of steady state runs of a system code at different depletion cycle points are required for FRAPCON simulations. The data include system pressure, inlet temperature, and coolant mass flux around the simulated fuel rod. These data can be constant or time dependent. Axial cladding surface temperature from the system code result can also be used in FRAPCON at each time step.

5.2.1.3 Information Flow from FRAPCON to a Systems Code

Part of the outputs from FRAPCON simulations are used to prepare for the steady state run of a system LOCA model. The data include initial gap internal pressure, fission gas composition in the plenum, radial displacement due to fission gas-induced fuel swelling and densification, radial displacement due to cladding creepdown, and oxide layer thickness. These inputs from FRAPCON output are used to obtain correct stored energy and to set initial conditions for the transient fuel performance models.

5.2.2 Best Practices on Coupling Fuels Performance and Systems Analysis

Due to their separate development paths and goals, reactor system codes and fuel performance codes have inconsistent models and interfaces for coupled analyses. For example, a recently published paper on improving the coupled calculations between TRACE and FRAPCON [Porter, 2015] shows quite large uncertainties for key parameters with different models and coupling methods, i.e., up to 20% difference in stored energy, 20% difference for hydrogen content for high burn up fuel rods at the end of third cycle. The root reasons for the differences come from both ends of the simulations.

The fuel performance codes were developed for single fuel rod. They lack the ability to capture and model detailed TH conditions due to the impact from neighboring fuel rods and assemblies. Fuel performance codes also do not have best-estimate two-phase flow and heat transfer models used in system codes. Therefore, detailed axial dependent TH information including cladding surface temperature from a system code needs to be used for a fuel performance simulation. By using axial dependent cladding surface temperature and coolant pressure for each concerned fuel rod, more accurate results can be obtained from fuel performance codes. Otherwise, not taking account of localized TH conditions can lead to non-conservatism in terms of steady-state fuel rod licensing limits such as ECR and hydrogen uptake [Porter, 2015].

System codes lack detailed fuel performance models; therefore axial varying fuel rod dimensional changes and burn-up from fuel performance code output should be used in a system code model. The parameters include cladding creep, fuel swelling/densification, oxide layer thickness, and burn-up dependent material in each axial fuel node. Only using “average” value for each axial fuel node would be misrepresentation of the conditions existing at either the center or the top and bottom of the rod [Porter, 2015].

5.3 Potential Applications with Vendors and Plant Operators

Results gathered at this stage of the project are here used to foresee potential applications of the RIMM IEM for vendors and plant owner/operators as the final product mature from the current conceptual design (Phase-2) to an industry-grade tool.

The RIMM IEM is expected to facilitate a paradigm shift and anticipate industry trends toward a risk informed approach. The process started by developing a methodology that effectively addresses the limitations in the status quo. The vision for the RIMM IEM is summarized in the following value propositions:

1. Provide analytical capabilities to enable rapid decisions on considered changes within the LOCA issue space (as regulated under the new 10 CFR 50.46c).
2. Enable factoring current knowledge into the process to enhance safety and operation optimization.
3. Quantify currently unquantified uncertainties and trend to a truly realistic representation of the LOCA which provides insights on the design.
4. Develop new knowledge and understanding of the LOCA scenario, which is currently obscured by the engineering assumptions of typical licensing calculations. Enable a more effective 'exploration' of the issue space.
5. Eliminate the issues associated with the Wilks' approach (variability in the estimator, risk of under-prediction of or over-prediction of FOM, lack of knowledge in what is limiting in the design, incapacity to perform sensitivity studies, etc.)

The RIMM IEM product is integrated with a 'plug-and-play' design philosophy where user selected simulators are coupled to create a multi-physics analytical framework. The RIMM IEM is not intended to replace licensing Analysis of Records, but rather to replace or aid the 'engineering judgment' which is typically applied in the management and maintenance of those AORs. The goal is an analytical and computational device that can represent a power plant realistically with all the uncertainties included and that considers all physical disciplines involved in an integrated fashion, i.e. an IEM.

A 'plug-and-play' approach will enables plant owners and vendors to consider and further develop RIMM Framework for use within their established codes and methods.

It is also possible that the RIMM IA1 technology could be advanced in the future to a level of fidelity and maturity that it could be used for some licensing or regulatory situations. An example would be the reporting of LOCA analysis ΔPCT and ΔECR due to LOCA analysis input errors that are required by 10 CFR 50.46.

The tool will enable a plant operator or vendor to manage the entire body of knowledge to inform decisions that minimize or manage the risks of exceeding the LOCA criteria while allowing a safe and economical operation of the plant by eliminating or reducing the need for expensive re-analyses. At a minimum, the RIMM IEM tool will be a very valuable tool to inform licensees and regulator about real margin available in their plants on an interim basis while new license-grade evaluation models are being rolled out.

Getting into the specifics of the potential utilization of this technology requires the identification of the specific 'pains' that vendors and licensees suffer today. Vendors and plants operators have different missions and needs, therefore it is appropriate to cast the value proposition for each industry group. These are highlight in Section 5.3.1 and 5.3.2. Then Section 5.3.3 highlights how the RIMM IEM can support such propositions.

5.3.1 Fuel Vendor Value Proposition

For a fuel vendor the RIMM IA1 methodology and tool is envisioned as a LOCA analysis scoping tool with the following potential uses:

- Provide quantitative estimates of design or operational margin loss or gain associated with various combinations of changes in LOCA analysis inputs
- Provide quantitative estimates of impact on the LOCA analysis figures-of-merit due to errors in LOCA analysis inputs
- Develop marketing strategies related to LOCA analysis
- Provide LOCA inputs related studies in response to customer inquiries and requests
- Respond to LOCA-related regulatory inquiries and requests for additional information

1. The starting point for such analyses is an approved Analysis of Record (AOR). In the framework of Best-Estimate Plus Uncertainty (BEPU) method, current industry practice (AREVA and WEC) is to infer a 95/95 probabilistic safety statement applying non-parametric order statistics Wilks-derived procedures. Wilks-based procedures rely on the generation of rather small random samples of LB-LOCA event simulations (of the order of 100 run-sets) using validated codes.
2. Despite the procedure satisfies compliance with 10 CFR 50.46, the size of the sample has limited information and there is no simple way to perform the type of engineering assessment discussed in the wish list above.
3. In the US, the AORs are generated by the vendors under contract by the plant operators. The vendor is responsible of the development of code and methods while seeking generic approval of the methodology over a target class of plants. The vendor then performs the plant specific analysis for the licensee to demonstrate compliance with the 10 CFR 50.46 criteria. The plant owner/operator manages the analysis inputs and maintains the AORs. The vendor is responsible for managing the analysis process and assessing impact of inputs errors which may be found after the AOR is in place.

5.3.2 Plant Owner-Operator Value Proposition

Currently there are no nuclear plant owner-operators in the US that performs LOCA analysis for determining compliance with 10 CFR 50.46. A limited number of owner-operators perform LOCA analysis for other purposes, such as pipe break mass and energy release or training simulator validation. For an owner-operator the RIMM IA1 methodology and tool has two distinct types of potential applications. The more likely type of potential applications is for LOCA analysis related work contracted to the fuel vendor, which could include the following potential uses:

- Obtain quantitative estimates of design or operational margin loss or gain associated with various combinations of changes in LOCA analysis inputs
- Obtain quantitative estimates of impact on the LOCA analysis figures-of-merit due to errors in LOCA analysis inputs (including reporting of LOCA analysis ΔPCT and ΔECR due to LOCA analysis input errors that are required by 10 CFR 50.46)

A less likely but possible type of potential application is to use the RIMM IA1 methodology and tool as an independent owner-operator LOCA analysis capability. This capability could be used to perform vendor-independent LOCA scoping or audit calculations that would facilitate decision making related to the impact of plant and fuel design changes, as well as provide an enhanced vendor oversight capability. An owner-operator could develop this capability with in-house staff or by outsourcing to an engineering services or consulting entity.

The type of analyses involved are technically similar to the one described in Section 5.3.1 and similar issues apply.

5.3.3 RIMM IEM Potential Applications

The first step in obtaining the technical capability to perform the type of analyses discussed in Sections 5.3.1 and 5.3.2 is to revisit how uncertainty are propagated across the stream of physical disciplines involved. Regardless the specific codes used to model the physics involved, the methodology discussed here is a different strategy in managing the uncertainties.

The primary characteristic of the RIMM IEM is to be an integrated multiphysics tool (see Figure 1-4 in Section 1.3) and it is in sharp contrast with the current divide-and-conquer approach where every physics is resolved independently and coupling addressed by complex interface procedures. There are significant assumptions and engineering judgments in setting up those procedures which make the propagation of uncertainties across the disciplines complex and prone to errors.

In the RIMM IEM framework uncertainties are propagated directly following a "brute-force" approach. The interactions between the various model parameters are directly solved within the IEM framework. This not only facilitates the automation of the process but it is also mathematically more robust because the advanced procedure considered to propagate uncertainties and/or perform global sensitivity studies requires inputs sampled to be independent. This requirement is hard to achieve following the traditional "divide-and-conquer" approach. The actual integration will be performed by the RAVEN tool.

Despite its widespread adoption by the industry (AREVA, GE and WEC), the use of small sample sizes to infer statement of compliance to the 10 CFR 50.46 rule, have been a major cause of unrealized operational margin in today best-estimate plus uncertainty methods. Moreover the debate on the proper interpretation of the Wilks' theorem in the context of safety analyses is not fully resolved yet more than a decade after its introduction in the frame of safety analyses in the nuclear industry. This represents both a regulatory and applicant risk in rolling out new methods.

The proposed rule adds another layer of complexity for the demonstration of compliance. Under the current rule PCT, Maximum Local Oxidation (MLO) and Core Wide Oxidation (CWO) limits are set to specific value (2200 F, 17% and 1% respectively). Using Wilks compliance is easily demonstrated by ranking the corresponding values obtained from the simulations in the sample and ensuring the rank representing the 95/95 estimate from a small sample is below those limits. Considering there are three outcomes (PCT, MLO and CWO) Rank 1 from a sample of 124 can be chosen for example.

With the proposed rule the limit is a curve. More specifically both PCT and MLO (maximum ECR in this case) limits are function of cladding hydrogen content which varies from rod to rod in the core. Applying Wilks the method would require to define new figure of merits that synthetize this relationship. For example applicant may consider the following two outputs:

1) Minimum distance to the PCT limit within the core

2) Minimum distance to the ECR limit within the core

The minimum sample size to infer a joint-probability statement on the two outcomes would be N=93.

If the analyst is interested in tracking the margin in each core region that would not be possible unless a much larger sample is used. Moreover, as stated in Section 2.2, the variability of the such estimators when dealing with multiple-outcomes are considered will be quite large and would make Wilks approach ineffective.

These Wilks estimator issues have been explained in details in Section 2. As discussed, the answer is to move toward full MC simulations when it comes to managing uncertainties. However, this comes to a cost. Moving toward full MC simulations requires the generation of large simulation samples (run-sets) when compared to today practice in the LOCA analysis arena. This is becoming at least attainable from a computational capacity stand point.

The granularity of a typical LOCA analysis is such that an instance (or simulation) of a specific transient is performed on a processor in the course of few hours (4-6 hrs) today but many runs can be broadcasted a large computer cluster. A high performance computing (HPC) platform which access an order of 1000 processors is attainable, especially in the context of National Laboratories, therefore a sample of few thousands simulation is feasible within a 24 hrs turnaround today, as long as the process is amenable to extensive automation.

It is noted that the sample size needed to reduce the confidence interval on the estimate (standard error) to the magnitude desired may requires sample sizes in excess of 10,000 cases. One recognized gap to address as technology moves in that direction of such large samples is the reliability of thermal-hydraulic computer codes (RELAP, TRAC and COBRA derivatives). Numerical instabilities are intrinsic in these tools and run failure rates of about 10% are common. Solution and its convergence is quite sensitive to time and space discretization scheme used. Constitutive relationships are not smooth and prone to unstable solutions. The resolution of these issues will be important to enable the degree of automation needed to perform the simulations required within the RIMM IEM framework and retain a reasonable turn-around time.

An interim solution to cover this computational gap in the near time is the adoption of emulators. The current method proposes to use surrogates or meta-models to act as very fast approximations to the input/output relationship. After an initial set of computer code evaluations required to build or train the surrogate, the surrogate model is used in place of the computer code in the Monte Carlo sampling scheme. The surrogate model based approach to UQ was proposed as part of the original CSAU method for propagating uncertainties. When using a surrogate model based approach, it is very important to include an estimate of the surrogate's own predictive uncertainty. The most common type of emulator is the Gaussian Process (GP) regression model.

The use of GP emulators can also provide another source of margin. Given the high cost of a typical LOCA safety analysis, current practice is to considers expanded ranges of the inputs which are not only cover the current state of the plant but project state of the plant into the future to ensure the analysis holds over the course of several fuel cycles. Fast running GP emulators could be trained over the expanded range but UQ conducted over a more restricted range which better represent the actual state and therefore capture analytical margin. It is even conceivable to develop further this technology to enable an on-line LOCA margin monitoring system.

A LOCA analysis can be conducted on a reload basis using this technology. This is an interesting proposition, especially in the context of the new 10 CFR 50.46c. The reason is that a detailed 3D core map of margin to ECR limit makes the LOCA analysis tightly coupled with core design. In general, the technology is instrumental in risk analyses associated with defining optimal core management strategies.

Regardless the method selected to create these large samples, the global sensitivity procedures described in Section 2 provide are the next major value-added in the RIMM IEM. Variance-based techniques such as the method of Sobol' indices and the Fourier Amplitude Sensitivity Test (FAST) are capable of ranking which inputs control the variance of an output.

Information gained from global sensitivities can be utilized to address different practical questions:

1. Down select unimportant contributors to the safety metrics to aid engineers to respond rapidly to LOCA analysis input changes (JCO, JPO, LARs, etc.)
2. Focus resources on most controlling design parameters in the effort of reducing those uncertainties
3. Prioritize LOCA code V&V efforts by focusing the attention on better characterizing model parameters which are most influential on the outcome

BIBLIOGRAPHY

SECTION 1

1. C. Frepoli, J. Yurko, R.H. Szilard, C.L. Smith, R. Youngblood, “10 CFR 50.46c Rulemaking: A Novel Approach in Restating the LOCA Problem for PWRs,” in *NURETH-16*, Chicago, IL, USA, 2015.
2. G. Hache and H. Chung, "The History of the LOCA embrittlement criteria," OECD, 2001.
3. "Report of Advisory Task Force on Emergency Cooling," TID-24226.
4. "Interim Acceptance Criteria for Emergency-Core-Cooling Systems for Light-Water Power Reactors," U.S. Federal Register 36 (125). 1971, p. 12247-12250.
5. W. Cottrell, "ECCS rulemaking hearings," Nuclear Safety, 15, pp. 30-55, 1974.
6. U.S. Nuclear Regulatory Commission, "Regulatory Guide 1.157 - Best-Estimate Calculations of Emergency Core Cooling System Performance," U.S. NRC, Washington D.C, 1989.
7. U.S. Nuclear Regulatory Commission, "Regulatory Guide 1.203 Transient and Accident Analysis Methods," U.S. NRC, Washington, DC, December 2005.
8. B. Dunn and e. al., "Realistic Large Break LOCA Methodology for Pressurized Water Reactors, Revision 2," AREVA NP Inc., 2010.
9. P. R. Martin and L. D. O'Dell, "Development Considerations of AREVA NP Inc.'s Realistic LB-LOCA Analysis Methodology," *Science and Technology of Nuclear Installations,* vol. 2008, p. 13, 2008.
10. M. Y. Young, S. M. Bajorek, M. E. Nissley and L. E. Hochreiter, "Application of Code Scaling Applicability and Uncertainty Methodology to the Large Break Loss of Coolant," *Nuclear Engineering and Design,* vol. 186, no. 1-2, 1998.
11. M. E. Nissley, "Method for Satisfying 10 CFR 50.46 Reanalysis Requirements for Best-Estimate LOCA Evaluation Models," Westinghouse Electric Compnay, LLC, Pittsburgh, PA, 2004.
12. M. E. Nissley, C. Frepoli, K. Ohkawa and K. Muftuoglu, "Realistic Large-Break LOCA Evaluation Methodology Using the Automated Statistical Treatment of Uncertainty Method (ASTRUM)," Westinghouse Electric Company, Pittsburgh, PA, 2003.
13. C. Frepoli, "Review Article - An Overview of Westinghouse Realistic Large Break LOCA Evaluation Model," *Science and Technology of Nuclear Installations,* vol. 2008, Article ID 498737, p. 15, 2008.
14. C. Frepoli and K. Ohkawa, "Westinghouse Experience in Licensing and Applying Best-Estimate LOCA Methodologies within the Industry: Past, Present and Future," in *Workshop on Best Estimate Methods and Uncertainty Evaluations*, Barcelona, Spain, 2011.
15. U.S. Nuclear Regulatory Commission, "Safety Evaluation by the Office of the Nuclear Reactor Regulation Topical Report WCAP-16009-P. Revision 0, "Realistic Large Break LOCA Evaluation Methodology Using Automated Statistical Treatment of Uncertainty Method (ASTRUM)"," U.S. NRC, Washington, DC, November 5, 2004.
16. U.S. Nuclear Regulatory Commission, ADAMS Accession Number ML051670395, U.S. NRC, Washington, DC, June 10, 2005.
17. "http://pbadupws.nrc.gov/docs/ML1211/ML121100200.pdf".
18. "http://www.gpo.gov/fdsys/pkg/FR-2014-03-24/pdf/2014-05562.pdf".
19. "http://pbadupws.nrc.gov/docs/ML1435/ML14358A493.pdf".

20. R. Borchard and M. Johnson, "10 CFR 50.46c Rulemaking: Request to Defer Draft Guidance and Extension Request for Final Rule and Final Guidance," U.S. Nuclear Regulatory Commission, Washington, DC, March 4, 2013.
21. R. Szilard, R. Youngblood, C. Frepoli, J.P. Yurko, G. Swindlehurst, H. Zhang, H. Zhao, P.D. Bayless, C. Rabiti, A. Alfonsi, C.L. Smith, "Industry Application Emergency Core Cooling System / Cladding Acceptance Criteria Problem Statement," Idaho National Laborary Report: INL-EXT-15-35073, April 2015.
22. C. Smith, C. Rabiti, R. Martineau, "Risk-Informed Safety Margins Characterization (RISMC) Pathway Technical Program Plan," INL-EXT-11-22977, Revision 2, September 2014.
23. R.H. Szilard, C.L. Smith, R. Youngblood, "RISMC Advanced Safety Analysis Project Plan – FY 2015 – FY 2019," INL-EXT-14-33186, September 2014.
24. U.S. Nuclear Regulatory Commission, "Regulatory Guide 1.174, U.S. NRC, Washington D.C, 1989.
25. L. Pagani, "On the Quantification of Safety Margins" (MIT, 2004).
26. Draft NEI White Paper, NEI-NRC Risk-Informed Steering Committee (RISC), January 2015.
27. Task group on Safety Margins Action Plan (SMAP). "Safety Margins Action Plan – Final Report" NEA/CSNI/R(2007)9.
28. F. Fouet, P. Probst, J.M. Lanore, "Impact on Safety Margins of a 10% Power Up-Rate for Zion NPP SBO Transient," Proceedings of PSAM-10.
29. Assessing Safety Margins: the impact of a power uprate on risk from Small and Medium LOCA scenarios, Vinh N. Dang, Tae-Wan Kim, Martin A. Zimmermann, and Annalisa Manera, Proceedings of PSAM-10.
30. "Technical Framework for Management of Safety Margins--Loss of Main Feedwater Pilot Application, EPRI 1023032," S. Hess (Project Manager), J. Gabor, R. Sherry, and D. True, Principal Investigators (EPRI, 2011).
31. Failure domain characterization: Loss of Main and Auxiliary Feed Water Example. V. Rychkov, EDF R&D, IDPSA workshop, Stockholm, 19-21 November 2012
32. Application of the Damage Domain approach to the calculation of exceedance frequencies, Javier HORTALa *, José M. IZQUIERDOa, César QUERALb, and Luisa IBAÑEZ, Proceedings of PSAM-10.
33. Technical Basis for Revision of the Pressurized Thermal Shock (PTS) Screening Limit in the PTS Rule (10 CFR 50.61), NUREG/1806 (NRC, 2007).
34. U.S. Nuclear Regulatory Commission, Draft Regulatory Guide DG-1263, ADAMS Accession Number ML12284A323, U.S. NRC, Washington, DC.
35. J. V. Cathcart, R. E. Pawel, R. A. McKee, R. E. Druscel, G. J. Yurek, J. J. Cambell and S. H. Jury, "Zirconium Metal-Water Oxidation Kinetics IV. Reaction Rate Studies", ORNL/NUREG-17, Aug. 1977.
36. U.S. Nuclear Regulatory Commission, Draft Regulatory Guide DG-1261, U.S. NRC, Washington, DC.
37. U.S. Nuclear Regulatory Commission, Draft Regulatory Guide DG-1262, ADAMS Accession Number ML12284A324, U.S. NRC, Washington, DC.
38. U.S. Nuclear Regulatory Commission , ADAMS Accession Number ML093350101, U.S. NRC, Washington, DC.
39. C.A. Wemple, H-N.M. Gheorghiu, R.J.J. Stamm'ler, E.A. Villarino, *The HELIOS-2 Lattice Physics Code*, 18th AER Symposium on VVER Reactor Physics and Reactor Safety (2009) PHISICS.

40. C. Rabiti, Y. Wang, G. Palmiotti, A. Alfonsi, A. Epiney, H. Hiruta, T. Grimmet, *PHISICS: Parallel and Highly Innovative Simulation for INL Code System,* INL/EXT-11-21384, Novembre 2011.

41. The RELAP5-3D© Code Development Team, "RELAP5-3D© Code Manual Volume I: Code Structure, System Models, and Solution Methods," Idaho National Laboratory Report, INEEL-EXT-98-00834, Rev. 4, June, 2012.

42. N. Horelik, B. Herman, B. Forget, K. Smith, "**B**enchmark for **E**valuation **A**nd **V**alidation for **R**eactor **S**imulations (BEAVRS) v1.01," Proc. Int. Conf. Mathematics and Computational Methods Applied to Nuc. Sci. & Eng., Sun Valley, Idaho, 2013.

43. American National Standard for Decay Heat Power in Light Water Reactors, ANSI/ANS-5.1-1979, August 1979.

44. WCAP-9272-P-A, "Westinghouse Reload Safety Evaluation Methodology," July 1985.

45. AREVA NP, BAW-10179NP-A, "Safety Criteria and Methodology for Acceptance Cycle Reload Analyses," ADAMS Accession Number ML102210443, Lynchburg, VA, Revision 8, May 2010.

46. U.S. NRC, "FRAPCON-3.5: A Computer Code for the Calculation of Steady-State, Thermal-Mechanical Behavior of Oxide Fuel Rods for High Burnup," NUREG/CR-7022, Vol. 1 Rev.1 PNNL-19418, Vol. 1 Rev.1, May 2014.

47. U.S. NRC, "FRAPTRAN-1.5: A Computer Code for the Transient Analysis of Oxide Fuel Rods," NUREG/CR-7023, Vol. 1 Rev.1 PNNL-19400, Vol. 1 Rev.1, May 2014.

48. J. D. Hales, et al., "BISON Theory Manual, The Equations behind Nuclear Fuel Analysis," Idaho National Laboratory, Jan., 2015.

49. J. D. Hales, et al., "BISON Users Manual," Idaho National Laboratory, Jan., 2015.

50. INL, *RELAP5-3D Code Manual Volume V: User's Guidelines*, INEEL-EXT-98-00834, Rev. 4, June, 2012.

51. L. J. Siefken et al., FRAP-T6: A Computer Code for the Transient Analysis of Oxide Fuel Rods, NUREG/CR-2148, EGG-2104, Idaho National Engineering Laboratory, May 1981.

52. U.S. Nuclear Regulatory Commission , ADAMS Accession Number ML13329A086; ML13329A090, U.S. NRC, Washington, DC, Fall 2013.

53. U.S. Nuclear Regulatory Commission , ADAMS Accession Number ML14358A493, U.S. NRC, Washington, DC, December 2014.

54. Kang, D.G., et al., "A Combined Deterministic and Probabilistic Procedure for Safety Assessment of Beyond Design Basis Accidents in Nuclear Power Plant: Application to ECCS Performance Assessment for Design Basis LOCA Redefinition," Nuclear Engineering and Design, Vol. 260, pg. 165–174, 2013.

55. C. Smith, et al., "Risk Informed Safety Margin Characterization (RISMC) Advanced Test Reactor Demonstration Case Study," Idaho National Laboratory, INL/EXT-12-27015, August 2012.

56. Pagani, L.P., Apostolakis, G.E., Hejzlar, P., 2005. The impact of uncertainties on the performance of passive systems. Nucl. Technol. 149 (2), 129–140.

57. NEA, 2007. Safety Margins Action Plan – Final Report, NEA/CSNI/R(2007)9, Task Group on Safety Margins Action Plan (SMAP), Committee on the Safety of Nuclear Installations. OECD Nuclear Energy Agency.

58. D.G. Kang and S.H. Chang, "The safety assessment of OPR-1000 nuclear power plant for station blackout accident applying the combined deterministic and probabilistic procedure," Nuclear Engineering and Design, Vol. 275, pp.142-153 (2014).

59. A. Alfonsi, C. Rabiti, D. Mandelli, J. Cogliati, and R. Kinoshita, “Raven as a tool for dynamic probabilistic risk assessment: Software overview,” in Proceeding of M&C2013 International Topical Meeting on Mathematics and Computation, CD-ROM, American Nuclear Society, LaGrange Park, IL (2013).

60. D. Mandelli, C. Smith, Z. Ma, T. Riley, J. Nielsen, A. Alfonsi, C. Rabiti, J. Cogliati, ” Risk-Informed Safety Margin Characterization Methods Development Work,” INL/EXT-14-33191, INL, September 2014.

61. A. Alfonsi, C. Rabiti, D. Mandelli, J. Cogliati, R. Kinoshita, A. Naviglio, “Dynamic Event Tree Analysis Through RAVEN”, International Topical Meeting on Probabilistic Safety Assessment and Analysis (PSA 2013), September 22-26, Columbia, SC, USA, (2013).

62. A. Alfonsi, C. Rabiti, D. Mandelli, J. Cogliati, and R. Kinoshita, “RAVEN: Development of the adaptive dynamic event tree approach,” Tech. Rep. INL/MIS-14-33246, Idaho National Laboratory (INL), (2014).

63. J. C. Lee and N. J. McCornick, Risk and Safety Analysis of Nuclear Systems, Wiley, 2011.

64. R. Youngblood and C. Smith, “Technical Approach and Results from the Fuels Pathway on an Alternative Selection Case Study,” INL/EXT-13-30195, INL, September 2013.

SECTION 2

1. U.S. Nuclear Regulatory Commission, Draft Regulatory Guide DG-1263, ADAMS Accession Number ML12284A323, U.S. NRC, Washington, DC

2. NUREG/CR-6975

3. U.S. NRC, “FRAPCON-3.5: A Computer Code for the Calculation of Steady-State, Thermal-Mechanical Behavior of Oxide Fuel Rods for High Burnup,” NUREG/CR-7022, Vol. 1 Rev.1 PNNL-19418, Vol. 1 Rev.1, May 2014

4. J. V. Cathcart, R. E. Pawel, R. A. McKee, R. E. Druscel, G. J. Yurek, J. J. Cambell and S. H. Jury, "Zirconium Metal-Water Oxidation Kinetics IV. Reaction Rate Studies", ORNL/NUREG-17, Aug. 1977

5. J. Coleman, C. Rabiti, C. Smith, R. Szilard, R. Youngblood and H. Zhang, "Advanced Safety Analysis Program Strategy and Use-Case Analysis," Idaho National Laboratory, 2013.

6. C. Stoots and et al, "Verification and Validation Strategy for LWRS Tools," 2012.

7. S. Hess, "Risk Informed Safety Margin Characterization for Effective Long Term Nuclear Power Plant Safety Management," in 3rd International Conference on NPP Life Management (PLIM) for Long Term Operations (LTO), Salt Lake City, 2012.

8. EPRI, "2014 Research Portfolio - Risk and Safety Management," 2013. [Online]. Available: http://portfolio.epri.com/ProgramTab.aspx?sId=NUC&rId=275&pId=7807&suId=7811.

9. N. Capps and e. al, "Verification and Benchmarking of Peregrine Against Halden Fuel Rod Data and Falco," in TopFuel 2013, Charlotte, 2013.

10. C. Smith, D. Schwieder, C. Phelan, A. Bui and P. Bayless, "Risk Informed Safety Margin Characterization (RISMC) Advanced Test Reactor Demonstration Case Study," Idaho National Laboratory, 2012.

11. T. Ehresman, "INL Programs - The Advanced Test Reactor (ATR)," [Online]. Available: https://inlportal.inl.gov/portal/server.pt/gateway/PTARGS_0_1646_9670_0_0_18/atr.pdf. [Accessed October 2013].

12. C. Smith, C. Rabiti and R. Martineau, "Risk Informed Safety Margin Characterization (RISMC) Pathway Technical Program Plan," INL, 2013.

13. D. Gaston and e. al, "Physics-based Multiscale Coupling for Full Core Nuclear Reactor Simulation," Annals of Nuclear Energy, (submitted for publication).

14. "Fuel Analysis and Licensing Code: Falcon MOD01: Volume 1: Theoretical and Numerical Bases," EPRI, Palo Alto, CA, 2004. 1011307.

15. R. Montgomery and e. al, "Peregrine: Advanced Modeling of Pellet-Cladding Interaction (PCI) Failure in LWRs," in Proceedings of the TopFuel 2012 Reactor Fuel Performance Conference, Manchester, United Kingdom, September 2-6, 2012.

16. R. Montegomery and e. al, "Peregrine: Validation and Benchmark Evaluation of Integrated Fuel Performance Modeling Using Test Reactor Data and Falcon," 2013.

17. C. Smith, R. Szilard and K. McCarthy, "Advanced Safety Analysis Program Objectives and Value Proposition," Idaho National Laboratory, INL-EXT-13-30460, 2014.

18. E. Zio, “Reliability engineering: Old problems and new challenges,” Reliability Engineering and System Safety, vol. 94(2), pp. 125-141, 2009.

19. D. Gaston, G. Hansen and C. Newman, “MOOSE: A Parallel Computational Framework for Coupled Systems for Nonlinear Equations,” in International Conference on Mathematics, Computational Methods, and Reactor Physics, Saratoga Springs, NY, 2009.

20. "http://www.nrc.gov/reactors/operating/licensing/power-uprates.html".

21. "US NRC ADAMS Accession Number ML14141A084".

22. E. Kolstad, H. Devold and V. Tosi, "High Burn-Up Fuel Behavior Studies by In-Pile Measurements," in International Topical Meeting on LWR Fuel Performance 'Fuel For the 90's', Avignon, France, 1991.

23. W. Wiesenack, "Assessment of UO2 Conductivity Degradation Based on In-PIle Temperature Data," in Proceedings of the 1997 International Topical Meeting on Light Water Reactor Fuel Performance, Portland, OR, 1997.

24. K. J. Geelhood, W. G. Luscher and C. E. Beyer, "FRAPCON-3.4: A Computer Code for the Calculation of Steady-State, Thermal-Mechancial Behavior of Oxide Fuel Rods for High Burnup," U.S. Nuclear Regulatory Commission, Pacific Northwest National Laboratory, Richland, WA, 2011.

25. European Commission Nuclear Safety and the Environment, "Fuel Cladding Failure Criteria," European Commission, September, 1999.

26. D. D. Lanning, C. E. Beyer and C. L. Painter, "FRAPCON-3: Modifications to Fuel Rod Material Properties and Performance Models for High-Burnup Application," Pacific Northwest National Laboratory, Richland, WA, 1997.

27. Korea Electric Power Corporation, "The Impact of Fuel Thermal Conductivity Degradation on APR1400," KEPCO.

28. U.S. Nuclear Regulatory Commission, "NRC Requests Information from 11 Nuclear Plants Regarding Fuel Performance During Accidents," U.S. NRC, Washington, DC, February 17, 2012.

29. PWR Owners Group, "PWROG 50.46(b) Margin Assessment," PWROG, April 29, 2011.

30. S. M. e. a. Bajorek, "Code Qualification Document for Best Estimate LOCA Analysis," Westinghouse Electric Compnay, LLC, Pittsburgh, PA, 1998.

31. Westinghouse Electric Company, LLC, "Introduction to Full Spectrum LOCA Concept," WEC, Pittsburgh, PA, December 13, 2005.

32. U.S. Nuclear Regulatory Commission, "NRC Information Notice 2009-23, Supplement 1: Nuclear Fuel Thermal Conductivity Degradation," U.S. NRC, Washington, DC, October 26, 2012.

33. U.S. Nuclear Regulatory Commission, "NRC Information Notice 2011-21: Realistic Emergency Core Cooling System Evaluation Model Effects Resulting from Nuclear Fuel Thermal Conductivity Degradation," U.S. NRC, Washington, DC, December 13, 2011.

34. Florida Power and Light, "Response to NRC SRXB RAI Regarding EPU LAR No. 205 and Thermal Conductivity Degradation," FPL, Homestead, FL, January 16, 2012.

35. Florida Power and Light, "Response to NRC SRXB RAI Regarding EPU LAR No. 205 and Thermal Conductivity Degradation," FPL, Homestead, FL, December 31, 2011.

36. R. W. Borchardt, "Final Rule: Risk-Informed Changes to Loss-of-Coolant Accident Technical Requirements (10 CFR 50,46a) (RIN 3150-AH29)," U.S. Nuclear Regulatory Comission, Washington, DC, December 10, 2010.

37. S. J. Hong, S. S. Jeon and Y. S. Bang, "Loss of Coolant Accident Analysis Using Best Estimate Plus Uncertainties Considering the Change of Fuel Thermal Conductivity with Burnup," in Proceedings of ICAPP, Nice, France, May 2-5, 2011.

38. U.S. Nuclear Regulatory Commission, "Regulatory Guide 1.203 Transient and Accident Analysis Methods," U.S. NRC, Washington, DC, December 2005.

39. B. Boyack and e. al., "Quantifying Reactor Safety Margins," 1989.

40. U.S. Nuclear Regulatory Commission, "Regulatory Guide 1.157 - Best-Estimate Calculations of Emergency Core Cooling System Performance," U.S. NRC, Washington D.C, 1989.

41. "http://pbadupws.nrc.gov/docs/ML1004/ML100470547.pdf".

42. "http://pbadupws.nrc.gov/docs/ML1200/ML12009A113.pdf".

43. "US NRC ADAMS Accession ML093350101".

44. "Interim Acceptance Criteria for Emergency-Core-Cooling Systems for Light-Water Power Reactors," U.S. Federal Register 36 (125). 1971, p. 12247-12250.

45. W. Cottrell, "ECCS rulemaking hearings," Nuclear Safety, 15, pp. 30-55, 1974.

46. "New acceptance criteria for emergency core-cooling systems of light-water-cooled nuclear power reactors,," Nuclear Safety, 15, pp. 173-184., 1974.

47. "http://pbadupws.nrc.gov/docs/ML1211/ML121100200.pdf".

48. "http://www.gpo.gov/fdsys/pkg/FR-2014-03-24/pdf/2014-05562.pdf".

49. "http://pbadupws.nrc.gov/docs/ML1435/ML14358A493.pdf".

50. J. V. Cathcart, P. R. E. and a. et., "Zirconium Metal-Water Oxidation Kinetics IV. Reaction Rate Studies," ORNL/NUREG-17, 1977.

51. P. Parsons, E. Hindle and C. and Mann, "PWR fuel behaviour in design basis accident conditions. A State-of-the-Art Report by the Task Group on Fuel Behaviour of CSNI Principal Working Group No 2," Committee on the Safety of Nuclear Installations, OE.

52. D. Hobson and P. Rittenhouse, "Embrittlement of Zircaloy Clad Fuel Rods by Steam During LOCA Transients," Oak Ridge National Laboratory, ORNL-4758, 1972.

53. D. Hobson, "Ductile-brittle behavior of Zircaloy fuel cladding," in ANS Topical Meeting on Water Reactor Safety, Salt Lake City, 1973.

54. R. Pawel, "Oxygen diffusion in β Zircaloy during steam oxidation," Journal of Nuclear Materials, pp. pp. 247-258, 1974.

55. A. Keane and P. Nair, Computational Approaches for Aerospace Design: The Pursuit of Excellence, John-Wiley & Sons, 2005.

56. L. Brevault, M. Balesdent, N. Berend and R. Le Riche, "Challenges and future trends in Uncertainty-based Multidisciplinary Design Optimization for space transportation system design," in 5th European Conference for Aerospace Sciences (Eucass), Munich, Germany, 2013.

57. "[Online], Managning Uncertainty in Complex Models Toolkit," [Online]. Available: http://www.mucm.ac.uk/.

58. D. Higdon, M. Kennedy, J. Cavendish, J. Cafeo and R. Ryne, "Combining field data and computer simulations for calibration and prediction," SIAM Journal on Scientific Computing, vol. 26, pp. 448-466, 2004.

59. D. Higdon, J. Gattiker, B. Williams and M. Rightley, "Computer model calibration using high-dimensional output," Journal of the American Statistical Association, vol. 103, no. 482, 2008.

60. C. Rasmussen and C. Williams, Gaussian Processes for Machine Learning, Springer-Verlag, 2004.

61. " Proposed Rules," Federal Register, Vol. 79, No. 56, Monday, March 24, 2014.

62. NRC, "Staff Requirements - SECY-10-0161 - Final Rule: Risk-Informed Changes to Loss-of-Coolant Accident Technical Requirements (10 CFR 50.46a) (RIN 3150-AH29)," U.S. Nuclear Regulatory Commission, Washington, DC, April 26, 2012.

63. C. Miller, "Recommendations for Enhancing Reactor Safety in the 21st Century, The Near-Term Task Force Review of Insights from the Fukushima Dai-ichi Accident," U.S. Nuclear Regulatory Commission, Washington, DC, 2011.

64. "Report of Advisory Task Force on Emergency Cooling," TID-24226.

65. G. Hache and H. Chung, "The History of the LOCA embrittlement criteria," OECD, 2001.

66. C. Frepoli and e. al., "Realisitic LOCA Evauluation Methodology Applied to the Full Spectrum of Break Sizes (FULL SPECTRUM LOCA Methodology)," Westinghouse Electric Company LLC, Pittsburgh, PA, 2010.

67. N. Mamish, "Weekly Information Report - Week Ending February 24, 2012," U.S. Nuclear Regulatory Commission, Washington, DC, February 29, 2012.

68. FPL, "Florida Power & Light Company Turkey Point Units 3 and 4 Docket Nos. 50-250 and 50-251 License Amendment Request for Extended Power Uprate (LAR 205)," Florida Power and Light, Oct 21, 2010.

69. C. Frepoli, "Theory and Practice in the Use of Order Statistics in Best-Estimate Plus Uncertainty Safety Analyses," in The 15th International Topical Meeting on Nuclear Reactor Thermalhydraulics, Pisa, Italy, May12-17, 2013.

70. R. Borchard and M. Johnson, "10 CFR 50.46c Rulemaking: Request to Defer Draft Guidance and Extension Request for Final Rule and Final Guidance," U.S. Nuclear Regulatory Commission, Washington, DC, March 4, 2013.

71. P. Clifford, "ECCS Performance Safety Assessment - 2014 Update," U.S. Nuclear Regulatory Commission, Washington, DC, December 30, 2014.

72. T. Blount, "Final Safety Evaluation for Global Nuclear Fuel - Americas Topical Reports NEDC-33256P, NEDC-33257P, and NEDC-33258P, "The PRIME Model for Analysis of Fuel Rod Thermal-Mechanical Performance" (TAC No. MD4114)," U.S. Nuclear Regulatory Commission, Washington, DC, January 22, 2010.

73. "NUREG/CR-5074," INL, 1988.

74. I. Catton, "Application of Fractional Scaling Analysis (FSA) to Loss of Coolant Accidents (LOCA) - Part 3. Component Level Scaling for Peak Clad Temperature (NURE," in The 11th International Topical Meeting on Nuclear Reactor Thermal-Hydraulics (NURETH-11), Avignon, France, 2005.

75. Florida Power and Light, "Response to NRC SRXB RAI Regarding EPU LAR No. 205 and Thermal Conductivity Degradation - ADAMS Accession No ML12009A113," FPL, Homestead, FL, December 31, 2011.

76. Dominion, "Dominion Energy Kewaunee, Inc. Kewaunee Power Station Response to Request for Additional Information Related to the Estimated Effect on Peak Cladding Temperature Resulting from Thermal Conductivity Degradation in the Westinghouse Furnished Realistic...," ADAMS Accession No ML12164A786, June 8, 2012.

SECTION 3

1. R. Sanchez, “Assembly homogenization techniques for core calculations,” Progress in Nuclear Energy - Progress Nuclear Energy, vol. 51, no. 1, pp. 14-31, 2009

2. T. Takeda, N. Uto, “Comparison of cell homogenization methods considering interaction effect between fuel cells and control rod cells”, INIS, vol. 22, no. 4, 1988

3. C.A. Wemple, H. Gheorghiu, R. Stammler, E. Villarino, “The HELIOS-2 Lattice Physics Code”, 18th AER Symposium on VVER Reactor Physics and Reactor Safety, 19-23 September 2011, Eger, Hungary

4. C. Rabiti, A. Alfonsi, A. Epiney, “New Simulation Schemes And Capabilities For The Phisics/Relap5-3d Coupled Suite”, in publication Nuclear Science and Engineering (2015)

5. C. Rabiti, Y. Wang, G. Palmiotti, H. Hiruta, J. Cogliati, A. Alfonsi, “PHISICS: a New Reactor Physics Analysis Toolkit”, Proc. 2011 ANS Annual Meeting, Hollywood, Florida, USA, June 26–30, 2011, American Nuclear Society (2011)

6. A. Alfonsi, C. Rabiti, A. Epiney, Y. Wang, J. Cogliati, ""PHISICS Toolkit: Multi-Reactor Transmutation Analysis Utility – MRTAU", Proc. PHYSOR 2012 Advances in Reactor Physics Linking Research, Industry, and Education, on CD-ROM, American Nuclear Society, LaGrange Park, Ill (2012), Knoxville, Tenn., April 15-20, 2012.

7. A. Epiney, C. Rabiti, A. Alfonsi, G. Strydom, “PHISICS multi-group transport neutronic capabilities for RELAP5”, Proc. of conf. ICAPP 2012, Chicago, USA, 2012.

8. N. Horelik, B. Herman, B. Forget, K. Smith, “Benchmark for Evaluation and Validation of Reactor Simulations (BEAVRS), v1.0.1”, Proc. Int. Conf. Mathematics and Computational Methods Applied to Nuc. Sci. & Eng., Sun Valley, Idaho, 2013.
9. T. Bilic, D. Pevec, T. Smuc, “Investigating a possibility to implement 24-month cycle in NPP Krsko”, Proc. Of conf. Nuclear Energy in Central Europe '98, Terme Catez, 7-10 September, 1998
10. U.S. NRC, “FRAPCON-3.5: A Computer Code for the Calculation of Steady-State, Thermal-Mechanical Behavior of Oxide Fuel Rods for High Burnup,” NUREG/CR-7022, Vol. 1 Rev.1 PNNL-19418, Vol. 1 Rev.1, May 2014.
11. U.S. NRC, “FRAPTRAN-1.5: A Computer Code for the Transient Analysis of Oxide Fuel Rods,” NUREG/CR-7023, Vol. 1 Rev.1 PNNL-19400, Vol. 1 Rev.1, May 2014.
12. J. D. Hales, et al., “BISON Theory Manual, The Equations behind Nuclear Fuel Analysis,” Idaho National Laboratory, Jan., 2015.

SECTION 4

1. C. Frepoli and S. Iyengar,” A Comparison of Non-Parametric Tolerance Limits with Linear Combinations of Order Statistics in Safety Analysis,” Proceedings of ICAPP, Nice, France, May 2-5, 2011.
2. G.E. Wilson and C.B. Davis, “Best Estimate Versus Conservative Model Calculations of Peak Clad Temperature: An Example Based on the LOFT Facility.” Ninth International Topical Meeting on Nuclear Reactor Thermal Hydraulics (NURETH-9). San Francisco, California: October 3-8, 1999. 21, 22.
3. http://pbadupws.nrc.gov/docs/ML1114/ML11140A159.pdf, Letter Report: OG-11-143 PWROG 50.46(b) Margin Assessment.

SECTION 5

1. I. Porter, T. W. Knight and P. Raynaud, “Potential Impacts of Modeling Full Reactor Cores Using Combined Fuel Performance and Thermal Hydraulics Codes,” Nuclear Technology, Vol. 190, pp. 174 to 182, 2015.
2. F. Gleicher, J. Ortensi, B. Spencer, et al., “The coupling of the neutron transport application RattleSnake to the nuclear fuels performance application bison under the moose framework”, Proc. Of conf. PHYSOR 2014 - The Role of Reactor Physics toward a Sustainable Future, Kyoto, Japan, September 28 - October 3, 2014
3. A. David, R. Berry, D. Gaston, R. Martineau, J. Peterson, H. Zhang, H. Zhao, L. Zou, “RELAP-7 Level 2 Milestone Report: Demonstration of a Steady State Single Phase PWR Simulation with RELAP-7,” Idaho National Laboratory: INL/EXT-12-25924 (2012).
4. A. T. Godfrey, “VERA Core Physics Benchmark Progression Problem Specifications,” CASL-U-2012-0131-004, CASL (2014)

APPENDIX

1. I. Catton et al., "Quantifying Reactor Safety Margins Part 6: A physically Based Method of Estimating PWR Large Break Loss of Coolant Accident," Nuclear Engineering and Design, no. 119, pp. 109-117, 1990.

2. I. Catton et al., "Application of Fractional Scaling Analysis to Loss of Coolant Accidents: Component Level Scaling for Peak Clad Temperature," Journal of Fluids Engineering, vol. Vol. 131 , no. 121401, 2009.

3. B. Harding, C. Tremblay and D. Cousineau, "Standard errors: A review and evaluation of standard error estimators using Monte Carlo simulations," The Quantitative Methods for Psychology, vol. 10, no. 2, 2014.

4. J. Hessling and P. Hedberg, "Sampling Variance and Bias of Wilks' Conservative Estimate of Confidence Intervals," in NURETH-16, Chicago, IL, USA, 2015.

5. A. Saltelli, S. Tarantola and K. P.-S. Chan, "A Quantitative Model-Independent Method for Global Sensitivity Analysis of Model Output," TECHNOMETRICS, vol. 41, no. 1, 1999.

6. A. Saltelli, S. Tarantola, F. Campologno and M. Ratto, Sensitivity Analysis in Practice: A Guide to Assessing Scientific Models, Wiley, 2004.

7. J. Oakley and A. O'Hagan, "Probabilistic Sensitivity Analysis of Complex Models: A Bayesian Approach," J.R. Statist. Soc. B., vol. 66, no. 3, pp. 751-769, 2004.

8. D. Langewisch, "Uncertainty and Sensitivity Analysis for Long-Running Computer Codes: A Critical Review," MIT CANES, MIT-NSP-TR-024, 2010.

9. R. Cukier, C. Fortuin, K. Shuler, A. Petschek and J. Schaibly, "Study of the Sensitivity of Coupled Reaction Systems to Uncertainties in Rate Coefficients I Theory," The Journal of Chemical Physics, vol. 59, pp. 3873-3878, 2973.

10. R. Cukier, H. Levine and K. Shuler, "Nonlear Sensitivity of Multiparameter Model Systems," Journal of Computational Physics, vol. 26, pp. 1-42, 2978.

11. R. Cukier, J. Schaibly and K. Schuler, "Study of the Sensitivity of Coupled Reaction Systems to Uncertainties in Rate Coefficients, III. Analysis of The Approximations," The Journal of Chemical Physics, vol. 63, pp. 1140-1149, 1975.

12. J. Schaibly and K. Shuler, "Study of the Sensitivity of Coupled Reaction Systems to Uncertainties in Rate Coefficients. II. Applications," Journal of Chemical Physics, vol. 59, pp. 225-239, 1973.

13. O. Osidele and S. Mohanty, "Application of Regionalized Sensitivity Analysis to a Performance Assessment Model of a High-Level Waste Repository," in Proceedings of the International High-Level Radioactive Waste Management Conference, Las Vegas, Nevada, 2006.

14. S. Brooks, A. Gelman, G. Jones and X. Meng, Handbook of Markov Chain Monte Carlo, Chapman & Hall/CRC Press, 2011.

15. C. Davidson-Pilon, "Probabilistic Programming: Bayesian Methods for Hackers," 2015. [Online]. Available: http://camdavidsonpilon.github.io/Probabilistic-Programming-and-Bayesian-Methods-for-Hackers/.

16. W. Wulff, "Uncertainties in Modeling and Scaling in the Prediction of Fuel Stored Energy and Thermal Response," BNL-NUREG-40498.

17. J. N. Reyes and L. Hochreiter, "Scaling analysis for the OSU AP600 test facility (APEX)," Nuclear Engineering and Design, p. Vole. 186 pp 53–109, 1998.

18. C. Rabiti, A. Alfonsi, D. Mandelli, J. Cogliati, R. Kinoshita, "RAVEN, a New Software for Dynamic Risk Analysis," PSAM 12 Probabilistic Safety Assessment and Management, Honolulu, Hawaii, June 2014.

19. C. Rabiti, A. Alfonsi, D. Mandelli, J. Cogliati, R. Martinueau, C. Smith, "Deployment and Overview of RAVEN Capabilities for a Probabilistic Risk Assessment Demo for a PWR Station Blackout," Idaho National Laboratory report: INL/EXT-13-29510 (2013).

20. A. Alfonsi, C. Rabiti, D. Mandelli, J. Cogliati, R. Kinoshita, and A. Naviglio, "RAVEN and dynamic probabilistic risk assessment: Software overview," in Proceedings of ESREL European Safety and Reliability Conference (2014).

21. S. Lee, B. Chung, Y. Bang, S. Bae, "Analysis of uncertainty quantification method by comparing monte-carlo method and Wilks' formula", Nuclear Engineering and Technology, vol. 46, no. 4, pp 481–488, 2014

22. A. Alfonsi, C. Rabiti, D. Mandelli, J. Cogliati, R. Kinoshita, "Hybrid Dynamic Event Tree Sampling Strategy in RAVEN Code"

23. D. Maljovec, S. Liu, B. Wang, D. Mandelli, P. Bremer, V. Pascucci, C. Smith, "Analyzing simulation-based PRA data through traditional and topological clustering: A BWR station blackout case study", Reliability Engineering & System Safety, 2015

24. D. Mandelli, S. Prescott, C. Smith, A. Alfonsi, C. Rabiti, J. Cogliati, R. Kinoshita, "A Flooding Induced Station Blackout Analysis for a Pressurized Water Reactor Using the RISMC Toolkit", Science and Technology of Nuclear Installations, vol. 2015, no. 308163, 2015

25. F. Di Maio, A. Bandini, E. Zio, A. Andrea, C. Rabiti, "An Approach Based on Support Vector Machines and a K-D Tree Search Algorithm for Identification of the Failure Domain and Safest Operating Condition in Nuclear Systems." Submitted to Computer Methods in Applied Mechanics and Engineering, 2015.

26. S. Sen, D. Maljovec, A. Alfonsi, C. Rabiti, "Developing and Implementing the Data Mining Algorithms in RAVEN," Idaho National Laboratory Report: INL-EXT-15-36632, September 2015.

APPENDIX

A-1. Reduced Order Models Description and Equations

The purpose of this work was to develop a first proof of concept of the RIMM IEM. To achieve fast prototyping most of the physical disciplines associated with a realistic Large Break LOCA (LB-LOCA) analysis are approximated by Reduced Order Models (ROMs). In this context, the term Reduce Order Model (ROM) denotes simplified physical models (sometimes referred to as "glass box" models). In the full implementation of the RIMM IEM, the ROMs will be replaced by the corresponding simulators (RELAP, PHYSICS, Fuel Performance code, etc.)

The disciplines involved in a LOCA analysis are:

- Core physics
- Fuel rod thermomechanics
- Clad corrosion
- LOCA thermal-hydraulics

The ROMs will be described in a slightly different order than they were in Section 2. First, the pre-LOCA steady-state calculations will be summarized, followed by the LOCA transient solution. The Fuel Rod Design calculations will be given, then all of the Core Design calculations will be discussed. The order was changed because it simplified the presentation of some of the assumptions and expressions which are shared between the different disciplines.

A-1.1 Steady-State pre-LOCA event

In the following equations the subscript 'o' denotes a steady-state condition. It is important to make this distinction since ultimately the clad temperature will be computed through time.

The steady-state axial temperature profile calculation starts by computing the axial bulk coolant temperature profile. Assuming the bulk coolant is a single-phase incompressible fluid, the steady-state energy balance reduces simply to:

$$T_{b,o}(z) - T_{b,o,IN}(z) = \frac{1}{\left(\dot{m}c_p\right)_o} \int_{z_{IN}}^{z} q'_o(z')\,dz' \tag{2}$$

It is important to note that in Eq. (2), the mass flow rate, $\dot{m}$, corresponds to the mass flow rate around a single pin. Assuming, a uniform flow distribution within the core the average mass flow rate per pin is:

$$\dot{m} = \frac{\dot{m}_{TOT}}{N_{pin}} \tag{3}$$

The linear heat rate axial shape is described is detailed in the description of the core physics ROM. Therefore, the integral in Eq. (2) is redefined in terms of the fraction of the pin power generated up to a particular axial elevation:

$$\int_{z_{IN}}^{z} q'_o(z')dz' \equiv \dot{q}_o \beta(z) \tag{4}$$

The axial bulk coolant temperature profile therefore becomes:

$$T_{b,o}(z) = T_{b,o,IN} + \frac{\dot{q}_o}{\left(\dot{m}c_p\right)_o}\beta(z) \tag{5}$$

Given the coolant temperature and the linear rate as functions of axial elevation, the clad surface temperature is computed using a simple thermal resistance network calculation. The clad surface temperature is:

$$T_{co}(z) = T_b(z) + \frac{q'_o(z)}{\left(2\pi R_{co}\right)h_{b,o}} \tag{6}$$

In Eq. (6), $h_{b,o}$ is the steady-state heat transfer coefficient between the clad surface and the bulk coolant. The heat transfer coefficient is assumed to be constant along the fuel pin.

The steady-state pin weighted average temperature is very important because it is related to the stored energy within the pin at the start of the LOCA. The pin weighted average temperature is computed relative to the clad surface temperature with a thermal resistance network. The resistance between the two temperatures is expressed as an "effective thermal conductivity" following the Catton et al.'s (2009) FSA work. The pin weighted average effective thermal conductivity expression is:

$$\frac{1}{\overline{K}_{pin}(z)} = \frac{1}{\{\rho c\}_{pin}} \sum_{i=f,c} \left(\frac{a\rho c}{\overline{K}(z)} \right)_i \tag{7}$$

Equation (7) is a weighted average between the effective thermal conductivities of the average fuel, $\overline{K}_f(z)$, and average clad, $\overline{K}_c(z)$. These effective thermal conductivities are weighted by the fuel and clad volumetric heat capacities with respect to the pin cross-sectional area weighted average volumetric heat capacity. The area fractions are defined as:

$$a_f = \frac{A_f}{A_{pin}}, \qquad a_c = \frac{A_c}{A_{pin}} \tag{8}$$

Where the effective pin cross sectional area is simply the sum of the fuel and clad cross-sectional areas:

$$A_{pin} = A_f + A_c \tag{9}$$

The cross sectional area of the gap between the pellet and the clad is neglected. The pin weighted average volumetric heat capacity is:

$$\{\rho c\}_{pin} = \sum_{i=f,c} \left(a\rho c\right)_i \tag{10}$$

The average fuel and average clad effective thermal conductivities relate the average fuel and average clad temperatures to the clad surface temperature. Following Catton et al. (2009), these are written in the following format:

$$\frac{1}{\overline{K}_i(z)} = \frac{C_i(z)}{8\pi\overline{k}_f(z)}, \qquad i = f,c \tag{11}$$

The fuel thermal conductivity is assumed constant over the fuel pellet and is computed in the Fuel Rod Design (FRD) ROM. The resistance parameters, $C_i(z)$, capture the radial temperature profile through the fuel pin. The resistance parameter between the average fuel temperature and clad surface temperature is:

$$C_f(z) = 1 + \frac{4\bar{k}_f(z)}{R_{gap} h_{gap}} + \frac{4\bar{k}_f(z)}{k_c(z)} \log\left[\frac{R_{co}}{R_{ci}}\right] \tag{12}$$

The resistance parameter between the average clad temperature and the clad surface temperature is:

$$C_c(z) = \frac{4\bar{k}_f(z)}{k_c(z)}\left(\frac{1}{2} - \left(\frac{R_{ci}^2}{R_{co}^2 - R_{ci}^2}\right)\log\left[\frac{R_{co}}{R_{ci}}\right]\right) \tag{13}$$

Using these definitions, the pin weighted average temperature is computed as:

$$\{T\}_o(z) = T_{co,o}(z) + \frac{q'_o(z)}{\bar{K}_{pin}(z)} \tag{14}$$

The brackets around the temperature in Eq. (14) denote that the pin weighted average temperature is an area averaged quantity. The average fuel and average clad effective thermal conductivities can be used to compute the average fuel and average clad temperatures in similar fashion:

$$\{T\}_{f,o}(z) = T_{co,o}(z) + \frac{q'_o(z)}{\bar{K}_f(z)} \tag{15}$$

$$\{T\}_{c,o}(z) = T_{co,o}(z) + \frac{q'_o(z)}{\bar{K}_c(z)} \tag{16}$$

Equations (14)-(16) allow any of the area averaged temperatures to be related to each other.

A-1.2 LOCA event

The clad surface temperature transient calculation is divided into the traditional LB-LOCA phases:

- Blowdown heatup
- Blowdown cooling
- Refill heatup
- Reflood

Here the blowdown heatup is further divided in two sub-phases, e.g.:

- (Initial) rapid blowdown heatup
- gradual blowdown heatup

Each phase uses different assumptions and approximations in order to estimate the clad surface temperature through time. Due to the large number of equations, important equations are highlighted.

The blowdown heatup phase was broken into two sub-phases, an initial rapid temperature rise followed by a much more gradual increase in the temperature. This approach was chosen to reflect that very early on in the transient (less than ~5 seconds), the temperature rise is dominated by the stored-energy release and the subsequent temperature redistribution within the fuel pin. After this, the clad surface temperature evolves in a more complex fashion because of the interaction of the stored-energy release, decay heat generation, and complex flow field dynamics which impact the convective cooling on the surface of the fuel pin. Approximating

this behavior was beyond the scope of this ROM. Therefore, the gradual heatup is an attempt to represent a time averaged temperature increase over this portion of the transient.

In each blowdown sub-phase, the clad surface temperature response is approximated with a linear trend. The initial and final points in time and temperature values must therefore be known in order to determine the slope of the linear trend.

A double-lumped parameter model for the fuel pin response was used to help determine the slope during this subphase. The double lumped parameter model represents the fuel pin response by linking together the response of the average fuel and average clad temperatures through time. Assuming the fuel volumetric heat capacity is constant over the cross-sectional area of fuel pellet, the time rate of change of the average fuel temperature is:

$$A_f\left(\rho c\right)_f \frac{d}{dt}\left(\left\{T\right\}_f(z,t)\right) = q'_D(z,t) - q'_g(z,t) \tag{17}$$

Again, the brackets in Eq. (17) are used to denote the temperature is an area averaged quantity. The RHS of Eq. (17) denotes the balance between the (linear) decay heat generation and the (linear) heat transfer rate through the gap. The analogous expression for the average clad temperature response is the time rate of change of the average clad temperature:

$$A_c\left(\rho c\right)_c \frac{d}{dt}\left(\left\{T\right\}_c(z,t)\right) = q'_g(z,t) - q'_b(z,t) \tag{18}$$

The second term on the RHS of Eq. (18) is the (linear) heat transfer rate between the clad surface and the bulk coolant. Summing Eqs. (17) and (18) yields that the time rate of the change of the pin weighted average temperature is equal to the balance of the (linear) heat generation rate and the (linear) heat transfer to the coolant.

The LHS of (18) is then rewritten as:

$$A_{pin}\left\{\rho c\right\}_{pin} \frac{d}{dt}\left(\left\{T\right\}(z,t)\right) \equiv A_f\left(\rho c\right)_f \frac{d}{dt}\left(\left\{T\right\}_f(z,t)\right) + A_c\left(\rho c\right)_c \frac{d}{dt}\left(\left\{T\right\}_c(z,t)\right) \tag{19}$$

Thus

$$A_{pin}\left\{\rho c\right\}_{pin} \frac{d}{dt}\left(\left\{T\right\}(z,t)\right) = q'_D(z,t) - q'_b(z,t) \tag{20}$$

The decay heat generation is assumed to have the same axial shape as the steady-state linear heat rate axial profile. The decay heat generation trend through time is a simple approximate decay heat fraction relative to the steady-state value:

$$f(t) = 0.066t^{-0.2} \tag{21}$$

The (linear) decay heat generation expression as a function of axial elevation and time is therefore:

$$q'_D(z,t) = q'_o(z)f(t) \tag{22}$$

The (linear) heat transfer rate through the gap is represented as the thermal resistance network between the average fuel and clad temperatures:

$$q'_g(z,t) = \overline{K}_g(z)\left(\left\{T\right\}_f(z,t) - \left\{T\right\}_c(z,t)\right) \tag{23}$$

The effective thermal conductivity through the gap, $\overline{K}_g(z)$, is assumed to be constant during the transient and equal to its steady-state value. The effective thermal conductivity through the gap is related to the average fuel and average clad effective thermal conductivities via:

$$\frac{1}{\overline{K}_g(z)} = \frac{1}{\overline{K}_f(z)} + \frac{1}{\overline{K}_c(z)} \tag{24}$$

The (linear) heat transfer rate between the clad surface and the bulk coolant is also represented with a simple thermal resistance network:

$$q'_b(z,t) = \left(2\pi R_{co}\right) h_b(z,t)\left(T_{co}(z,t) - T_b(z,t)\right) \tag{25}$$

Equation (25) is rewritten in terms of the average clad temperature by substituting Eq. (6) for $T_{co}(z,t)$ in Eq. (25). Re-arranging yields:

$$q'_b(z,t) = \overline{K}_{c,b}(z,t)\left(\{T\}_c(z,t) - T_b(z,t)\right) \tag{26}$$

Where the effective thermal conductivity between the average clad and bulk coolant temperature is:

$$\frac{1}{\overline{K}_{c,b}(z,t)} = \frac{1}{\overline{K}_c(z)} + \frac{1}{\left(2\pi R_{co}\right) h_b(z,t)} \tag{27}$$

The double-lumped parameter fuel pin system of equations are then:

$$A_f\left(\rho c\right)_f \frac{d}{dt}\left(\{T\}_f(z,t)\right) = q'_o(z) f(t) - \overline{K}_g(z)\left(\{T\}_f(z,t) - \{T\}_c(z,t)\right) \tag{28}$$

$$A_c\left(\rho c\right)_c \frac{d}{dt}\left(\{T\}_c(z,t)\right) = \overline{K}_g(z)\left(\{T\}_f(z,t) - \{T\}_c(z,t)\right) - \overline{K}_{c,b}(z,t)\left(\{T\}_c(z,t) - T_b(z,t)\right) \tag{29}$$

Instead of substituting in the steady-state linear heat rate expression into Eq. (28), the decay heat generation term will be related to the steady-state temperature drop through the pin by plugging Eq. (14) into Eq. (28). The average fuel temperature time rate of change is then:

$$\begin{aligned} A_f\left(\rho c\right)_f \frac{d}{dt}\left(\{T\}_f(z,t)\right) = {} & \overline{K}_{pin}(z)\left(\{T\}_o(z) - T_{co,o}(z)\right) f(t) \\ & - \overline{K}_g(z)\left(\{T\}_f(z,t) - \{T\}_c(z,t)\right) \end{aligned} \tag{30}$$

The double-lumped parameter equations can be normalized following the normalization in Catton et al. (2009) by dividing Eqs. (29) and (30) with the steady-state pin weighted average temperature difference. The following normalized average fuel temperature difference:

$$\{\theta\}_f(z,t) = \frac{\{T\}_f(z,t) - T_{co,o}(z)}{\{T\}(z,t) - T_{co,o}(z)} \tag{31}$$

The normalized average clad temperature difference:

$$\{\theta\}_c(z,t) = \frac{\{T\}_c(z,t) - T_{co,o}(z)}{\{T\}(z,t) - T_{co,o}(z)} \tag{32}$$

The normalized bulk coolant temperature difference:

$$\theta_b(z,t) = \frac{T_b(z,t) - T_{co,o}(z)}{\{T\}(z,t) - T_{co,o}(z)} \tag{33}$$

The normalized clad surface temperature difference:

$$\theta_{co}(z,t) = \frac{T_{co}(z,t) - T_{co,o}(z)}{\{T\}(z,t) - T_{co,o}(z)} \tag{34}$$

And the normalized pin weighted average temperature difference:

$$\{\theta\}(z,t) = \frac{\{T\}(z,t) - T_{co,o}(z)}{\{T\}(z,t) - T_{co,o}(z)} \tag{35}$$

One of the benefits with this choice of normalization is that at steady-state, the normalized pin weighted average temperature value is 1 while the normalized clad surface temperature is 0. Additionally, the steady-state values for the other normalized temperature differences are only functions of the fuel pin heat transfer properties. The steady-state normalized bulk coolant temperature is the negative of the inverse of the effective pin Biot number:

$$\theta_{b,o}(z) = \frac{T_{b,o}(z,t) - T_{co,o}(z)}{\{T\}(z,t) - T_{co,o}(z)} = \frac{-q'_o(z) / \left(2\pi R_{co}\right) h_{b,o}}{q'_o(z) / \bar{K}_{pin}(z)} = -\frac{\bar{K}_{pin}(z)}{\left(2\pi R_{co}\right) h_{b,o}} \triangleq -\frac{1}{N_{Bi,o}(z)} \tag{36}$$

The steady-state normalized average fuel temperature is the ratio of the pin effective thermal conductivity to the average fuel effective thermal conductivity:

$$\{\theta\}_{f,o}(z) = \frac{\{T\}_{f,o}(z) - T_{co,o}(z)}{\{T\}(z,t) - T_{co,o}(z)} = \frac{\bar{K}_{pin}(z)}{\bar{K}_f(z)} \tag{37}$$

Similarly, the steady-state normalized average clad temperature is the ratio of the pin effective thermal conductivity to the average clad effective thermal conductivity:

$$\{\theta\}_{c,o}(z) = \frac{\{T\}_{c,o}(z) - T_{co,o}(z)}{\{T\}(z,t) - T_{co,o}(z)} = \frac{\bar{K}_{pin}(z)}{\bar{K}_c(z)} \tag{38}$$

Using these definitions, the normalized average fuel time rate of change is:

$$\frac{d}{dt}\left(\{\theta\}_f(z,t)\right) = \frac{\bar{K}_{pin}(z)}{A_f\left(\rho c\right)_f} f(t) - \frac{\bar{K}_g(z)}{A_f\left(\rho c\right)_f}\left(\{\theta\}_f(z,t) - \{\theta\}_c(z,t)\right) \tag{39}$$

Before writing the normalized average clad time rate of change, a few more definitions will be given to simplify notation. First, define the clad effective Biot number:

$$N_{Bi,c}(z,t) = \frac{\left(2\pi R_{co}\right) h_b(z,t)}{\bar{K}_c(z)} \tag{40}$$

Then rewrite the effective thermal conductivity between the average clad and bulk coolant temperature in terms of the pin effective thermal conductivity and the clad effective Biot number:

$$\bar{K}_{c,b}(z,t) = \bar{K}_{pin}(z,t) \frac{N_{Bi}(z,t)}{N_{Bi,c}(z,t)+1} \tag{41}$$

Substitute Eq. (41) into Eq. (29) along with the definitions for the normalized temperature differences to yield the normalized average clad temperature time rate of change:

$$\begin{aligned} \frac{d}{dt}\left(\{\theta\}_c(z,t)\right) = & \frac{\bar{K}_g(z)}{A_c\left(\rho c\right)_c}\left(\{\theta\}_f(z,t) - \{\theta\}_c(z,t)\right) \\ & - \frac{\bar{K}_{pin}(z)}{A_c\left(\rho c\right)_c}\left(\frac{N_{Bi}(z,t)}{N_{Bi,c}(z,t)+1}\right)\left(\{\theta\}_c(z,t) - \theta_b(z,t)\right) \end{aligned} \tag{42}$$

The double-lumped parameter model ODEs given in Eqs. (39) and (41) were integrated with a simple Forward Euler time integrator. The time integrator was setup to allow different combinations of $\bar{K}_f(z)$, $\bar{K}_c(z)$, and $h_b(z,t)$ to be experimented with. The results were consistent with the double-lumped parameter model given in Wulff's BNL Report, which showed the initial rapid heatup peak occurring in less than 5 seconds. After numerous runs, it was observed that the rapid heatup peak occurred roughly when the normalized average fuel temperature equaled the initial normalized pin weighted average temperature. Due to the normalization described earlier, this corresponds to when the normalized fuel average temperature equals 1.

The condition to estimate the time to reach the initial rapid heatup peak is therefore:

$$t = t_I^*: \quad \{\theta\}_f(z,t_I^*) \approx \{\theta\}_o(z) = 1 \tag{43}$$

In order to derive an analytic expression for the time to reach the initial rapid heatup peak, Eq. (39) was integrated from $t = 0$ to $t = t_I^*$:

$$\{\theta\}_f(z,t_I^*) - \{\theta\}_{f,o}(z) = \frac{\bar{K}_{pin}(z)}{A_f\left(\rho c\right)} \int_{t=0}^{t_I^*} f(t)\,dt - \frac{\bar{K}_g(z)}{A_f\left(\rho c\right)} \int_{t=0}^{t_I^*} \left(\{\theta\}_f(z,t) - \{\theta\}_c(z,t)\right) dt \tag{44}$$

The first integral on the RHS of Eq. (44) can be evaluated analytically. However, the resulting expression has time raised to a power. To allow an analytic result for t_I^*, this integral will also be approximated by a linear trend:

$$\int_{t=0}^{t_I^*} f(t)\,dt = \frac{0.066}{0.8}\left(t_I^*\right)^{0.8} \triangleq F(t_I^*, t_o) \approx F_s t_I^* + F_o \tag{45}$$

The parameters, F_S and F_o, are determined using a best-fit line over a desired time interval from the actual integral of the decay heat fraction.

The second integral on the RHS of Eq. (44) is the integral of the (linear) heat transfer rate through the gap. In general, this integral is analytical intractable. However, since both the average fuel and average clad temperatures are approximated with linear relationships, this integral can be easily evaluated. The normalized average fuel temperature linear trend within this sub-phase is:

$$\{\theta\}_f(z,t) = \{\theta\}_{f,o}(z) + m_{f1}t \tag{46}$$

The slope is simply the change in the normalized fuel average temperature over the time interval:

$$m_{f1} = \frac{\{\theta\}_f(z,t_I^*) - \{\theta\}_{f,o}(z)}{t_I^*} \tag{47}$$

Since the value of the normalized average fuel temperature is assumed known and equal to one, the slope is completely determined by estimating the time to reach the initial rapid heatup peak.

The linear trend in the normalized average clad temperature is:

$$\{\theta\}_c(z,t) = \{\theta\}_{c,o}(z) + m_{c1}t \tag{48}$$

The slope in the normalized average clad temperature is:

$$m_{c1} = \frac{\{\theta\}_c(z,t_I^*) - \{\theta\}_{c,o}(z)}{t_I^*} \tag{49}$$

The initial rapid heatup peak value for the normalized average clad temperature is assumed to be equal to a fraction of the Catton CSAU estimated clad temperature blowdown rise. This approximation assumes that the average clad temperature is roughly equal to the clad surface temperature at t_I^*. Since the steady-state clad effective Biot number is already less than 1, the reduced heat transfer coefficient during the first few seconds of the LOCA would yield a clad effective Biot number less than 0.1, justifying this assumption. Denoting the time to reach the blowdown peak as t^*, and the normalized CSAU estimated blowdown peak as $\Theta^*_{CSAU}(z)$, the average clad temperature at the initial rapid heatup peak is:

$$\{\theta\}_c(z,t_I^*) = \gamma^*_{BD}\{\theta\}_c(z,t_I^*) \approx \gamma^*_{BD}\Theta^*_{CSAU}(z) \tag{50}$$

The expression for the normalized CSAU estimated blowdown peak, $\Theta^*_{CSAU}(z)$, is described in Eq. (59). **The multiplier on the CSAU estimated blowdown peak, γ^*_{BD}, is assumed to be equal to 0.75**.

Using the linear trends through time, the integral for the heat transfer rate through the gap simply becomes:

$$\int_{t=0}^{t_I^*} \left(\{\theta\}_f(z,t) - \{\theta\}_c(z,t)\right) dt \approx \left(\overline{\{\theta\}}_f(z) - \overline{\{\theta\}}_c(z)\right) t_I^* \tag{51}$$

The normalized temperatures on the RHS of Eq. (51) are simply the average normalized temperature values over the time period of interest:

$$\overline{\{\theta\}}_f(z) = \frac{1}{2}\left(\{\theta\}_f(z,t_I^*) + \{\theta\}_{f,o}(z)\right)$$
$$\overline{\{\theta\}}_c(z) = \frac{1}{2}\left(\{\theta\}_c(z,t_I^*) + \{\theta\}_{c,o}(z)\right) \tag{52}$$

Using Eqs. (45) and (51) allows rewriting Eq. (44) as:

$$\{\theta\}_f(z,t_I^*) - \{\theta\}_{f,o}(z) \approx \frac{\overline{K}_{pin}(z)}{A_f(\rho c)}\left[F_s t_I^* + F_o\right] - \frac{\overline{K}_g(z)}{A_f(\rho c)}\left[\left(\overline{\{\theta\}}_f(z) - \overline{\{\theta\}}_c(z)\right)t_I^*\right] \tag{53}$$

Solving Eq. (53) for t_I^* gives the expression for the time to reach the initial rapid heatup peak to be:

$$t_I^* \approx \frac{A_f(\rho c)_f\left(\{\theta\}_f(z,t_I^*) - \{\theta\}_{f,o}(z)\right) - F_o\overline{K}_{pin}(z)}{\overline{K}_{pin}(z)F_s - \overline{K}_g(z)\left(\overline{\{\theta\}}_f(z) - \overline{\{\theta\}}_c(z)\right)} \tag{54}$$

With t_I^* known, the slope in the clad surface temperature is known. In normalized terms, during the initial rapid heatup subphase, the clad surface temperature response is simply:

$$\theta_{co}(z,t) = \left(\frac{\gamma_{BD}^*\Theta_{CSAU}^*(z)}{t_I^*}\right)t, \qquad t < t_I^* \tag{55}$$

The slope in Eq. (55) applies the assumption on the value of the clad surface temperature at t_I^* given in Eq. (50).

After the initial rapid heatup, the clad temperature is assumed to increase linearly up to the CSAU estimated blowdown temperature peak. This section describes how the CSAU estimated blowdown peak is computed as well as how the time to reach the blowdown peak is computed. Catton et al. (1990) provides a simple relationship between the blowdown temperature rise and the linear heat rate:

$$\Delta\hat{T} = aq' \tag{56}$$

It is important to note though that this expression uses units of [kW/ft] for the linear heat rate and [^{o}F] for the temperature rise. Equation (56) is modified to be consistent with the SI units used throughout the LB-LOCA ROM, to allow using a linear heat rate. The modified CSAU expression is:

$$\Delta T_{CSAU}^*(z) = \xi_a aq'(z) \tag{57}$$

Where ξ_a is the appropriate conversion factor equal to:

$$\xi_a = \frac{5/9}{1000 \cdot 3.3} \tag{58}$$

Because the CSAU temperature rise is defined as the difference between the blowdown peak with the initial steady-state value, the normalized CSAU temperature rise is computed by simply dividing Eq. (57) with the normalizing factor:

$$\Theta_{CSAU}^*(z) = \frac{T_{co}^*(z) - T_{co,o}(z)}{\{T\}_o(z) - T_{co,o}(z)} = \frac{\Delta T_{CSAU}^*(z)}{\{T\}_o(z) - T_{co,o}(z)} \tag{59}$$

The time to reach the blowdown peak is assumed to occur at the average between the time to finish blowdown and the time to reach the initial rapid heatup peak:

$$t^* = \frac{1}{2}\left(t_I^* + t_{BD,end}\right) \tag{60}$$

One of the benefits of this approach is that the parameters that impact the time to complete blowdown will impact the time to reach the blowdown peak. This represents that the depressurization phenomena which impact the flow dynamics through the primary system during the LB-LOCA also impact the blowdown peak. The time to complete blowdown is described in detail later on.

The normalized clad surface temperature during this sub-phase is:

$$\theta_{co}(z,t) = \gamma_{BD}^* \Theta_{CSAU}^*(z) + \left(\frac{\Theta_{CSAU}^*(z)\left(1-\gamma_{BD}^*\right)}{t^* - t_I^*}\right)\left(t - t_I^*\right) \tag{61}$$

The clad temperature response during the blowdown cooling phase is also assumed to have a linear trend through time. As with the linear trends during the blowdown heatup phase, the slope requires estimating the temperature at the end of blowdown as well as the time to reach the end of blowdown.

As given in Catton et al. (1990), the blowdown cooling ratio is defined as (using Catton's notation):

$$\frac{\hat{T} - \overline{T}_s}{\breve{T} - \overline{T}_s} = 1.09 + 0.9m\left(\breve{t} - \hat{t}\right) \tag{62}$$

In Eq. (62), $\overline{T}_s$ is the average coolant saturation temperature during the blowdown cooling phase and the coefficient *m* depends on the average heat transfer coefficient during the blowdown cooling phase. The clad temperature at the end of blowdown is represented by $\breve{T}$, while $\breve{t}$ is the time at the end of blowdown and $\hat{t}$ is the time at the blowdown peak.

Equation (62) was generalized by treating values 1.09 and 0.9 as uncertain inputs which will be sampled. The two inputs will be denoted by ξ_{C1} and ξ_{C2}, i.e.:

$$\frac{\hat{T} - \overline{T}_s}{\breve{T} - \overline{T}_s} = \xi_{C1} + \xi_{C2} m\left(\breve{t} - \hat{t}\right) \tag{63}$$

The coefficient *m* is written in terms of the average heat transfer coefficient as:

$$m = \frac{2\pi R_{co}}{A_{pin}\left\{\rho c\right\}_{pin}} \int_{t^*}^{t_{BD,end}} h_b(z,t)dt = \frac{2\pi R_{co}}{A_{pin}\left\{\rho c\right\}_{pin}} \overline{h}_{b,C}(z) \tag{64}$$

Keeping with the notation used throughout this report, the average coolant saturation temperature will be denoted as $\overline{T}_b$. Then, using the definitions for the normalized temperature differences given in Eqs. (33) and (34) , the normalized CSAU blowdown cooling ratio is:

$$\breve{\Theta}_{CSAU,R} \approx \frac{\theta_{co}(z,t^*) - \overline{\theta}_b(z)}{\theta_{co}(z,t_{BD,end}) - \overline{\theta}_b(z)} = \xi_{C1} + \xi_{C2}\frac{\left(2\pi R_{co}\right)\overline{h}_{b,C}(z)}{A_{pin}\left\{\rho c\right\}}\left(t_{BD,end} - t^*\right) \tag{65}$$

Rearranging and substituting in the fact that at the blowdown peak, $\theta_{co}(z,t^*) = \Theta^*_{CSAU}(z)$, the normalized clad surface temperature at the end of blowdown is:

$$\theta_{co}(z,t_{BD,end}) = \overline{\theta}_b(z) + \frac{\Theta^*_{CSAU}(z) - \overline{\theta}_b(z)}{\breve{\Theta}_{CSAU,R}} \tag{66}$$

The average coolant saturation temperature during the blowdown cooling phase is estimated to be equal to the average between the primary system steady-state average temperature and the saturation temperature at the end of blowdown:

$$\overline{T}_b(z) \approx \frac{1}{2}\left[T_{AVG,o} + T_{sat}\left(P\left(t_{BD,end}\right)\right)\right] \tag{67}$$

The pressure at the end of blowdown, $P(t_{BD,end})$, is an uncertain input to the LB-LOCA ROM.

The average heat transfer coefficient during the blowdown cooling phase is estimated by multiplying the average heat transfer coefficient over the initial rapid heatup sub-phase with a constant multiplier. The multiplier, γ_{hb}, is an uncertain input to the LB-LOCA ROM. The average heat transfer coefficient during the blowdown cooling phase is assumed to be constant along the pin and is therefore equal to:

$$\overline{h}_{b,C}(z) = \overline{h}_{b,C} = \gamma_{hb}\overline{h}_{b,I} \tag{68}$$

The time to reach the end of blowdown, $t_{BD,end}$, is estimated by determining the characteristic "process time" for the blowdown. That "process time" is approximated by the inverse of the maximum Fractional Rate of Change (FRC) that governs the system depressurization rate, which corresponds to the energy flow out the break:

$$t_{BD,end} \propto \frac{1}{\omega_{FRC,out,o}} \tag{69}$$

The term $\omega_{FRC,out,o}$ is the FRC for the energy flow out the break evaluated at a particular reference condition. It can be shown that the inverse of the maximum FRC is equal to the product of the system residence time and fluid dilation as defined in Reyes and Hochreiter (1998):

$$\frac{1}{\omega_{FRC,out,o}} = \tau_{SYS}\epsilon_o \tag{70}$$

where:

$$\tau_{SYS} = \frac{M_o}{C_d A_B G_{out,o}}, \qquad \epsilon_o = \frac{P_o\left(\frac{\partial e}{\partial P}\right)_{v,o}}{\left[h_{out} - e + v\left(\frac{\partial e}{\partial v}\right)_P\right]_o} \tag{71}$$

The system residence time, τ_{SYS}, is therefore just the reference system mass divided by the reference break mass flow rate. The reference break mass flow rate is written in terms of the break discharge coefficient, C_d, the break area, A_B, and the reference mass flux out the break, $G_{out,o}$. The fluid dilation, ϵ_o, relates how quickly the system pressure responds to an agent-of-change.

To provide an analytic expression for the blowdown time, the reference break flow is modeled as critical flow of single phase vapor. The single phase vapor is assumed to behave as an ideal gas. Because of this assumption, the fluid dilation reduces to the inverse of the ratio of specific heats:

$$\epsilon_o \approx \frac{c_v}{c_p} = \frac{1}{\gamma} \tag{72}$$

The critical mass flux for an ideal gas is given by:

$$G_c = \left[\gamma \frac{P^2}{RT} \left(\frac{2}{\gamma+1} \right)^{\frac{\gamma+1}{\gamma-1}} \right]^{\frac{1}{2}} \tag{73}$$

In Eq. (73), R is the specific gas constant. The reference temperature is assumed to be equal to the steady-state hot leg temperature, T_H, and the reference pressure is equal to the saturation pressure at T_H.

Assuming the reference break flow is that for an ideal gas is a gross over simplification of the complex two-phase critical flow phenomena. For those reasons, a tuning parameter, c_{BD}, was introduced so that the blowdown time would occur between roughly 25 and 40 seconds. The blowdown time expression is therefore:

$$t_{BD,end} = c_{BD} \frac{M_o}{C_d A_B G_{out,o}} \epsilon_o \tag{74}$$

Comparing Eq. (74) to the expression for the blowdown time in Catton et al. (1990) (Eq. (22)), the CSAU coefficient c_1 can be seen to be equivalent to:

$$c_1 = \frac{c_{BD}}{C_d} \frac{\epsilon_o}{G_{out,o}} \tag{75}$$

The blowdown time expression is therefore identical to that given in Catton et al. (1990):

$$\boldsymbol{t_{BD,end} = c_1 \left(\frac{M_o}{A_B} \right)} \tag{76}$$

The clad surface temperature response during refill is estimated by assuming the fuel pin heats up adiabatically. Assuming there is only a slight variation in the temperature within the pin at this point in the transient, the clad surface temperature is approximately equal to the pin weighted average temperature. The normalized clad surface temperature time rate of change is therefore:

$$\frac{d}{dt}\left(\{\theta\}(z,t) \right) \approx \frac{d}{dt}\left(\theta_{co}(z,t) \right) \approx \frac{\bar{K}_{pin}(z)}{A_{\text{pin}} \{\rho c\}_{pin}} f(t) \tag{77}$$

Integrating Eq. (77) from the blowdown time up to an arbitrary time during refill gives:

$$\theta_{co}(z,t) \approx \theta_{co}(z,t_{BD,end}) + \left(\frac{\bar{K}_{pin}(z)}{A_{pin} \{\rho c\}_{pin}} \right) \left[\int_{t_{BD,end}}^{t} f(t')dt' \right] \tag{78}$$

The term in parenthesis before the integral of the decay heat fraction is defined by Catton et al. (2009) as the decay heat FRC:

$$\omega_{D,o}(z) = \frac{\bar{K}_{pin}(z)}{A_{pin}\left\{\rho c\right\}_{pin}} \tag{79}$$

The refill heatup rate as a function of time however was modified using the CSAU refill heatup estimate. This was done in case the adiabatic heatup rate is a poor assumption. A correction factor was computed by comparing the temperature at the end refill from the Catton et al. (1990) CSAU expression with that estimated from Eq. (78). The CSAU normalized temperature at the end of refill is:

$$\Theta_{CSAU}^{FILL}(z) = \frac{\Delta T_{CSAU}^{FILL}}{\left\{T\right\}_o(z) - T_{co,o}(z)} = \frac{1}{\left\{T\right\}_o(z) - T_{co,o}(z)}\left(\frac{dT}{dt}\right)_{FILL}\left(t_{FILL} - t_{BD,end}\right) \tag{80}$$

The CSAU refill heatup rate, $(dT/dt)_{FILL}$, is an uncertain input to the LB-LOCA ROM. The correction factor is equal to:

$$\boldsymbol{\Gamma_{FILL}} = \frac{\boldsymbol{\Theta_{CSAU}^{FILL}(z)}}{\boldsymbol{\omega_{D,o}(z)}\left[\int_{t_{BD,end}}^{t_{FILL}} \boldsymbol{f(t)\,dt}\right]} \tag{81}$$

The "corrected" normalized clad surface temperature during refill is then:

$$\theta_{co}(z,t) \approx \theta_{co}(z,t_{BD,end}) + \Gamma_{FILL}\omega_{D,o}(z)\left[\int_{t_{BD,end}}^{t} f(t')dt'\right] \tag{82}$$

The refill duration is estimated by assuming an average accumulator injection rate over the refill phase. The accumulator flow rate that penetrates into the lower plenum depends on the assumed bypass ratio, η_{bypass}, which is an uncertain input to the LB-LOCA ROM. Defining the lower plenum volume (which is assumed to be completely empty at the end of blowdown) as V_{LP}, the average accumulator injection mass flow rate as, $\dot{m}_{ACC}$ and the accumulator liquid density as ρ_{ACC}, the refill duration is:

$$t_{FILL} - t_{BD,end} = \frac{V_{LP}\rho_{ACC}}{\dot{m}_{ACC}\left(1 - \eta_{bypass}\right)} \tag{83}$$

During reflood, the clad surface temperature is assumed to follow a parabolic trend from the end of refill to the quench time. This shape was chosen because it seems to approximate the general trend observed in reflood experiments and plant simulated clad surface temperature.

Additionally, by assuming a parametric form on the clad surface temperature itself, the heat transfer coefficient time history during reflood did not need to be approximated. The parabolic shape is defined between the time at the end of refill, t_{FILL}, and the time the quench front reaches a particular axial elevation, $t_q(z)$. The parabola therefore depends on the axial elevation. After the quench front reaches a particular axial elevation, that location is assumed to have a clad temperature equal to the saturation temperature.

The surface temperature response is:

$$T_{co}(z,t)=\begin{cases} a_R(z)t^2+b_R(z)t+c_R(z), & t\le t_q(z) \\ T_{sat}\left(P(t_{BD,end})\right), & t>t_q(z) \end{cases} \tag{84}$$

In order to determine the three unknown coefficients, three pairs of times and temperatures need to be specified. The first is the clad surface temperature at the end of refill, $(t_{FILL}, T_{co}(z,t_{FILL}))$. The clad surface temperature at the end of refill is known. The second is the clad surface temperature at the time when the quench front reaches that particular axial elevation, $\left(t_q(z), T_{co}(z,t_q(z))\right)$. The time it takes the quench front to reach a particular axial elevation depends on the quench front velocity which is described later. The third point is denoted as the reflood-quarter time and quarter time temperature, $\left(t_{1/4}(z), T_{co}(z,t_{1/4}(z))\right)$.

The reflood-quarter time is defined as:

$$t_{1/4}(z)=\frac{1}{4}\left(t_q(z)-t_{FILL}\right)+t_{FILL} \tag{85}$$

The reflood-quarter time temperature is assumed to be equal to the modified CSAU reflood temperature rise. The choice that the CSAU reflood temperature rise is reached within the first 25% of reflood time period is quite arbitrary but judged adequate for the purpose of the ROM.

In Catton et al. (1990) the CSAU reflood temperature rise corresponds to the maximum clad surface temperature during reflood. Here though, a parabola is fit between these three specified points and thus the quarter-reflood temperature may or may not correspond to the reflood temperature peak. To simplify the notation, the quarter-reflood temperature is denoted as $T_{co}^{1/4}(z)$. The clad surface temperature at the end of refill is also shortened to $T_{co}^{FILL}(z)$.

The quarter-reflood temperature was assumed to impact $T_{co}(z,t_q(z))$. If the quarter-reflood temperature, at a particular elevation, is less than the assumed quench temperature, T_Q, then $T_{co}(z,t_q(z))$ is assumed equal to the coolant saturation temperature rather than the quench temperature. This can impact an axial elevation with a very low linear heat rate. The clad surface temperature at $t_q(z)$ is written as:

$$T_Q^*(z)=\begin{cases} T_Q, & \text{if} \quad T_{co}^{1/4}(z)\ge T_Q \\ T_{sat}\left(P(t_{BD,end})\right), & \text{if} \quad T_{co}^{1/4}(z)<T_Q \end{cases} \tag{86}$$

Using these definitions, the parabolic coefficients in Eq. (84) can be solved for. Their expressions are:

$$a_R(z)=\frac{T_Q^*(z)-T_{co}^{1/4}(z)}{\left(t_q(z)-t_{1/4}\right)\left(t_{1/4}-t_{FILL}\right)}-\frac{T_{co}^{FILL}(z)-T_Q^*(z)}{\left(t_{FILL}-t_q(z)\right)\left(t_{1/4}-t_{FILL}\right)} \tag{87}$$

$$b_R(z)=\frac{T_{co}^{FILL}(z)-T_Q^*(z)}{t_{FILL}-t_q(z)}-a_R(z)\left(t_{FILL}+t_q(z)\right) \tag{88}$$

$$c_R(z)=T_{co}^{1/4}(z)-\left(\frac{t_{1/4}}{t_{FILL}-t_q(z)}\right)\left(T_{co}^{FILL}(z)-T_Q^*(z)\right)-a_R(z)t_{1/4}\left(t_{1/4}-t_{FILL}-t_q(z)\right) \tag{89}$$

The reflood-quarter time temperature is estimated by modifying the CSAU reflood temperature rise expression. The CSAU reflood temperature rise is scaled at a particular axial elevation by the fraction of power generated up to that elevation with respect to the power generated up to the peak linear heat rate elevation. For

all elevations above the peak linear heat rate location, the full CSAU reflood temperature rise is assumed. The quarter-reflood temperature rise is therefore defined as:

$$\Delta T_{rise}^{1/4}(z) = \begin{cases} \Delta T_{CSAU}^{*R} \dfrac{\beta(z)}{\beta(z_M)}, & z < z_M \\ \Delta T_{CSAU}^{*R}, & z \geq z_M \end{cases} \tag{90}$$

In Eq. (90) z_M is the axial elevation for the peak linear heat rate and $\beta(z)$ is defined in Eq. (4).

The CSAU reflood temperature rise is related to the cold-reflood rate, U_R, and is equal to:

$$\Delta T_{CSAU}^{*R} = \frac{5}{9} K U_R^{-n} \tag{91}$$

The coefficient, *K*, and exponent, *n*, are uncertain input parameters to the LB-LOCA ROM.

The cold reflood rate is estimated based on the assumed ECCS safety injection (SI) mass flow rate during reflood. Defining, the ECCS SI liquid density is denoted as ρ_{SI} and the core flow area as A_{core}, the cold reflood rate expression:

$$U_R = \frac{\dot{m}_{SI}}{\rho_{SI} A_{core}} \tag{92}$$

The quench front velocity is assumed to be a constant multiple of the cold reflood rate. The multiplier, m_{RR}, is an uncertain input to the LB-LOCA ROM. The quench front velocity is:

$$U_Q = m_{RR} U_R \tag{93}$$

Since the quench front velocity is constant along the pin, the time that the quench front reaches a particular elevation, $t_q(z)$, is easily computed as:

$$t_q(z) = t_{FILL} + \frac{z}{U_Q} \tag{94}$$

A-1.3 Computation of ECR

The correlation recommended for the estimation of the local cladding oxidation rate is based on the Cathcart and Pawel (1977) model (see NUREG-17). The correlation follows a parabolic rate law:

$$w_o \frac{dw_o}{dt} = 0.1811 \exp\left(-\frac{39940}{RT}\right) \tag{95}$$

Where w_o is the total oxygen consumed in gm/cm^2, R is the gas constant (=1.987 cal/gm mole/K) and T is the clad temperature T (K).

This is converted in weight of clad reacted knowing that $w = 2.85 \cdot w_o$ from the stoichiometry or the reaction (2.85=91.2/32):

$$w \frac{dw}{dt} = 1.471 \exp\left(-\frac{39940}{RT}\right) \tag{96}$$

Rearranging and integrating over a timestep Δt yields:

$$\int_{w_i}^{w} w\ dw = 1.471 \int_{0}^{\Delta t} \exp\left(-\frac{39940}{RT}\right) dt \tag{97}$$

Where w_i is the initial weight (gr/cm^2) of the cladding (before the LOCA event). The equation above can be numerically integrated. The cladding temperature can be assumed constant over the time step Δt, and the Equation may be integrated to yield:

$$\frac{w^2 - w_i^2}{2} = 1.471 \exp\left(-\frac{39940}{RT}\right) \Delta t \tag{98}$$

The integration is carried out knowing the clad temperature trajectory.

The ECR(%) is then computed from the following relationship:

$$ECR(\%) = \frac{w}{\rho_z s} \tag{99}$$

Where ρ_z is the density of the Zirconium in (**= 6.50 gr/cm^3**) and s the original thickness of the cladding in cm.

A-1.4 Fuel Rod Design (FRD) ROM

The Fuel Rod Design (FRD) ROM determines the effective (mean) fuel thermal conductivity. This allows the LB-LOCA ROM to assume a constant fuel thermal conductivity in all of its calculations. The effective fuel thermal conductivity is defined as:

$$\overline{k}_f(z) = \frac{1}{T_{CL}(z) - T_{fo}(z)} \int_{T_{fo}(z)}^{T_{CL}(z)} k(T) dT \tag{100}$$

The FRD ROM therefore computes the fuel thermal conductivity integral over the fuel pellet. $T_{fo}(z)$ and $T_{CL}(z)$ are the fuel pellet surface and fuel centerline temperatures, respectively. These two temperatures must be known in order to evaluate the above integral. All of the calculations are done at steady-state operating conditions.

A simple thermal resistance network calculation is used to compute the fuel pellet surface temperature at a particular axial elevation. The bulk coolant temperature and clad (outer) surface temperature are computed as given in Eqs. (5) and (6). The clad inner surface temperature is computed from:

$$T_{ci}(z) = T_{co}(z) + q'(z) \frac{\log\left(R_{co}/R_{ci}\right)}{2\pi k_c} \tag{101}$$

The fuel pellet surface temperature is then:

$$T_{fo}(z) = T_{ci}(z) + \frac{q'(z)}{2\pi R_{gap} h_{gap}} \tag{102}$$

The fuel centerline temperature cannot be computed analytically. It is approximated by linearly interpolating between known (pre-computed) fuel thermal conductivity integral values. A thermal resistance network

expression is first used to relate the fuel thermal conductivity integral at the fuel centerline temperature to that at the fuel pellet surface temperature:

$$\frac{q'(z)}{4\pi} = \int_{T_{fo}(z)}^{T_{CL}(z)} k(T)dT = \int_{T_{ref}}^{T_{CL}(z)} k(T)dT - \int_{T_{ref}}^{T_{fo}(z)} k(T)dT \tag{103}$$

In Eq. (103), T_{ref}, denotes a pre-determined minimum reference temperature. Denoting each of the integrals as:

$$F_k(T_f) = \int_{T_{ref}}^{T_f} k(T)dT \tag{104}$$

The integral value corresponding to the fuel centerline temperature is simply:

$$F_k(T_{CL}(z)) = F_k(T_{fo}(z)) + \frac{q'(z)}{4\pi} \tag{105}$$

The centerline temperature is then computed by inverting the above expression:

$$T_{CL}(z) = F_k^{-1}\left(F_k(T_{fo}(z)) + \frac{q'(z)}{4\pi} \right) \tag{106}$$

The effective fuel thermal conductivity can then be easily estimated from:

$$\overline{k}_f(z) = \frac{F_k(T_{CL}(z)) - F_k(T_{fo}(z))}{T_{CL}(z) - T_{fo}(z)} \tag{107}$$

The inverse operator defined in Eq. (106) is performed via linear interpolation.

The actual thermal conductivity correlation was taken from the FRAPCON-3.4 (NUREG/CR-7022, Vol. 1) which adopted the expression developed by the Nuclear Fuels Industries (NFI) model. The correlation is reproduced below in Figure A-1 for convenience:

$$K_{95} = \frac{1}{A + a \cdot gad + BT + f(Bu) + (1 - 0.9\exp(-0.04Bu))g(Bu)h(T)} + \frac{E}{T^2}\exp\left(-\frac{F}{T}\right) \quad (2\text{-}52)$$

where

K_{95}	=	thermal conductivity for 95% TD fuel (W/m-K)	
T	=	temperature (K)	
Bu	=	burnup (GWd/MTU)	
$f(Bu)$	=	effect of fission products in crystal matrix (solution)	
$f(Bu)$	=	$0.00187 \cdot Bu$	(2-53)
$g(Bu)$	=	effect of irradiation defects	
$g(Bu)$	=	$0.038 \cdot Bu^{0.28}$	(2-54)
$h(T)$	=	temperature dependence of annealing on irradiation defects	
		$h(T) = \frac{1}{1 + 396e^{-Q/T}}$	(2-55)
Q	=	temperature dependence parameter ("Q/R") = 6380 K	
A	=	0.0452 (m-K/W)	
a	=	constant = 1.1599	
gad	=	weight fraction of gadolinia	
B	=	2.46E-4 (m-K/W/K)	
E	=	3.5E9 (W-K/m)	
F	=	16361 (K)	

Figure A-1. Thermal Conductivity Correlation Used in FRAPCON-3.4. [NUREG/CR-7022, Vol.1]

A-1.5 Core Design (CD) ROM – Core Power Distribution

There are three regions in the core: the fresh fuel region (Region 0), the once-burned region (Region 1), and the twice-burned region (Region 2). A Hot Assembly (HA) is defined in each region being the assembly with the highest axially integrated power within each region. Every HA contains a Hot Rod (HR) which is assumed to have a 6% ($\gamma = 1.06$) augmented power relative to the average rod power within that HA.

In core design, the core power distribution is simply characterized by the following ratios:

$F_{\Delta H}$ = Ratio of the integral of linear power along the hot rod (rod with the highest power) to the average rod power in the core

F_Q = Ratio of the maximum local rod linear power density to average fuel rod linear power density

$\bar{P} = F_{\Delta H}/\gamma$ = Ratio (PBAR) of the hot assembly power to the core average assembly power in the core.

The factor γ is the ratio between the power of the hot rod in an assembly and the average rod power within that assembly. The hot rod typically runs at 4 to 6% hogher power than the surrounding. A value of $\gamma = 1.06$ will be considered here.

Note that F_Q is not used in the CD ROM but it will be needed to define the axial power shape. Note also that despite a single nominal value of $F_{\Delta H}$ is applied to each region of the core, its uncertainty will be treated

independently for Region 0 and 1 and with no uncertainty in Region 2. The regions 0 and 1 $F_{\Delta H}$ after including the uncertainty will be identified as $F^{U}_{\Delta H,0}$ and $F^{U}_{\Delta H,1}$.

Now, let's define the following:

$\dot{Q}_{TOT}$ = Total core power (W)

N_j = Number of assemblies in region j

$N_{tot} = \sum_{j=0} N_j$ = Total number of assemblies in the core

n = number of rods per assembly

$\langle \dot{q}_A \rangle_{core} = \frac{\dot{Q}_{TOT}}{N_{tot}}$ = Core-average assembly power (W)

$\langle \dot{q}_A \rangle_j = \frac{\dot{Q}_j}{N_j}$ = Region-average assembly power (W)

$\dot{q}_j^{HA}$ = Hot Assembly (HA) power within region j (W)

The following relationship holds:

$$\dot{Q}_{TOT} = \sum_{j=0} \left[\dot{q}_j^{HA} + \left(N_j - 1 \right) \left\langle \dot{q}_A \right\rangle_j \right] \equiv N_{tot} \left\langle \dot{q}_A \right\rangle_{core} \tag{108}$$

The hot assembly PBAR with region j is given by:

$$\overline{P}_j = \frac{\dot{q}_j^{HA}}{\left\langle \dot{q}_A \right\rangle_{core}} \tag{109}$$

Let's also define the ratios Γ_j between the average assembly power with the region and the core-average assembly power, often called core radial factor:

$$\Gamma_j = \frac{\left\langle \dot{q}_A \right\rangle_j}{\left\langle \dot{q}_A \right\rangle_{core}} \tag{110}$$

From Eq. (108) the following relationship is obtained:

$$\sum_{j=0} \left[\frac{\dot{q}_j^{HA}}{\left\langle \dot{q}_A \right\rangle_{core}} + \left(N_j - 1 \right) \frac{\left\langle \dot{q}_A \right\rangle_j}{\left\langle \dot{q}_A \right\rangle_{core}} \right] = N_{tot} \tag{111}$$

Which yields to:

$$\sum_{j=0} \left[\overline{P}_j + \left(N_j - 1 \right) \Gamma_j \right] = N_{tot} \tag{112}$$

The following assumptions are made for the CD ROM:

$$
\begin{aligned}
&\Gamma_0 = \Gamma_1 = \Gamma_x \\
&\Gamma_2 \equiv P_{low} \\
&\overline{P}_0 = \frac{F^U_{\Delta H,0}}{\gamma} \\
&\overline{P}_1 = \frac{F^U_{\Delta H,1}}{\gamma} \\
&\overline{P}_2 = P_{low}\frac{F_{\Delta H}}{\gamma}
\end{aligned}
\tag{113}
$$

$\dot{Q}_{TOT}$ $\dot{Q}_{TOT}$ is given and $F_{\Delta H}$, γ, P_{low}, N_0, N_1, N_2 are the variables optimized in core design analyses and here provided in input to the CD ROM. All other variables can be then deduced from those parameters. For instance, substituting Eq. (113) in (112) yield to the following:

$$
\Gamma_x = \frac{1}{N_0 + N_1 - 2}\left[N_{tot} - \overline{P}_0 - \overline{P}_1 - \overline{P}_2 - \left(N_2 - 1\right)P_{low}\right] \tag{114}
$$

Which yields to:

$$
\Gamma_x = \frac{1}{N_0 + N_1 - 2}\left[N_{tot} - \frac{F^U_{\Delta H,0}}{\gamma} - \frac{F^U_{\Delta H,1}}{\gamma} - P_{low}\frac{F_{\Delta H}}{\gamma} - \left(N_2 - 1\right)P_{low}\right] \tag{115}
$$

The power in each representative assembly in the core can then be derived:

$$
\dot{q}_0 = \left\langle \dot{q}_A \right\rangle_0 = \Gamma_x \left\langle \dot{q}_A \right\rangle_{core} \tag{116}
$$

$$
\dot{q}_1 = \left\langle \dot{q}_A \right\rangle_1 = \left\langle \dot{q}_A \right\rangle_0 \tag{117}
$$

$$
\dot{q}_2 = \left\langle \dot{q}_A \right\rangle_2 = P_{low} \left\langle \dot{q}_A \right\rangle_{core} \tag{118}
$$

$$
\dot{q}_0^H = \frac{F_{\Delta H}}{\gamma}\left\langle \dot{q}_A \right\rangle_{core} \tag{119}
$$

$$
\dot{q}_1^H = \dot{q}_0^H = \frac{F_{\Delta H}}{\gamma}\left\langle \dot{q}_A \right\rangle_{core} \tag{120}
$$

$$
\dot{q}_2^H = \frac{F_{\Delta H}}{\gamma} P_{low} \left\langle \dot{q}_A \right\rangle_{core} \tag{121}
$$

Assembly power is assumed constant trough the cycle of operation. Each rod is assumed to "burn" at a rate proportional to its respective power and therefore at a constant rate through time. This is a gross approximation because in reality the linear heat rate in a specific assembly will vary during the cycle as result of breeding and depletion.

A-1.6 Core Design (CD) ROM – Burnup Through Time

The cycle length will be denoted as $\Delta t_C = t_F - t_I$ where t_F denotes the cycle length and t_I is the initial start time, which is assumed to be zero. At the end of the cycle, the average Region 0 discharge burnup is assumed to be $BU(t_1)$, while the average Region 1 discharge burnup is $BU(t_2)$. These two values must be specified as inputs.

Assuming the rod power is constant throughout the cycle, the burn-rate will depend on the specific rod power values within each region. Higher power rods will "burn" faster than the associated region average rods. The burnup as a function of time for the average assembly in Region 0 is:

$$BU_0(t) = \frac{BU(t_1)}{\Delta t} t \tag{122}$$

The burnup as a function of time for the hot assembly in Region 0 is:

$$BU_0^{HA}(t) = \frac{F_{\Delta H,0}^U}{\gamma} \frac{BU(t_1)}{\Delta t} t \tag{123}$$

The burnup for the HR within the HA is simply:

$$BU_0^{HR}(t) = \gamma BU_0^{HA}(t) \tag{124}$$

The burnup through time expressions in Region 1 are nearly identical to those in Region 0. The only difference is that the initial burnup in Region 1 is not zero, but assumed to be equal to $BU(t_1)$. The Region 1 average and hot assembly burnup expression are:

$$BU_1(t) = BU(t_1) + \frac{\left[BU(t_2) - BU(t_1)\right]}{\Delta t} t \tag{125}$$

$$BU_1^H(t) = BU(t_1) + \frac{F_{\Delta H,1}^U}{\gamma} \frac{\left[BU(t_2) - BU(t_1)\right]}{\Delta t} t \tag{126}$$

And

$$BU_1^{HR}(t) = BU(t_1) + F_{\Delta H} \frac{\left[BU(t_2) - BU(t_1)\right]}{\Delta t} t \tag{127}$$

The discharge burnup in Region 2 (the twice-burned region) will not be specified by the average assembly discharge burnup. In order to ensure the maximum discharge burnup is below the limit:

$$BU_{LIM} = 62\ GWd/MTU$$

A maximum (exit) discharge burnup will be specified as an input, $BU_2^H(t_F)$. The resulting expressions for the Region 2 burnup through time are similar to those in Regions 0 and 1. The Region 2 hot assembly burnup through time expression is:

$$BU_2^{HR}(t) = BU(t_2) + F_{\Delta H} P_{low} \frac{BU_2^H(t_F) - BU(t_2)}{\Delta t} t \tag{128}$$

The Region 2 average assembly burnup through time expression is:

$$BU_2^H(t) = BU(t_2) + \frac{F_{\Delta H} P_{low}}{\gamma} \frac{BU_2^H(t_F) - BU(t_2)}{\Delta t} t \tag{129}$$

And finally for the low power assemblies:

$$BU_{\ 2}(t) = BU(t_2) + P_{low} \frac{BU_2^H(t_F) - BU(t_2)}{\Delta t} t \tag{130}$$

A very simple model is devised to establish the relationship between rod burnup and hydrogen content (hydrogen pickup) for the rod at any location.

The following crude assumptions are made. First, burnup does not depend on the axial location. It only depends on the rod power history. And second, Corrosion or more specifically hydrogen content (in wppm) is accrued at a constant rate. Figure 1-2 (in Section 1.1) shows a few data points on different cladding materials. Let's consider the data point at the extreme right reported for ZIRLO at 70 GWD/MTU. The reported hydrogen content can be as high as 600 wppm at that burnup for ZIRLO cladding.

From the second assumption, the relationship between hydrogen content and burnup is simply:

$$H2(BU) = \frac{600}{70} BU \tag{131}$$

Where *BU* is the burnup of the rod in GWD/MTU and *H2* is the hydrogen content in wppm.

The proposed limit to the 10 CFR 50.46c is presented in DG-1263 and also shown in Figure 1-1 in Section 1.1.

The analytical limit can be expressed as follows:

$$ECR_{5046} = \begin{cases} 18 - \dfrac{12}{400} H2 & \text{if} \quad \text{H2<400 wppm} \\ 6 - \dfrac{4}{400}\left(H2 - 400\right) & \text{if} \quad \text{H2>400 wppm} \end{cases} \tag{132}$$

The 50.46 rule also reduced the PCT limit when hydrogen content is greater than 400 wppm. This additional criteria is not considered in the ROM.

The reacted clad thickness determined by Eq. (98) has to be converted to % ECR. ECR is defined as the total thickness of cladding that would be converted to stoichiometric ZrO2 from all the oxygen contained in the fuel cladding as ZrO2 and oxygen in solid solution in the remaining metal phase.

A-1.7 Core Design (CD) ROM – Power Shape Methodology

A triangular shape will be assumed to enable ranging FQ, FdH and the peak location. As an example, the Rod Bundle Heat Transfer (RBHT) test facility (NUREG/CR-6975) triangular shape is shown in Figure 2-11 in Section 2.1.

The expression is the following:

$$\begin{aligned} f(x) &= f_0 + \frac{\left(f_M - f_0\right)}{x_M} x \qquad \text{for } x < x_M \\ f(x) &= f_M - \left(f_M - f_0\right) \frac{x - x_M}{1 - x_M} \qquad \text{for } x \geq x_M \end{aligned} \tag{133}$$

Where:

$$x = \frac{z}{H}$$

H = Core Height (m)

z = Distance from bottom of the core

x_M = Location of the peak

f_M = Maximum power factor

f_0 = Power factor at the edge of the core (134)

The power at the edge is calculated to ensure

$$\dot{q}_n = \int_0^H q'(z)\,dz = q'_n H \int_0^1 f\left(x\right)dx \Rightarrow 1 = \int_0^1 f(x)\,dx \tag{135}$$

Which yields to:

$$f_0 = 2 - f_M \tag{136}$$

The power of the individual rod is scaled based on Fq and FdH (same axial form assumed for all rods):

Equation (133) is the power factor for the core average rod. The power factors for the individual rods in the core need to be scaled by the specific rod $F_{\Delta H}$, i.e.:

$$q'_i(x) = \langle q' \rangle \left(F_{\Delta H}\right)_i f\left(x\right) \tag{137}$$

Finally the definition of $F_q = \frac{\max q'}{\langle q' \rangle}$ the following expression for f_M is derived:

$$f_M = \frac{F_q}{\max\left(F_{\Delta H}\right)} \tag{138}$$

A-2. Uncertainty Quantification Summary Statistics

The uncertainty in the uncertain input parameters are propagated onto the various Figures of Merit (FOMs) via Monte Carlo Sampling. The resulting uncertainty in each FOM (the PCT and ECR) are summarized by histograms as well as estimators on several summary statistics: the mean, median, standard deviation, 5th and 95th quantiles. The mean and median estimators provide statistics on central tendency, while the standard deviation and quantiles provide statistics on dispersion. The standard error for each estimator is also provided. The following sub-sections detail the calculation for each estimator and its corresponding standard error.

Specifically for nuclear safety analysis, the 95th quantile is the statistic that is compared to the Regulatory limit. Therefore the estimated 95th quantile and its associated standard error is compared to Wilks-based estimators, which are the prevalent estimator of choice currently.

A-2.1 Summary Statistic Estimators and Standard Errors

Each of the estimators and their corresponding standard errors are given in Harding et al. (2014). The standard error of a sample statistic is formally defined as the standard deviation of that statistic, assuming that a large number of samples is taken. Typically, the standard error on the population (or sample) mean is given, but the standard error on any summary statistic can be estimated. The following sub-sections provide the equations for each of the summary statistics used in this work.

A-2.1.1 Mean

The sample mean and its standard error is commonly reported in many texts. The sample mean, $\overline{\mathrm{X}}$ of a dataset of $\mathrm{N_S}$ samples, $\mathrm{X} = \mathrm{X_1}, \ldots, \mathrm{X_i}, \ldots, \mathrm{X_{N_S}}$ is simply:

$$\overline{\mathbf{X}} = \frac{1}{N_S}\sum_{i=1}^{N_S} X_i \tag{139}$$

The standard error on the mean can only be approximated because the true standard deviation is itself unknown. The unbiased estimator on the standard deviation is:

$$s_{\mathbf{X}} = \left[\frac{1}{N_S - 1}\sum_{i=1}^{N_S}\left(X_i - \overline{\mathbf{X}}\right)^2\right]^{\frac{1}{2}} \tag{140}$$

The standard error on the mean is then:

$$SE_M = \frac{s_{\mathbf{X}}}{\sqrt{N_S}} \tag{141}$$

A-2.1.2 Median

The median is defined as the point of a distribution where the number of data points on each side of the median is equal. The median is therefore the 50th quantile. To be consistent with Harding et al. (2014) the estimator for the median of a dataset will be defined as $\widetilde{\mathrm{X}}$ and is found using:

$$\widetilde{\mathbf{X}} = \begin{cases} X_{\left(\frac{N_S+1}{2}\right)} & \text{if } N_S \text{ is odd} \\ \frac{1}{2}\left[X_{\left(\frac{N_S}{2}\right)} + X_{\left(\frac{N_S+1}{2}\right)}\right] & \text{if } N_S \text{ is even} \end{cases} \tag{142}$$

In the above notation, $X_{(i)}$ refers to the i-th datum when the sample is sorted in ascending order. The standard error on the median is estimated via:

$$SE_{MD} = \sqrt{\frac{\pi}{2}} \frac{s_{\mathbf{X}}}{\sqrt{N_S}} \tag{143}$$

Comparing Eq. (143) with Eq. (141) shows that SE_{MD} is roughly 1.25 times larger than SE_{M}. Thus even though the median is more robust than the mean (since outliers do not influence the median as much as the mean) the median is estimated less reliably than the mean.

A-2.1.3 Standard Deviation

The estimator on the standard deviation was already given by Eq. (140). As shown in Harding et al. (2014), the standard error on the standard deviation is more involved than either the mean or median standard error expressions. The complicated expression (Eq. (18) in Harding et al. (2014) can however be approximated by:

$$SE_S \approx \frac{s_{\mathbf{X}}}{\sqrt{2\left(N_S - 1\right)}} \tag{144}$$

A-2.1.4 Quantiles

Quantiles are division of a dataset into equal sized groups. There are numerous methods for estimating quantiles for a given percentile p. Regardless of the choice for estimating quantiles, there are more steps involved than estimating either of the above summary statistics.

1. The sorted values in **X** are taken as the $(0.5/N_S), (1.5/N_S), \ldots, ([N_S - 0.5]/N_S)$ quantiles.
2. `quantile()` uses linear interpolation to compute quantiles for probabilities between $(0.5/N_S)$ and $([N_S - 0.5]/N_S)$.
3. For quantiles corresponding to the probabilities outside that range, `quantile()` assigns the minimum or maximum values in **X**.

Just as with estimating the quantiles themselves, there are many different ways to compute the quantile standard errors. The specific form chosen for this work is:

$$SE_{Q_p} = \frac{s_{\mathbf{X}}\sqrt{p\left(1-p\right)}}{\phi\left(z\left(p\right)\right)\sqrt{N_S}} \tag{145}$$

In Eq. (145), z(p) is the p-th quantile of the standard normal distribution and $\phi\left(z(p)\right)$ is the density function of the standard normal distribution evaluated at z(p). Notice that the standard error on the p-th quantile can be written in terms of the standard error on the mean:

$$SE_{Q_p} = \frac{\sqrt{p\left(1-p\right)}}{\phi\left(z\left(p\right)\right)} \frac{s_{\mathbf{X}}}{\sqrt{N_S}} = \frac{\sqrt{p\left(1-p\right)}}{\phi\left(z\left(p\right)\right)} SE_M \tag{146}$$

For p=0.5 (the median) Eq. (143) is recovered. For the 95th quantile, p=0.95 the above expression is approximately equal to:

$$SE_{Q_{0.95}} \approx 2.11 \cdot SE_M \tag{147}$$

Therefore, the 95th quantile Monte Carlo estimator is roughly twice as uncertain as the mean estimator.

A-2.1.5 Confidence Intervals and Comparison to Wilks-Based Estimators

The Wilks-based estimator to a quantile is constructed by providing an estimate $\hat{x}_\alpha$ to an upper bound x_α for confidence with given probability bound β:

$$P\left(\hat{x}_\alpha \geq x_\alpha\right) \geq \beta \tag{148}$$

For the 95th quantile, $\alpha = 0.95$ and β provides the probability or degree of conservatism on that upper bound. Typically $\beta = 0.95$ yielding the common "95/95" estimator.

The Monte Carlo estimators provided in Section A-2.1 also have their own confidence intervals. Harding et al. (2014) provides the exact formulation of each of their confidence intervals, but as an approximation this work provides the 95% confidence interval (CI) on each estimator as:

$$\mathrm{CI}_{x_J,0.95} = \hat{x}_J \pm 2 \cdot SE_J \tag{149}$$

where $\hat{x}_J$ is an estimator and SE_J is its associated standard error. Eq. (149) is an approximation to the true CI, but for large sample sizes it is a reasonable approximation.

After a single Monte Carlo sampling sequence of N_S samples, the various summary statistics and their corresponding standard errors are computed. Additionally, the Wilks-based estimators are computed N_{WG} times where:

$$N_{WG} = \mathrm{floor}\left(N_S / N_{Wr}\right) \tag{150}$$

and N_{Wr} is the required minimum number of samples to achieve a desired Wilks-based estimator confidence level and probability bound. For example, if $N_S = 590$ Monte Carlo samples and $N_{Wr} = 59$ then there are $N_{WG} = 10$ groups of 59 samples. The 59 sample Wilks-based estimator can be computed 10 different times. The sample mean and variability in the Wilks-based estimator can then be compared directly to the Monte Carlo estimator to the 95th quantile.

A-2.2 Overview Sensitivity Analysis (SA)

To quote Saltelli: "The objective of sensitivity analysis (SA) of model output can be defined (loosely) as 'to ascertain how a given model (numerical or otherwise) depends on its input [parameters]'". There are two primary ways of structuring SA, local and global. Local SA various one parameter at a time while keeping all of the other parameters fixed at their nominal values. The input is varied by a small perturbation to estimate partial derivatives for the output response with respect to each input parameter. This information can be used to perform Uncertainty Quantification (UQ) through Taylor series expansions. Thermal hydraulic system codes do not use this approach for UQ because of the large variations in some of the uncertain input parameters.

Global SA is somewhat harder to define, but it has two key attributes: first that the whole range of values of the input parameters are considered, and second that all inputs are varied at the same time. The fact that the "whole range" of the inputs are considered represents that Global SA is linked to UQ. The input parameter ranges that are being considered are based on their (assumed) uncertainty distributions. The input parameters influence the output through both their (local) sensitivity as well as their uncertainty. A particular input that is "very" uncertain, might control the resulting uncertainty in the output than other input parameters even if the output is not particularly "sensitive" to that input over a local space.

The following subsections provide several different types of SA procedures that allow answering the following objectives:

- Identify and prioritize the most influential input parameters

- Identify the input parameters that are mostly responsible for producing realizations of the output in a given region

The above bullet points are not the only objectives SA can help answer, but those are the two this work specifically focused on. See the book "Sensitivity Analysis in Practice" by Saltelli et al. (2004) for a complete list of all SA objectives. The first objective is achieved with variance-based SA algorithms, specifically the method of Sobol' and the Fourier Amplitude Sensitivity Test (FAST). The second objective is achieved through Monte Carlo Filtering (also known as Regionalized Sensitivity Analysis) and Limit Surfaces (implemented with likelihood free Markov Chain Monte Carlo).

One final type of SA is included in this work. This SA type is intended for analyzing the impact of an assumption on a particular input parameter. This type will be referred to as "Distributional SA".

A-2.3 Variance-Based SA

A-2.3.1 Overview

In variance-based SA, the goal is primarily to rank the input parameters according to the amount of output uncertainty that is removed when we learn the true value of a given input parameter. The uncertainty is quantified by the variance, therefore the output variance is being decomposed into contributions from the variances of the different uncertain input parameters. In many respects, variance-based SA is very similar to analysis of variance (ANOVA) methodologies. The variance is decomposed into terms of increasing dimensionality, starting from first-order or main effects, two-way interactions, and then higher-order interactions. The following subsections will summarize these concepts and discuss how they are used to rank inputs.

A-2.3.2 Variance Decomposition

The nomenclature and syntax in this subsection is consistent with Saltelli's notation in "Sensitivity Analysis in Practice". A majority of the content in this subsection is found in that reference, but the following discussion is a summary of the key points.

Before describing how the output variance will be decomposed, several important concepts need to be discussed. The uncertainty in the model output, $y = f(X)$, is quantified by its unconditional variance $V(Y)$. X is a D-dimensional vector of all uncertain input parameters The goal is to rank input parameters according to the amount of output variance that is reduced when we learn the "true" value of a given input $X_i = x_i^*$. If we could know the "true" value of a particular input, we could then compute the output variance conditioned on knowing the associated input precisely, $V(Y|X_i = x_i^*)$. Note that the variance is taken over all factors but X_i. Thus to be more formal, the conditional variance could have been written as $V_{X_{-i}}(Y|X_i = x_i^*)$ where X_{-i} denotes the vector of all inputs except the i-th input. Of course the only problem with this setup is that we do not know the "true" value of any of the inputs. The conditional variance is therefore averaged over all possible values of X_i:

$$\mathbb{E}\left[V\left(Y \mid X_i\right)\right] \tag{151}$$

Equation (151) dropped the explicit dependence on $X_i = x_i^*$, and as before we could write the more formal statement that denotes the expectation is taken with respect to X_i:

$$\mathbb{E}_{X_i}\left[V_{\mathbf{X}_{-i}}\left(Y \mid X_i\right)\right] \tag{152}$$

Equation (152) denotes that the integrations required to compute the variance are performed over all inputs but the i-th input, while the "outer" expectation is performed over the i-th input.

Once Eq. (152) (or (151) is evaluated for all inputs, the input with the smallest value is the most important. The unconditional variance on the output can be expressed in terms of Eq. (152) using the law of total variance:

$$V(Y) = \mathbb{E}_{X_i}\left[V_{\mathbf{X}_{-i}}(Y \mid X_i)\right] + V_{X_i}\left(\mathbb{E}_{\mathbf{X}_{-i}}[Y \mid X_i]\right) \tag{153}$$

Examining Eq. (153) reveals that identifying the input with the smallest $\mathbb{E}[V(Y|X_i)]$ is equivalent to identifying the input with the largest $V(\mathbb{E}[Y|X_i])$ term. For this reason, the sensitivity measure is based on calculating for each input parameter:

$$V_i \square V_{X_i}\left(\mathbb{E}_{\mathbf{X}_{-i}}[Y \mid X_i]\right) \tag{154}$$

Dividing by the output unconditional variance yields the (Sobol) sensitivity index for the i-th input:

$$S_i = \frac{V_i}{V(Y)} \tag{155}$$

Eq. (155) is specifically the "first-order" or "main effect" sensitivity index of X_i on Y. Higher-order indices capture the interactions between two (or more) particular inputs. For example, the effect of two orthogonal inputs X_i and X_j on the output Y can be defined as:

$$\begin{gathered} V_{ij} = V_{X_i,X_j}\left(\mathbb{E}_{\mathbf{X}_{-i,-j}}[Y \mid X_i, X_j]\right) - V_{X_i}\left(\mathbb{E}_{\mathbf{X}_{-i}}[Y \mid X_i]\right) - V_{X_j}\left(\mathbb{E}_{\mathbf{X}_{-j}}[Y \mid X_j]\right) \\ V_{ij} = V_{X_i,X_j}\left(\mathbb{E}_{\mathbf{X}_{-i,-j}}[Y \mid X_i, X_j]\right) - V_i - V_j \end{gathered} \tag{156}$$

The term V_{ij} is the joint effect of X_i and X_j minus the first order effects for the same inputs. It is known as the "two-way" or "second-order" effect between the i-th and j-th inputs. Higher-order terms are defined in similar fashion.

With the above definitions, we can now write the variance decomposition as a functional ANOVA when the inputs are orthogonal:

$$V(Y) = \sum_i V_i + \sum_i \sum_{j>i} V_{ij} + \cdots + V_{12\ldots D} \tag{157}$$

The first summation is the summation over the first-order or main-effect terms, while the remaining summations are over all of the higher-order interaction terms. The higher-order terms will reflect how the various inputs interact with each other within the computational model. If the higher-order terms are all zero, the computational model is additive in its inputs and thus:

$$V(Y) = \sum_i V_i \to 1 = \sum_i S_i \tag{158}$$

If there are interactions present within the computational model, the higher-order terms will thus not be zero. The first-order sensitivity indices will therefore not sum to 1.

When ranking the inputs, the first-order sensitivity indices are the proper measure of sensitivity that should be considered. Therefore, whether the inputs interact or not within the computational model, the inputs with the highest first-order sensitivity indices are the most important. The following sections describe two different ways to estimate the first-order indices.

A-2.3.3 Sobol Indices via Monte Carlo Sampling

Sampling Sequences

The sensitivity indices given by Eq. (155), will be estimated by Monte Carlo sampling. To denote the sensitivity indices from those estimated by the FAST algorithm in the next section, the Monte Carlo estimated sensitivity indices will be specifically referred to as the Sobol indices. The following Monte Carlo sampling strategy is summarized from Section 5.9 in "Sensitivity Analysis in Practice". Start with two Monte Carlo sequences, M_1 and M_2:

$$\mathbf{M}_1 = \begin{bmatrix} x_1^{(1)} & x_2^{(1)} & \cdots & x_D^{(1)} \\ x_1^{(2)} & x_2^{(2)} & \cdots & x_D^{(2)} \\ \vdots & \vdots & \ddots & \vdots \\ x_1^{(N_S)} & x_2^{(N_S)} & \cdots & x_D^{(N_S)} \end{bmatrix} \tag{159}$$

$$\mathbf{M}_2 = \begin{bmatrix} x_1^{(1')} & x_2^{(1')} & \cdots & x_D^{(1')} \\ x_1^{(2')} & x_2^{(2')} & \cdots & x_D^{(2')} \\ \vdots & \vdots & \ddots & \vdots \\ x_1^{(N_S')} & x_2^{(N_S')} & \cdots & x_D^{(N_S')} \end{bmatrix} \tag{160}$$

Each sequence contains N_S samples for the D-dimensional input parameter vector. The superscript (n) in Eq. (159) denotes the n-th sample in sequence 1 and (n′) in Eq. (160) denotes n'-th sample in sequence 2. The samples in both sequences are i.i.d. samples from the (assumed) uncertain input distributions. It is very important to note that the following algorithm requires the inputs to be orthogonal (essentially independent). Each row of the M_1 and M_2 matrices corresponds to a particular evaluation of the computational model output (there are thus two sets of N_S samples of Y).

From M_1 and M_2 construct a third matrix N_j:

$$\mathbf{N}_j = \begin{bmatrix} x_1^{(1')} & x_2^{(1')} & \cdots & x_j^{(1)} & \cdots & x_D^{(1')} \\ x_1^{(2')} & x_2^{(2')} & \cdots & x_j^{(2)} & \cdots & x_D^{(2')} \\ \vdots & \vdots & \ddots & \vdots & \ddots & \vdots \\ x_1^{(N_S')} & x_2^{(N_S')} & \cdots & x_j^{(N_S)} & \cdots & x_D^{(N_S')} \end{bmatrix} \tag{161}$$

All columns of N_j are identical to those in M_2 except the j-th column which corresponds to the j-the column in M_1. As described by Saltelli, M_1 is essentially the "sample" matrix and M_2 is the "resample" matrix, thus N_j is the matrix where all inputs except X_j are re-sampled.

Sobol Indices Calculations

The first-order Sobol index for the j-th input is estimated as:

$$S_j = \frac{\hat{V}_j}{\hat{V}} \tag{162}$$

where:

$$V_j \approx \hat{V}_j = \hat{U}_j - \left(\hat{\mathbb{E}}(Y)\right)^2 \tag{163}$$

and $\hat{\mathbb{V}}$ is the Monte Carlo estimator on the variance. The estimator $\hat{\mathbb{U}}_j$ is defined as:

$$\hat{U}_j = \frac{1}{N_S - 1}\sum_{n=1}^{N_S}\left\{f\left(\mathbf{M}_1(n,:)\right) f\left(\mathbf{N}_j(n,:)\right)\right\} \tag{164}$$

The notation $\mathbf{M}_1(n,:)$ denotes the n-th row of the $\mathbf{M}_1$ matrix, which corresponds to the n-th sample from the first Monte Carlo sequence. The estimator $\hat{\mathbb{U}}_j$ is therefore computed from the "sample" matrix multiplied by values of the output computed when all inputs except the j-th input are "resampled". If the j-th input is a "dummy" or non-influential input, $\hat{\mathbb{U}}_j \approx \left(\hat{\mathbb{E}}(Y)\right)^2$ and thus $S_j \approx 0$. If the j-th input is very important, then $\hat{\mathbb{U}}_j - \left(\hat{\mathbb{E}}(Y)\right)^2 \approx \hat{\mathbb{V}}$ and thus $S_j \approx 1$. When computing the $\hat{\mathbb{V}}_j$ estimators, Saltelli notes that the squared mean estimate should be computed in the following manner:

$$\left(\hat{\mathbb{E}}(Y)\right)^2 = \frac{1}{N_S}\sum_{n=1}^{N_S}\left\{f\left(\mathbf{M}_1(n,:)\right) f\left(\mathbf{M}_2(n,:)\right)\right\} \tag{165}$$

In addition to computing the first-order indices, this algorithm is also capable of estimating the total-effect indices. The total effect index for the j-th input captures the influence of all interaction terms that include the j-th input. Although, there is some debate on how to use the total effect indices, the total effect indices are useful since they allow capturing some of the interaction and non-additive effects present within the computational model. The j-th total effect index is:

$$S_{Tj} = \frac{V(Y) - V\left(\mathbb{E}\left[Y \mid \mathbf{X}_{-j}\right]\right)}{V(Y)} \approx \hat{S}_{Tj} = 1 - \frac{\hat{U}_{-j} - \left(\hat{\mathbb{E}}(Y)\right)^2}{\hat{V}(Y)} \tag{166}$$

where:

$$\hat{U}_{-j} = \frac{1}{N_S - 1}\sum_{n=1}^{N_S}\left\{f\left(\mathbf{M}_2(n,:)\right) f\left(\mathbf{N}_j(n,:)\right)\right\} \tag{167}$$

In Eq. (167) the j-th input is now the only input that is different in the product of $f(\mathbf{M}_2(n,:))$ and $f\left(\mathbf{N}_j(n,:)\right)$. Effectively, the j-th input is the only input that is resampled, though the term resample is now reversed from the definition given previously. The squared mean term in Eq. (166) is computed differently than the squared mean in Eq. (163). Saltelli recommends to compute the squared mean term for the total indices using the following expression:

$$\left(\mathbb{E}(Y)\right)^2 = \left(\frac{1}{N_S}\sum_{n=1}^{N_S} f\left(\mathbf{M}_1(n,:)\right)\right)^2 \tag{168}$$

Computational Cost

Although the "sample" and "resample" sequences, M_1 and M_2, are two separate Monte Carlo sequences. The N_j sequence must be repeated for each of the D input parameters. If each sequence consists of N_S samples, then the total number of samples required for estimating the Sobol indices is:

$$N_{Sobol} = N_S\left(D+2\right) \tag{169}$$

A-2.3.4 FAST

Overview

The Fourier Amplitude Sensitivity Test or FAST is an alternative procedure for estimating the first-order sensitivity indices. Classical FAST was developed by Cukier et al. (1973) and formalized more thoroughly by Cukier et al. (1978) and Koda et al. (1979). Extended FAST was formulated by Saltelli et al. (1999) to allow estimating the total sensitivity indices, in addition to the first-order indices. This work however only uses the classical FAST implementation of Koda et al. (1979), implementing the extended FAST would be the subject of future work.

FAST uses Fourier analysis to express variations in the output in terms of harmonics on the input parameters. The importance of the different input parameters can then be determined by analyzing the strength of the various frequency components that are present in the output "signal." FAST does not randomly sample input values, but rather choosing input values sequentially so that each input oscillates between its respective high and low values with a specific frequency unique to that input. The following sections will summarize how the input values are chosen and then how the inputs are ranked using FAST.

Search Curve

The input parameters are parameterized using a single "search variable", s:

$$x_i\left(s\right) = G_i\left(\sin\left(\omega_i s\right)\right) \tag{170}$$

where G_i is a transformation function and $\{\omega_i\}_{i=1}^{D}$ is a set of different frequency (integer) values. The transformation function maps the search variable value to each of the different input parameters via that input's respective frequency. The functional form of G_i depends on the assumed sampling distribution for each input parameter, with various forms outlined in Saltelli et al. (1999). The transformation function proposed by Koda et al. (1979) which was used in this work is:

$$x_i = \bar{x}_i\left(1+\bar{v}_i\sin\left(\omega_i s\right)\right) \tag{171}$$

where $\bar{x}_i$ is the nominal input value and $\bar{v}_i$ represents the range of that input. For a uniformly distributed input between 0 and 1, $\bar{x}_i = 1/2$ and $\bar{v}_i = 1$. As discussed by Saltelli et al. (1999), this transformation function does not yield an exact representation of a uniform distribution. However, it was found to yield more reliable results than other transformation functions.

The frequencies themselves are required to be incommensurate (not linearly dependent):

$$\sum_{i=1}^{D} a_i\omega_i \neq 0; \qquad -\infty < a_i < +\infty \tag{172}$$

The frequency set also impacts the minimum required number of samples based upon issues with aliasing and interferences. Those details are not discussed here but are described in multiple references by Cukier and Saltelli.

An incommensurate set of frequencies ensures that the search variable curve is space-filling. When that is the case, the r-th moment of the output:

$$\mathsf{E}\left[y^{(r)} \right] = \int f^r \left(x_1, x_2, \ldots, x_D \right) p\left(x_1, x_2, \ldots, x_D \right) d\mathbf{x} \tag{173}$$

can be rewritten as a single dimensional integral over the search variable:

$$\mathsf{E}\left[y^{(r)} \right] = \lim_{T \to \infty} \frac{1}{2T} \int_{-T}^{T} f^r \left(s \right) ds \tag{174}$$

where

$$f\left(s \right) = f\left(x_1\left(s \right), x_2\left(s \right), \ldots, x_D\left(s \right) \right) \tag{175}$$

Equation (174) assumes that the input variables are uniformly distributed between 0 and 1. The output variance can then be written as:

$$V\left(Y \right) = \mathsf{E}\left[Y^{(2)} \right] - \left(\mathsf{E}\left[Y^{(1)} \right] \right)^2 \tag{176}$$

Spectral Decomposition

However, a space-filling search variable curve is only an idealization due to the finite precision of computers. Any set of chosen frequencies will be thus be commensurate, and hence there exists a finite positive rational number T such that $f(s) = f(s + T)$ and thus the search variable curve is a closed path. Cukier et al. (1973) showed that if the frequencies are positive integers, then $T = 2\pi$. By considering the output, $f(s)$, over a finite interval $(-\pi, \pi)$ Eq. (174) can be rewritten:

$$\mathsf{E}\left[y^{(r)} \right] = \frac{1}{2\pi} \int_{-\pi}^{\pi} f^r \left(s \right) ds \tag{177}$$

And thus the output variance can be written as:

$$V\left(Y \right) \approx \hat{V} = \frac{1}{2\pi} \int_{-\pi}^{\pi} f^2 \left(s \right) ds - \left(\frac{1}{2\pi} \int_{-\pi}^{\pi} f\left(s \right) ds \right)^2 \tag{178}$$

$\hat{\mathrm{V}}$ denotes the estimate on the output variance. The output is then expanded in a Fourier series:

$$y = f\left(s \right) = \sum_{j=-\infty}^{+\infty} \left\{ A_j \cos\left(js \right) + B_j \sin\left(js \right) \right\} \tag{179}$$

with Fourier coefficients:

$$A_j = \frac{1}{2\pi} \int_{-\pi}^{\pi} f\left(s \right) \cos\left(js \right) ds \tag{180}$$

$$B_j = \frac{1}{2\pi}\int_{-\pi}^{\pi} f(s)\sin(js)\,ds \tag{181}$$

over the domain of integer frequencies:

$$j \in \mathbb{Z} = \{-\infty, \ldots, -1, 0, +1, \ldots, +\infty\} \tag{182}$$

The spectrum of the Fourier series is defined as:

$$\Lambda_j = A_j^2 + B_j^2, \qquad j \in \mathbb{Z} \tag{183}$$

The Fourier coefficients and spectrum have the following properties:

$$A_{-j} = A_j, \quad B_{-j} = -B_j, \qquad \Lambda_{-j} = \Lambda_j \tag{184}$$

By evaluating the spectrum for the fundamental frequency ω_i and its higher harmonics $p\omega_i$ the portion of the output variance arising from the variance of the i-th input can be estimated:

$$\hat{V}_i = \sum_{p \in \mathbb{Z}^o} \Lambda_{p\omega_i} = 2\sum_{p=1}^{+\infty} \Lambda_{p\omega_i} \tag{185}$$

In Eq. (185):

$$\mathbb{Z}^o = \mathbb{Z} - \{0\} \tag{186}$$

is the set of all relative integers except 0. By summing all of the Fourier spectrums, the output variance is estimated as:

$$\hat{V} = \sum_{j \in \mathbb{Z}^o} \Lambda_j = 2\sum_{j=1}^{+\infty} \Lambda_j \tag{187}$$

The first-order sensitivity indices as estimated by FAST are therefore:

$$S_i^{FAST} = \frac{\hat{V}_i}{\hat{V}} \tag{188}$$

A-2.3.5 Monte Carlo Filtering (Regionalized Sensitivity Analysis)

Overview

Monte Carlo Filtering (MCF) which is also known as Regionalized Sensitivity Analysis (RSA) addresses the second objective listed in A-2.2. This objective is fundamentally different from ranking the inputs based upon their influence onto the output variance. With this objective we want to determine which inputs influence the output at exceeding a particular threshold, or having values within some specified range. This is particularly important in nuclear safety applications where we are interested in identifying inputs that lead to PCT and ECR exceeding their regulatory limits. Another application as shown in Osidele and Mohanty (2006) is to identify which inputs influence the output exceeding predefined quantiles, such as the 5th, median, and 95th quantiles.

However, MCF does have limitations. It is not suitable for identifying if interactions between inputs are causing the output to exceed the predefined threshold value. Therefore MCF should not be the only type of SA considered when trying to rank inputs or identify un-important inputs.

Implementation

As with Section A-2.3, the nomenclature used throughout this section is consistent with Saltelli's. MCF is rather straightforward to implement. As part of this work, MCF is implemented as a post-processing step after a standard Monte Carlo sampling sequence. Alternatively, MCF can be implemented during the sampling process itself, either implementation is correct. Either way, the samples will be divided into two subsets or bins B or $\bar{B}$. Using PCT as an example, B could represent the set of all samples where the PCT exceeds the specified threshold value (whether the NRC limit or a desired quantile value), while $\bar{B}$ would be the set of samples with the PCT below the threshold value. By binning or filtering the samples into these two subsets, two subsets of input parameter samples also exist for each i-th input: $(X_i|B)$ with N_{Sm} samples and $(X_i|\bar{B})$ with N_{Sn} samples. Note that $N_S = N_{Sm} + N_{Sn}$.

The goal is to answer if the input parameter distributions within each bin are the same or not. To do so, the Smirnov two-sample (two-sided version) test is used for each input independently of the others. The null hypothesis is that the two distributions $p_m(X_i|B)$ and $p_n(X_i|\bar{B})$ are identical:

$$\begin{aligned} H_0 &: \; p_m\left(X_i \mid B\right) = p_n\left(X_i \mid \bar{B}\right) \\ H_1 &: \; p_m\left(X_i \mid B\right) \neq p_n\left(X_i \mid \bar{B}\right) \end{aligned} \tag{189}$$

The test statistic is defined by:

$$d_{m,n}\left(X_i\right) = \sup_{\mathrm{Y}} \left\| F_m\left(X_i \mid B\right) - F_n\left(X_i \mid \bar{B}\right) \right\| \tag{190}$$

where F denotes the marginal cumulative density function (CDF). The test statistic is therefore simply the max difference between the two CDFs over the support of the i-th input parameter. The Smirnov test answers the following question: "At what significance level α does the computed value of $d_{m,n}$ determine the rejection of H_0?" A low level for α implies a significant difference between $p_m(X_i|B)$ and $p_n(X_i|\bar{B})$, suggesting that X_i is a key factor in producing the defined behavior for the model. Keeping the same PCT example, X_i would thus be important to the PCT exceeding the specified threshold value. A high level for α however supports H_0, implying an unimportant factor: any value in the predefined range is likely to fall in either B or $\bar{B}$. Since the i-th input can take on any value, whether the PCT exceeds its threshold value or not, by itself X_i does not significantly influence the PCT at exceeding its threshold value.

The significance level α, which is the probability of rejecting the null hypothesis, is inversely related to the importance of the uncertainty of each input. Following Saltelli, the input parameters are grouped into three sensitivity classes, based on the significant level for rejecting the null hypothesis:

1. Critical ($\alpha < 1\%$)
2. Important ($1\% \leq \alpha \leq 10\%$)
3. Insignificant ($10\% > \alpha$)

To implement the Smirnov test, a critical value $D(\alpha)$ is computed for the boundaries on the sensitivity classes. The critical value depends on the desired significance level, as well as the number of samples within each bin:

$$D\left(\alpha\right) = c\left(\alpha\right)\sqrt{\frac{N_{Sm} + N_{Sn}}{N_{Sm}N_{Sn}}} \tag{191}$$

For the specific sensitivity class boundaries: $c(\alpha = 0.01) = 1.63$ and $c(\alpha = 0.1) = 1.22$. For the i-th input, if $d_{m,n} > D(\alpha)$, then the null hypothesis is rejected with significance level α.

A-2.4 Limit Surface

A-2.4.1 Overview

The limit surface identifies all combinations of input values that lead to the output meeting some defined condition. The name "limit surface" itself implies that those particular input values lead to the output reaching some "limiting" or "safety critical" condition. With these combinations identified, the probability of such an event occurring can be estimated.

Within this work however, the primary goal is to identify the combination of input values that lead to the desired output condition, not necessarily to compute the probability of such an event occurring. This may or may not be the true "limiting case", i.e. the PCT and ECR exceeding their Regulatory limits but rather some pre-defined situation. For example, this allows identifying the input combinations that correspond to the PCT exceeding its 95th quantile.

In many respects, the limit surface is very similar to MCF. Both are trying to identify input value combinations that cause the output to meet some predefined condition. From that viewpoint, both are inverse problems in that we know the condition we want to satisfy and our goal is to identify the input values that allow that condition to occur. Thus, MCF could be used to identify the limit surface. The downside though is the sampling efficiency is directly related to the probability of the limit surface occurring. For example, if the limit surface is defined as all PCT values exceeding the 95th quantile estimate, the sampling efficiency will be roughly 5%. To try and improve the sampling efficiency Likelihood-Free Markov Chain Monte Carlo (LF-MCMC) is applied instead.

The remainder of this section summarizes the LF-MCMC algorithm used within this work.

A-2.4.2 Likelihood-Free Markov Chain Monte Carlo (LF-MCMC)

Limit Surface Probability Model

Likelihood-Free Markov Chain Monte Carlo (LF-MCMC) is a particular class of MCMC sampling schemes where the likelihood function is analytically intractable. The term likelihood function comes from Bayesian analysis which relates the unknown of interests to observed data. The Bayesian framework is employed here, because as described earlier the limit surface is fundamentally an inverse problem. The input parameter values that correspond to the limit surface are unknown, but the output condition that defines to the limit surface is known. Therefore, the output condition is treated as the "observed" data. The assumed sampling distributions on the uncertain inputs are treated as the priors on the possible space of input values to search over. The "posteriors" on the input parameters correspond to the combination of values that allow the specified output condition to be met.

The goal of MCMC is to draw samples from an unknown posterior distribution. In unnormalized terms, the posterior distribution of interest in the likelihood free (LF) setting is:

$$p\left(\mathbf{x}, y \mid y_{LIM}\right) \propto p\left(y_{LIM} \mid y, \mathbf{x}\right) p\left(y \mid \mathbf{x}\right) p\left(\mathbf{x}\right) \tag{192}$$

where $\mathbf{x}$ is the vector of uncertain input parameters, y is the output of interest, and y_{LIM} is the specific output value that defines the limit surface. Equation (192) provides a joint probability statement about the computer code output values, $y = f(\mathbf{x})$, and the uncertain input parameter values, $\mathbf{x}$, that exist given the limit surface condition. For simplicity, this work assumed that the limit surface was simply defined as the output meeting or exceeding the desired threshold value, $y \geq y_{LIM}$. In general, more complicated limit surface definitions could be used.

The likelihood function between the limit surface and the output is also defined simply as:

$$p\left(y_{LIM} \mid y, \mathbf{x}\right) \propto \begin{cases} \text{constant}, & y \geq y_{LIM} \\ 0, & \text{else} \end{cases} \tag{193}$$

Equation (193) therefore places a hard constraint on the limit surface boundary. Any output prediction less than the limiting value is considered to have a probability of zero. The fact that the non-zero portion of the likelihood probability model is only written up to a normalizing constant is perfectly valid within the MCMC sampling scheme. The exact likelihood function does not need to be defined for MCMC sampling. This is one of the benefits of using a sampling based approach to Bayesian inference.

The term $p(y|\mathbf{x})$ in Eq. (192) is the density function of a specific output value, given a specific set of input parameter values. This conditional probability statement is also unknown and will not have to be evaluated directly within the LF-MCMC sampling scheme. The exact mathematical details as to why are not given in this work but are provided in Ch. 12 of "The Handbook of Markov Chain Monte Carlo."

Lastly, $p(\mathbf{x})$, is the prior density function on the uncertain input parameters. If all of the inputs are scaled between 0 and 1 and are assumed to be independent and uniformly distributed the prior distribution is simply:

$$p\left(\mathbf{x}\right) = \prod_{i=1}^{D} p\left(x_i\right), \qquad p\left(x_i\right) = \begin{cases} 1, & 0 \leq x_i \leq 1 \\ 0, & \text{else} \end{cases} \tag{194}$$

LF-MCMC Sampling Scheme

A Random Walk Metropolis (RWM) sampling scheme is employed in this work. The RWM sampler is a very basic sampler and numerous other MCMC schemes exist. As the name suggests, RWM is a random walk around the input parameter space. It effectively searches from a given initial guess to find the set of input parameter combinations that satisfy the limit surface definition. The RWM sampler for LF-MCMC has the following steps:

- Initialize $\mathbf{x}_0$ and compute the initial output response, $y_0 = f(\mathbf{x}_0)$
- For a current step *t*:
  - Generate $\mathbf{x}' \sim q(\mathbf{x}'|\mathbf{x}_t)$ from a proposal distribution $q(\cdot)$
  - Generate the proposal output from the computer model, $y' = f(\mathbf{x}')$
  - Compute the acceptance probability (see "Handbook of MCMC" for mathematical details):

$$\alpha_{MH} = \frac{p\left(y_{LIM} \mid y', \mathbf{x}'\right) p\left(\mathbf{x}'\right) q\left(\mathbf{x}' \mid \mathbf{x}_t\right)}{p\left(y_{LIM} \mid y_t, \mathbf{x}_t\right) p\left(\mathbf{x}_t\right) q\left(\mathbf{x}_t \mid \mathbf{x}'\right)} \tag{195}$$

  - With probability $\min(1, \alpha_{MH})$ accept the proposal $(\mathbf{x}_{t+1}, y_{t+1}) = (\mathbf{x}', y')$ otherwise reject the proposal $(\mathbf{x}_{t+1}, y_{t+1}) = (\mathbf{x}_t, y_t)$
  - Repeat

Equation (195) is the Metropolis-Hastings acceptance probability. A Gaussian proposal distribution centered at the current step's value for the input parameters is used. This simplifies Eq. (195) since the Gaussian proposal is a symmetric distribution, and thus $q(\mathbf{x}'|\mathbf{x}_t) = q(\mathbf{x}_t|\mathbf{x}')$.

The specific form of the proposal distribution is:

$$q\left(\mathbf{x}' \mid \mathbf{x}_t\right) = \mathsf{N}\left(\mathbf{x}_t, \sigma_j^2 \mathsf{I}\right) \tag{196}$$

where σ_j^2 is a jumping variance and $\mathbb{I}$ is the identity matrix. The proposal distribution assumes the parameters are uncorrelated for simplicity, but that is not required in general. The jumping variance controls how far the proposal can "jump" or "step" in any of the input dimensions. To try and improve the sampling efficiency, the

jumping distribution is tuned to achieve a specified asymptotic optimal sampling efficiency for the RWM scheme.

A-2.5 Distributional SA

Distributional SA does not fit into any of the previously described categories. It is global in that all of the uncertain input parameters are still varied simultaneously over their entire ranges of possible values. It is essentially a sensitivity to various assumptions. Those assumptions can be the specified (assumed) sampling distribution on any one of the uncertain input parameters, or even values of inputs that were considered to be constant. The original assumptions will be referred to as the base case, while the modified assumptions will be referred to as the modified case.

The steps involved are straightforward:

- Perform UQ via Monte Carlo sampling on the base case
- Modify the specific assumption, re-perform UQ via Monte Carlo sampling
- Compare the resulting distributions on the outputs of interest

If the resulting output distributions are different between the base case and the modified case, then that assumption change was indeed an important change. The other SA types should therefore be re-performed to see if the input sensitivities also changed with the modified case.

A-3. Additional Insights from the Analysis Results

A-3.1. Non-parametric Statistical Analysis Results (Small Sample Size Results)

Purpose of Appendix A-3 is to provide additional insights on the analysis of results presented in Section 3.4 and to provide the motivation behind the choice of the RIMM IEM to move toward larger sample sizes with MC estimators.

Under the proposed rule PCT and ECR need to be presented as a function of the pre-transient hydrogen content. Instead, [OG-11-143 PWROG 50.46(b)] was used to correlate the hydrogen content with the fuel rod average burnup for Zircaloy-4 cladding. [OG-11-143 PWROG 50.46(b)] shows the pre-transient hydrogen pickup content (PPM) versus fuel rod average burnup for Zircaloy-4 cladding. A curve fitting for [OG-11-143 PWROG 50.46(b)] was done to yield the following:

$$\mathrm{H} = 0.0035\mathrm{BU}^3 - 0.1235\mathrm{BU}^2 + 5.1073\mathrm{BU} + 21.075 \quad (1)$$

where H is the hydrogen content in PPM and BU is the fuel assembly average burnup in GDW/MT.

Different Wilks based estimators are compared along with the Monte Carlo estimator for the (small) sample size of 124 (random) samples at each of the 8 exposure points. In all of the results, note that the ECR values are doubled from the RELAP5-3D calculated values for the non-burst fuel rods to comply with current industry practice.

Figure A-2 shows the Wilks-59 sample based 95/95 estimators as a function of the hydrogen content for both PCT and ECR. The estimator associated with each exposure point is denoted with a colored 'x'. Note that there are two consecutive 59 run-sets for each exposure point. That is why there are two 'x' markers for each exposure point in Figure A-2. The results for the hot rod in the first cycle of irradiation are in blue whereas results for the second and third cycles of irradiations are respectively in purple and green. Figure A-2 shows that two of the 95/95 PCT estimators are almost on top of the limit line (denoted by red). If there were only 59 samples used, it would appear that the PCT predictions would be at the NRC limit. However, as shown in Figure A-2 at the same two exposure points, the second 59-sample 95/95 estimators are roughly 100 degrees Kelvin below the NRC limit. This is an illustration of the variability of the 59-sample 95/95 Wilks estimator, which will be discussed in more detail when analyzing the large sample size results. Also note that the 59-sample 95/95 Wilks based estimator can only be used for a single output of interest. The PCT and ECR 95/95 estimators are marginal estimators that do not consider the joint structure between the two. Wilks-based estimators for 2 outputs are considered as part of the large sample size results analysis later on.

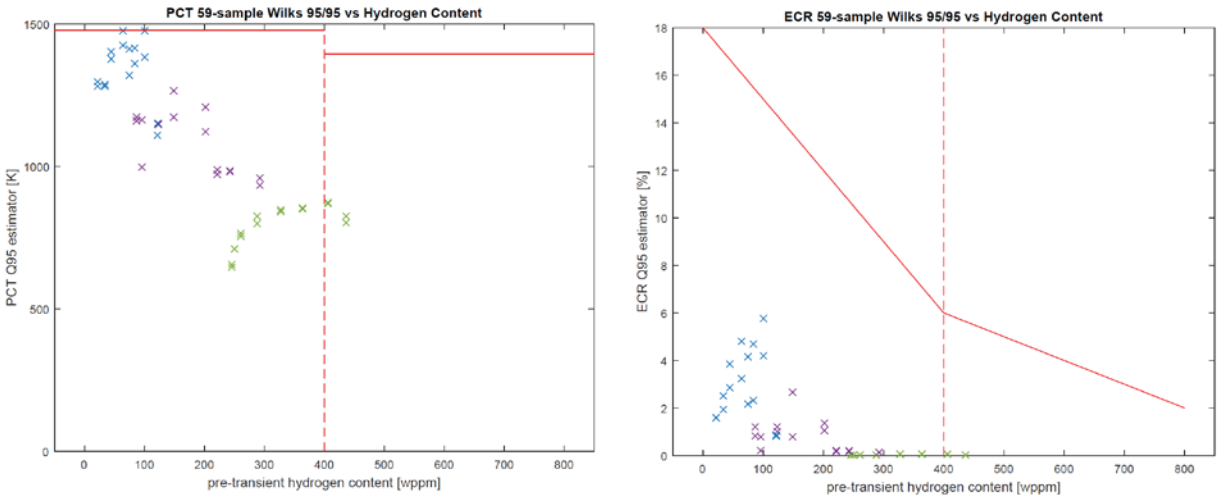

Figure A-2. Wilks 59-Sample Based 95/95 PCT and ECR Estimators During LB-LOCA Transients (Blue=Fresh Fuel, Purple=Once-Burnt, Green=Twice-Burnt).

Figure A-3 shows the analogous plots for the Wilks 124-sample based 95/95 (rank k=3) PCT and ECR estimators. The higher order 124-sample Wilks estimators indicate that the LB-LOCA results are in compliance, at each of the 8 exposure points. This represents that the two 59-sample estimators at the NRC limit in Figure A-2 are most likely in the extreme tails of their respective PCT distributions. The higher order Wilks estimator truncates these tail values.

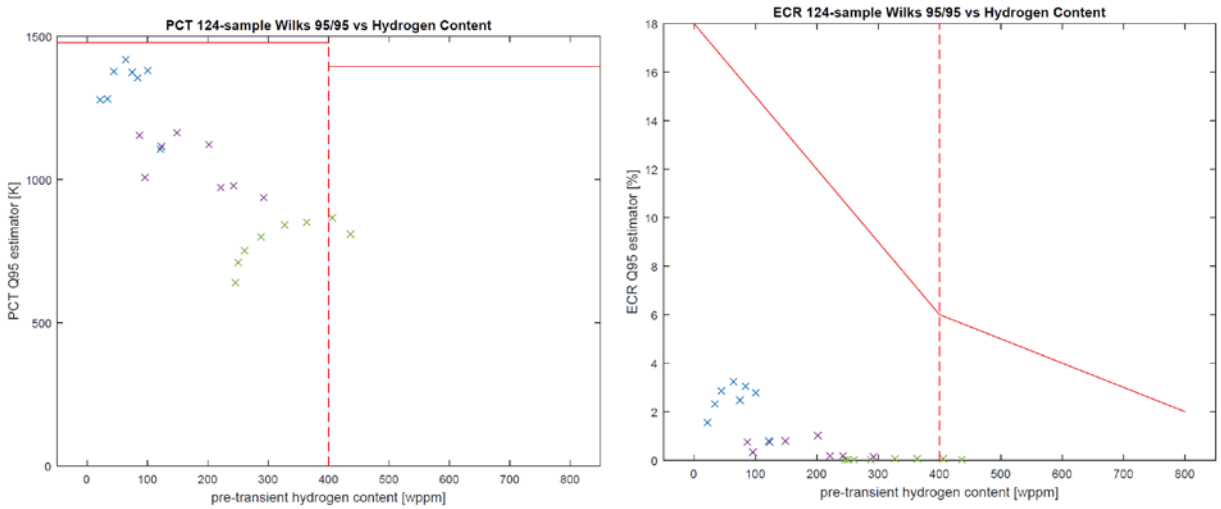

Figure A-3. Wilks 124-Sample Based 95/95 PCT and ECR Estimators During LB-LOCA Transients (Blue=Fresh Fuel, Purple=Once-Burnt, Green=Twice-Burnt).

The entire dataset (all samples within each region of the core) is shown in the left plot in Figure A-4. It is easy to see that the two 59-sample Wilks estimators correspond to the two highest PCT values in the entire dataset. The right hand side plot in Figure A-4 shows the Monte Carlo 95th quantile estimator with corresponding 95th confidence interval represented by the error bar at each exposure point. The approximate 95% confidence interval for the 95th quantile estimator is defined in Appendix A-2. With such a small sample size (124 random samples) the 95th quantile estimators are rather uncertain. The 95% confidence interval around each estimator in the fresh fuel region of the core spans roughly 100 degrees Kelvin. The reason why the other two regions are estimated with more precision is easy to see by inspecting the left hand side plot in Figure A-4. The once-burnt and twice-burnt regions PCT samples span smaller ranges compared to the fresh-fuel PCT samples, and thus the once and twice burnt region PCTs have smaller sample standard deviation. As described in Appendix A-2, a small sample standard deviation leads to a smaller standard error on the Monte Carlo estimators. The analogous figures for all ECR samples and the Monte Carlo 95th quantile estimators within each region at all of the exposure points are shown in Figure A-5.

As a reminder, when examining Figure A-2 through Figure A-5, the core is characterized by a triplet of PCT and ECR values at any given time in cycle (exposure point). The “triplet state” corresponds to the PCT and ECR values for the hot rods in each of the regions: fresh-fuel (1st cycle), once-burnt (2nd cycle), and twice-burnt (3rd cycle). The triplet is highlighted by the ‘ellipse’ in Figure A-4. As time in cycle increases, the “triplet state” moves to the right. For the specific core design considered in this study, the 95th quantile PCT estimator closest to the limit occurs for the hot rod during its first cycle of irradiation. The most limiting ECR condition is a little more difficult to define because the NRC limit decreases with time in cycle, but the highest 95th quantile ECR estimator also occurs in the first cycle of irradiation. Since the first cycle predictions have higher uncertainty throughout the cycle length than the other two regions of the core, it seems that for specific core design considered in this study, the limiting conditions on both PCT and ECR occur in the fresh-fuel region of the core.

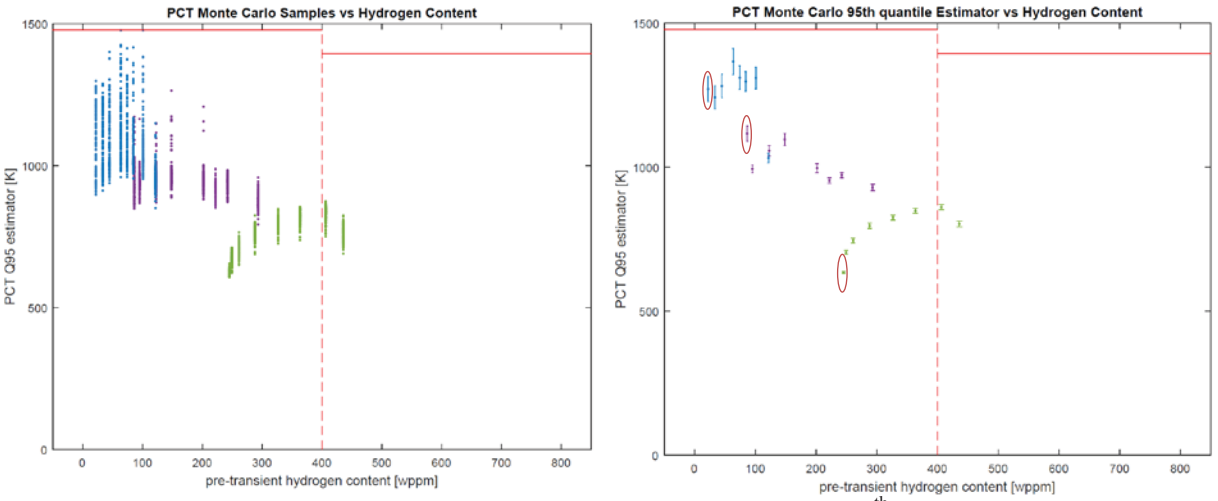

Figure A-4. All 124 Monte Carlo PCT Samples and the Monte Carlo 95th Quantile Estimators per Exposure Point (Blue=Fresh Fuel, Purple=Once-Burnt, Green=Twice-Burnt), the "Triplet State" at BOC is Marked by Ellipses.

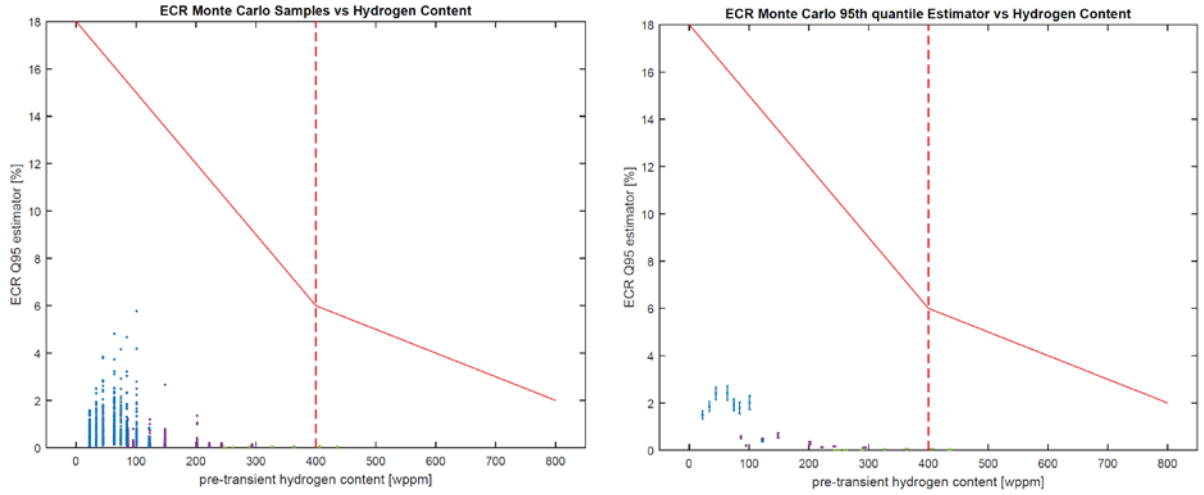

Figure A-5. All 124 Monte Carlo ECR Samples and the Monte Carlo 95th Quantile Estimators per Exposure Point (Blue=Fresh Fuel, Purple=Once-Burnt, Green=Twice-Burnt).

The 124 samples are analyzed in more detail at three specific times in cycle, BOC, 300 days, and 500 days. These three times were chosen because they are the three specific times in cycle used in the large sample analysis. The following figures can therefore be directly compared to the figures in Section 4.3.2 which used 1240 samples per exposure point.

Figure A-6 through Figure A-8 show both the histograms and CDFs for all three regions in the core at the three specific exposure points of BOC, 300 days, and 500 days, respectively. At the BOC, there are clearly not enough samples to discern a "shape" to the PCT distribution in the first and second cycles of irradiation. As the time in cycle increases, a more discernable "shape" to the PCT histogram starts to appear, and a very long tail develops to the PCT distribution in first cycle of irradiation. It is important to remember that results are specific to the core design and RELAP5 model used in this study. The observed trends may not generalize to actual plants, but similar visualization and statistical analyses can be conducted to reveal interesting and useful relationships.

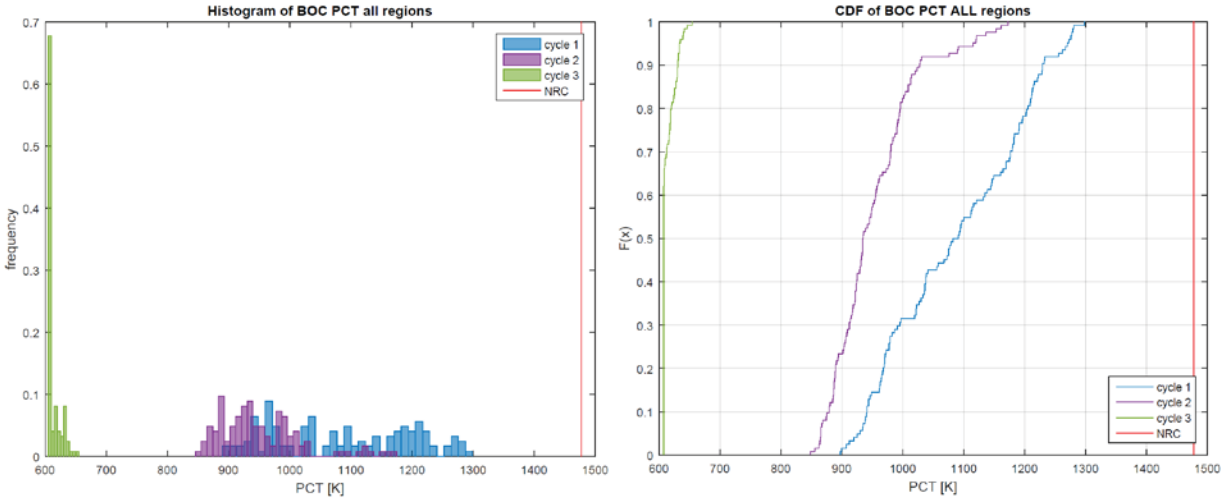

Figure A-6. PCT Histograms and CDFs at BOC (Small Sample N=124).

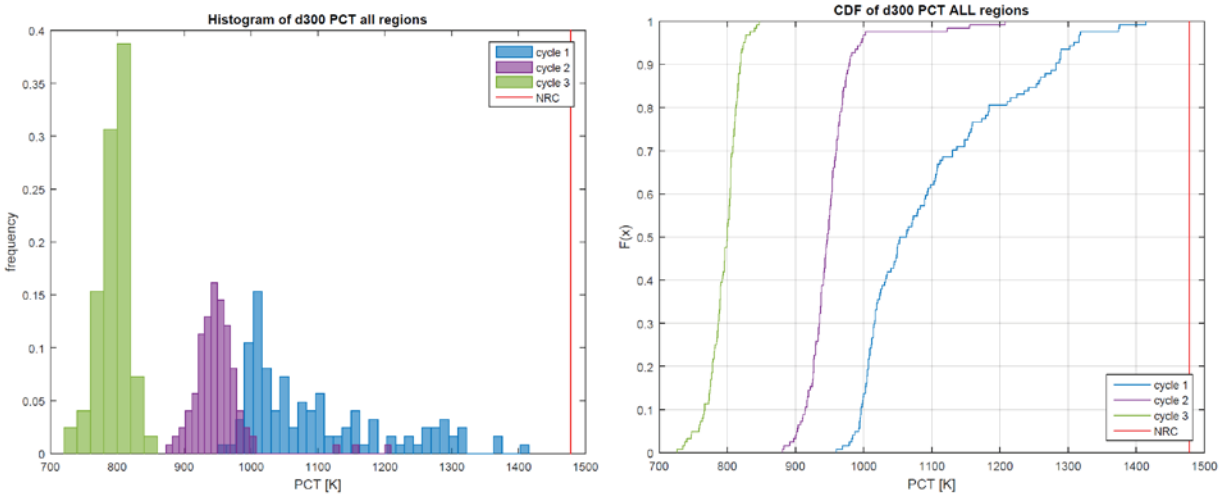

Figure A-7. PCT Histograms and CDFs at 300 Days in the Cycle (Small Sample N=124).

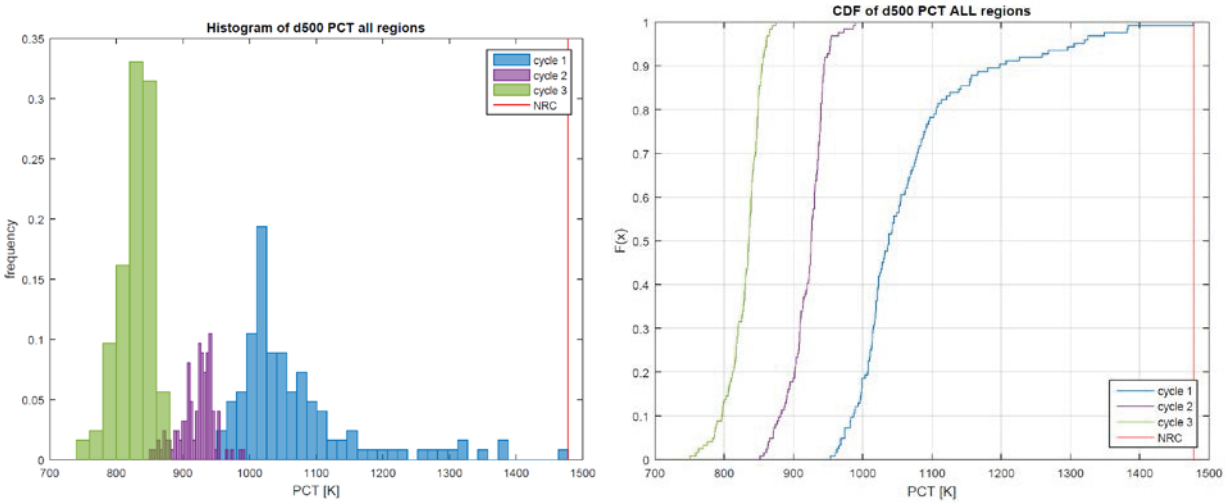

Figure A-8. PCT Histograms and CDFs at 500 Days in the Cycle (Small Sample N=124).

Figure A-6 reveals another interesting trend that at the BOC there is considerable overlap between the PCT histograms during the first and cycles of irradiation. The 95th quantile estimator of the PCT in the first cycle is considerably higher than the 95th quantile estimator of the PCT in the second cycle. Although this was already visualized by Figure A-4, Figure A-9 illustrates this concept in more detail. The left plot in Figure A-9 is the CDF for the PCT in cycle 1 at the BOC and the right plot is the CDF for the PCT in cycle 2 at the BOC. In both plots, the solid black line marks the Monte Carlo 95th quantile estimator and the black dashed lines are the 95% confidence interval bounds. As already mentioned, the 95% confidence interval bound spans roughly 100 K in cycle 1 at the BOC. The upper bound on the 95th quantile estimator's confidence interval (CI) in cycle 2 is almost 100 K below the lower bound on cycle 1's 95th quantile estimator.

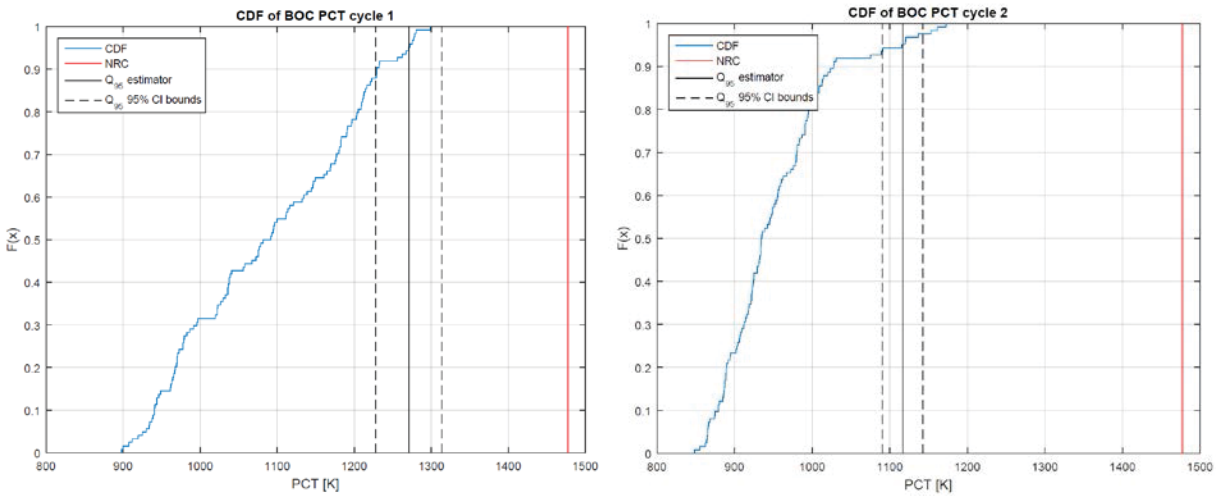

Figure A-9. PCT CDFs with 95th Quantile Estimator and Confidence Interval (CI) Bounds for Cycle 1 (Left) and Cycle 2 at BOC.

Figure A-10 and Figure A-11 compare different Wilks 95/95 estimators to the "full" Monte Carlo 95th quantile estimator (which used all 124 samples) at the BOC and 500 days, respectively. Previously, Figure A-2 and Figure A-3 only used Wilks estimators that considered one output at a time (specifically the max of 59 samples and the third highest of 124 samples). Figure A-10 and Figure A-11 also include the Wilks estimators that consider two outputs simultaneously. The lowest order two-output Wilks estimator is the max of 93 samples and a higher order estimator is the second highest of 124 samples. These figures also reveal that cycle 1 has the highest 95th quantile estimators, regardless of the type of estimator chosen to approximate the 95th quantile. As with Figure A-2, the 59-sample Wilks based estimator has two points because there are two consecutive sequences of 59 random samples within 124 random samples. The left and right plots in Figure A-12 zoom in on the estimators at the BOC in cycle 1 and cycle 2, respectively. The small sample size makes it difficult to draw conclusions about the variability in the Wilks based estimators versus "full" Monte Carlo analysis, at a specific time in cycle. More samples are therefore needed, which provides motivation for analyzing the large sample size results in the next section.

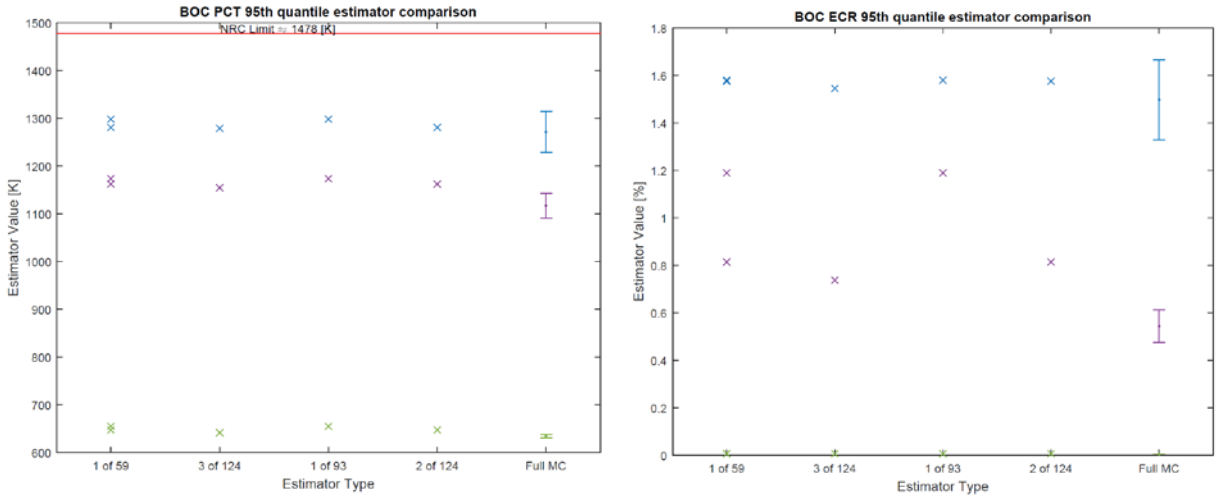

Figure A-10. PCT and ECR 95th Quantile Estimator Comparisons at the BOC (Blue=Fresh Fuel, Purple=Once-Burnt, Green=Twice-Burnt).

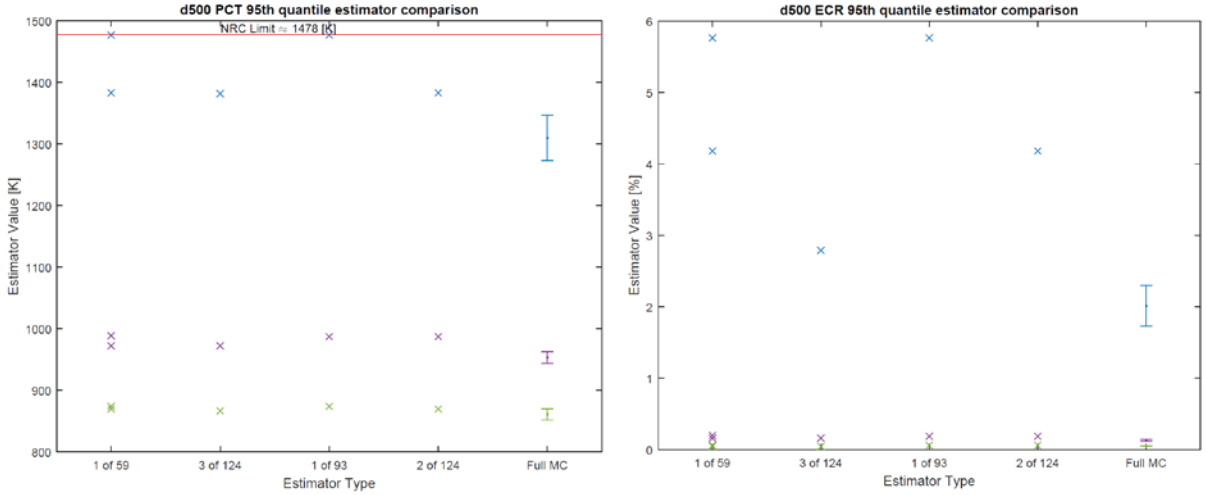

Figure A-11. PCT and ECR 95th Quantile Estimator Comparisons at 500 Days (Blue=Fresh Fuel, Purple=Once-Burnt, Green=Twice-Burnt).

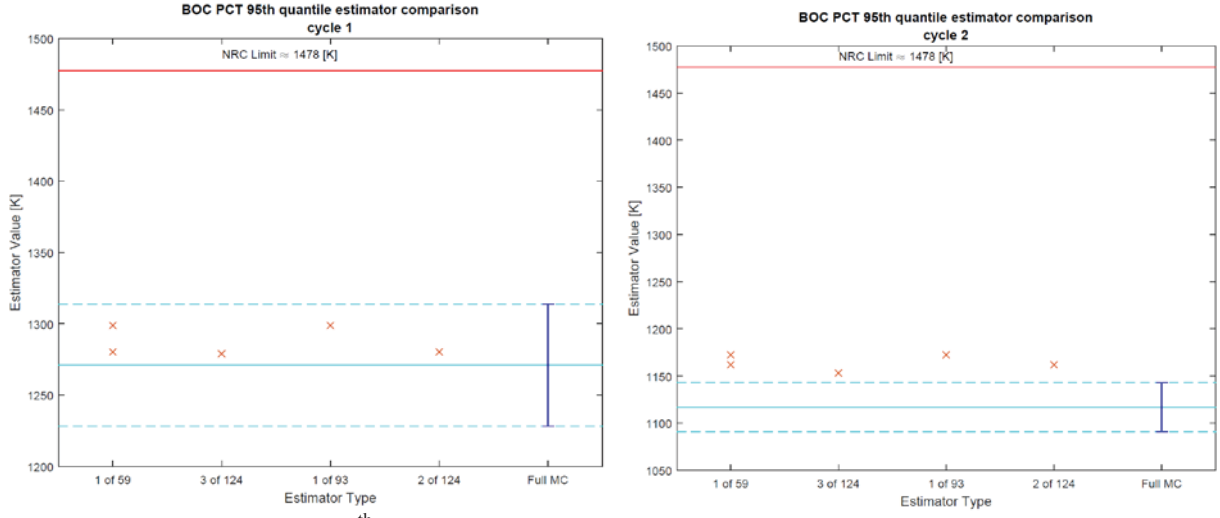

Figure A-12. PCT and ECR 95th Quantile Estimator Comparisons at the BOC in Cycle 1 (Left) and Cycle 2 (Right).

A-3.2. Monte Carlo Analysis Results (Large Sample Size Results)

With more samples, the benefit of "full" MC analysis over Wilks becomes more apparent. This section used 1240 random samples at three times in cycle, namely the BOC, 300 days and 500 days. Typically, the exact number of Monte Carlo samples is chosen to achieve a desired standard error value. However in this work, 1240 samples were chosen because that gives 10 consecutive sequences of 124 random samples. Ten consecutive 124-sample Wilks based estimators can therefore be evaluated. These 10 samples will be used to represent the possible variability in the 124-sample Wilks based estimator.

Figure A-13 shows the PCT and ECR results for the three 1240 run-sets performed at BOC, 300 and 500 days, as a function of the pre-transient hydrogen content. Figure A-4 showed all of the 124 random samples at each of the 8 exposure points considered in the small sample analysis. That figure did not show any samples considerably above the NRC limit. However, with ten times the number of samples several random cases do in fact exceed the Regulatory limit on PCT. This does not mean the design is out of compliance since those cases are associated to a very low probability. Remember that the 50.46 rule simply states "[…] *uncertainty must be accounted for, so that, when the calculated ECCS cooling performance is compared to the criteria […], there is a high level of probability that the criteria would not be exceeded*". General practice is to estimate the 95th quantile of the possible outcome and ensure that value is below the regulatory limit. More on the interpretation of the rule is given in Section 4.3.3.

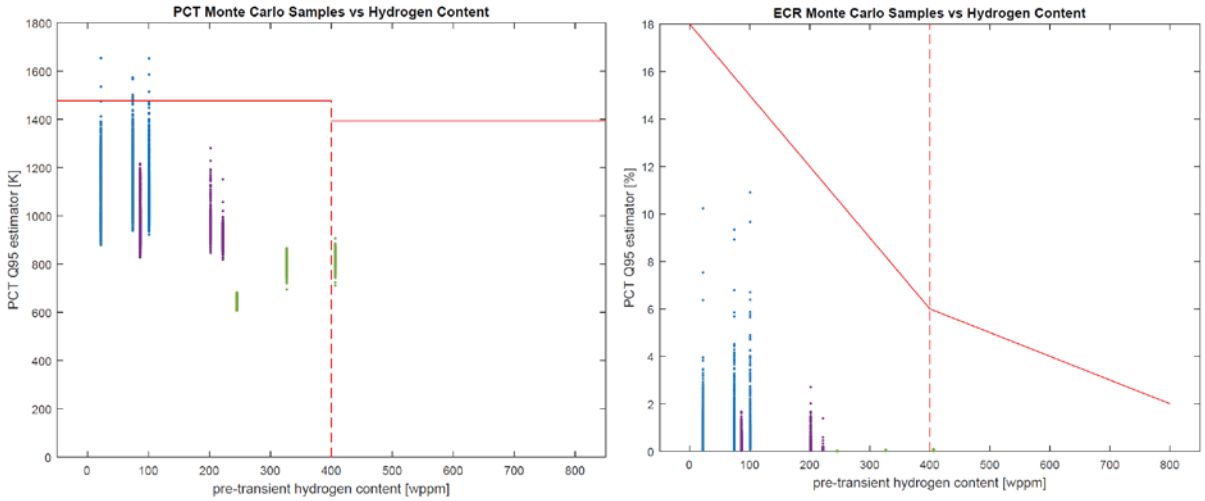

Figure A-13. All 124 Monte Carlo PCT (Left) and ECR (Right) Samples at the BOC, 300 Days and 500 Days (Blue=Fresh Fuel, Purple=Once-Burnt, Green=Twice-Burnt).

Just as in the previous section, various 95th quantile estimators will be compared to the NRC limits on both PCT and ECR. However with 1240 samples compared to 124 samples, the "full" Monte Carlo estimator will be evaluated with higher precision. As already mentioned there are 10 consecutive samples of the 124-sample Wilks estimator, as well as 21 consecutive samples of the 59-sample Wilks estimators. These samples are used to estimate the mean Wilks based estimator, along with its associated standard error. To illustrate the variability on the Wilks based estimators, a vertical line is included between the minimum and maximum Wilks based estimator sample values. A particular random realization of the Wilks based estimator can occur anywhere along that vertical line, though the most likely value is near the mean Wilks based estimator value.

Figure A-14 and Figure A-15 provide the Wilks based estimators on the PCT and ECR, respectively. In each figure, the left hand side plot shows the 59-sample Wilks based estimator and the right hand side plot shows the 124-sample Wilks based estimator. The mean Wilks based estimators are shown as error bars with their colors indicating the core region, just as in the previous figures. The vertical lines which span the range of the Wilks based estimator samples are shown behind their corresponding mean Wilks based estimator. The most important observation to take away from Figure 19 and Figure 20 is that the 124-sample Wilks based estimator clearly has

less variability than the 59-sample Wilks based estimator. For example, at the BOC the 59-sample Wilks based estimator in cycle 1 spans a range of nearly 400 K. The upper portion of that range is clearly out of compliance. The 124-sample Wilks based estimator, however, spans a range of only roughly 100 K. This concept is even more pronounced on the ECR, since as shown in Figure A-13 the cycle 1 ECR samples have very long tails.

If the 59-sample Wilks based estimator was used to assess if the design complies with the NRC rule, there is a random chance that this specific core design and LB-LOCA transient results would appear to be out of compliance. On average (as indicated by the mean 59-sample Wilks based estimator), the 59-sample Wilks based estimator at the BOC would be compliant, but a single safety analysis (which corresponds to a single realization of the 59-sample Wilks based estimator) might be out of compliant. This concept is shown further by Figure 21 at the BOC. Figure A-16 is analogous to Figure A-10, except an additional Wilks based estimator is included the 208-sample based 95/95 (rank k=6) estimator. The mean 208-sample estimator is estimated from the 5 consecutive 208 random samples within the 1240 random samples at each of the three times in cycle. With only 5 samples, the mean 208-sample Wilks based estimator is rather imprecise compared to its relatively small range. As with Figure A-10 the last estimator shown in Figure A-16 is the "full" Monte Carlo estimator with its 95% confidence interval. It is quite clear that the Monte Carlo estimator is capable of recovering a substantial amount of margin compared to the Wilks based estimators, especially since there is a random chance that a single Wilks based estimator may significantly over-estimate the "true" 95th quantile.

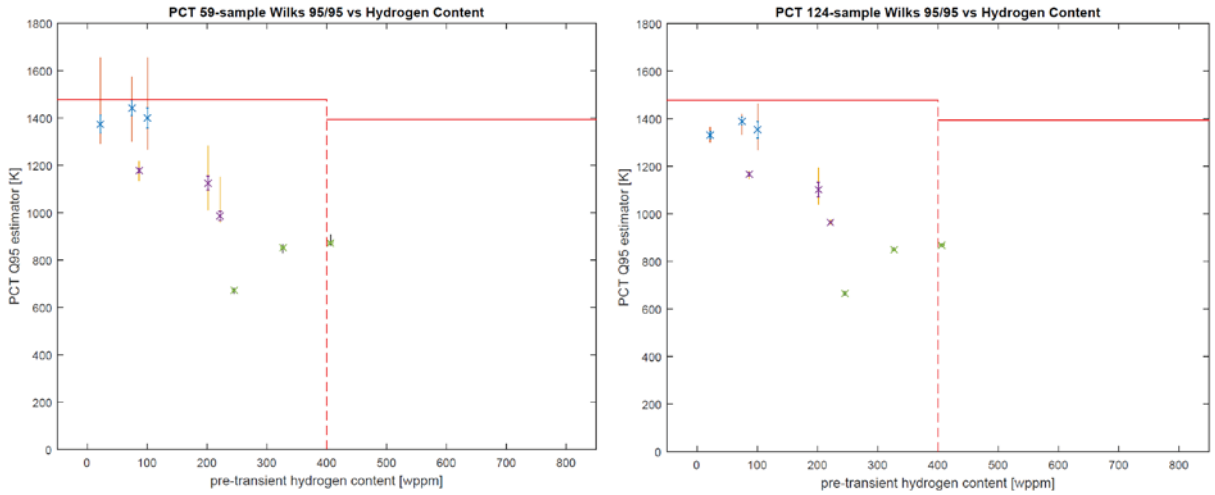

Figure A-14. 14. Wilks 59-Sample Based 95/95 PCT Estimators during LB-LOCA Transients (Blue=Fresh Fuel, Purple=Once-Burnt, Green=Twice-Burnt).

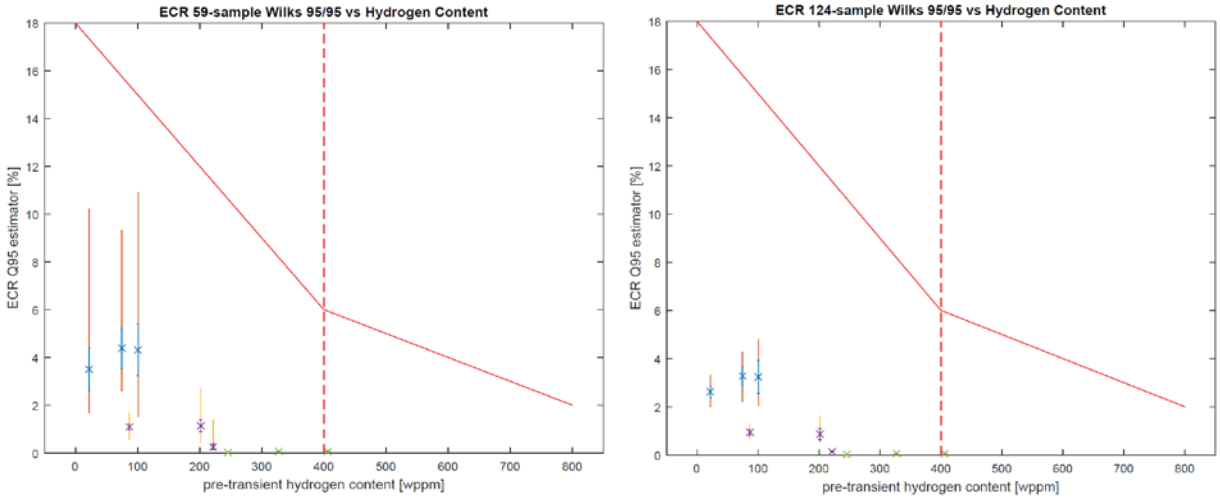

Figure A-15. Wilks 124-Sample Based 95/95 ECR Estimators during LB-LOCA Transients (Blue=Fresh Fuel, Purple=Once-Burnt, Green=Twice-burnt).

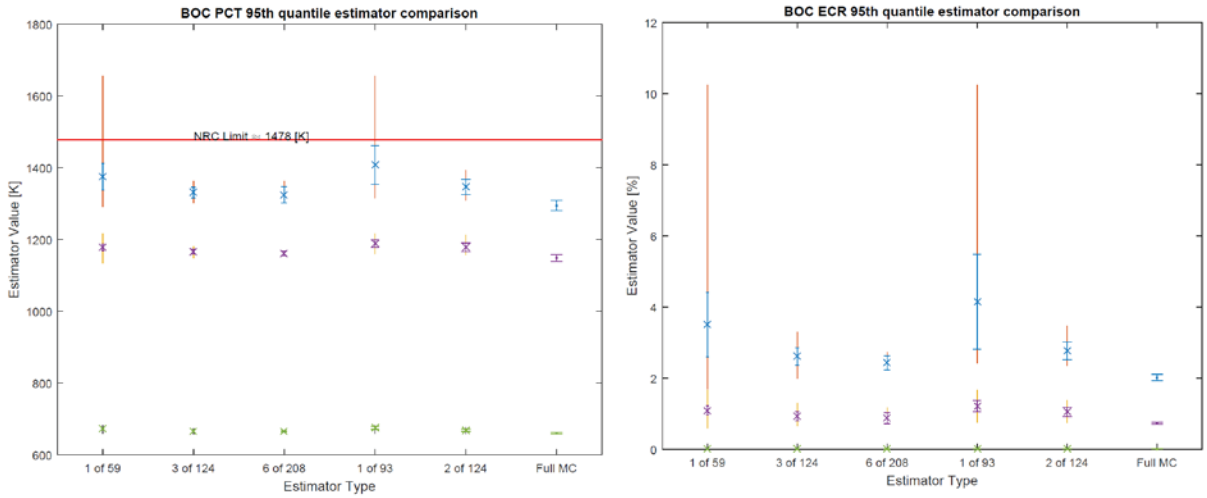

Figure A-16. Comparison between Wilks and MC Estimators for PCT and ECR at BOC (Blue=Fresh Fuel, Purple=Once-Burnt, Green=Twice-burnt).

Although slightly difficult to see, Figure A-16 also shows that there is a finite chance that the Wilks-based estimators under-predict the "true" 95th quantile. The left hand side plot of Figure 22 zooms in on the 95th quantile estimators for cycle 1 at the BOC. As a comparison, the right hand side plot of Figure A-17 is a copy of the left hand side plot of Figure A-12, which provided the same analysis on the 124 random samples. Note that the y-axis scales are different between the left and right plots in Figure A-17 Comparing the left and right plots reveals several important observations. First, the lowest 59-sample Wilks based estimator from the 124 sample size data set are actually less than the minimum value observed in the 1240 sample size data set. This is allowable since the minimum value is only the minimum observed value and not necessarily the "absolute" minimum possible value the 59-sample Wilks based estimator could obtain. Second, the Monte Carlo estimator from the 124 sample size data set is significantly lower than the Monte Carlo estimator from the 1240 sample size data set (compare the cyan horizontal lines between the left and right hand side plots in Figure A-17. Thus, even though both 59-sample Wilks based estimators appeared higher than the Monte Carlo estimator in the 124 sample size data set, the lower of those two is in fact **less** than the (more precise) Monte Carlo estimator from the 1240 sample size data set. Therefore, if that particular realization from the 124 sample size data set had been used to demonstrate compliance, it would appear moving to a larger sample size would lose margin. This should not be construed as a negative against moving to larger sample sizes, since as shown by Figure A-17, on average "full" Monte Carlo estimators to the 95th quantile will recover margin relative to Wilks based estimators.

Figure A-17 also illustrates the importance of including the Monte Carlo standard error on the 95th quantile estimator. The upper 95% confidence interval bounds on the Monte Carlo estimator are rather similar between the 124 and 1240 sample size datasets. As shown with the Framework Demo results, such will not always be the case, but the 95% confidence interval bounds provide a clear visualization of the uncertainty on the estimator due to the finite sample size. Such information is not accessible for the Wilks based estimators, because the Wilks based estimators have such a concept "folded into" them already. The Monte Carlo estimator upper confidence interval bound helps reduce the chance that the true 95th quantile is being under estimated.

As described previously, the Wilks based estimators that use the max of 59 samples and the third highest of 124 samples cannot be used for LB-LOCA analysis because there is more than one output of interest. In order to ensure that the estimators are bounding to the unknown true 95th quantiles simultaneously for both PCT and ECR essentially requires adding additional conservative to the estimating quantities This is also illustrated by Figure A-17 which includes the range and mean to the max of 93 samples and the second highest of 124 samples. **Since these more conservative Wilks based estimators are actually used under the current NRC rule, the chance that larger sample size Monte Carlo estimators recover margin is even higher**. Under the proposed rule, a single summary oxidation calculation such as MLO cannot be considered since the ECR limit

line depends on the pre-transient hydrogen content, which depends on the core region. Thus, the number of outputs that must be tracked would increase leading to potentially very conservative Wilks based estimators.

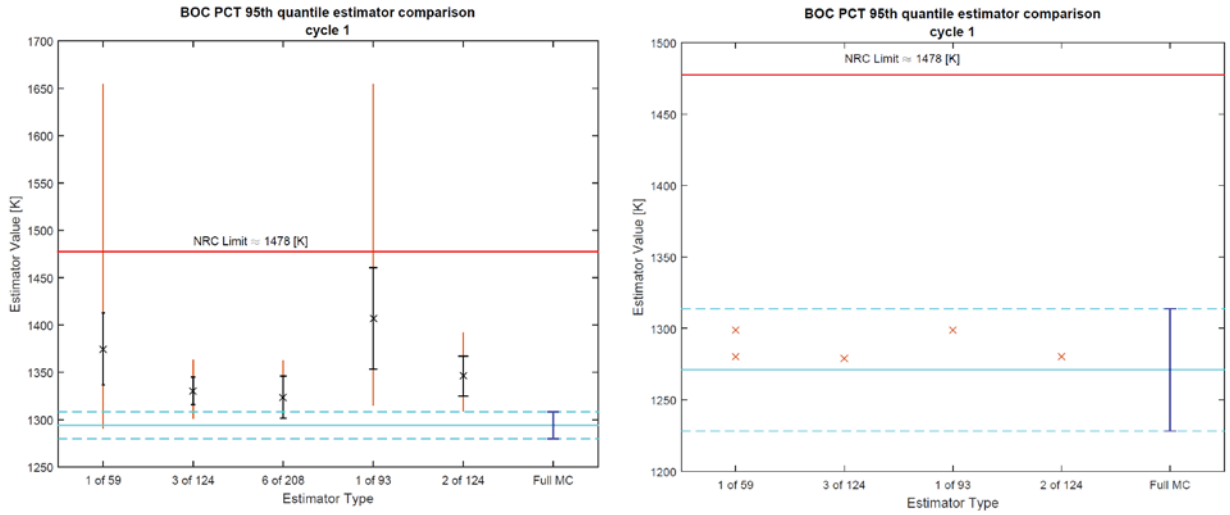

Figure A-17. Comparison between Wilks and MC Estimators for PCT and ECR at BOC, 1240 Sample Size (Left), 124 Sample Size (Right).

With Monte Carlo estimators, the number of outputs that must be tracked does not impact the required number of samples. Monte Carlo does not suffer from the "curse of dimensionality" in either the input or output spaces. Rather, as already discussed the sample size depends on achieving desired precision levels on the outputs of interest (by tracking their associated standard errors). The PCT and ECR "full" Monte Carlo 95th quantile estimators with their associated confidence intervals as the three exposure points considered in the 1240 sample size data set are shown in Figure A-18.

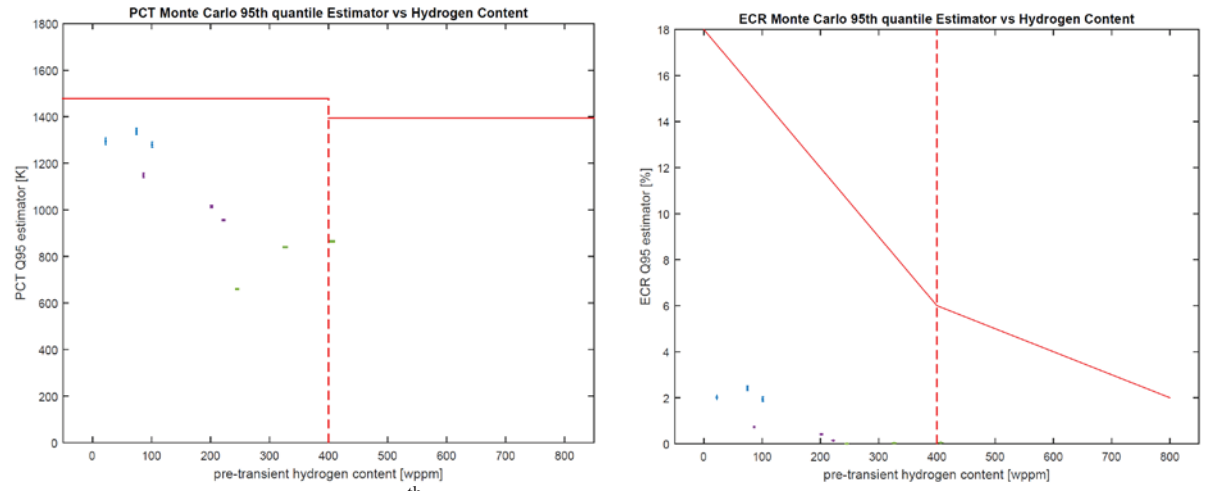

Figure A-18. Monte Carlo 95th Quantile PCT and ECR Estimators during LB-LOCA Transients (Blue=Fresh Fuel, Purple=Once-Burnt, Green=Twice-Burnt).

The histograms of the PCT at the three times in cycle are shown below in Figure A-19 through Figure A-21with the larger sample size data set. As expected, with more samples the distributions (as summarized by the histograms) are better resolved. Figure A-19 through Figure A-21 show several similar trends observed in Figure A-6 through Figure A-8. First, at the BOC the cycle 1 and cycle 2 PCT histograms show considerable overlap. Their overlap decreases as the time in cycle increases. Second, the cycle 1 PCT histogram develops a considerably long tail away from the central tendency as the time in cycle increases. Figure A-6 was not able to resolve any "shape" the cycle 1 PCT distribution. With more samples, it appears that the cycle 1 PCT

distribution is multimodal, with two peaks similar “height”. A single mode appears to start to dominate as the time in cycle increases.

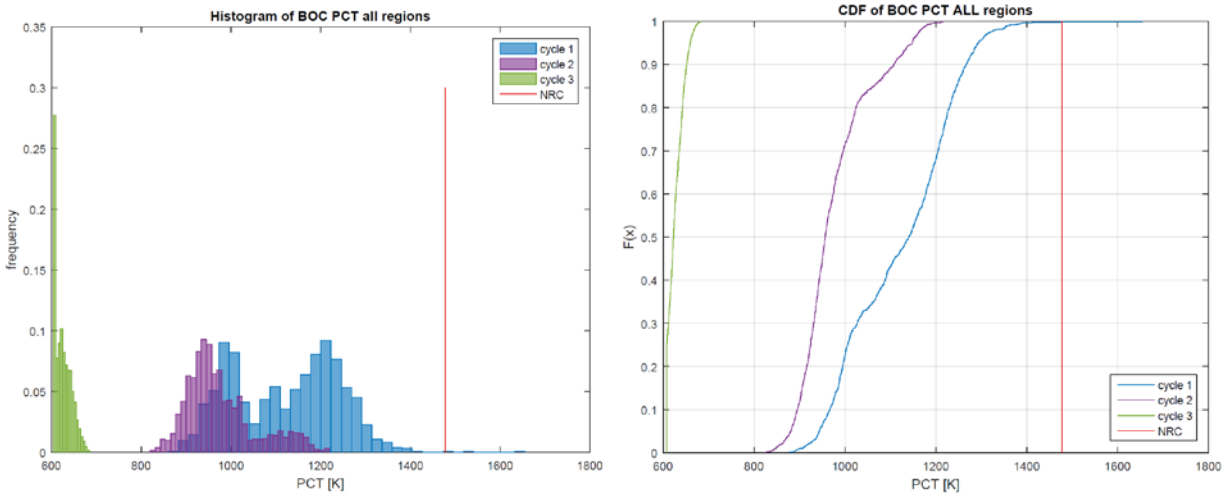

Figure A-19. PCT Histograms and CDF at BOC (Large Sample N=1240).

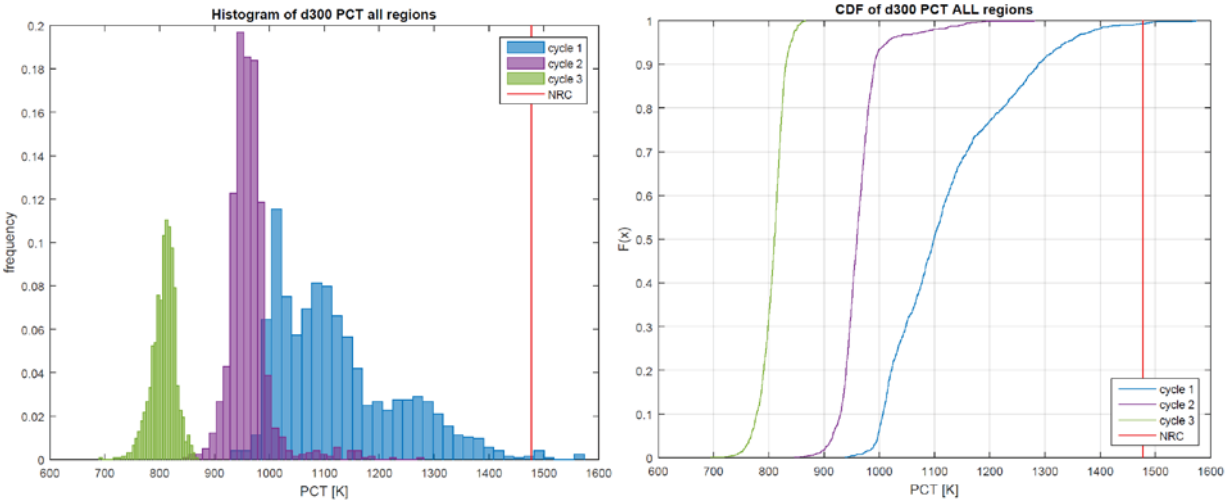

Figure A-20. PCT Histograms and CDFs at 300 Days in the Cycle (Large Sample N=1240).

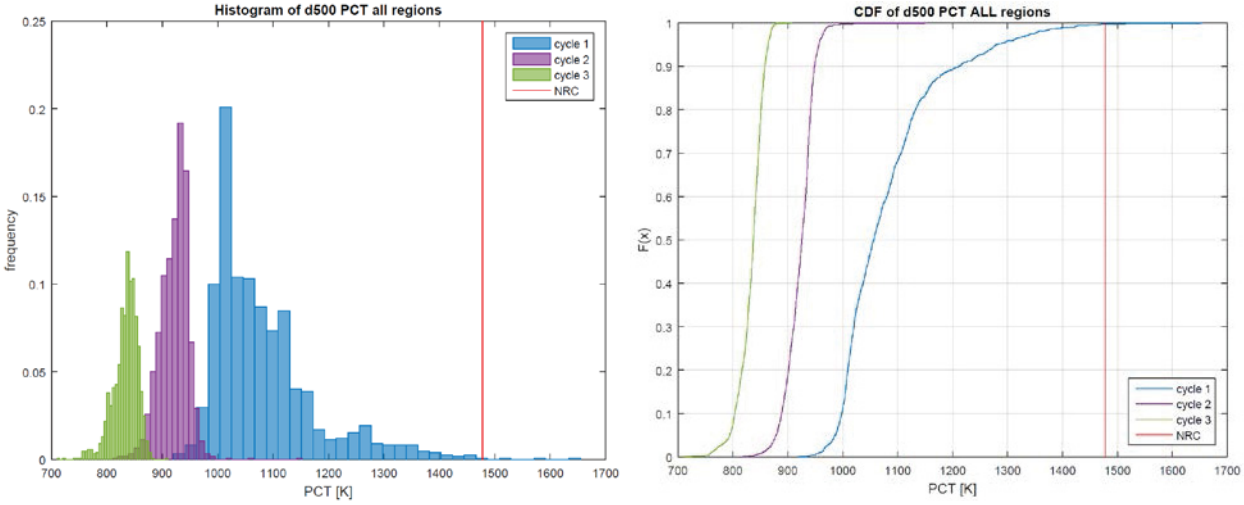

Figure A-21. PCT Histograms and CDFs at 500 Days in the Cycle (Large Sample N=1240).

Figure A-19 through Figure A-21 only considered marginal distribution of the PCT within each region of the core, at the different times in cycle. They did not consider the ECR associated with each PCT sample. Figure A-22 provides the scatter plot between the cycle 1 PCT and ECR at the BOC, which exhibits the expected trend of a quadratic relationship between oxidation and PCT. In addition to the samples, Figure A-22 also provides the 95th quantile estimators and associated confidence intervals based on the marginal PCT and ECR distributions. Looking at the ECR at a particular PCT value provides the conditional distribution of ECR. As shown in Figure A-22, at the "slice" along the PCT 95th quantile estimator there is a finite chance that the ECR exceeds its 95th quantile estimator, as well as a finite chance that the ECR is below its 95th quantile estimator. This study focused on comparing the marginal PCT and marginal ECR 95th quantile estimators to the NRC limits. The marginal distribution on PCT integrates out the effect of ECR, and vice versa.

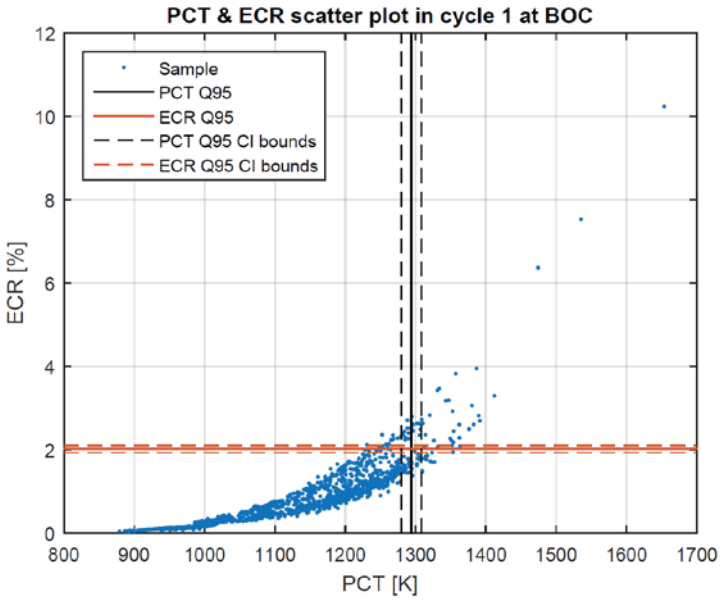

Figure A-22. Scatter Plot between PCT and ECR for Cycle 1 at the BOC (Large sample N=1240).

A-4. A RAVEN-Based LB-LOCA Computational Toolkit

The coupling of RAVEN with a Reactor Physics/TH suite (see Section 5.1), allows performing a classical probabilistic analysis using Wilk's formula, testing that with 95% probability and 95% confidence the failure limits are not achieved. This study could be performed either for a selected number of depletion points or making the time of the maneuver a randomly sampled variable. Since the maneuver that generates the pre LOCA skewed power shape is supposed to take place in a random fashion during the cycle, embedding this parameter in the set of parameters randomly sampled seems to be the most appropriate choice. This would be possible only if the integration of the depletion and the LOCA analysis will be implemented as explained in Section 5.1.

The number of samples required by the Wilk's formula is fairly limited and therefore the implementation of this step will not pose particular computational challenges.

The analysis suggested in the following requires a much larger number of runs and therefore are computationally more challenging. For this reason it could be useful for some of those analysis use a surrogate model. Surrogate models are system of equation of easy solution whose coefficients could be chosen so that the equation system mimics a given physical system. The coefficients of a surrogate model are "trained" using known responses of the system to a set of point in the input space (training set). The accuracy of a surrogate model usually increases with the size of the training set as also the training and evaluation cost.

The choice to use a surrogate or use the direct representation of the physical system (RELAP5-3D and PHISICS) will be made case by case depending on the accuracy requested by each specific type of analysis of the system. Preference, when computationally affordable, will be given to the usage of the physic-based model.

No matter which choice will be taken for each specific type of analysis there will be the need to sample at least once intensively the system. This will be a very computationally challenging task and the best methodology to perform this, given the type of problem at hand, will be the Hybrid Dynamic Event Tree.

The Dynamic Event Tree (DET) approach allows to achieve large computationally saving and to treat system with intrinsic stochastic behavior (aleatory uncertainties). The simultaneous presence of aleatory and epistemic variables, as in our case, requires the usage of a hybrid approach (Hybrid Dynamic Event Tree, H-DET) where an outer loop sampling the epistemic variables is wrapped around the DET algorithm. While this implementation is already available in RAVEN, a further improvement might be required to improve even more the computational efficiency. Given the fact that some of the parameters considered epistemic variables effect the system behavior only after the onset of the LOCA event, instead of sampling those parameters since the beginning of the simulation the sampling could be done after the beginning of the LOCA.

An example could be formulated using the time of the beginning of the LOCA and the break size (% of the pipe) respectively as the aleatory and stochastic variable (this is just an example and the variables used in the final analysis will be different from those).

Figure A-23 shows how a classic hybrid dynamic event tree is implemented while Figure 2 shows how the schema will be enhanced. Horizontal blue lines correspond to simulation time, vertical blue lines correspond to simulation branching, green arrows indicates where different sizes of the break lead to starting new simulations while black lines indicates where the different time (weeks) at which the LOCA takes place during the cycle drives the branching of the simulation

The simulation option shown in figure 2 has clearly less computational cost (computational cost is proportional to the horizontal blue lines).

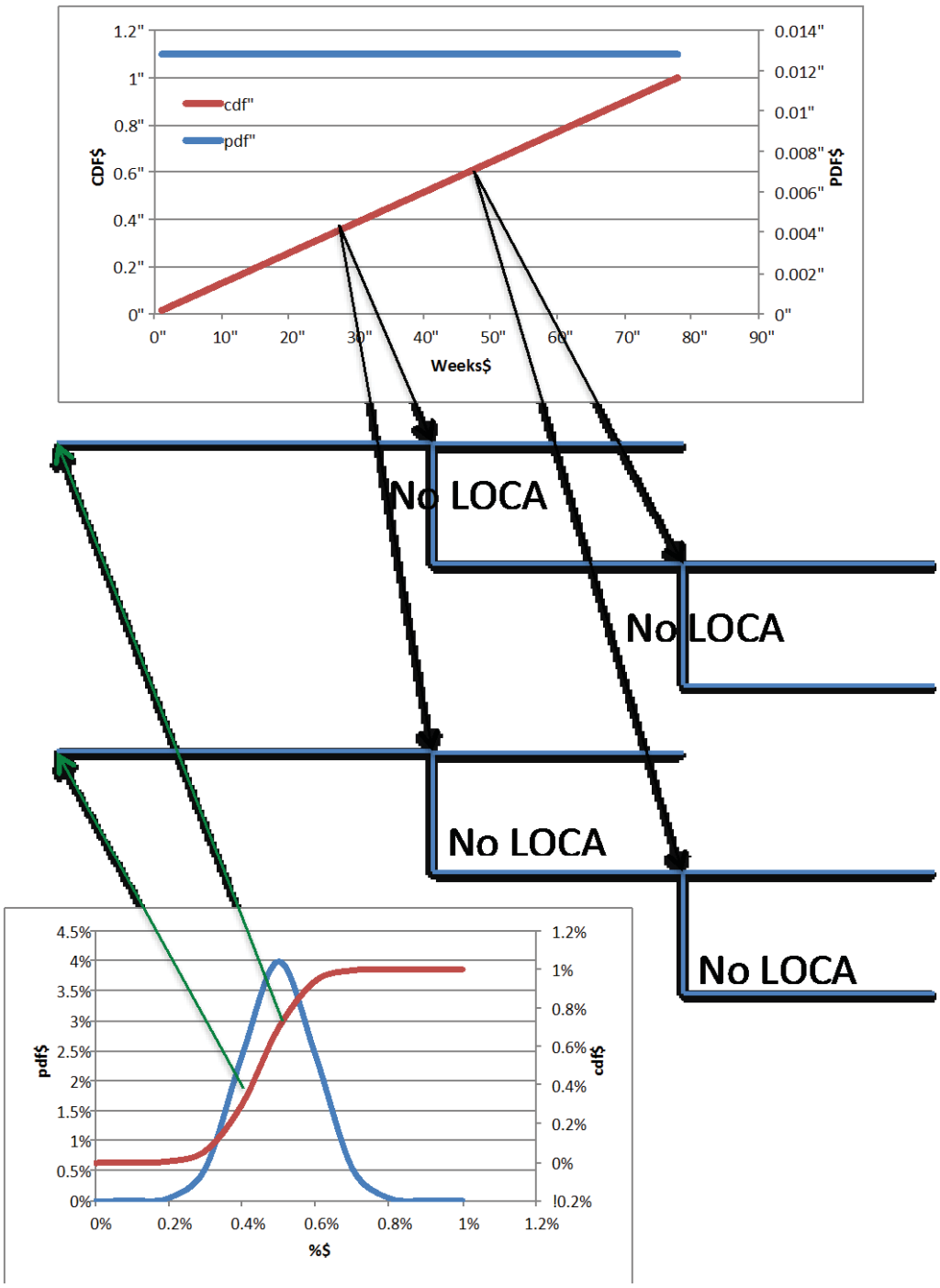

Figure A-23. Classical Hybrid Dynamic Event Tree Approach.

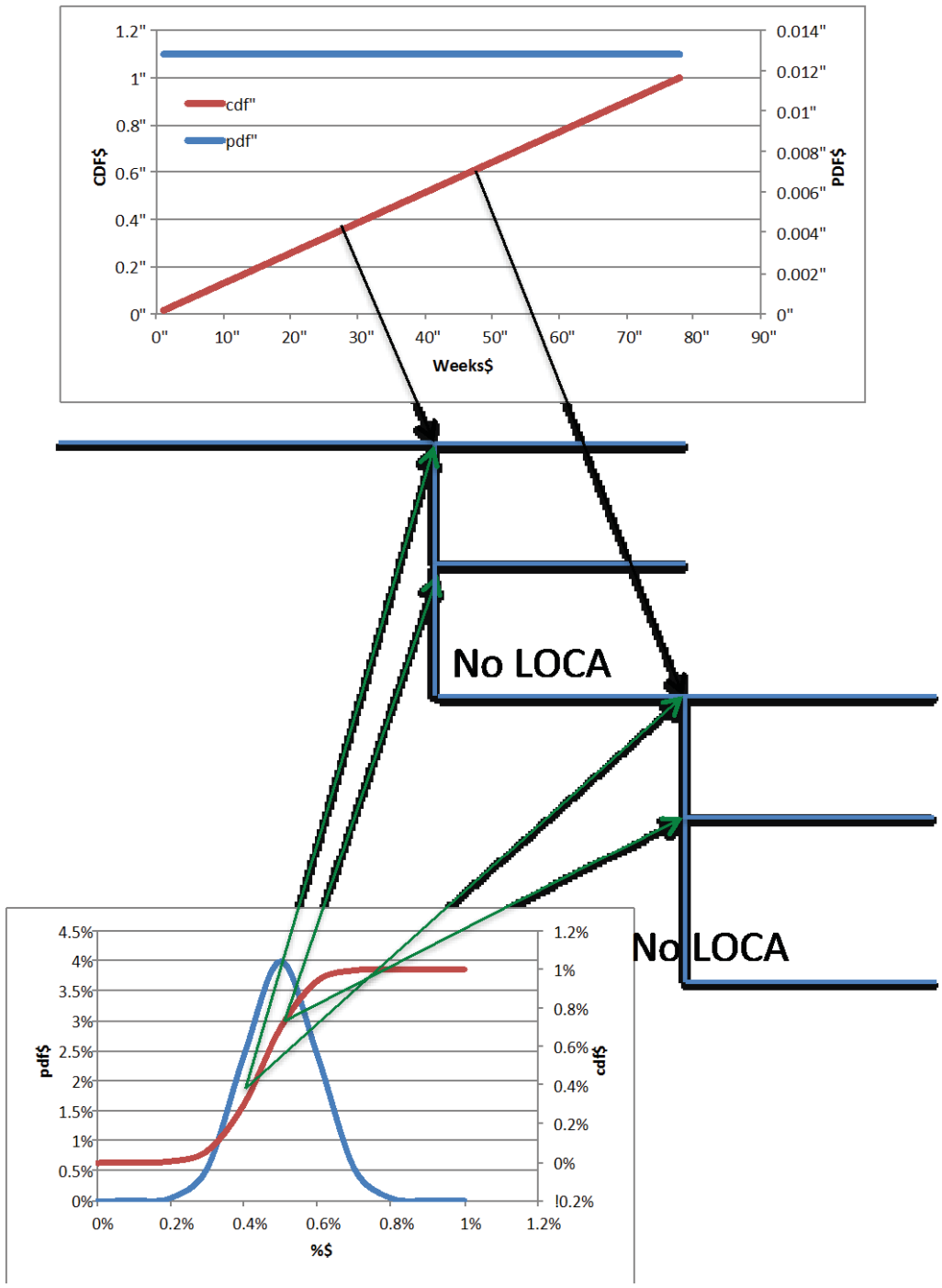

Figure A-24. Enhanced Hybrid Dynamic Event Tree Approach.

The implementation of the scheme in Figure A-24 will be performed soon in the next fiscal year so to have the needed computational capabilities.

Next step will the sensitivity analysis. This type of analysis is used to establish the relationship between the uncertain input parameters (e.g. fuel thermal conductivity) design parameters and figure of merits used to assess the severity of the accident. For example the sensitivity coefficients establish, under a linearity assumption, a direct linking between the uncertainties in the input parameters and in the FOMs.

For example the sensitivity coefficient ($\frac{\partial T_{max}}{\partial Tc}$) relates the thermal conductivity of the fuel (Tc) and its sigma (σ_{Tc}) to the sigma ($\sigma_{T_{max}}$) on the max clad temperature during the LOCA (T_{max}) by:

$$\sigma_{T_{max}} = \frac{\partial T_{max}}{\partial Tc}\sigma_{Tc}$$

RAVEN currently possesses global sensitivity analysis and local sensitivity analysis based on topological decomposition of the considered figured of merit (e.g. T_{max}). Without going into the details of the topological based analysis (found in INL-EXT-15-36632), the response of the system (FOM) is decomposed in patches adjoining minimum and maximum of the FOM and for each patch a sensitivity analysis is determined.

Figure A-25 shows the outcome of the topological sensitivity analysis performed for fuel performance. The uncertainty parameters are power scaling factor, grain radius, and fuel thermal expansion coefficient (in the figure respectfully: power_scalef, grainradius_scalef, and thermal_expansion). The response of the system (middle-plane von misses clad stress) is clustered in two different regions (blue and yellow) and on the right is reported a table summarizing the sensitivity coefficients for the two regions.

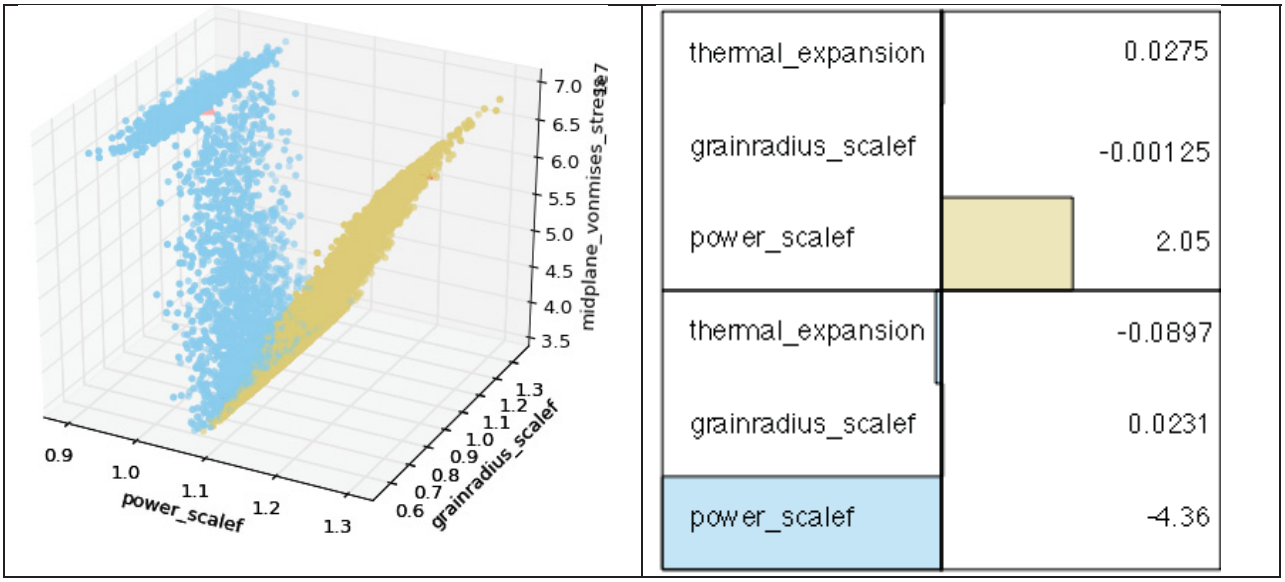

Figure A-25. Topological Sensitivity Analysis Performed for Fuel Performance.

The sensitivity analysis is used in several different ways for example the parameter with the highest (in module) relative sensitive coefficient is the parameter more important in controlling the behavior of the FOM. Given a FOM, its mean or nominal value $\langle FOM \rangle$, a set of parameter p_i and its mean or nominal value $\langle p_i \rangle$, the value of $s_i = \left|\frac{\partial FOM}{\partial p_i}\frac{\langle p_i \rangle}{\langle FOM \rangle}\right|$ could be used to construct a ranking of importance of the p_i (highest importance corresponded to the higher s_i). The determination of the importance of each single parameter allows plan management optimization (if the parameter is part of the control space of the plant) or to reduce the uncertainty in the risk assessment by reducing the uncertainty on the parameter itself (additional experiments if the parameter is experimental measured or higher fidelity simulation if the parameter is the output of a simulation).

Another common use of sensitivity analysis is an approximate evaluation of margins. For example, if the FOM is the maximum temperature achieved during a transient and the failure of the system is determined by exceeding a certain threshold ($T_{max} > T_{Tr}$) and the T_{max} is assumed normally distributed one can use the distance between the threshold and the mean value of the max temperature measured in sigmas ($\frac{T_{max}-T_{Tr}}{\sigma_{T_{max}}}$) to assess the probability of exceeding the threshold.

One of the challenges in the case of interest of this work is that it is not possible to construct a continuous function (FOM) that could be explicitly used as cost function to determine the success failure of the system. The maximum allowable temperature of the clad is a discontinuous function of the burn up. Consequently it is not possible to use the approximated approach described above to compute probabilistic margins.

Exactly for situations like this, the limit surface searching algorithms have been implemented in RAVEN. The limit surface is a hyper-surface in the input parameter space that classifies the values of the parameters leading to a failure of the system to the one leading to a success. For the specific case, the algorithm will identify the input space for which the limit temperature (burn up dependent) is not exceeded. Once such a space is identified RAVEN can compute the volume surrounded by the limit surface weighted by the probability of the parameters to have realization with such space. The result of such a process is the probability of failure of the system.

Figure A-26 shows a limit surface where the allowable space (safe region not leading to clad damage) has been identified for 3 parameters (Power level, Diesel Failure time, Diesel Recovery time) in a demo case of station black-out (SBO).

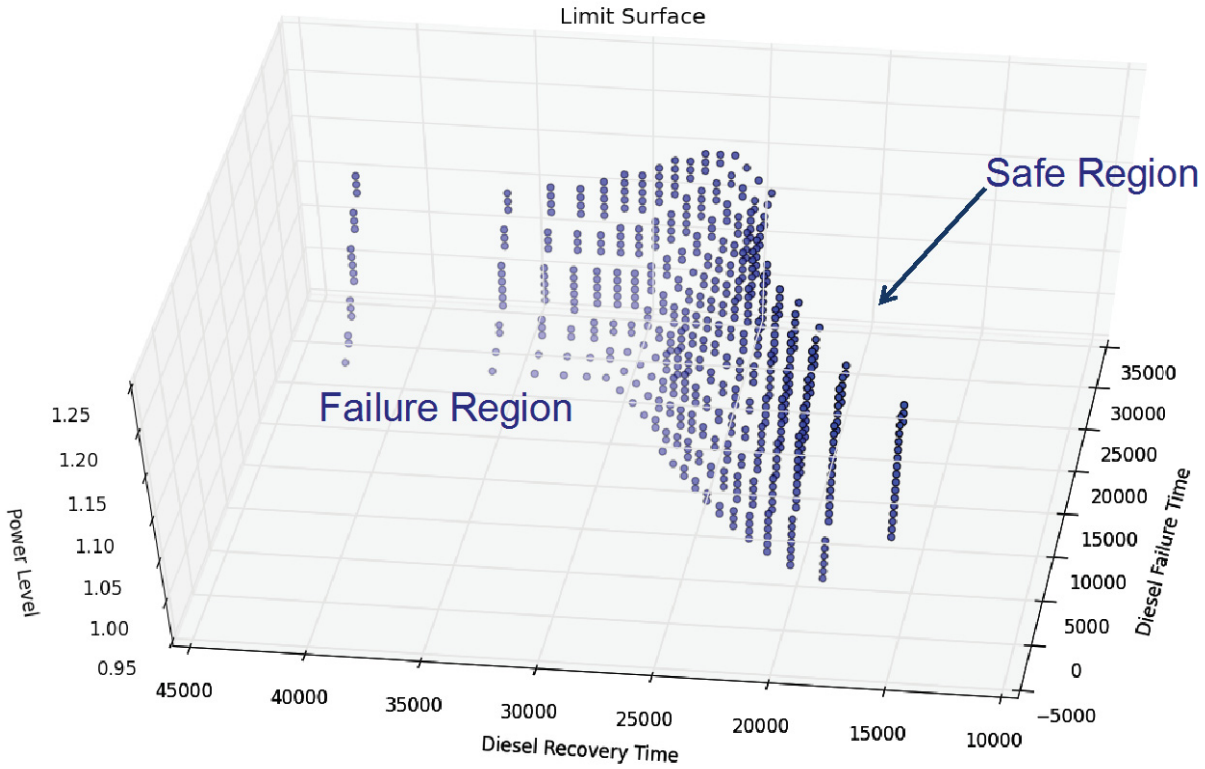

Figure A-26. An Example of Limit Surface for a Station Black-Out Demonstration.

While when using the global sensitivity analysis it is coherent with the underlying approximation to assume that variation of the failure of the system is given by (using the previous example):

$$\left.\frac{\partial N\left(\langle T_{max}\rangle, \sigma_{T_{max}}\right)}{\partial T_{max}}\right|_{T_{max}=T_{Tr}} \frac{\partial T_{max}}{\partial Tc}$$

Where $N\left(\langle T_{max}\rangle, \sigma_{T_{max}}\right)$ is a normal distribution.

When using the limit surface approach this evaluation is not straightforward due to the absence of an explicitly definition of the FOM subject to the failure constrain. There are currently ongoing efforts to define surface integrals of the probability flow crossing the limit surface. At this point the work has been only explorative.

RAVEN can determine given a set probabilistic parameters $\{p_{p,i}\}$ (e.g. fuel thermal conductivity), and a set of operational parameters $\{p_{o,i}\}$ (e.g. initial boron concentration, mass flow rate) which is the point that statistically has the lowest chances to lead to a failure of the system (safest point). For each realization of the uncertain parameters the farthest point from the limit surface is chosen as being the safest, several realization of the uncertain parameters are generated and the probability weighted average of the coordinate of each safest point is considered the global safest point.

This type of approach could be extended to treat several operative questions but probably could not be extended to perform risk adverse load pattern optimization analysis. Currently industry, given the high dimensionality and discontinuity of the problem, uses genetic algorithms. Combining load pattern search optimization for fuel utilization with probabilistic risk analysis could become quickly overwhelming. A possible solution could be generate surrogate models of the core transient simulation as a function of the burn up of the single assemblies and combine these with the genetic algorithm classically used.